University *of*
Leicester

Absorption Line Variability in BALQSOs and NGC 4151

Conor Wildy

Supervisor:

Michael Goad

Thesis submitted for the degree of
Doctor of Philosophy
at the University of Leicester.

X-ray & Observational Astronomy Group
Department of Physics and Astronomy
University of Leicester

September 22, 2015

Absorption Line Variability in BALQSOs and NGC 4151

Conor Wildy

ABSTRACT

Blueshifted AGN absorption lines indicate outflowing material from the central engine. Many repeat spectral observations of AGN have observed variability in the shape and strength of these lines, however there is no scientific consensus regarding the dominant mechanism which drives this variability. The main purpose of this thesis is to investigate this mechanism in a sample of BALQSOs and a Seyfert 1 galaxy.

The BALQSO sample consists of 50 quasars, in which we test the dependence of broad absorption line variability on several variables. To do this a novel technique is used (Non-negative matrix factorisation) to reconstruct the entire emission profile, allowing accurate measurement of variability even in cases of absorption line overlap with the corresponding broad emission line. No significant correlations between variability and any of the investigated properties are found. The lack of luminosity correlation suggests ionisation changes do not play a dominant role in the variability of the BALQSO population.

The most variable BALQSO in the 50 quasar sample, SDSS J113831.4+351725.3, shows extraordinary BAL variability, with one C IV BAL lying outside the random walk model which accurately predicted the BAL behaviour in a large BAL study. Co-ordinated BAL changes in this object, despite being separated by thousands of km s^{-1}, together with results of photoionisation simulations and the behaviour of the continuum, strongly suggest that the variability mechanism is ionisation fraction changes driven by variations in the input ionising continuum.

The Seyfert 1 galaxy NGC 4151 is noted for its continuum variability, however its absorption line variability is less well studied. Examination of the variability of metastable helium absorption lines, which are sensitive to high column densities, suggests a crossing-clouds scenario in which changes to the line-of-sight covering fraction occur, thereby driving spectral changes. Photoionisation calculations suggest a mass outflow rate which is too small to result in galaxy feedback effects.

Publications

A significant amount of work contained in this thesis has been published in the following papers:

Wildy, C., Goad, M. R. and Allen, J. T., "Quasar broad absorption line variability measurements using reconstructions of unabsorbed spectra", MNRAS, 2014, 437, 1976

Wildy, C., Goad, M. R. and Allen, J. T., "SDSS J1138+3517: a quasar showing remarkably variable broad absorption lines", MNRAS, 2015, 448, 2397

Acknowledgements

Firstly I would like to thank my supervisor, Mike Goad, for his help and support throughout my time as a PhD student in Leicester. I'd also like to thank all those with whom I have shared the G24A office with since my arrival in October 2011, their good humour and helpfulness is greatly appreciated. Thanks must also go to Klass Wiersema for his advice on many aspects of spectroscopy. I could not have got to this point without the love and financial support of my parents, to whom I am extremely grateful. I am also indebted to my collaborators James Allen and Hermine Landt whose contributions have made the work in this thesis possible. Much of the data used in this thesis was obtained from the Sloan Digital Sky Survey. Funding for the SDSS and SDSS-II has been provided by the Alfred P. Sloan Foundation, the Participating Institutions, the National Science Foundation, the U.S. Department of Energy, the National Aeronautics and Space Administration, the Japanese Monbukagakusho, the Max Planck Society, and the Higher Education Funding Council for England. The SDSS Web Site is http://www.sdss.org. I would like to acknowledge funding for my PhD from the STFC.

Contents

List of Figures

List of Tables

Chapter 1

Introduction

A small fraction of galaxies show excess emission from their central regions which cannot be explained by stellar phenomena. The bright nuclei of these galaxies, which can outshine the entire combined stellar emission, are known as active galactic nuclei (AGN) and are the most powerful persistent sources in the universe. These objects are now known to be strong emitters across a frequency range spanning many decades and with a bolometric magnitude likewise spanning an extraordinarily large range ($10^{40} \leq L_{bol} \leq 10^{48}$ erg s^{-1}) (Filippenko et al., 1993; Banerji et al., 2015). The first spectroscopic observation of what was to become known as an AGN was that of NGC 1068 obtained from the Lick Observatory 1908 by E.A. Fath (Fath, 1909). A later, higher resolution spectrum of the same galaxy observed by V.M. Slipher enabled measurement of the width of the emission lines, which were found to extended over hundreds of kilometres per second.

Further understanding of the phenomenon resulted from the work of Carl Seyfert (Seyfert, 1943). He noted that several galaxies shared certain unusual properties, specifically in relation to intense emission from a point-like object at their centres. These objects were found to be the source of the emission lines of the type observed in NGC 1068, hence introducing the idea that these galaxies could be said to form a distinct category (now known as "Seyfert galaxies"). Seyfert galaxies were subsequently divided into 'Types' according to their emission line properties (Khachikian & Weedman, 1971). Seyfert's realisation helped pave the way for research in the coming decades and the eventual acceptance of a unified explanation for the AGN phenomenon based on the model of an accreting black hole providing the energy source.

Much progress in the second half of the twentieth century came initially from the rapidly advancing field of radio astronomy. An unusual class of object was noted, for example in the 3C catalogue (Edge et al., 1959), which exhibited radio emission from optically unresolved sources. These objects became known as quasi-stellar radio sources (quasars for short) due to the stellar-like (point source) nature of the images taken. In 1963 Maarten Schmidt, a researcher at Caltech, realised that many of the hitherto unidentifiable optical and ultra-violet (UV) emission lines from the radio source 3C 273 could be explained in terms of a consistent *redshift* of about 16 per cent from the laboratory rest frame (Schmidt, 1963). A spectroscopic redshift (z) can be defined as follows:

$$z = \frac{\lambda - \lambda_0}{\lambda_0}\,, \tag{1.1}$$

where λ is the observed wavelength and λ_0 is the wavelength in the source rest-frame. This redshift was attributed to the 'stretching' of light from distant sources due to the expansion of the universe. By applying Hubble's law ($d = cz/H_0$, where H_0 is the Hubble constant), the finding inferred distances to quasars which were greater than any object yet discovered. Approximately 10 percent of quasars are defined as *radio-loud*, with the remainder defined as *radio-quiet*. This fraction, however, may be a strong function of redshift and luminosity (Jiang et al., 2007). The definition of a radio-loud quasar is based on the ratio of radio flux to optical flux. A quasar that is labelled as radio-quiet is not necessarily radio silent.

With the dawn of X-ray astronomy in the 1960s, enabled initially through the use of sounding rockets, an isotropic background of X-ray emission was detected, with several peaks in emission discovered as originating from sources such as the galactic centre and the crab nebula (Giacconi et al., 1962; Bowyer et al., 1964). The first observation of an AGN in X-rays was carried out by Friedman & Byram (1967), who detected emission from the 16.4 Mpc-distant active galaxy M87. Due to the high energy environment of the innermost regions of AGNs, X-ray observations continue to be of vital importance and are studied using major space-based observatories such as *XMM-Newton* and *Chandra*, both of which were launched in 1999. Detection of AGN at even higher energies, within the Gamma-ray regime, have also played an important role in their understanding. These observations came of age with the launch of the Compton Gamma Ray Observatory in 1991.

1.1 AGN structure and emission features

1.1.1 The power generation mechanism

Historically, a puzzling question regarding the nature of AGNs concerned the mechanism which allowed vast quantities of power to be generated in a relatively tiny volume. Observations using telescopes with the highest angular resolution (such as the Hubble Space Telescope) of the nearest AGNs fail to resolve the central continuum source, indicating the luminosity must originate in a volume less than $\sim$1 pc across. The processes occurring in AGN can only be satisfactorily explained by accretion of matter onto a massive central object, as any possible configuration of stars numerous enough to produce sufficient luminosity would collapse on rapid timescales compared to a galaxy lifetime.

The accretion explanation is rooted in the need to extract large amounts of energy per infalling mass. For the nuclear fusion process that occurs in stars, this energy efficiency is 0.7 percent that of the annihilation energy (given by E=mc^2). For accretion onto a compact object, this value can be much higher. If the central accreting source is a supermassive black hole (SMBH), masses of 10^8 $M_\odot$ should be common. Calculating the energy liberated by the accretion process requires knowledge of the Schawrzschild radius, which represents the radius of the event horizon of non-rotating black hole. This is given by

$$R_S = \frac{2GM}{c^2}\,, \tag{1.2}$$

where G is the gravitational constant, M is the mass of the black hole and c is the speed of light in a vacuum. For a Kerr (rotating) black hole, the radial location of the *innermost stable orbit* (R_{in}) of a test particle can be calculated using:

$$R_{in} = \frac{R_S}{2}\left[3 + Z_2 \mp \sqrt{(3 - Z_1)\,(3 + Z_1 + 2Z_2)}\right] \tag{1.3}$$

where the upper sign is used when the particle is co-rotating with the black hole and the lower sign is used when it is counter-rotating. The parameters Z_1 and Z_2 are given by

$$Z_1 = 1 + \left(1 - \frac{4a^2}{R_S^2}\right)^{\frac{1}{3}} \left[\left(1 + \frac{2a}{R_S}\right)^{\frac{1}{3}} + \left(1 - \frac{2a}{R_S}\right)^{\frac{1}{3}}\right] \tag{1.4}$$

and

$$Z_2 = \sqrt{\frac{12a^2}{R_S^2} + Z_1^2} \tag{1.5}$$

with a being a parameter which includes the black hole angular momentum J_{BH} and is given by

$$a = \frac{J_{BH}}{Mc^2} \tag{1.6}$$

with the maximum allowed angular momentum occurring at $a = GM/c^2$. The rate of energy emission from the accreted matter can be expressed as $L = \eta \dot{M} c^2$, where $\dot{M}$ is the rate of mass accretion and η is the efficiency relative to the annihilation of this mass. This efficiency can be expressed in terms of R_{in} by

$$\eta = 1 - \sqrt{1 - \frac{R_S}{3R_{in}}} \tag{1.7}$$

The theoretical maximum efficiency occurs when matter accretes onto a maximally-rotating black hole in the co-rotational sense, giving $\eta = 0.42$. Accretion onto a non-rotating ($a = 0$) black hole is lower (although still much greater than the stellar fusion efficiency) at $\eta = 0.057$. It is therefore simple to show that, for typical AGN luminosities, accretion rates up to the order of a solar mass per year are sufficient to explain their energy output, with the most luminous quasars requiring in excess of 100 $M_\odot$ yr^{-1}. The success of accretion theory in providing an explanation of AGN luminosity has resulted in a scientific consensus regarding the existence of a SMBH in the central engine powering the phenomena (Peterson, 1997).

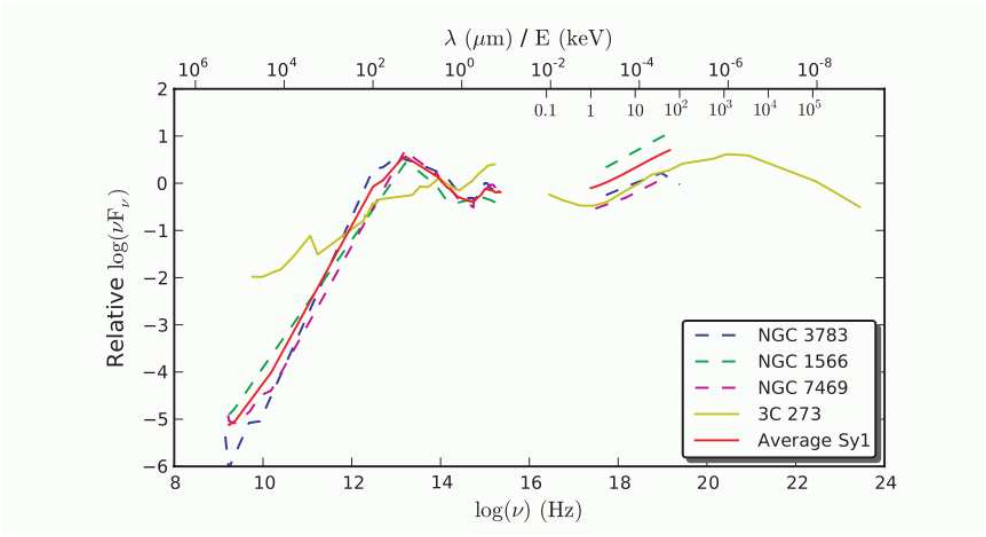

Figure 1.1: The object rest-frame SEDs of several AGN, including three Seyfert 1 galaxies (NGC 3783, NGC 1566 and NGC 7469) and their average SED, along with the SED of the quasar 3C 273. The gap in coverage from approximately 10^{-2} to 10^{-1} μm is due to absorption by neutral hydrogen. This image originally appeared as 'Figure 3' in the article "The spectral energy distribution of the central parsecs of the nearest AGN" by Prieto et al. (2010).

1.1.2 The AGN Spectral Energy Distribution

Power generated by the accretion mechanism is converted, both directly and indirectly, to a 'featureless' continuum spanning several decades in frequency space via several processes, some of which are still poorly understood. Typical Spectral Energy Distributions (SEDs) of this continuum are shown in Figure 1.1.

The SED curves are relatively flat across spectral wavebands ranging from optical to hard x-rays. One notable feature is the presence of a 'Big Blue Bump' of excess flux peaking at extreme ultraviolet (EUV) wavelengths, which is thought to be the peak of thermal emission corresponding to a blackbody temperature of T$\sim 10^5$ K. The components of AGN thought to give rise to various parts of this SED are described in the following subsections.

1.1.3 The accretion disc

Material falling inwards toward the central black hole converts much of its initial gravitational potential energy into thermal energy by means of viscous processes within a relatively flat structure known as an accretion disc. This disc lies at distances from the black hole greater than its innermost stable orbit and is thought to consist of material in an optically thick, geometrically thin configuration (Shakura & Sunyaev, 1973). In thermal equilibrium, all of the thermal energy gained by the accretion disc from infalling matter is subsequently radiated. Due to the disc's optical thickness, the direct emission from the disc is in the form of blackbody radiation given by Planck's Law:

$$B_\nu(T) = \frac{2h\nu^3}{c^2} \frac{1}{e^{\frac{hv}{kT}} - 1}\,, \tag{1.8}$$

where $B_\nu(T)$ is the intensity of blackbody radiation at frequency ν and temperature T, k is the Boltzmann constant and h is Planck's constant. The disc is fuelled by the inflow of material, which provides the energy powering the AGN luminosity. The peak frequency of Blackbody emission can be found using the Wien displacement law given by

$$h\nu_{max} = 2.82kT\,, \tag{1.9}$$

where ν_{max} is the frequency of the emission peak.

The temperature of a particular location on the accretion disc is a function of its radial distance from the black hole (r). The radial temperature distribution can be estimated by considering a mass inflow rate $\dot{M}$ within an annulus of a small radial size dr at some r. The rate of change of the potential energy of this mass is then:

$$\frac{dU}{dt} = \frac{GM\dot{M}}{r^2} dr\,, \tag{1.10}$$

If half of this energy goes into kinetic energy (subsequently advected into the black hole) and the other half is ultimately radiated, the luminosity at r is given by:

$$L = \frac{GM\dot{M}}{2r^2} dr \,, \tag{1.11}$$

The luminosity per unit area of a blackbody emitter is σT^4, where σ is the Stefan-Boltzmann constant. Therefore, using the fact that the (double-sided) area of such an annulus is $4\pi r dr$ and the luminosity expression in Equation 1.11, it is simple to show that:

$$\sigma T^4 = \frac{GM\dot{M}}{8\pi r^3} \,, \tag{1.12}$$

This expression can be re-arranged to provide the radial temperature distribution as follows:

$$T = \left(\frac{GM\dot{M}}{8\pi\sigma r^3} \right)^{\frac{1}{4}} \,, \tag{1.13}$$

However, this relation does not account for viscous energy transfer in the disc. Correcting for this yields a more accurate temperature distribution, which is given by:

$$T(r) = \left[\frac{3GM\dot{M}}{8\pi\sigma r^3} \left(1 - \sqrt{\frac{R_{in}}{r}} \right) \right] \,, \tag{1.14}$$

This equation can be simplified by imposing the condition $r \gg R_{in}$ to obtain:

$$T(r) \approx \left(\frac{3GM\dot{M}}{8\pi\sigma R_S^3} \right)^{\frac{1}{4}} \left(\frac{r}{R_S} \right)^{-\frac{3}{4}} \,, \tag{1.15}$$

It is useful to re-write Equation 1.15 so that it includes the *Eddington accretion rate* ($\dot{M}_E$) since many supermassive black holes powering AGN are accreting at substantial fractions of this rate. The Eddington accretion rate is defined as the rate of accretion of a black hole whose disc is radiating at the *Eddington luminosity*, which is the energy output an object requires to balance the inward gravitational force on surrounding matter with the outward radiation pressure. The Eddington luminosity can be derived by considering a situation where a source of luminosity L produces a force due to radiation pressure on an electron. The electrons will be accelerated much more readily than protons due to their

much lower mass. As electrons are 'pushed' outward by the radiation pressure, the electrostatic attraction on protons in the plasma will tend to 'drag' them along with the electrons. However, due to their much greater mass, the source's gravity exerts a much greater pull on the protons than the electrons. The situation in which radiation pressure balances gravitational attraction can therefore be described by setting the force due to radiation pressure on an electron equal to the gravitational force on a proton at a distance r from the source, as follows

$$\frac{\sigma_e L}{4\pi c r^2} = \frac{GMm_p}{r^2}\,, \tag{1.16}$$

where σ_e is the Thomson cross-section and m_p is the proton mass. The luminosity in this case is the Eddington luminosity L_E, so re-arranging Equation 1.16 gives:

$$L_E = \frac{4\pi G c m_p M}{\sigma_e}\,, \tag{1.17}$$

By assuming a typical accretion efficiency of η=0.1, the Eddington accretion rate can be expressed as $\dot{M}_E = 0.1mc^2$. Equation 1.15 can therefore be re-written as

$$T(r) \approx 6.3 \times 10^5 \left(\frac{\dot{M}}{\dot{M}_E}\right)^{\frac{1}{4}} \left(\frac{M}{10^8 M_\odot}\right)^{-\frac{1}{4}} \left(\frac{r}{R_S}\right)^{-\frac{3}{4}} K\,, \tag{1.18}$$

which is the radial temperature distribution of an accretion disc around a SMBH in an AGN.

1.1.4 The Broad Emission Line Region

One of the earliest noted features of the optical spectra of Seyfert galaxies and quasars was the presence of broad emission lines in transitions such as the Balmer series and He II λ4686. Those AGN exhibiting these broad emission line components in their spectra, unless labelled as quasars, are known as Type 1 Seyfert Galaxies (Seyfert 1s). A defining feature of the active nucleus in Seyfert 2 galaxies is the absence of these broad components from their emission lines. The broad emission lines have typical FWHM of 5000 km s^{-1}, with velocity widths ranging from 500 km s^{-1} to over 10 000 km s^{-1}, and span a range of ionisation states from neutral hydrogen to highly ionised species such as N V. The

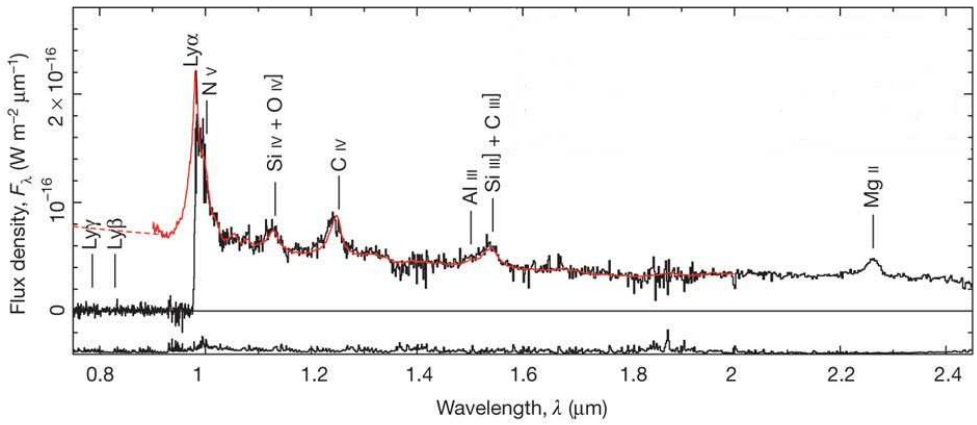

Figure 1.2: Near-infrared spectrum of the quasar ULAS J112001.48+064124.3, with broad emission lines labelled (Mortlock et al., 2011). These lines have been shifted from the UV, which is the spectral region they would occupy in the rest-frame of the quasar, to the observed wavelengths due to its large redshift (z=7.085).

advance of telescope technology has led to these lines also being observed in UV and Near-infrared (NIR) transitions.

A possible simple assumption is that this large range of Doppler shifts is the result of thermal motions in the emitting gas, resulting in a temperature estimate of over 10^9 K. However at such high temperatures, the observed atomic and ionic species producing the lines could not exist, indicating that another explanation is needed. The correct description is based on the proximity of the gas to a massive compact object (in this case the SMBH), allowing material with very large Keplerian orbit velocities to exist at relatively small distances from the black hole. Therefore, bulk motion of the gas orbiting as clouds close to the central object, in a region known as the *broad line region* (BLR), can produce the observed broad lines, with the source of ionising photons being the region near the accretion disc.

An estimate of an approximate range of electron temperatures present in the BLR can be made using the following methods: (i) An upper limit of $T_e \leq 35\,000$ K on the BLR plasma's electron temperature is inferred from the presence of Fe II emission (Osterbrock & Ferland, 2006), such as in the feature known as the 'small blue bump' in the UV spectrum, as above this temperature almost all Fe II would be ionised via electron impacts to Fe III, and (ii) line ratios can be used to constrain the temperature range, indicating it is between roughly 13 000 and 37 000 K (Popović, 2003). However there are significant uncertainities in these temperature limits due to the possibility that BLR properties vary by location. The BLR density range can be estimated from the presence and absence of various broadened emission

lines in the spectra if the *critical density* of these lines is known. The critical density is the electron density at which suppression of the emission line through collisional de-excitation becomes significant. The absence of a significant broad emission component of the forbidden [O III] λ4363 line, given its critical density of $\sim 10^8$ cm^{-3}, means this value can be taken as an approximate lower limit to the BLR density (Peterson et al., 1998). The semi-forbidden C III] λ1909 line shows a strong broad component in Type 1 AGN, implying an upper limit to the BLR density of $\sim 10^{10}$ cm^{-3}. However, this value may underestimate the densest parts of the BLR given the difference in location of the C III] λ1909 emitting material with respect to the gas contributing to other broad lines such as C IV and Lyα, as indicated by reverberation mapping (Ferland et al., 1992).

Reverberation mapping

The size of the BLR can be investigated using a technique known as *reverberation mapping*. This method utilises the time delay between the observed change in the continuum (produced in the environment of the accretion disc) and observed changes in the broad emission lines. Due to the relatively high density of the BLR, the recombination rate τ given by τ=1($n_e \sigma_{rec}$, where σ_{rec} is the recombination rate coefficient, is rapid compared to the variability timescale of AGN far UV emission (which is the main contributor to BLR photoionisation). For example, H II recombines on timescales of $\sim$4000 seconds at $n_e \sim 10^9$ cm^{-3} and $T_e \sim$=20 000 K, while for high ionization species such as C III, C IV, Si III and Si IV this timescale is even shorter (Osterbrock & Ferland, 2006; Schippers et al., 2001). This compares with characteristic UV variability timescales in even the most variable AGN of 1 day or more, e.g. Crenshaw et al. (1996). This allows the delay to be considered a measurement of the light-travel time between the continuum emitting region and the BLR, and hence to be used to calculate the distance between the two (Blandford & McKee, 1982). Since the accretion disc is small compared to the BLR, this distance is effectively the BLR radius. Typical time delays are between 1 and 100 days depending on source luminosity, resulting in BLR radius estimates of approximately 2×10^{13} to 2×10^{15} m. Time delays are generally shorter for more highly ionised lines due to the greater intensity of ionising radiation in regions closer to the SMBH, e.g. Grier et al. (2012), suggesting the possibility that the BLR is spatially extended. Faster response times for more highly ionised transitions requires the rate of ionising photon emission to decrease more steeply with radial distance than gas density in the BLR. Reverberation measurements have now been carried out for approximately 50 nearby AGN (Peterson, 2014).

1.1.5 The hot corona

Although the thermal emission from the accretion disc peaks in the UV portion of the spectrum, the SED continues to much higher energies (hard X-rays and beyond, see Figure 1.1). Mechanisms which can produce such energetic photons are thus required to fully explain the AGN continuum emission. X-ray photons of energies up to 10 keV are thought to originate in a region of high energy electrons, which 'up-scatter' UV photons to higher energies via the inverse-Compton process (Haardt & Maraschi, 1991). The change in photon wavelength due to a photon-electron scattering event is given by

$$\lambda' = \lambda + \frac{h}{m_e c} \left(1 - \cos(\theta)\right) \ , \tag{1.19}$$

where λ and λ' are the photon wavelengths before and after the collision respectively, m_e is the electron mass and θ is the electron-photon scattering angle. Photons of energies higher than $\sim$10 keV can be produced in bremsstrahlung radiation, although the precise physics of the process producing the hard X-ray and γ-ray continuum of AGNs is beyond the scope of this thesis.

1.1.6 The Narrow line region

In addition to the broad emission lines, a second component of emission is visible at much narrower velocity widths, typically less than 1000 km s^{-1}, which are detectable in all types of AGN except blazars. The relative narrowness of these lines indicates that the emitting gas is orbiting at a much lower velocity and hence is located at a much greater distance than the clouds which give rise to the broad emission lines. This location is known as the *narrow line region* (NLR) and can extend over several kpc from the central SMBH, e.g. Pogge (1989b). It is photoionised by the same ionising continuum emission which powers the BLR. The large distances over which the NLR extends allows parts of the region to be resolved in nearby AGN, as indicated in Figure 1.3.

The NLR appears to have a much lower density than the BLR as indicated by the presence of narrow forbidden lines in their spectra. An example is the emission due to [O III] at 4959 Å and 5007 Å, the critical density of both these transitions being 7.0×10^5 cm^{-3}. This indicates that the density must be much lower than 10^6 cm^{-3} with a typical value as determined from the observed line ratios of

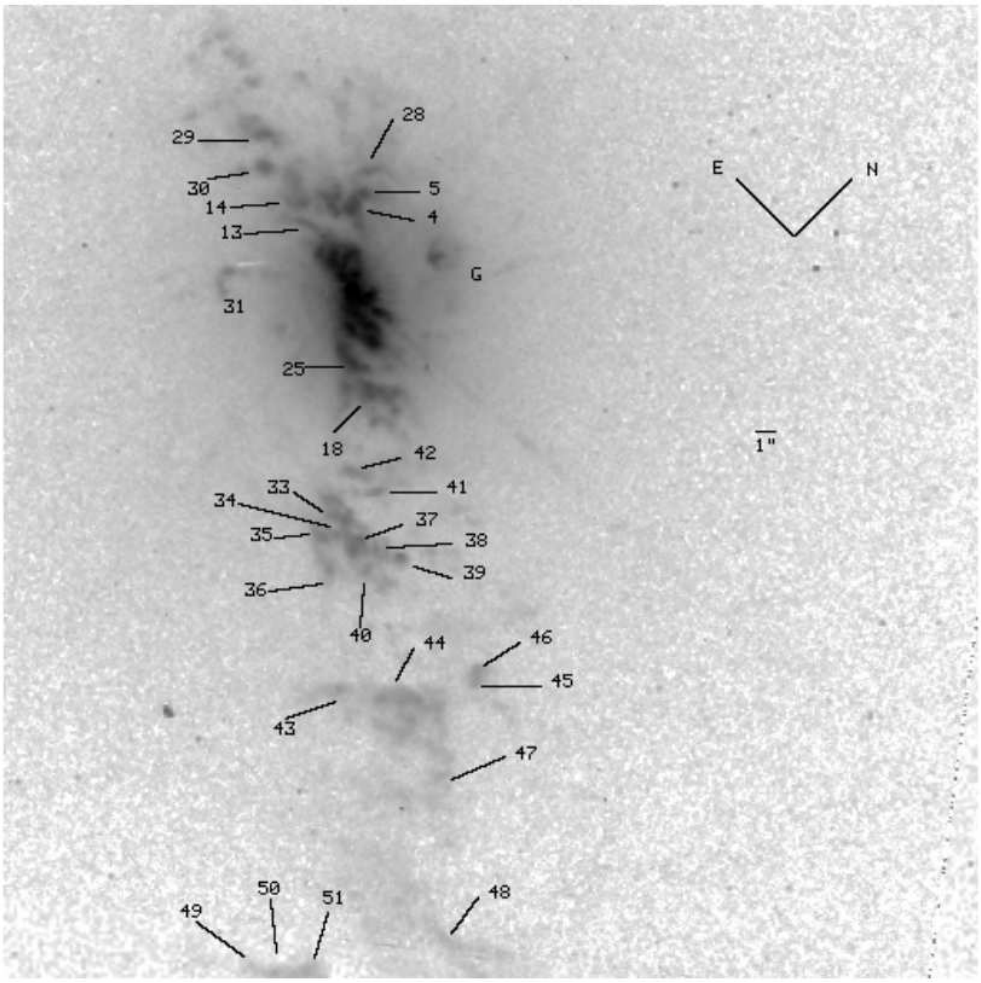

Figure 1.3: Direct Hubble Space Telescope Wide Field Camera image of the nuclear region of NGC 4151 using the F502N filter. Forbidden [O III] emission from the narrow line region is spatially resolved and labelled in this image (image taken from "The resolved narrow-line region in NGC 4151" by Kaiser et al. (2000), more details such as the properties of the labelled clouds are therein).

$\sim 10^3$ cm^{-3} (Koski, 1978). Temperatures in the NLR are thought to be similar to those in the BLR. The NLR clouds exist within a cone-shaped region, with this geometry due to the existence of an 'ionisation cone' exposed to substantial amounts of ionising continuum radiation. Some objects show evidence for an 'extended' narrow line region within this ionisation cone, extending up to 20 kpc from the SMBH, with correspondingly much lower line widths ($\sim$45 km s^{-1}) than those typically seen for NLR clouds (Unger et al., 1987). This emission is thought to originate in gas ionised by the AGN continuum but moving at velocities typical of galactic rotation at that distance.

1.1.7 The torus

A substantial proportion of the continuum in the near-infrared portion of the spectrum is attributable to blackbody emission from a dusty torus. The dust, which is located within a few pc of the central black hole, is heated by the central continuum source, allowing its hot inner regions reach a temperature of just over one thousand Kelvin (Barvainis, 1987; Rodríguez-Ardila & Mazzalay, 2006). Re-processing of the emission from the central AGN ionising continuum source as the torus heating mechanism is supported by simultaneous studies of the X-ray and infra-red emission from AGN, which indicate a correlation in their behaviour (Gandhi et al., 2009).

The existence of the torus plays a key role in theories of AGN unification, which attempt to ascribe differences in AGN classification to the viewing angle. In this scheme, the torus, which is generally illustrated as being co-planar with the accretion disc, obscures the nuclear continuum region along with the BLR when viewed 'edge-on', as is thought to be the case with Seyfert 2s. In these galaxies, no broad emission lines are visible, and the continuum is on average weaker than that observed for Seyfert 1s. Conversely, when the viewing angle is above the plane of the torus (but not directly down the jet), the full strength of the continuum and the BLR is visible. The fact that the torus reprocesses ionising photons into low energy photons explains the existence of the ionisation cones within which the NLR resides, as ionising radiation cannot penetrate beyond the torus at small angles with respect to its plane, as indicated in Figure 1.4.

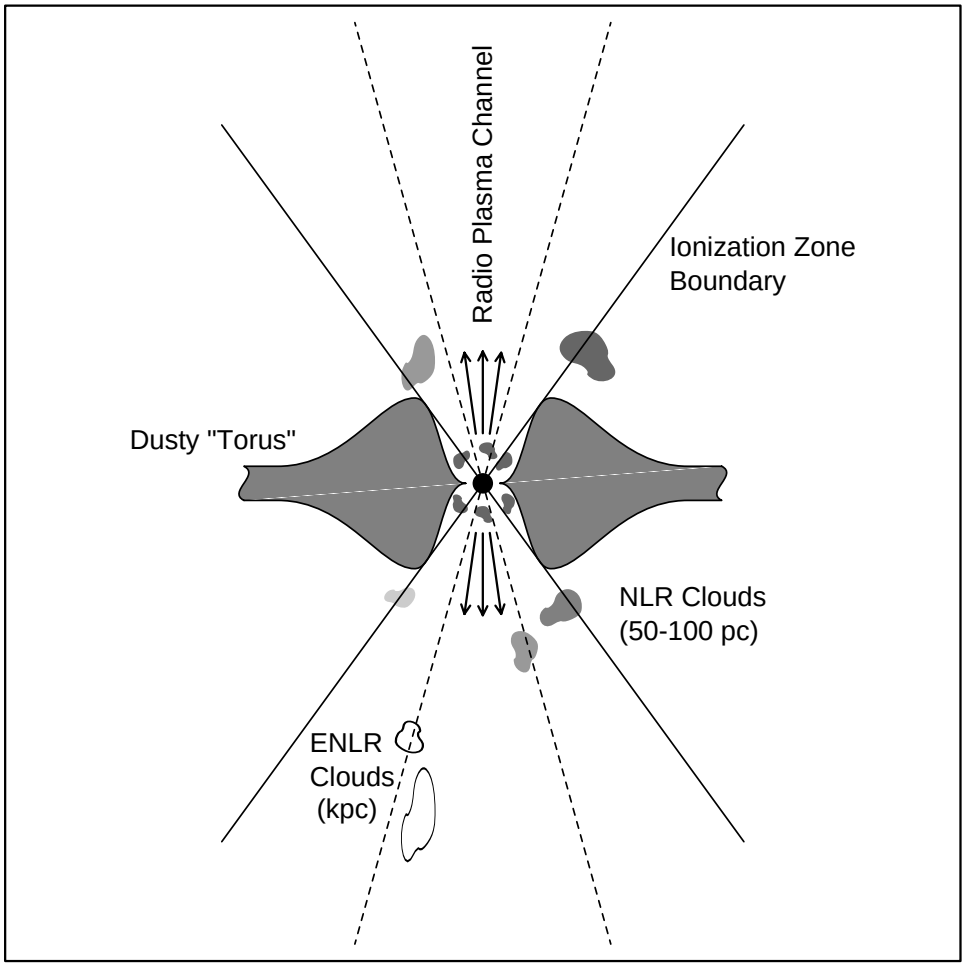

Figure 1.4: Torus and ionisation cone structure within an AGN, image adapted from Pogge (1989a).

1.1.8 AGN jets

The jets observed in AGN are highly collimated outflows moving at relativistic speeds, whose production mechanism is still not well understood. They originate close to the central black hole and can extend up to several Mpc into the surrounding environment, e.g. Godfrey et al. (2012). Due to their high velocity and extended spatial range, AGN jets can have a significant impact on the surrounding galactic and inter-galactic environments (Beall et al., 2003; Gaibler, 2014). Jets and their associated lobes are thought to be the origin of radio emission in radio-loud AGN, as well as generating photons with energies up to those found in the γ-ray part of the spectrum. These photons are generated through synchrotron emission resulting from the interaction of fast-moving charged particles in the jet with its complex arrangement of magnetic field lines. The gyrofrequency of such a charged particle undergoing

helical motion due to the presence of a magnetic field is given by:

$$\omega = \frac{qB}{\gamma mc}\,, \tag{1.20}$$

where q is the charge on the particle, B is the magnetic field strength, m is the particle mass and γ is the Lorentz factor.

1.1.9 AGN unification

Sources categorised as AGN, despite their similarities, can be sub-divided into smaller groupings based on spectral features such as the presence or absence of broad emission lines and the degree of radio loudness. These differences require explanations, while retaining a plausible mechanism for the very large power output of AGNs. As described in previous sub-sections, the absence of broad lines in Seyfert 2 galaxies can be thought of as resulting from a line-of-sight in which the central regions are shrouded from view by a molecular torus. This raises the possibility of differences in AGN categorisation being predominantly due to orientation effects, e.g. Urry & Padovani (1995). This scenario is known as the AGN unification model and is illustrated schematically in Figure 1.5.

At small line-of-sight angles with respect to the jet axis, the continuum is dominated by very strong non-thermal emission from the jet itself. Objects in this category are known as blazars. As the angle with respect to this axis increases, the synchrotron continuum decreases, allowing features in the inner portion of the AGN to become visible. These objects include quasars and Seyfert 1 galaxies, which exhibit broad emission lines in their UV, optical and IR spectra. At angles close to 90°, the viewing angle is directed towards the molecular torus, which obscures the BLR and reduces the observed strength of the continuum in the UV and optical parts of the spectrum. These objects are labelled Seyfert 2 galaxies or radio galaxies. Aside from the appealing simplicity of the model, support for AGN unification also emerges from spectropolarimetry of Seyfert 2 galaxies, which reveals otherwise obscured broad emission lines in light scattered from dust in the AGN environment (Antonucci & Miller, 1985; Ogle et al., 1997).

As the study of AGNs has advanced, sub-types with properties intermediate to those of Seyfert 1s and Seyfert 2s have been identified, such Seyfert 1.5s or 'narrow-line Seyfert 1s'. The Seyfert sub-

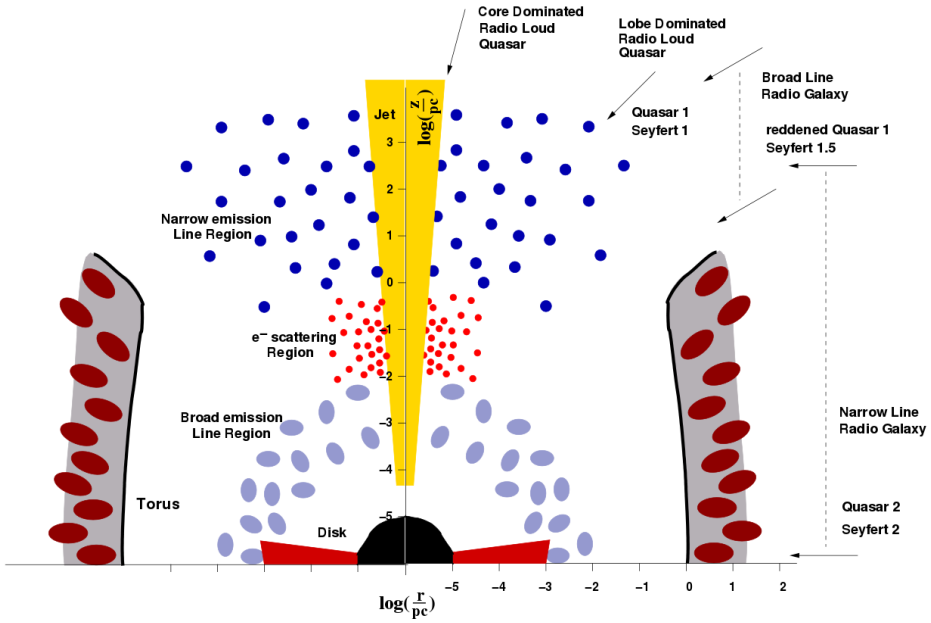

Figure 1.5: Unification of radio-loud AGN taxonomy based on differing lines-of-sight, image adapted from Zier & Biermann (2002), reproduced with permission © ESO.

type depends on the relative strengths of certain lines, e.g. Osterbrock & Ferland (2006). It has also emerged that some quasars show properties normally associated with Seyfert 2 galaxies, leading to the new designation of 'type 2 quasar' for these lesser-studied objects, e.g. Alexandroff et al. (2013). Quasars and Seyfert galaxies can also be divided in two categories, 'radio-quiet' and 'radio-loud', based on the strength of their radio emission. Radio emission is produced by synchrotron emission in jets and 'lobes' as described in Section (1.1.8).

1.2 AGN outflows

A characteristic signature of ionised material outflowing from the central engine of AGNs can be witnessed in many objects as absorption lines, which are blue-shifted relative to the wavelength of the corresponding atomic transition in the AGN rest-frame. These lines are distinguished from those due to absorbers located on an intergalactic scale along the line-of-sight to the AGN, such as in the case of the many absorption lines seen blueward of the Lyα emission line in quasars known as the Lyα forest, indicating intervening zones of neutral hydrogen towards high-redshift sources. The wavelength shift of intrinsic absorbers is considered to be indicative of outflowing material since the simplest ex-

planation for it is the Doppler effect, indicating gas which is moving towards the observer along the line-of-sight to the AGN. The velocity can be calculated for outflow speeds up to significant fractions of the speed of light using the relativistic Doppler shift formula:

$$\frac{v}{c} = \frac{1 - \left(\frac{\lambda_{rest}}{\lambda_{obs}}\right)^2}{1 + \left(\frac{\lambda_{rest}}{\lambda_{obs}}\right)^2}, \tag{1.21}$$

where λ_{rest} is the quasar rest-frame wavelength of the transition and λ_{rest} is the wavelength of the absorption line in the AGN rest-frame. Calculations of these velocities have indicated that the outflowing material, in certain objects, can be outflowing at speeds of up to 0.2c, e.g. (Pounds et al., 2003; Hamann et al., 2013). Absorption lines originating from outflows are also observed to have a large variety of velocity widths, which can be categorised on a purely phenomenological basis. The broadest lines are observed in quasars and belong to a category known as broad absorption lines (BALs), which have a continuous extent of over 2000 km s^{-1} and can be as broad as 30 000 km s^{-1}. Narrow absorption lines (NALs) are seen in quasars and Seyfert galaxies and extend over a few hundred km s^{-1}, while those lines of intermediate widths between BALs and NALs are known as mini-BALs (Narayanan et al., 2004; Hamann & Sabra, 2004). In some cases the outflowing gas is thought to be able to extend to a maximum of a few hundred parsecs from the AGN itself e.g. Barlow (1994), however other studies indicate an absorber location much closer to the central engine than this e.g. Crenshaw & Kraemer (2007); Wildy et al. (2015). The exact location and line profile seen could be line-of-sight dependent (see Section 1.2.3). Significant amounts of energy that can be transported by such high velocity flows and could therefore have significant consequences for the surrounding galactic environment, a fact which provides a principal motivator for their study. An artist's impression of a quasar outflow is shown in Figure 1.6.

1.2.1 The acceleration mechanism

There are various ways in which AGN outflows (also known as 'winds') can be accelerated to high velocity. A popular model is that the intense radiation originating from the emission region accelerates gas in the vicinity of the AGN by exerting pressure on the ions, in a process known as radiation-driving or line-driving. In this case, the continuum radiation from the central source imparts momentum to the ions through absorption of the photons by strong resonance lines (Murray et al., 1995). Modelling of

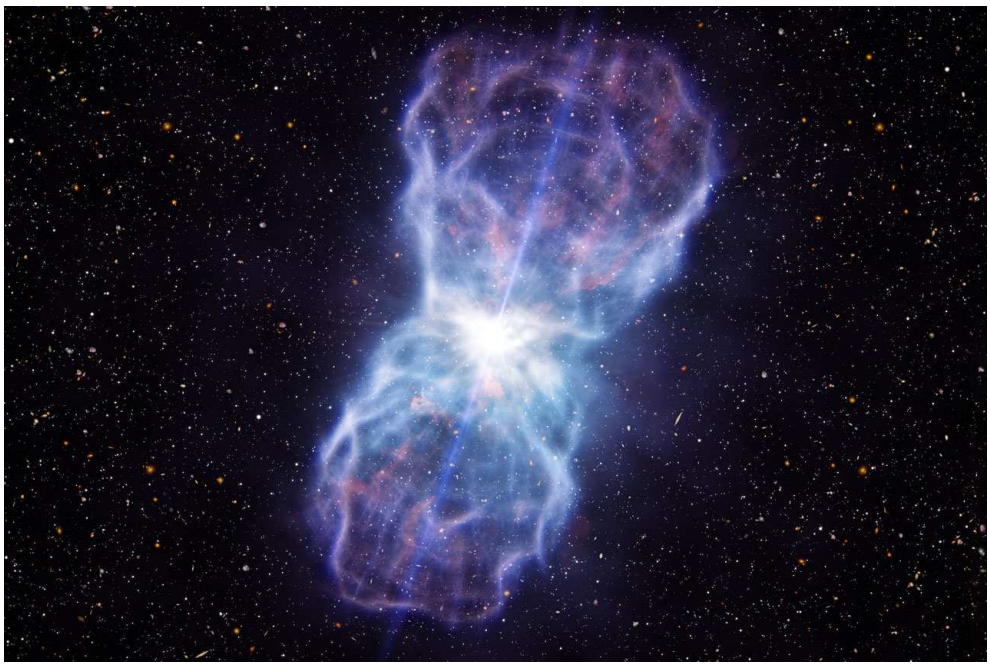

Figure 1.6: Artist's impression of the highly energetic outflow from the quasar SDSS J110644.95+193930.6. (*Image credit:* ESO/L. Calcada)

radiation-driven winds suggest this is a method which could accelerate material to the sub-relativistic velocities seen in some AGN, e.g. Proga et al. (2000); Chelouche & Netzer (2001), allowing the flow to exceed the black hole's escape velocity at a given distance and thus enabling the outflow to have an impact on the host galaxy. Tentative evidence for radiation driving is observed through the possible existence of a feature known as 'the ghost of Lyα' (Korista et al., 1993; Arav, 1996) seen in some broad absorption line quasars, which could indicate resonant line absorption of Lyα photons from the emission region by N V ions outflowing at the line separation interval of 5 900 km s^{-1}. However, the ubiquity of this phenomenon is far from conclusive (Cottis et al., 2010). Alternatives to the radiatively-driven scenario are thermally driven winds (Bottorff et al., 1997; Giustini & Proga, 2012) or magnetocentrifugal effects (Blandford & McKee, 1982; Everett, 2005).

1.2.2 Outflow interactions with the host galaxy

The energy carried by AGN outflows, known as the 'kinetic luminosity', can be a substantial fraction of the object's total power output, for instance in some quasars the kinetic luminosity has a value which is several percent of the bolometric luminosity, e.g. Zakamska & Greene (2014). Outflows could

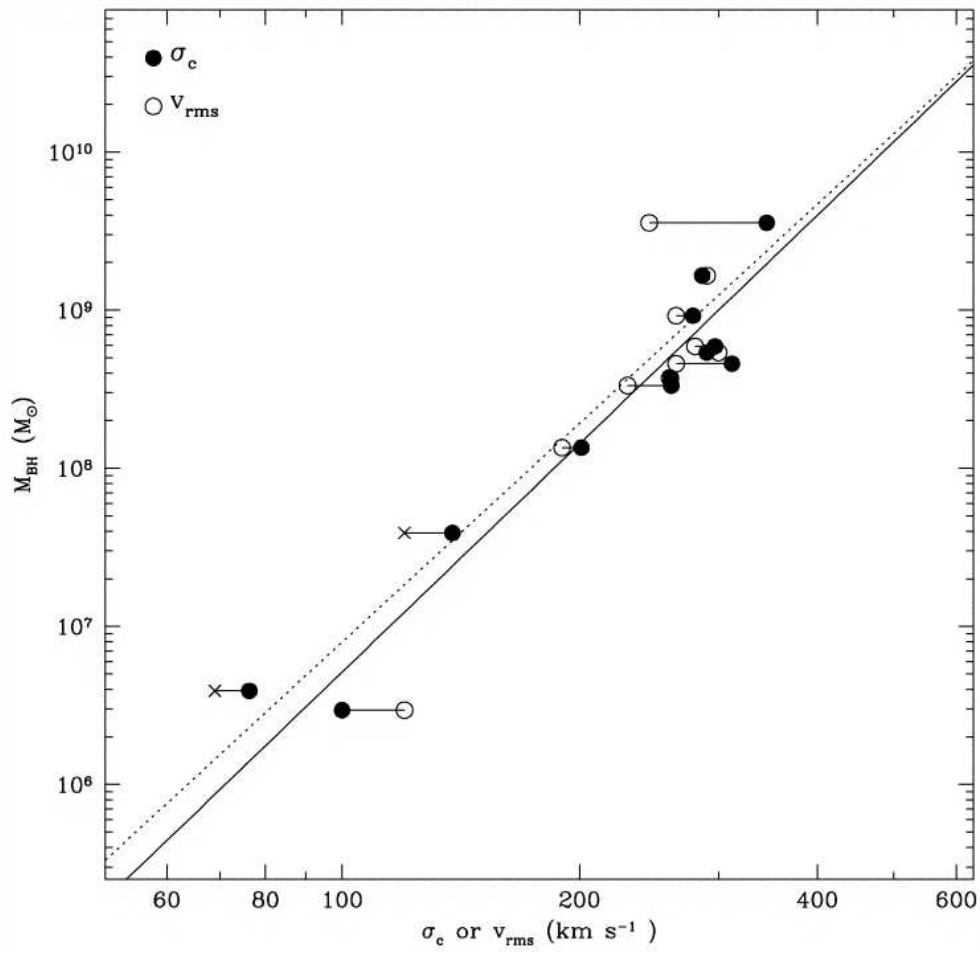

Figure 1.7: The mass of central black holes in several galaxies versus the stellar velocity dispersion of the galactic bulge(σ_c) and stellar rms velocity v_{rms} . The solid and dashed lines indicate the best fit for σ_c and v_{rms} respectively. Image is taken from "A fundamental relation between supermassive black holes and their host galaxies" by Ferrarese & Merritt (2000).

therefore extend the sphere of influence of a black hole deep into the host galaxy in a process known as feedback, which may also apply to inactive galaxies if they also went through an active phase at some point in their history. Given this, outflows could explain certain characteristics of galaxies that seem to depend on the properties of their central black holes. The relationship between black hole mass and the mass of their host galactic bulges (Magorrian et al., 1998; Silk & Rees, 1998) is one such example, as is the correlation between the black hole mass and the velocity dispersion of stars within the bulge, also known as the M-σ relation (Ferrarese & Merritt, 2000) illustrated in Figure 1.7.

There is evidence that outflows may also be responsible for the quenching of star formation in the host galaxy and limiting black hole growth (Springel et al., 2005; King, 2010). This possible contribution of

outflows to galaxy evolution is a strong motivator for the study of AGN absorption lines. The properties of these lines as determined from spectroscopy has allowed physical properties of the absorbing gas to be determined and hence the kinetic luminosity to be calculated in many objects. This ability to calculate the power of the outflow can be used in conjunction with studies of the conditions needed to permit feedback effects, thereby providing knowledge of the likely significance of such effects in a particular galaxy (e.g. Hopkins & Elvis (2010)).

1.2.3 Broad absorption line quasars

Broad absorption line quasars (BALQSOs) are a special class of quasars which host at least one of an interesting type of absorption feature known as a broad absorption line (BAL) in their spectra. The strengths of absorption features can be measured using a quantity known as the *Equivalent Width* (EW), which is defined for absorption lines as follows:

$$EW = \int \frac{F_l\left(\lambda\right) - F_c\left(\lambda\right)}{F_c\left(\lambda\right)} d\lambda\,, \tag{1.22}$$

where $F_l(\lambda)$ is the flux density at a particular wavelength λ, and $F_c(\lambda)$ is the corresponding continuum flux density. They are so-called as they provide an estimate of the equivalent wavelength width of the continuum needed to be integrated over to give the same total flux as that absorbed by the line. A useful feature of the EW measurement is that it is independent of the resolution of the instrument used to obtain the spectrum, allowing useful measurements of the absorption-line strength even for relatively low quality spectra.

A common definition of BALs used in many studies is the quantity known as the *Balnicity Index* (BI), originally developed for C IV λ1549 BALs by Weymann et al. (1991). The BI is a modified equivalent width measure, being positive in quasars hosting at least one BAL and zero otherwise. In order to produce a positive BI value, an absorption trough is required to extend over at least 2000 km s^{-1} where the flux is less than 90 percent of the continuum level. In the original definition, maximum and minimum velocity bounds were also applied to limit overlap with broad emission line features, easing the calculation of absorber depth to those regions where only the continuum is absorbed (sometimes referred to as 'detached troughs'). This definition can be written as follows:

$$BI = -\int_{25000}^{3000} \left(1 - \frac{f(v)}{0.9}\right) C dv\,, \tag{1.23}$$

where f(v) is the continuum normalised flux at velocity v and C is a constant with value of unity when the normalised flux has been below 90 percent of the continuum level for a continuous 2000 km s^{-1} and is otherwise zero. This definition results in between 10 and 20 percent of all quasars being classified as BALQSOs (Reichard et al., 2003; Knigge et al., 2008; Scaringi et al., 2009). However, it may be as high as 41 percent if differential SDSS target selection effects are taken into account (Allen et al., 2011). It should be noted that the BI applies to individual absorption features, therefore an individual BALQSO can host multiple BALs, including more than one of the same ion. The most commonly accepted explanation for the fraction of BALQSOs in the quasar population is an orientation effect. In this model, BALQSOs are those quasars where the bulk of the outflow column is aligned with the line-of-sight to the quasar as seen form Earth, manifesting as large amounts of absorption in the quasar spectrum over a wide range of velocities (Elvis, 2000). This implies that the true proportion of quasars which produce large outflows may be much higher than the BAL fraction implies (Schmidt & Hines, 1999). A possible unification scheme for BAL and non-BAL quasars is shown in Figure 1.8.

The BALQSOs can be divided into two sub-categories depending on the ionisation state of the absorbers present. The more populated grouping is those quasars showing BALs of high-ionisation state such as Si IV λ1400, C IV λ1549 and N V λ1240 but not of low-ionisation such as Mg II λ2798 and Al III λ1860. These quasars are known as 'HiBALs' (Sprayberry & Foltz, 1992; Reichard et al., 2003). Those quasars having low-ionisation absorption in their spectra are known as 'LoBALs' and are found to always additionally have high-ionisation absorption in their spectra. A rarer subclass of LoBALQSOs additionally show broad absorption attributable to Fe II, these objects are known as 'FeLoBALs'. An investigation into the fractions of quasars showing LoBAL features has suggested that approximately 4 percent of quasars are ordinary LoBALs in the BI definition, while approximately 2.1 percent are FeLoBALs (Dai et al., 2012). The LoBALs demonstrate greater column density of outflows (Green et al., 2001), which may be due to low ionisation lines being visible in those quasars where the viewing angle allows observation of gas which is shielded from the highly ionising radiation by a sufficiently high column of highly ionised plasma (Elvis, 2000).

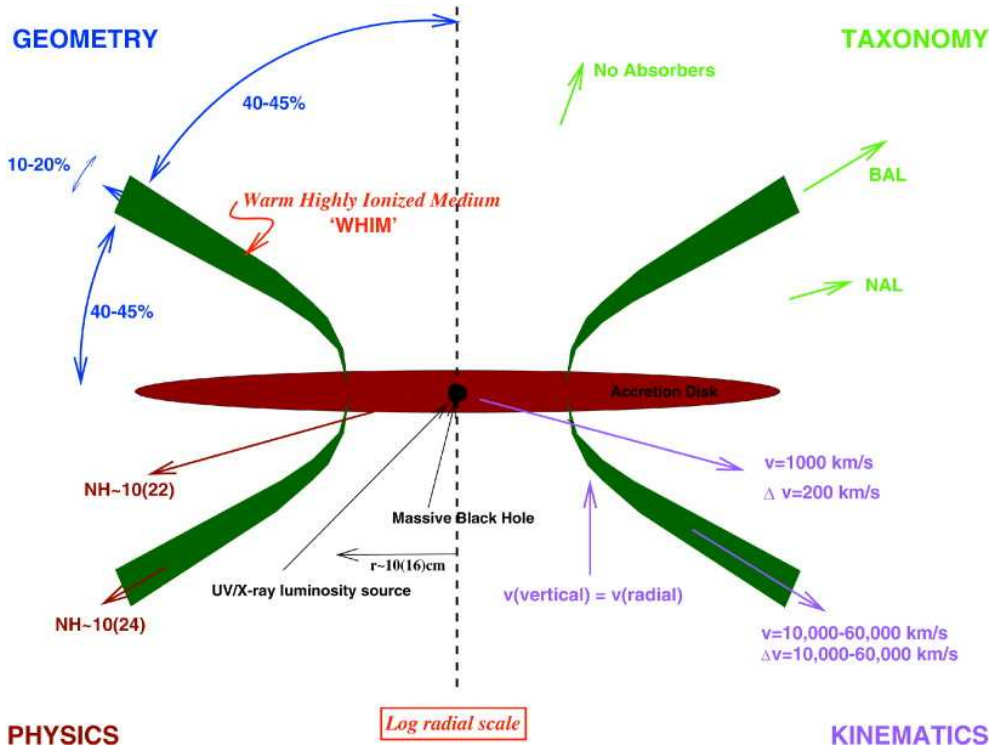

Figure 1.8: A possible structure for quasar outflows. The outflows are coloured green, with different viewing angles producing broad, narrow, or no absorption lines. Image is taken from "A structure for quasars" by Elvis (2000).

1.2.4 BAL variability

Broad absorption lines are observed to vary on timescales ranging from a few days to multiple years (Gibson et al., 2008; Capellupo et al., 2013). One of the first investigations into BAL variability was performed by Barlow (1993) who discovered significant variability in 15 out of 23 spectroscopically monitored BALQSOs, with variability being observed as changes in the continuum-normalised flux within the troughs. It is notable that there is a lack of conclusive evidence of absorption features undergoing acceleration (Hamann et al., 2008; Rodríguez Hidalgo et al., 2011), however velocity width changes are occasionally observed, sometimes even to the extent of transforming between mini-BALs and BALs (Rodriguez Hidalgo et al., 2012). The published literature generally considers one of two possibilities for the mechanism driving BAL variations. One is changes in the ionisation state of the gas result in a change in the column density of the absorbing ion, e.g. Wildy et al. (2015). The other possibility considered is the effect of a change in the fraction of the AGN emission surface obstructed by absorbing material as seen from the Earth, resulting from this material moving across the line-of-sight e.g. Gibson et al. (2008); Capellupo et al. (2012). The fraction of the AGN emission region

surface obstructed along the line-of-sight is known as the *covering fraction*.

Variability due to ionisation changes resulting from changes in the ionising continuum are considered a plausible explanation for BAL variability as this mechanism is understood to be the main driver of changes in the broad emission lines, e.g. Peterson et al. (1998); Vanden Berk et al. (2004); Wilhite et al. (2006). Early evidence for this mechanism was reported in Barlow (1993). Changes of this type can only take place where there is an equilibrium between the ionisation rate and the recombination rate. Photoionisation equilibrium only occurs within AGN-related plasmas where the gas is sufficiently dense such that the recombination time is fast enough to respond to the continuum changes. Since the absorbing material is along the line-of-sight to the quasar ionising source, there should be no time-delay between a continuum change driving the variability and the response of the absorption lines unless gas densities are low. Following the line-of-sight model for different observed velocity centroids and velocity widths indicated in Figure 1.8, a co-ordinated change in the strength of absorption lines which are widely separated in velocity space is considered strong evidence for this process (Filiz Ak et al., 2013).

Several variability studies published during the last decade lend support to the second variability mechanism possibility, namely absorbing clouds moving across the line-of-sight and hence changing the covering fraction (See Figure 1.9). Spectral changes occurring in narrow portions of the absorption troughs across several different ions at the same velocity are considered to lend support to this conclusion (Gibson et al., 2008; Hamann et al., 2008), since individual clouds are likely to have a low velocity dispersion, while ionisation changes should induce a coordinated change across the entire trough. Evidence of covering fraction changes could also show up as changes by the fractional EW (ΔEW/$\langle$EW$\rangle$, where $\langle$EW$\rangle$ is the average EW across the two observational epochs used to record variability) in all ions in the outflow, assuming the crossing clouds responsible for the variability have a similar ionisation state to the bulk of the outflow. This is true since such variability depends on changes in the total column of absorbing gas along the line-of-sight without any changes in the relative ion populations. Some recent studies support a combination of both covering fraction and ionisation change effects driving the variability across the BALQSO population (Capellupo et al., 2012; Filiz Ak et al., 2013; Wildy et al., 2014).

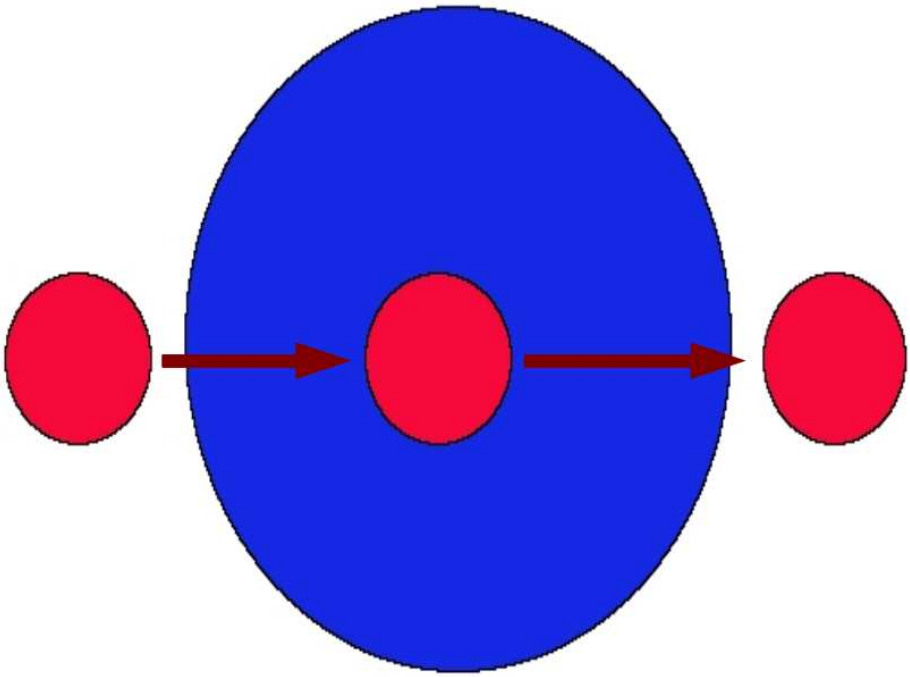

Figure 1.9: A simple example of a crossing clouds model as seen along the line-of-sight over three observational epochs. The background emission source is in blue, while a single absorber at each observational epoch is in red. Arrows denote the direction of travel of the absorber.

1.2.5 Measuring BAL variability

Measurement of BAL variablity requires knowledge of the true unabsorbed flux in the spectral region spanned by the absorber in order to measure the depth of absorption at each velocity or wavelength bin across the trough. This depth can be measured by taking the difference between the unabsorbed profile and the observed profile, which allows EW or similar measurements to be taken. A BAL can then be classified as variable if its EW varies significantly across two or more epochs of observation. Measurements of EW variability commonly specify either the absolute change (ΔEW) or the fractional change as described in Section 1.2.4.

In order to avoid the overlap between broad absorption lines and broad emission lines, many studies have opted to only examine those situations where the absorption trough is entirely 'detached' by introducing a lower outflow velocity limit to measurements (Lundgren et al., 2007; Filiz Ak et al., 2012), as variability in the emission line due the same transition can affect attempts to measure the true absorption line variability in cases where it is measured against the continuum only. Such a continuum

is part of the 'featureless' continuum observed as part of the quasar SED and is generally constructed in the UV region using a power-law of the form

$$F_\lambda = C\lambda^\alpha \,, \tag{1.24}$$

where F_λ is the flux density, α is the spectral index and C is a constant. These are generated by fitting to relatively line-free locations in the spectrum to minimise contamination from emission lines and therefore accurately replicate the underlying continuum. Many BALQSOs show evidence of absorption of both continuum and emission line flux by the BAL outflow (Turnshek, 1988), meaning that in cases of BAL/BEL overlap, more light is removed from the line of sight than a continuum based BAL depth measurement would suggest. Therefore some investigations have attempted to reconstruct the entire emission profile (including emission lines) in the spectral regions surrounding BALs (Capellupo et al., 2011; Wildy et al., 2014). As well as solving the problem of introducing a low velocity cutoff, this allows measurements to be taken for cases of high velocity ($>$13 500 km s^{-1}) Si IV outflows, which may overlap with the O I λ1304 and C II λ1334 emission lines (Trump et al., 2006). This unabsorbed emission profile is sometimes referred to as a 'pseudo-continuum' and allows unrestricted measurement of absorption depths across the spectral region covered by the model. This is usually achieved by first modelling the power-law continuum as described before and subsequently constructing one or more emission lines using a sum of multiple Gaussian models, e.g. Capellupo et al. (2011) or a Voigt profile, e.g. Gibson et al. (2010).

A possible alternative is to build an unabsorbed spectrum from real quasar components. One example of such a composite is described in Vanden Berk et al. (2001) where quasar spectra are generated using a geometric mean of a large sample of quasars. If this is restricted to only those quasars showing minimal absorption, templates could be constructed which combine large numbers of quasars into a small number of templates based on spectral properties such as emission line width, height or EW which then have broad applicability as pseudo-continua. A further possibility, used as the basis of BAL variability measurements in this thesis, is to use multiple unabsorbed quasar components to perform a reconstruction of the unabsorbed spectrum using non-negative matrix factorisation (NMF) as described in Allen et al. (2011), which was applied to BAL variability in Wildy et al. (2014). Quasar spectra constructed using NMF as part of the study in Allen et al. (2011) are widely used in this thesis. Uses of unabsorbed real quasar spectra as pseudo-continua have the advantage of representing more physically

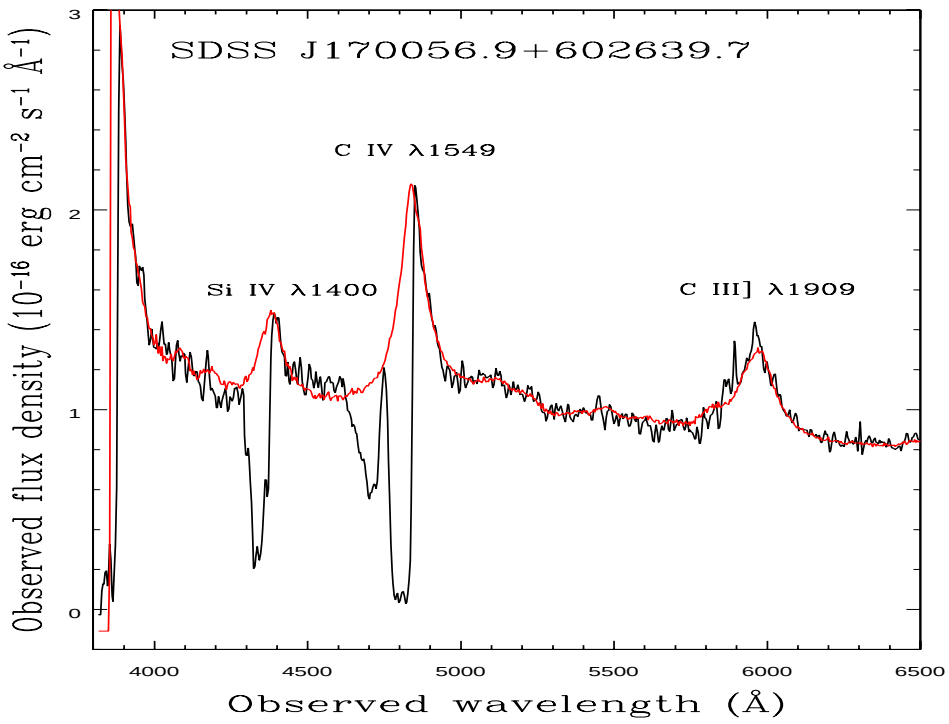

Figure 1.10: Example of a BALQSO spectrum including some prominent rest-frame UV emission lines (black line), along with the unabsorbed profile ('the pseudo-continuum') reconstructed using the NMF method described in Allen et al. (2011) (red line).

accurate emission line profiles than those modelled with single or multiple Gaussian or Voigt profiles. An example of an unabsorbed-spectrum reconstruction produced using the NMF method is shown in Figure 1.10.

It is possible for BALs to appear in regions of a quasar spectrum in which there was previously no significant absorption (Hamann et al., 2008). Conversely it is also possible for a BAL to weaken or narrow to the extent where it no longer meets the BAL definition. The disappearance of C IV λ1549 BALs was investigated using a sample of 582 quasars containing 952 C IV BALs in Filiz Ak et al. (2012), who found a disappearance rate of $\sim$2.3 percent. This disappearance rate was used to infer an average C IV BAL lifetime of 100–200 years based on the object rest-frame separation time between the epochs of observation. The C IV lifetime found in Wildy et al. (2014) was in broad agreement with this range, being $\sim$142 years. Additionally that paper investigated the disappearance rate of Si IV BALs, finding them to disappear at a rate of $\sim$5.3 percent, giving an average lifetime of $\sim$43 years. The greater incidence of disappearance in Si IV as opposed to C IV is in accordance with studies finding greater

amplitude and incidence of Si IV variability compared to C IV variability, e.g. Capellupo et al. (2012). Such disappearance rates should however be treated with caution as they are averages over a very large range of BAL strength. Since weaker BALs are more likely to vary than stronger ones, e.g. Capellupo et al. (2011), it would consequently be expected that weaker BALs have a larger disappearance rate (since disappearance is also a manifestation of BAL variability). Such susceptibility of weaker BALs to stronger variability may be a line-of-sight effect, whereby shallow BALs represent a view of a 'turbulent edge' of the outflow, thereby having lower line-of-sight column densities.

1.2.6 Saturation of AGN absorption lines

The depth of an absorption line at a given wavelength bin is dependent upon the optical depth (τ) which is a measure of the number of mean free paths traversed by a hypothetical photon travelling through an absorbing column to the observer. If the column density and hence optical depth is sufficiently large, the absorbing gas can become opaque at wavelengths corresponding to specific atomic transitions, resulting in saturation of the absorption line. In a situation where the gas completely covers the line-of-sight to the background emission source, this will result in the line reaching zero intensity over at least part of its wavelength extent. Such a line is on the non-linear part of the *Curve of Growth*, which describes the dependence of optical depth on ionic column density (Carroll & Ostlie, 2006).

A situation frequently encountered when analysing AGN absorption lines is *non-black saturation*, which often manifests as fine-structure components of a transition whose observed ratio of line optical depths are closer to 1:1 than atomic theory predicts, without any part of the lines reaching zero intensity. This is especially noticeable in many ultraviolet absorbers such as Si IV $\lambda\lambda$1394,1403 and C IV $\lambda\lambda$1548,1551 where the predicted optical depth ratio is 2:1. In these cases the effect is interpreted as resulting from an absorber which only partially covers the emission region along with the stronger component having become completely opaque (Arav, 1998). This assumption requires the outflow to leave at least some of the sky as seen from the AGN emission region uncovered, as opposed to the possibility of a spherical outflow covering 4π sr of the sky.

Saturation of doublet components can pose a problem for the accurate determination of outflow column densities since the uncertainty in the predicted column density becomes large at doublet component ratios close to unity. A solution to this problem is to observe lines with large optical depth ratios, ensuring

that, even at high column densities, the optical depth ratio remains small. An excellent candidate for this kind of work is absorption from the n=2 triplet state metastable level in the helium atom (He I*). This excited state has an average lifetime of $\sim$2.2 hours (Drake, 1971) and is 19.8 eV above the true ground state, ensuring that it is predominantly populated through recombination of He II rather than collisional excitation. As a result, the absorption lines from this level in the optical to NIR range occurring at 3889 Å and 10 830 Å are effectively high-ionisation transitions. One advantage of the study of these lines compared to that of the high ionisation, high column density sensitivity transitions resulting from P V $\lambda\lambda$1118,1128 is that they are not contaminated by Lyman-alpha forest absorption. The He I singlet level 2^1S can also be considered metastable, although its lifetime, at $\sim$0.11 seconds, is considerably shorter than that of the 2^3S level.

The usefulness of metastable helium in AGN absorption line research was demonstrated by Leighly et al. (2011), in which the first example of a He I* λ10 830 broad absorption line quasar was analysed and from which the outflow properties were constrained. Their investigation used the doublet components present in the NIR at 10 830 Å and optical at 3889 Å, which have a theoretical optical depth ratio of 23.3:1. A third absorption line representing a transition from the triplet metastable state is at 3188 Å, however it is outside the spectral range of optical observations. Recent studies of AGN metastable helium absorption also appear in Ji et al. (2015) and Liu et al. (2015).

1.3 NGC 4151

The Seyfert 1 galaxy NGC 4151, which was first recorded by William Herschel in the 18th Century, hosts one of the closest AGN to the earth, being approximately 19 Mpc distant according to a recent study (Hönig et al., 2014) and therefore having a relatively low redshift of z=0.0033. It is also one of the brightest, having an apparent visual magnitude of 10.04 (de Vaucouleurs et al., 1991). It falls in the radio-quiet category, however it does exhibit a radio jet (Liu & Zhang, 2002). Historically it has been categorised as a Type 1 Seyfert galaxy, however updates to the AGN classification scheme have resulted in it being considered to occupy the intermediate Type 1.5 category due to the presence of a narrow Hβ profile superimposed on a broad component (Véron-Cetty & Véron, 2006). The resulting observational accessibility due to NGC 4151's proximity and luminosity has enabled its extensive study across multiple wavelength bands, many of which have involved investigations of its spectral properties.

A multi-wavelength composite image of this AGN is shown in Figure 1.11.

One of the most interesting features of NGC 4151 is its dramatically variable continuum emission, which is detectable across X-ray, UV and optical wavebands, e.g. Edelson et al. (1996). This AGN has also been the target of reverberation mapping campaigns in an attempt to measure the size of the BLR and constrain the mass of the central black hole, e.g. Bentz et al. (2006). The galaxy is sufficiently proximate that the NLR can be resolved, indicating the presence of an *Extended narrow line region* (Penston et al., 1990). There is evidence of outflowing gas within the NLR, existing within a conical region with a total opening angle of $\sim 80^{\circ}$ and the line-of-sight to earth being 10° outside the cone (Hutchings et al., 1998). Absorption lines are visible in the X-ray, optical, UV and NIR regions of the spectrum, however their variability is not as well studied as the continuum variability.

In Hutchings et al. (2002) optical spectroscopic observations obtained from the Space Telescope Imaging Spectrograph (STIS) aboard the Hubble Space Telescope indicated that Balmer and metastable helium absorption features, which had previously only been observed in low continuum states, were also present during high continuum states. They also found higher outflow velocities at increased continuum flux. A series of papers (Crenshaw et al., 2000; Kraemer et al., 2001, 2005, 2006; Crenshaw & Kraemer, 2007) found that the absorption seen in UV and optical transitions across a range of ionisation states was dominated by a feature labelled "D+E". This feature was found to have a radial velocity centroid of ~ -500 km s^{-1} relative to the rest-frame of the source and to be located at a distance of $\sim$0.1 pc from the central engine with a number density of between 10^7 and 10^9 cm^{-3}. One of the aims of the work in Chapter 5 of this thesis is to discover if the absorber seen in the metastable helium transitions is the same as that reported in the high-ionisation UV transitions such as C IV reported in the aforementioned papers. This could be the case due to metastable helium being populated by recombinations of the high-ionisation He II ion, allowing measurements of its variability and column density to be performed using the He I* $\lambda\lambda$3889,10 830 transitions which are more sensitive to high column densities than the UV absorption lines.

1.4 Outline and aims of this thesis

The principal aim of this thesis is to investigate the variability of AGN absorption lines in BALQSOs and the Seyfert 1 galaxy NGC 4151. For BALQSOs the variability is investigated in quasar rest-frame

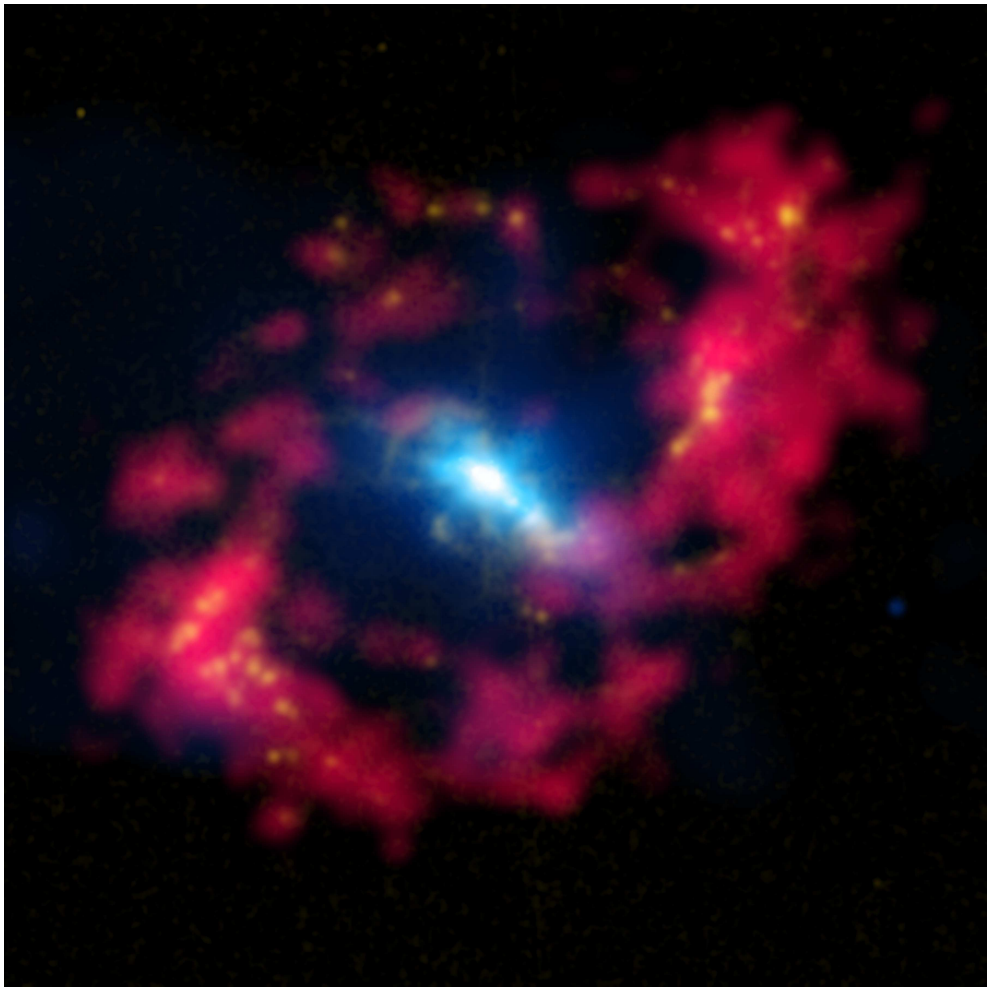

Figure 1.11: Multi-wavelength image of the central region of the Seyfert 1 galaxy NGC 4151. Blue indicates X-ray emission as detected by the *Chandra* satellite, yellow indicates optical emission and red indicates radio emission. The X-ray emission indicates the likely location of high energy processes associated with an accretion disc. *Image credit:* X-ray: NASA/CXC/CfA/J.Wang et al.; Optical: Isaac Newton Group of Telescopes, La Palma/Jacobus Kapteyn Telescope, Radio: NSF/NRAO/VLA.

UV lines resulting from transitions of species in a high-ionisation state. To study NGC 4151, absorption lines are identified resulting from atomic helium transitions in the optical and NIR, originating from the metastable 2^1S and 2^3S states and having laboratory emission line centres at 3889 Å, 10 830 Å and 20 587 Å. A major issue tackled is the question of what actually drives this variability. Predictions of the mass outflow rates (and hence kinetic luminosities), which can be used to determine the likely contribution of an outflow to galaxy feedback, are also made.

This thesis utilises spectroscopic observations of quasars in the optical waveband (rest-frame UV) with redshift ranging from z=2 to z=4, and optical and near-infrared (NIR) observations of the nearby Seyfert galaxy NGC 4151. Data from these observations is used to investigate the mechanism driving absorption line variability in these objects and to attempt to constrain the physical parameters of the absorbing material. Optical observations are obtained from the large database hosted by the Sloan Digital Sky Survey (SDSS), the William Herschel Telescope on the island of La Palma, Spain, the Gemini North and South observatories hosted on Mauna Kea, Hawaii, USA and Chile respectively, and the NASA Tillinghast telescope at the Fred Lawrence Whipple Observatory in Arizona, USA. Near-infrared observations are obtained from the NASA Infrared Telescope Facility (IRTF) sited on Mauna Kea. Further details of these observatories and their instrumentation, as well as details of the photoionisation code used, are provided in Chapter 2.

The research projects undertaken are described in corresponding chapters of this thesis as follows: Chapter 3 investigates a sample of 50 BALQSOs in an attempt to determine if the incidence and strength of Si IV λ1400 and C IV λ1549 BAL variability in the general BALQSO population has statistically significant dependences on certain BAL and host quasar properties. The procedure includes a new approach to measuring BAL strengths using physically realistic reconstructions of unabsorbed spectra which allow calculations of BAL equivalent widths to low velocities (including spectral regions which contain overlap of absoprtion and the corresponding broad emission line). Chapter 4 examines the variability in the most variable object from the 50 BALQSO sample in order to determine its variability driving mechanism and its kinetic luminosity. Chapter 5 explores what details can be learned about the physical properties of the helium outflow in NGC 4151, compares them to previous results and considers possibilities for the variability mechanism. Chapter 6 provides conclusions and scope for future work.

Chapter 2

Instrumentation and CLOUDY Simulations

This Chapter describes the instrumentation and data reduction processes used which provided spectroscopic observations of the BALQSOs studied in this thesis as well as NGC 4151. It also outlines the workings and implementation of photoionisation simulations undertaken using the CLOUDY code. For the observations undertaken in a particular science chapter, details of the dates, grating used, etc are provided at the beginning of that chapter.

2.1 The Sloan Digital Sky Survey

The Sloan Digital Sky Survey is a major ground-based optical survey undertaken using the 2.5 metre telescope at Apache Point Observatory in New Mexico, USA, which began taking science observations for the survey in 2000. (Gunn et al., 2006; York, 2000). It is supported by an international collaboration consisting of 23 Full Member Institutions, 21 Associate Member Institutions and 4 Participation Groups. As of 2015 the survey has entered its fourth phase (SDSS IV) (Tinker & SDSS-IV Collaboration, 2015) and had surveyed 14 555 square degrees of the sky by the time of the tenth data release (part of SDSS III) including optical spectra of 308 377 quasars (Ahn et al., 2014). The survey is now (April 2015) on its twelfth data release (DR12). The huge scope of the SDSS has revolutionised much of observational extragalactic astronomy, with data acquired from the SDSS having been used in over 5 800 publications worldwide. The survey is expected to continue collecting data for its current phase (SDSS IV) until 2020.

At redshifts ranging approximately between z=2 and z=4, the SDSS provides an excellent database of BALQSO spectra for the quasar rest-frame UV region spanning Si IV λ1400 and C IV λ1549 and was thus used as a source of data for the studies in this thesis. The required SDSS quasars were found and the spectra downloaded using the DR6 'Navigate tool' (skyserver.sdss.org/dr6/en/tools/chart/navi.aspx). These spectra provided the first epoch of observations ('epoch 1') for all BALQSOs studied in Chapters 3 and 4, with follow-up spectra obtained from other ground-based observatories, which are also described in this section. As described in Chapters 3 and 4, observations obtained from different instruments need to be corrected for differences in wavelength calibration and resolution before scientific studies can be carried out. The instrumentation used for the collection of data in the SDSS survey are described in the following subsections.

2.1.1 Imaging

The SDSS imaging data is collected by a camera consisting of 30 CCDs, each consisting of 2048×2048 pixels, divided among six columns of five CCDs each. Light arrives at the CCDs through one of five filters normalised to the AB magnitude system, labelled *u,g,r,i and z* respectively from shortest to longest wavelength (see Table 2.1 and Figure 2.1). Each filter covers one of the rows of six CCDs. The camera operates in what is known as *drift scan mode*, where the CCDs are read at the same time as observing the sky, with the telescope moving its position so that the five CCDs in a particular column each make one observation of an object, applying an integration time of 54 seconds. This therefore allows the light from a particular object to have passed through each of the five filters. An extra 24 CCDs positioned either side of the photometric CCDs collect calibration data. Further details on the operation of the imaging system are provided in Gunn et al. (1998).

2.1.2 Spectroscopy

There are now four types of spectrographs used as part of the SDSS, namely two identical instruments known as the *BOSS* (Baryon Oscillation Sky Survey) spectrographs, the infrared *APOGEE* (Apache Point Observatory Galactic Evolution Experiment) spectrograph, the *MARVELS* (Multi-Object Apache Point Observatory Radial Velocity Exoplanet Large-area Survey) spectrograph and the *MaNGA* (Mapping Nearby Galaxies at Apache Point Observatory) spectrograph used in the detection of exoplanets.

Table 2.1: Table of SDSS filter central wavelengths and effective bandwidths (Fukugita et al., 1996).

Filter	Central wavelength Å	$\Delta\lambda$ Å
u	3551	476
g	4686	996
r	6166	957
i	7480	1056
z	8932	1227

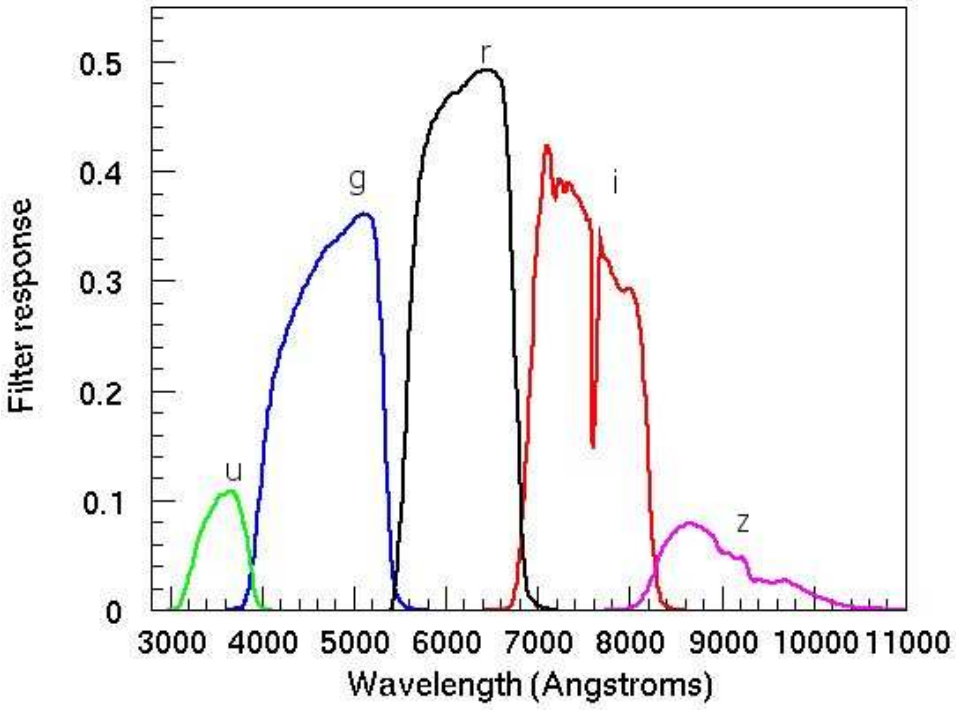

Figure 2.1: Curves of the responses of the five filter systems used for photometry in the SDSS. *Image credit:* SDSS (https://www.sdss3.org/instruments/camera.php).

Each spectrograph was built for a particular survey as indicated by its name, with the BOSS spectrographs being built from previous spectrographs used by the SDSS. Quasar spectra have predominantly been recorded using the BOSS spectrographs and their predecessors. The BOSS survey, for which these spectrographs were built, was an SDSS III survey designed to map the fluctuations in the density of galaxies due to baryon acoustic oscillations in the primordial plasma (Dawson et al., 2013). Additionally the extended BOSS survey (eBOSS), which attempts to answer questions regarding cosmic expansion and dark energy, is currently taking observations and is due for completion in 2020.

For BOSS's predecessor spectrographs, which were used in the acquisition of the SDSS observations of quasars in this thesis, a wavelength range of approximately 3900 to 9100 Å was spanned, with an approximate resolution of $\lambda/\Delta\lambda$=2000 at 5000 Å (Stoughton et al., 2002). Light was directed to these instruments from 640 optic fibres of diameter 3 arcsec positioned in holes drilled in an aluminium plate. Most of these holes correspond to positions in the focal plane of astronomical objects, a small number are placed at random blank parts of the sky to measure and therefore subtract off sky emission in the reduction process. For each fibre, this light is split into two channels, one spanning wavelengths 3800–6150 Å (blue channel) and another spanning 5800–9200 Å (red channel) with each channel directing light to the corresponding spectrograph used for the appropriate wavelength range. Wavelength calibration was performed using Hg, Cd and Ne arc lamps while flux calibration used observations of photometric standard stars, with the spectra generated having a resolution of $\sim$69 km s^{-1}. Exposures were taken for the duration necessary to exceed a signal-to-noise ratio of 4 for a for a fiducial fibre magnitude of g=20.2 and i=19.9. Further information on the SDSS data reduction process is available in Lupton et al. (2001) and Stoughton et al. (2002). The updated BOSS spectrographs provide a more advanced platform for observations, obtaining light from 1000 optic fibres of 2 arcsec diameter and providing a total wavelength coverage of 3600–10 400 Å.

2.2 The Gemini North and South Observatories

The Gemini Observatory consists of two 8.1 metre telescopes, one located in the northern hemisphere on Muana Kea in Hawaii, USA and another located in the southern hemisphere on Cerro Pachon in Chile. These telescopes can be used for optical and NIR observations. At both locations the observatory is equipped with optical spectrographs known as Gemini Multi-Object Spectrographs (GMOS)

(Hook et al., 2004), which were used to obtain BALQSO spectra used in this thesis. The GMOS spectrographs consist of three CCD detectors separated by gaps of 0.5 mm (corresponding to 39 unbinned pixels), which were used to obtain data for 42 target observations from both the northern and southern observatories using longslit spectroscopy used in thesis. Observations were made in *queue* mode, where observations are carried out by on-site personnel rather than the principal or co-investigators. These observations were used to follow-up those taken as part of the SDSS at earlier times, therefore forming part of the second epoch of observations ('epoch 2').

Each CCD at both the northern and southern telescopes consists of 2048x4096 pixels. The resulting spectra were used for the BALQSO variability study described in Chapter 3. Five of the observations were excluded from the final sample due to cloud cover issues, insufficient integration time or a deficiency of spectral regions containing unabsorbed continuum. A slit width of 1.5" was used at both locations for all Gemini observations in order to match typical seeing conditions. The grating configurations employed blaze wavelengths such that the spectral region of interest, extending from 1350 Å to C IV λ1549 in the quasar rest frame, was included in the total wavelength span. This ensured that all BAL features in the rest-frame UV could be observed, as well as sufficient line-free regions for continuum fitting. The B600 grating (resolution $\lambda/\Delta\lambda\approx$1688 at blaze wavelength 4610 Å) and R400 grating (resolution $\lambda/\Delta\lambda\approx$1918 at blaze wavelength 7640 Å) were used. Three quasars were observed in semester A 2008, the rest in Semesters 2011B and 2012A. The GMOS spectra were reduced using Version 1.11 of the Gemini/GMOS IRAF package as described later in this Chapter (Section 2.6). As well as being capable of long-slit spectroscopy, the GMOS spectrograph can also be used to perform multi-object and integral field spectroscopy.

There are additional instruments at the Gemini observatory which were not used to take data for this thesis, several of which are NIR instruments. The northern observatory is equipped with three NIR instruments. One of these instruments, The Near InfraRed Imager and Spectrometer (NIRI) provides imaging and spectroscopy in the wavelength range 1–5 μm (Hodapp et al., 2003). Another is the Near-Infrared Integral Field Spectrometer (NIFS) which allows integral field spectroscopy in the wavelength range 0.95–2.40 μm (McGregor et al., 2003). The third is known as GNIRS (Gemini Near InfraRed Spectrograph) which operates in the 1–5.4 μm range (Dubbeldam et al., 2000). The southern observatory also has three NIR instruments. Two are imagers, known as The Gemini South Adaptive Optics Imager (GSAOI) (McGregor et al., 2004), and the Gemini Planet Imager (GPI). These are both sensitive to wavelengths between 0.9 and 2.4 μm.

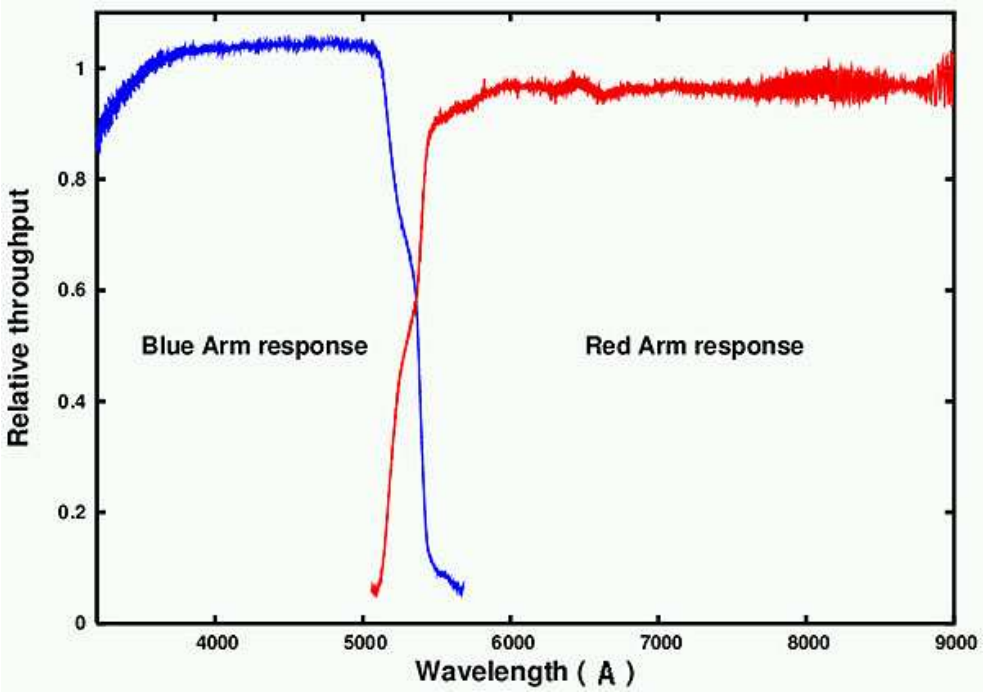

Figure 2.2: Blue and red arm response of the ISIS spectrograph on the WHT in the standard 5300 dichroic setup. The crossover region spans approximately 5200–5400 Å. *Credit:* Image courtesy of the Isaac Newton Group of Telescopes, La Palma.

2.3 The William Herschel Telescope

The William Herschel Telescope (WHT) is a 4.2 metre telescope located on Roque de los Muchachos on the island of La Palma, Spain as part of the Isaac Newton Group of Telescopes (Boksenberg, 1985). The main spectrometer on this telescope, known as The Intermediate dispersion Spectrograph and Imaging System (ISIS), was used for long-slit spectroscopy of 8 targets during Semester A 2008 which formed part of the sample used to investigate the signature of radiative line driving in Cottis et al. (2010) and which were subsequently used for the BAL variability investigation described in Chapter 3 of this thesis. These WHT observations used in Chapter 3 formed the second epoch of observations ('epoch 2'), following on from the earlier times at which the corresponding SDSS observations were made. The ISIS instrument is a double-armed (red and blue dichroic) spectrograph, providing spectral coverage from 3000 to 10 000 Å with a crossover located in a spectral region dependent on the setup (see Figure 2.2).

One of the targets in the sample used for Chapter 3 was SDSS J113831.4+351725.3. This quasar was

observed a further two times during Semester A 2011 and Semester A 2014 due to its exceptional variability, providing four observational epochs for this target in total, with the third and fourth observations ('epoch 3' and 'epoch 4') being observed as part of the ING service programme, which is similar to the 'queue' mode described previously in the sub-section detailing the Gemini Observatory. A detailed study of the BAL variability in SDSS J113831.4+351725.3 is provided in Chapter 4.

For all epoch 2 spectra the 5700 dichroic was used, providing spectra from the two arms with overlap in the range 5400 to 5700 Å. The R158B and R158R gratings, giving a nominal spectral resolution of 1.6 Å per pixel in the blue and 1.8 Å per pixel in the red, were also utilised for epoch 2. Epoch 3 and 4 observations of SDSS J113831.4+351725.3 employed the 5300 dichroic, giving an overlap range of 5200-5500 Å, while the R300B and R316R gratings were used for the blue and red observations, providing spectral resolutions of 0.86 Å per pixel and 0.93 Å per pixel respectively. In the dichroic overlap regions, an error weighted mean was used to combine the spectra from the two arms for each observation. For all WHT observations, a slit width of 1.5" was chosen to match typical seeing conditions and give reasonable throughput without compromising the spectral resolution. Multiple exposures were taken (in order to remove cosmic ray hits) bracketed by arc-lamp exposures for wavelength calibration. Standard star spectra were taken on the observing nights to allow flux calibration of the targets. These calibration observations were applied in the data reduction process described later in this Chapter.

2.4 The NASA Infra-red Telescope Facility

The NASA Infra-red Telescope Facility (IRTF) is a 3 metre telescope located on the summit of Mauna Kea. It is capable of both imaging and spectroscopy in the near and mid infrared parts of the spectrum. The following paragraphs describe the spectrographs and imaging cameras used on this telescope, including those used to record observations used in this thesis. The observations from this telescope used in this thesis were originally undertaken for previous studies in which the author of this thesis was not involved. The IRTF observations used in this thesis are linked to these original papers in Chapter 5.

The SpeX spectrograph (Rayner et al., 2003) was used for spectroscopy of the five observations undertaken of NGC 4151 which were used as part of the investigation in Chapter 5. These were observed 'quasi-simultaneously' with optical observations taken using the Tillinghast telescope over the period 2004–2010. The SpeX instrument was installed on the IRTF in 2000, upgraded in 2014 (the observa-

tions were undertaken prior to the 2014 upgrade) and has a wavelength range of 0.7 to 5.3 μm, allowing spectroscopy of the region near the He I* features at 10 830 and 20 587 Å. The observations employed the SXD grating which has a resolution of $\lambda/\Delta\lambda\sim$2000 and a spectral range of 0.7–2.4 μm. The detector on SpeX used for the observations consists of a CCD with a 1024x1024 pixel array. The SpeX instrument can also be used in imaging mode, although not for any data in this thesis.

In addition to the SpeX instrument, the IRTF also has several other instruments used for imaging and spectroscopy. For imaging, the NSFCam can be applied (Shure et al., 1994), which has a spectral range of 1–5 μm and uses a CCD detector measuring 2048x2048 pixels with a field of view of 81x81 arcsec at 0.04 arcsec/pixel. It was upgraded in 2012. The observatory also has a mid-infrared instrument capable of both spectroscopy and imaging, known as MIRSI (Mid-InfraRed Spectrometer and Imager) (Deutsch et al., 2003). This device offers complete spectral coverage in the range 8–14 μm within a total spectral range of 2–28 μm. Its field of view is 85x64 arcsec and it has a spectral resolution of $\lambda/\Delta\lambda\sim$200 at 10 μm and $\lambda/\Delta\lambda\sim$100 at 20 μm. A second NIR spectrograph on the IRTF is CSHELL, which offers high resolutions (up to $\lambda/\Delta\lambda\sim$30 000) in the spectral range 1–5.5 μm. This is due to be replaced by an even higher resolution instrument covering the same waveband known as iSHELL with resolution of up to $\lambda/\Delta\lambda\sim$80 000 in the range 1.2–2.5 μm and 67 000 from 3 μm to 5 μm (Rayner et al., 2012). The telescope is also equipped with adaptive optics equipment to correct for the distorting effects of the atmosphere. The data reduction for all IRTF observations used in this thesis was performed within the SPEXTOOL software package (Cushing et al., 2004), which was developed for the SpeX instrument.

2.5 The Tillinghast telescope

The Tillinghast telescope is a 1.5 metre optical telescope forming part of the Fred Lawrence Wipple Observatory (FLWO), which in turn is part of the Smithsonian Astrophysical Observatory. The FLWO is located on Mount Hopkins in Arizona, USA. Five spectroscopic observations of NGC 4151 between 2004 and 2010 (epoch 1 to epoch 5) were taken with this telescope and were used for the investigation undertaken in Chapter 5 of this thesis, with observations obtained using the FAst Spectrograph for the Tillinghast telescope (FAST) instrument. All the observations from this telescope used in this thesis were obtained from the FAST archive by Dr Hermine Landt (Durham University). As described in the previous subsection, these observation were taken quasi-simultaneously with the NIR observations

from the IRTF, allowing changes between epochs to be studied across the two wavebands.

The FAST instrument is an optical spectrometer having a maximum spectral coverage of 4000 Å using the 300 mm^{-1} grating, providing a 2-pixel resolution of 3 Å (Fabricant et al., 1998). Operational since 1994, it is the successor to the *Z-machine*, a spectrometer which was used on the Tillinghast telescope from 1978 until 1993. The FAST spectrograph can also be used with a 600 mm^{-1} grating, providing 2000 Å of spectral coverage with a 2-pixel resolution of 1.5 Å, and a 1200 mm^{-1} grating, which provides 1000 Å of spectral coverage at a 2-pixel resolution of 0.75 Å. Dispersed light is recorded on a CCD having 512x2688 15 μm pixels with a total length of 40 mm. The 512 pixels in the spatial axis allow a maximum slit length of 5 inches when undertaking long-slit spectroscopy. Wavelength calibration for FAST-obtained observations is performed by taking spectra of He-Ne-Ar Arc lamps of known emission lines. Wavelength calibration and the rest of the reduction process can then be performed in a similar way to the other optical telescopes described in this Chapter. Spectroscopic images taken by the FAST spectrograph which were used for the work in this thesis were reduced within the *procd* package in IRAF by using the *qfast* routine.

In addition to FAST, a second high-resolution, fibre-fed echelle spectrograph (which was not used to take data for this thesis) comprises part of the Tillinghast telescope system. This instrument is known as the Tillighast Reflector Echelle Spectrograph (TRES) and saw first light in June 2007. It is sensitive to a wavelength range of 3900–9100 Å and can be used in three different resolution settings $\lambda/\Delta\lambda\sim$60 000, 48 000 or 30 000 (see: www.sao.arizona.edu/flwo/60/tres/). The CCD which collects the dispersed light consists of 2048x4608 pixels, each having a size of 13.5 μm. The telescope also has an instrument known as the Atmospheric Dispersion Corrector (ADC) which has been in operation since 2011. As the name suggests, this instrument is used to correct for the effects of atmospheric dispersion and has improved the wavelength range and sensitivity of the TRES instrument (see: www.sao.arizona.edu/FLWO/60/ADC/adc-design.pdf).

2.6 Extracting a spectrum using IRAF

The data reduction process for images used in this thesis which were obtained from the Tillinghast telescope, the WHT and the Gemini Observatory telescopes was performed within the Image Reduction and Analysis Facility (IRAF) software (Tody, 1986). On obtaining the science images from the CCDs,

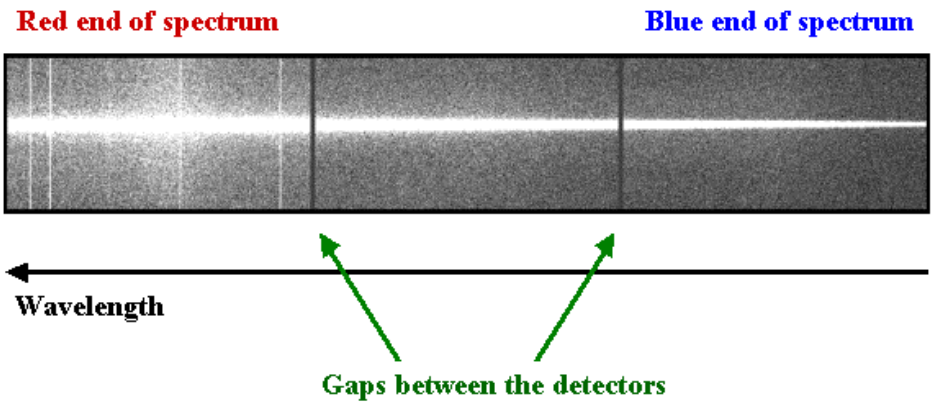

Figure 2.3: Example of a standard-star exposure taken with the GMOS instrument on the Gemini North telescope, with the horizontal direction being the dispersion axis and the vertical direction being the spatial axis. The horizontal line is the dispersed spectrum of the star, while the fainter vertical lines result from sky emission lines. The gaps between the chips are visible. *Image credit:* Gemini Observatory/AURA

calibration must be performed to correct for the effects of zero exposure noise and non-uniform illumination or non-uniform response of the CCD pixels. These two effects can be mitigated by obtaining *bias* and *flat-field* images respectively, and are detailed in the following subsections within this section. It was not considered necessary to obtain *dark* exposures due to the minimal effects of dark current in modern instruments such as GMOS and ISIS.

When making spectroscopic long-slit observations, light is dispersed by the grating across one axis of the CCD, hence this direction is called the dispersion axis. The perpendicular direction corresponds to the object's physical location on the long axis of the slit and is known as the spatial axis. A typical object exposure on the GMOS CCDs is shown in Figure 2.3

At each step of the reduction process, errors must be propagated to feed through to the final extracted spectrum. The high quality of modern instrumentation means that the major source of error in this spectrum is the sky background.

2.6.1 Zero correction using bias images

A bias image is a zero second exposure used to correct for variations in the pixel-to-pixel base-level reading. The image recorded in a bias frame will include noise associated with the readout and conver-

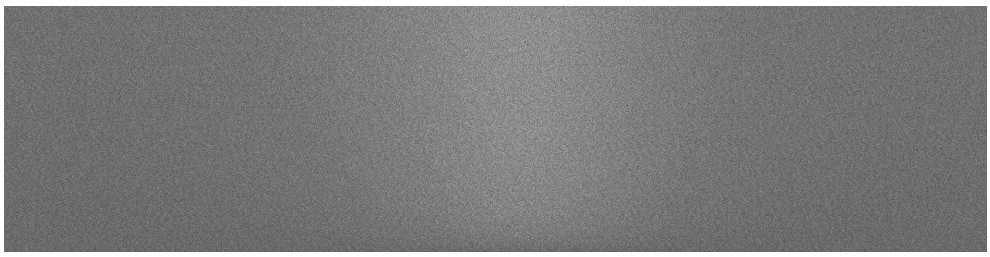

Figure 2.4: Example bias image taken with the Gemini North telescope.

sion to an image file. An example image is shown in Figure 2.4

Several bias images were taken on each observing night in order to reduce the noise associated with any individual image. For data obtained from the Gemini Observatory, bias images for each of the three CCDs were combined within the *gmos* package using the *gbias* routine to create a master bias. This was then subtracted from the arc lamp, flat field, standard star and target exposures using the *gsreduce* routine. For WHT/ISIS images, two separate master biases were created, one for the blue arm and one for the red arm, by combining either the red or blue bias images as appropriate taken on each observing night respectively for each arm, using the *zerocombine* routine within the *ccdred* package. Each master bias image was then subtracted from all images of the same type (either the red or blue images) in a similar way to the Gemini case using the *ccdproc* routine. The *ccdproc* routine was set to first remove the offset determined from the *overscan* (a few unexposed columns at the end of the chip) section of the images, which was subtracted by fitting a straight line to the measured function of counts against column position within the overscan region. Removal of the overscan offset was similarly performed for the Gemini/GMOS images before the combining of bias and flat-field images using the *gbias* and *gsflat* instructions as well as before the application of flat-field and bias correction to the target and standard star exposures within the *gsreduce* routine.

2.6.2 Flat-fielding

The response of pixels on a CCD to uniform illumination is not identical across the chip, instead any two pixels in an image will vary in their response by a multiplicative factor. To remove these effects an image of uniform illumination is taken which, in the case of the Gemini and WHT observations used in this thesis, is the diffuse light reflected from the dome interior under illumination from a flat-field lamp, known as a dome-flat. An alternative sometimes used (although not for observations in this thesis) is an

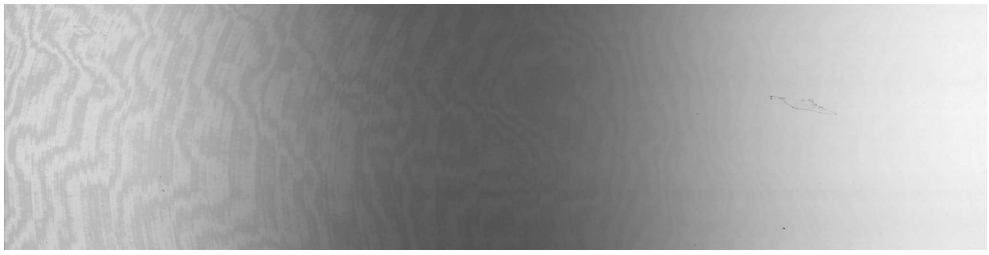

Figure 2.5: Example flat-field image taken with the Gemini South telescope.

image of the twilight sky, known as a sky-flat. An example dome-flat exposure is shown in Figure 2.5.

As with bias images, multiple flat-field images are generally taken on observing nights and then combined to create an average flat-field image which is used to apply the correction to the object (standard star and target) observations taken on the same night. For Gemini/GMOS images, flats were combined using the *gmos* package's *gsflat* routine. The most basic form of flat-field correction is to find the mean value recorded by the pixels in an image and normalise all pixels in the image to this value. In the object images, each pixel is then divided by the corresponding normalised value from the flat-field to produce the corrected image. This method was applied to the Gemini/GMOS object images using the *gsreduce* routine. For the WHT/ISIS object images, the *response* routine within the *specred* package was used to fit a function of counts vs. pixel position in the dispersion direction by collapsing the image in the spatial direction forming a function of intensity vs. pixel position along the dispersion axis, whose large-scale shape should match the shape of the flat-field light source. The *response* routine was then used to normalises each pixel in the flat-field image to the function value at that position along the dispersion axis. The object exposures were then divided by this normalised image to perform the flat-field correction. The use of *response* is particularly useful for removing artifacts such as the fringing visible towards the left (red-end) of the CCD image in Figure 2.5. Fringing of this kind results from light reflecting from the back to the front surface of the CCD, producing an interference pattern.

2.6.3 Wavelength calibration

Wavelength calibration was performed using arc lamps of known emission line wavelengths. This allowed the pixel position along the dispersion axis of the CCDs to be linked to the wavelength of the dispersed light. For both the Gemini/GMOs and WHT/ISIS observations CuAr lamps were observed. These lamp exposures were combined in the fashion described for flat-field and bias exposures before

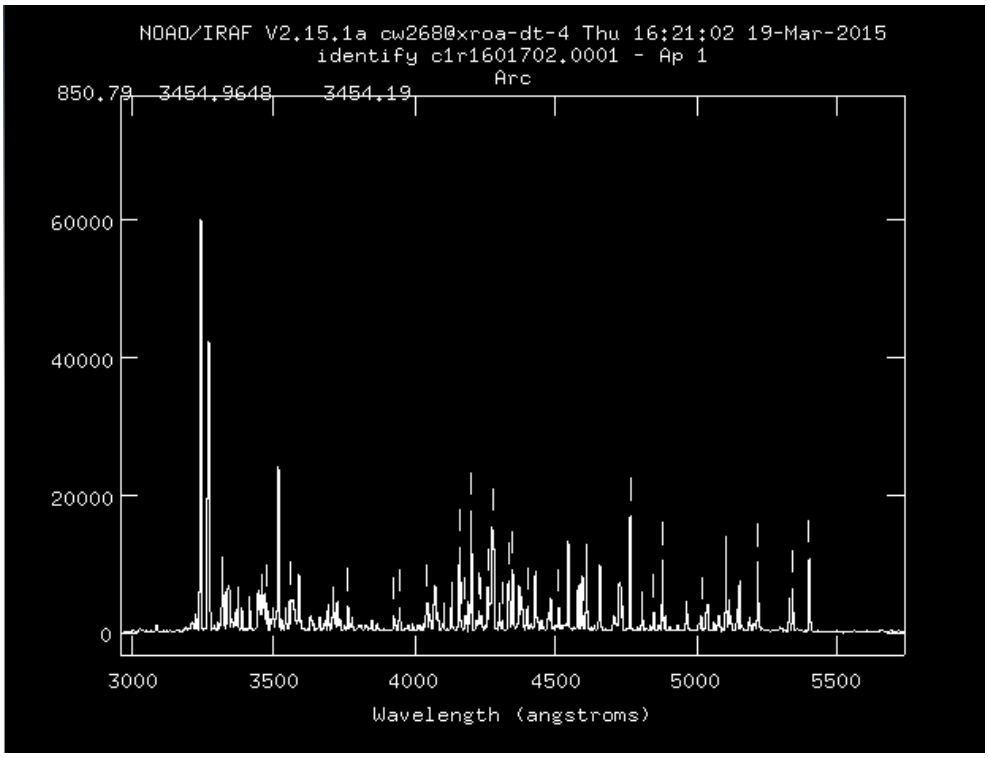

Figure 2.6: Arc lamp line-identification using *identify*

being fitted in IRAF with model functions of wavelength vs. pixel position, which were subsequently applied to object observations to provide wavelength calibration. For the Gemini/GMOS observations this procedure was performed using the *gstransform* routine in the *gmos* package. For WHT/ISIS observations, this step is performed after object extraction using the *apall* instruction in the *imred* package as described in the following subsection. Following the extraction, the *identify* task was used to mark the arc lamp emission lines (see Figure 2.6). Both methods require manual identification of the emission lines. Wavelength calibration is applied to object files observed with WHT/ISIS by adding a reference to the extracted arc lamp spectrum in the header and running the *dispcor* routine.

2.6.4 Spectrum Extraction

Extraction of the WHT/ISIS spectrum was accomplished by using the *apall* routine, and *gsextract* within the *gmos* package for the Gemini/GMOS observations. When extracting the spectrum, an extraction width needed to be chosen based on the width of the dispersion line along the spatial axis, as well as background regions along the spatial axis which defined the sky background emission to be

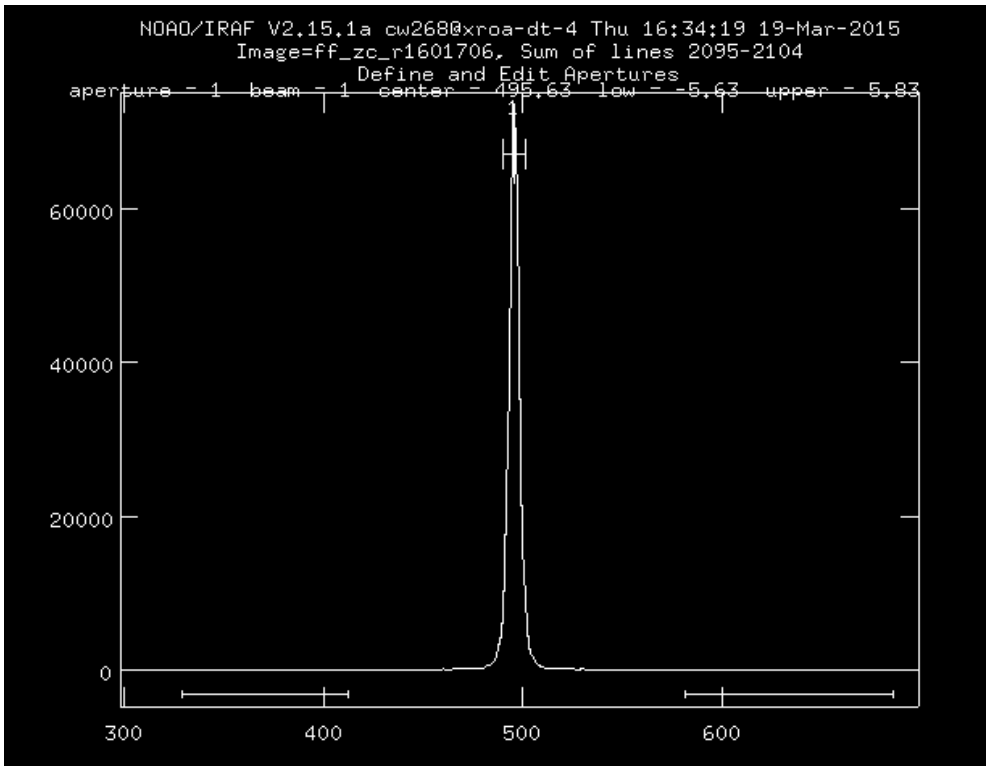

Figure 2.7: Identifying the extraction window and background regions using the *apall* aperture editor.

subtracted off. For the WHT/ISIS observations these tasks were performed using the aperture editor by choosing a location near the centre of the dispersion axis from which the width of the dispersion line and the background regions could be selected (see Figure 2.7). The background regions chosen varied from image to image based on their ease of identification. An extraction width of 10 pixels was used in all cases and the optimal extraction routine described in Horne (1986) was applied.

A similar method was used to select the aperture width using *gsextract*, with sky background subtraction taking place within the *gsskysubtract* routine. Once the dispersion line and the background regions had been identified, *apall* (or *gsextract* for Gemini data) allowed the fitting of a function to the *trace*, which is the direction the dispersion line takes across the CCD with a width equivalent to the extraction width. The dispersion line is never perfectly aligned with the dispersion axis, therefore the trace generally crosses a few pixels in the spatial direction between each end of the dispersion axis. An example of trace fitting is provided in Figure 2.8.

After extraction of the WHT/ISIS object spectra, the same aperture extraction setting is used to extract the spectrum of the arc lamp. This is followed by the use of the *dispcor* routine as described previously.

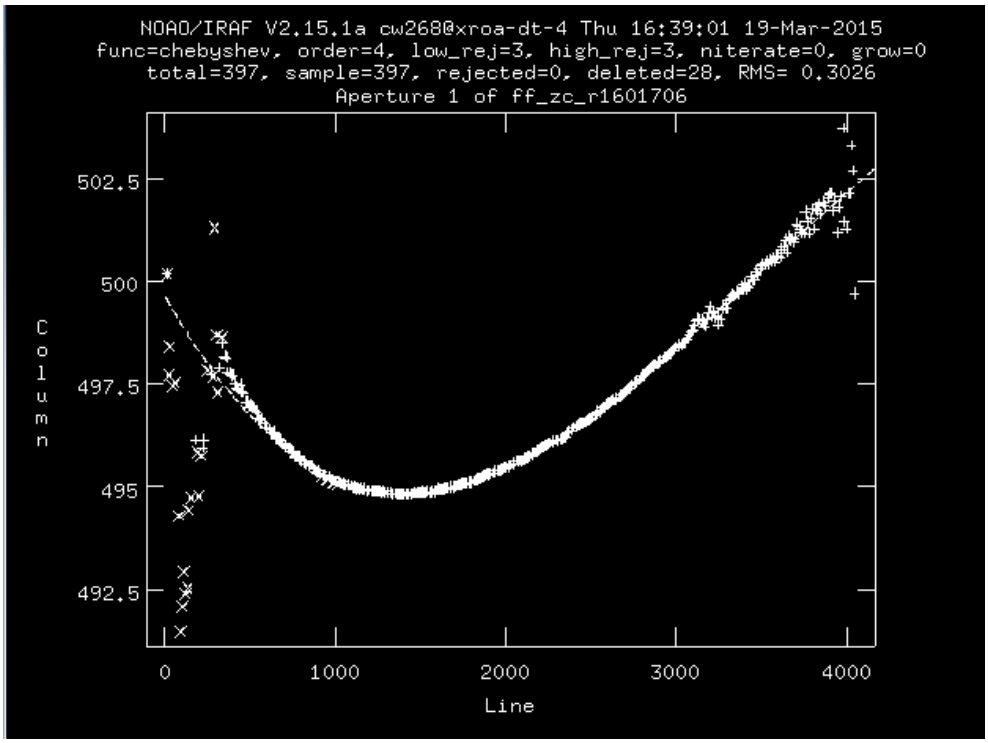

Figure 2.8: Identifying the trace using the *apall* task.

2.6.5 Flux calibration

Once the target and standard star spectra have been extracted, the spectrum of the latter can be used to calibrate the flux level by finding a suitable conversion between the counts per wavelength bin and the flux units (erg cm^{-2} s^{-1} Å^{-1}) known as a *sensitivity function*. For WHT/ISIS spectra this was performed using several routines within the *specred* package. Initially, WHT/ISIS standard star spectra should be corrected to the airmass at the mid point of the exposure, this was done using the *setairmass* routine. The *standard* routine was used to divide the spectral data into several bandpasses and divide the integrated flux by the exposure time, which was then used to fit a sensitivity function within the *sensfunc* task (see Figure 2.9). Both of these steps were performed by the *gsstandard* routine for Gemini/GMOS spectra.

Finally, to apply the flux calibration the *calibrate* routine, or its *gmos* equivalent, *gscalibrate* was used to apply the sensitivity function to the uncalibrated target spectra and hence create the final flux calibrated spectra. As part of the calibration, these routines also correct for atmospheric extinction using the mid-exposure airmass together with the appropriate table of extinction values as a function of

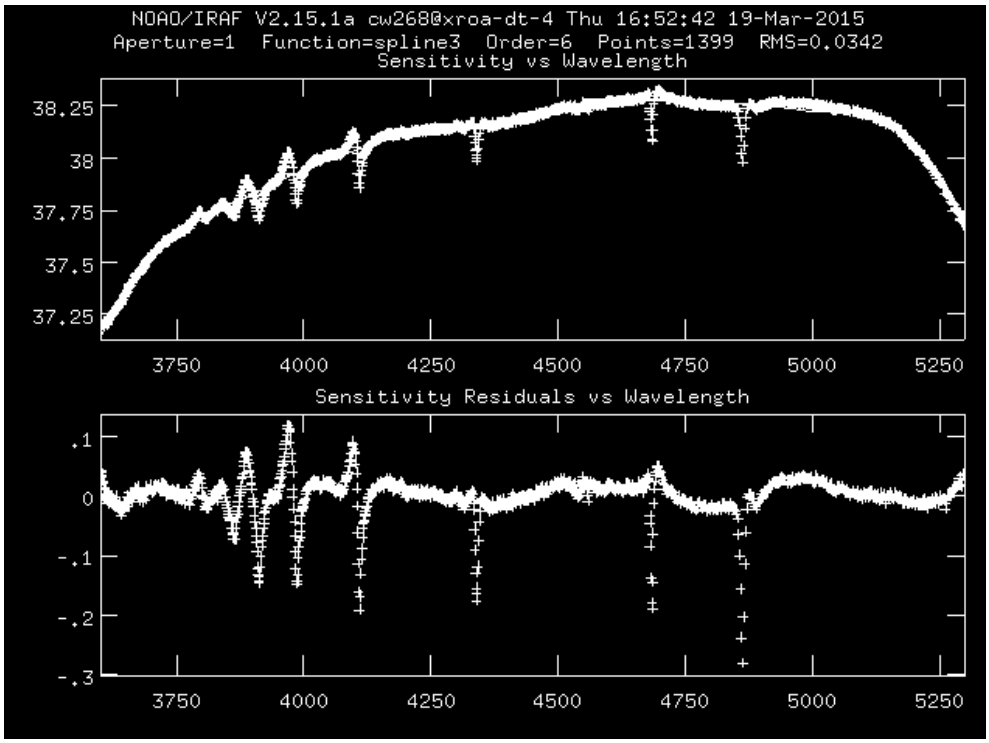

Figure 2.9: Identifying the sensitivity function using the *sensfunc* task.

wavelength at the telescope location. IRAF performs the extinction correction by applying an extinction correction factor equal to $10^{0.4 \times airmass \times extinction}$. For all the objects whose BAL variability was investigated, no attempt was made, such as through the use of grey shifts, to adjust the flux scale on the calibrated spectra towards levels which more closely matched across the epochs.

2.6.6 Correcting for Dust Reddening

Interstellar dust grains are made of molecules coalesced to form structures with typical sizes of the order of $\sim$0.1 μm. This kind of dust in both the host galaxy of an AGN and the Milky Way preferentially scatters light at the blue end of the optical and in the UV part of the spectrum, in comparison to longer wavelengths. The effects of this dust extinction on light passing through the Milky Way on its way to Earth-based telescopes can be corrected for by applying the *deredden* routine in the *imred* package within IRAF to the files containing the extracted and flux calibrated target spectra. This instruction bases the corrections upon the average extinction law defined by Cardelli et al. (1989). This extinction function at a given wavelength λ is defined as having the value $A(\lambda)/A(V)$, where

$A(\lambda)$ is the absolute extinction at wavelength λ and $A(V)$ is the extinction in the V–band, both of which are measured in magnitudes of extinction. The wavelength range over which it is defined covers 0.125 μm $\leq \lambda \leq$ 3.5 μm, which includes the entire spectral range spanned by all observations in this thesis in the observed frame and as such was an appropriate choice for making dust extinction corrections to the data obtained. Since the column of Milky Way dust is not the same along every line-of-sight from Earth, the amount of extinction will vary depending on where an extragalactic object is located on the celestial sphere. The *deredden* routine requires two parameters to be manually entered for the extinction correction to be made. These are $E(B-V)$, which is the colour excess when the V–band is subtracted from the B–band, and $R(V)$, which is the ratio given by:

$$R\left(V\right) = \frac{A\left(V\right)}{E\left(B-V\right)}\,, \tag{2.1}$$

For the interstellar medium in the Milky Way, $R(V)\sim$3.1 (Schultz & Wiemer, 1975). The appropriate values of the extinction in each of the bands U, B, V, R and I for a given extragalactic object reddened by foreground galactic extinction are listed in the Nasa Extragalactic Database (NED), having been originally deduced in Schlegel et al. (1998). Using the $A(V)$ value obtained from NED, it was therefore simple to work out $E(B-V)$ for a given object by assuming $R(V)$=3.1 in Equation 2.1. These values were found for all target objects studied in this thesis, allowing subsequent correction for foreground galactic extinction to be applied in all cases. No correction was applied for intrinsic (host galaxy) dust reddening since all measurements of absorption strength were made after normalising to an unabsorbed 'pseudo-continuum', so that any effects of such a reddening would cancel out on the division, thus negating the need to make difficult measurements of intrinsic dust features in the spectrum. Such dust reddening in AGN is typically assumed to be in the form of a power-law function of wavelength similar to those derived for the Magellanic Clouds (Gaskell & Benker, 2007).

2.7 The CLOUDY photoionisation code

Finding the physical properties of absorbers can be achieved by the use of photoionisation calculations. For the work in Chapters 4 and 5 of this thesis, such calculations were carried out within the CLOUDY code, version c13.02 (Ferland et al., 2013). This code is a 1-spatial-dimension package which simulates the irradiation of the plasma (or 'cloud') by a point source emitting a user-defined SED and is described

extensively in the documentation known as *Hazy* (available from www.nublado.org). A vast number of atomic, molecular and thermodynamic processes are taken into account by the code, rendering an attempt to describe them all in detail beyond the scope of this thesis.

Several input parameters can be specified by the user prior to running a calculation within CLOUDY. These calculations are performed based on the incident radiation field on the plasma derived from the aforementioned SED, the chemical composition of the plasma and its geometry. CLOUDY requires the SED to be defined over the range 1.001×10^{-8}–7.354×10^{6} Ryd. The code assumes by default that the source and the plasma are in an *open geometry* configuration, which is defined as the case where the plasma covers a very small proportion of the sky as seen from the radiation source. In this case, radiation emitted from the inner face of the cloud does not interact further with the cloud itself. A closed geometry is the opposite case, with the plasma having a covering factor of 4π sr, allowing reflected radiation to undergo further interaction with other parts of the cloud. For all calculations performed in this thesis an open geometry was specified, with the chemical composition of the cloud being a solar composition derived from Grevesse & Sauval (1998), Holweger (2001), and Allende Prieto et al. (2001, 2002). In order to ensure a plane-parallel cloud geometry, the very large default inner radius (distance from the emission source to incident face of the cloud) of 10^{30} cm was used.

CLOUDY performs calculations by dividing the plasma into shell-like *zones* of practically constant physical parameters, starting at the face which the radiation is incident on and working inwards through the cloud. This division into zones continues until the stopping criteria are met. These criteria can be specified in several different ways, typical examples being a user-defined total thickness of the cloud, a specific hydrogen column density being reached or when the zone temperature drops below a specified value. In the absence of a user-defined stopping criterion, CLOUDY will continue until the zone temperature falls below 4000 K. Several iterations of the code are needed in each run since the emission line optical depths are not known before the calculations begin. The code was set to perform iterations of the simulation until convergence of the optical depths.

As well as taking into account the effects of the incident radiation, CLOUDY also considers the effects of diffuse, transmitted and reflected radiation fields. The diffuse radiation results from photons produced in the plasma internal to the cloud, such as those from atomic transitions. The transmitted radiation is that which emerges from the outside face of the cloud with respect to the emission source and includes both the incident radiation remaining after interaction with the plasma and the diffuse radiation. The

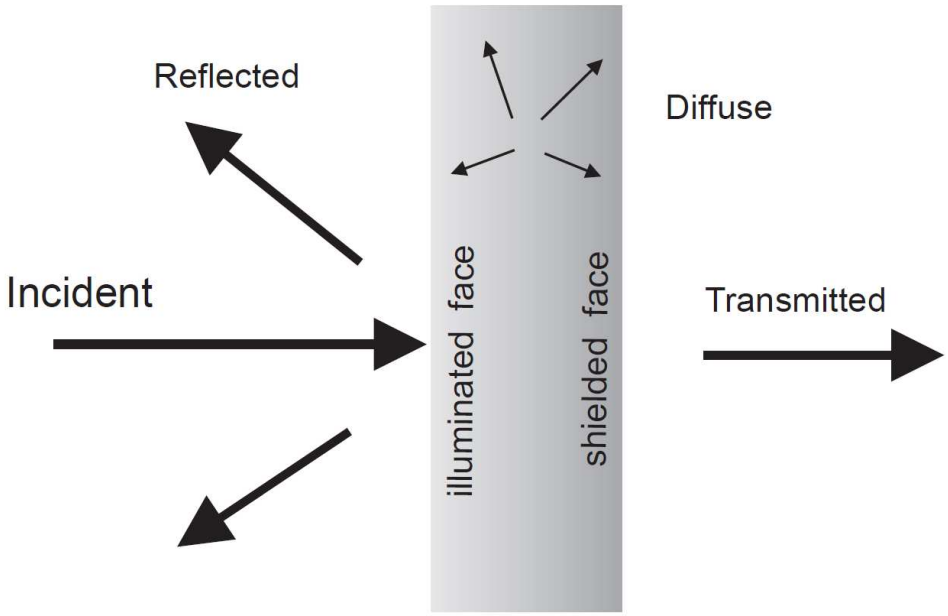

Figure 2.10: The various types of radiation field calculated by CLOUDY. Image copyright © 1978–2013 Gary J. Ferland and others. All rights reserved.

reflected radiation is the cloud emission which travels back towards the point emission source, with the exact definition requiring this radiation to be within 2π sr as seen from the source. In an open geometry, the secondary continua (transmitted and reflected) escape unimpeded. These radiation fields are illustrated in Figure 2.10.

The standard output provided by CLOUDY is in the form of .log files which detail the physical conditions of the zones such as the zone temperature, thickness and the fractions of each species in various ionised and excited states. Zone data is provided for the first and last zone of each iteration by default, it can be listed for every zone by using the *print every 1* command as was required for the zone integration procedures described in Chapter 5. CLOUDY considers the 30 lightest elements in detail and provides their column densities in different ionisation states calculated from the final iteration at the end of the file, as well as details for a large number of molecules. Among the excited states listed is the 2^3S metastable state and the sum of the n=2 singlet states in He I which were used for the investigations in Chapter 5.

The input continuum can be found by using the *save continuum* command. This procedure was necessary for the work carried out in this thesis as the large default inner radius setting required the SED to

be re-scaled to the true spectrum in order to find the correct inner radius. This scaling was carried out in two different ways, one was achieved by scaling the SED to a region on the observed spectrum as in Chapter 4, the other was scale to a known value of the object's bolometric luminosity, as was done in Chapter 5. The resulting output files provided the νf_{ν} values across the energy range spanned by the SED (in units of erg cm^{-2} s^{-1}) of the incident, transmitted, diffuse and reflected continua, with the incident continuum being representative of the input SED. The inner radius r could then be calculated by considering the equation used to define the ionisation parameter U, as given by:

$$U = \frac{Q\,(H)}{4\pi r^2 n_H c}\,, \tag{2.2}$$

where $Q(H)$ is the number of hydrogen ionising photons produced by the source per second, n_H is the total hydrogen number density of the cloud and c is the vacuum speed of light. The ionisation parameter is thus a measure of the ratio of hydrogen ionising photons to hydrogen atoms. All CLOUDY simulations performed in this thesis were used as part of user-defined grids in an appropriate parameter space, those parameters included the hydrogen number density and the ionisation parameter in all cases. Therefore, since the output value of $Q(H)$ must undergo the same scaling as that used to find the correct normalisation of the continuum and hence find its true value, it is clear that r must also undergo this same scaling to preserve the input value of U. This was therefore the method used to find the inner radius in Chapters 4 and 5. An example un-normalised SED used in Chapter 4 is given by Figure 2.11, with further details of its properties described within that chapter.

A similar input SED was used for Chapter 5, this time using the *AGN kirk* instruction which uses the SED parameters as described in Korista et al. (1997). All details of the photoionisation grid models produced using CLOUDY are provided in the relevant science chapters.

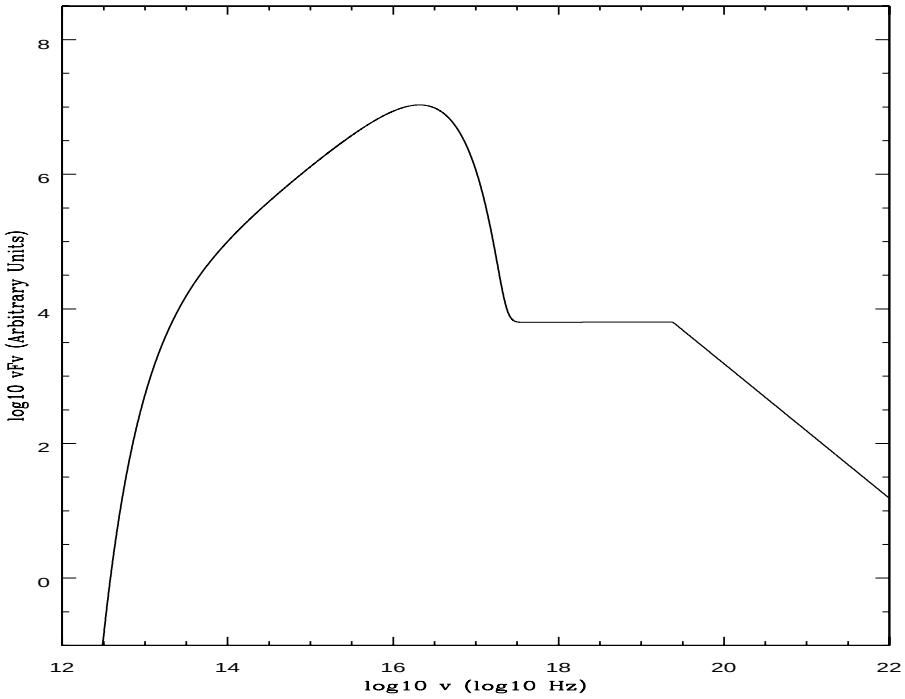

Figure 2.11: Example AGN input SED used in Chapter 4. The big blue bump temperature is T=240 000 K.

Chapter 3

BAL variability measurements using reconstructions of unabsorbed spectra

This chapter discusses a study to determine the variability properties of a 50-strong sample of BALQSOs selected from those objects which appear as spectroscopic observations in the SDSS survey. They were observed using initial data from the SDSS, with follow-up data from either the Gemini Observatories or the WHT. This provided two observational epochs for each quasar. The work carried out in this Chapter assumed a flat ΛCDM cosmology with H_0=70 km s^{-1} Mpc^{-1},Ω_M=0.3 and Ω_Λ=0.7.

3.1 Sample selection

The BALQSO sample selected for the work in this chapter included eight objects observed using the WHT ISIS instrument, which were initially chosen for the investigation into radiative line driving undertaken by Cottis et al. (2010). Spectroscopic observations of forty-two quasars obtained by the Gemini North and South observatories were additionally used, for which Dr Mike Goad was the author of the telescope proposal. In order to perform a large sample statistical study of BALQSOs, appropriate criteria must be chosen in order to select a sample which will yield relevant scientific results. Initially, a redshift range of approximately $1.9< z <4.1$ was selected so that the spectral region from the continuum band at 1350 Å to the continuum red-ward of C IV λ1549 was observable. Variability

was tested across two observational epochs, hereafter referred to as epoch 1 and epoch 2 for the earlier and later observations respectively, covering rest frame timescales of ≈10 months to 3.7 years. This epoch separation timescale is relatively unexplored in BAL variability studies published prior to the writing of this thesis. Epoch 1 used spectral data from objects imaged as part of the Sloan Digital Sky Survey, while epoch 2 observations were obtained from either the William Herschel Telescope or the Gemini Observatories.

The BALQSOs observed for the investigations in this chapter were selected from the BALQSO catalogue of Scaringi et al. (2009). This catalogue comprises 3552 BALQSOs and was compiled from a parent sample of 28421 QSOs published in the 5th data release (DR5) of the Sloan Digital Sky Survey (Adelman-McCarthy et al., 2007) using a hybrid classification scheme comprising a combination of simple metrics (e.g Balnicity Index), a supervised neural network and visual inspection. From the parent sample of 3552 BALQSOs only those objects tagged as definitely real (1353), and with BI$>$ 2 000 km s^{-1} were selected in order to minimise contamination by (possibly unrelated) narrow absorption line systems. A total of 595 objects satisfied all of these criteria. From this sample, objects were selected to span a broad range in balnicity ($BI > 2\,000$ km s^{-1}), redshift (approximately $z > 2$) and absolute i-band magnitude ($-28.75 < M_i(mag) < -25.75$). Of the 50 objects from this sample observed as part of the program undertaken in this chapter, a K-S test on the distribution functions of their observed properties (BI, z, M_i), showed that they are statistically consistent with those of the parent BALQSO population.

Non-BALQSO continuum variability is known to scale inversely with object luminosity and directly with redshift (Vanden Berk et al., 2004). As BALQSOs seem to be part of the same parent population as non-BALQSOs (Reichard et al., 2003) and given that ionisation is the main driver of variability in non-BALQSOs (Blandford & McKee, 1982; Peterson et al., 1998), if ionising continuum variations produce the variability seen in BALs it may be expected that lower luminosity BALQSOs would show the greatest BAL variations. In order to test the relationship between luminosity and variability the BALQSO sample chosen for this chapter spans a factor of 10 in i-band source luminosity. The redshift distribution of the BALQSOs from this sample peaks at the lower limit of the sample redshift range and was thus too small to give statistically reliable measurements of the dependence of BAL variability on redshift.

3.1.1 Observations

Details of the objects observed in this chapter are listed in Table 3.1 and Table 3.2.

3.2 Analysis

3.2.1 BAL Identification

Within the BALQSO sample, individual Si IV and C IV BALs were identified using a modified BI, differing from the original BI in that a lower velocity limit of 0 km s^{-1} relative to the observed wavelength of the red doublet component of the appropriate ion emission line was used, together with an undefined upper velocity boundary (in practice no C IV absorption features were identified blueward of the Si IV emission line, corresponding to an outflow velocity of $\approx$−30 000 km s^{-1}). A positive value of this modified BI for a particular absorption region categorised it as a BAL.

To carry out this procedure, the SDSS spectra and their Gemini or WHT counterparts were first resampled onto a 2.2 Å grid and smoothed using a 3 pixel boxcar smoothing algorithm to reduce the effects of noise on the determination of BAL wavelength ranges. This smoothing was applied only for the purposes of BAL identification and continuum fitting, it was not used in subsequent investigations. A power law continuum was fitted to both the SDSS and Gemini or WHT spectra using four spectral bands in each object judged to be relatively line free. Given the limited wavelength span of the Gemini observations, a liberal approach was taken to this fitting, allowing wavelength bands in quasar rest-frame wavelength ranges of 1250-1350, 1600-1800, 1950-2050 and 2150-2250 Å, the only restriction being that at least one of the four bands needed to be in the range 1250-1350 Å and at least one had to be in any of the other three. As a result, the quasar SDSS J032832.77-070750.3 was removed from the analysis as it contained no identifiable continuum regions in the 1250-1350 Å range. The modelled continuum had the form F_λ=C$\lambda^{-\alpha}$ where C and α were calculated using an iteratively updating procedure to minimise the chi-square value of the fit.

The SDSS spectrum and its modelled continuum for each object were examined by eye to search for regions of absorption which were plausible Si IV or C IV BAL candidates, the upper and lower boundaries of which corresponded to the points in velocity space at which the spectrum crossed the

Table 3.1: WHT/ISIS (upper panel) and Gemini/GMOS (lower panel) long-slit spectroscopic observations of SDSS quasars.

Object	z	Absolute i-band Magnitude mag	Exp. time (s)	Grating	Mean Airmass
SDSSJ101844.45+544015.6[d]	3.251±0.004	-26.852	3×1500	R158B & R158R	1.26
SDSSJ113831.42+351725.3[d]	2.122±0.002	-26.891	3×1200	R158B & R158R	1.14
SDSSJ114704.47+153243.3[d]	3.092±0.002	-27.848	2×1200	R158B & R158R	1.29
SDSSJ134458.82+483457.5[d]	2.048±0.002	-26.709	3×1500	R158B & R158R	1.24
SDSSJ162657.47+405848.0[d]	3.062±0.003	-27.576	4×1400	R158B & R158R	1.04
SDSSJ164152.30+305851.7[d]	2.016±0.002	-27.831	3×1500	R158B & R158R	1.06
SDSSJ170056.85+602639.7[d]	2.136±0.002	-27.367	3×1400	R158B & R158R	1.25
SDSSJ212412.60+095923.3[d]	1.921±0.002	-26.665	3×1200	R158B & R158R	1.17
SDSSJ001025.90+005447.6	2.861±0.002	-27.806	2×600	B600+G5323	1.54
SDSSJ004613.54+010425.7	2.149±0.002	-28.404	2×600	B600+G5323	1.32
SDSSJ025720.43-080322.5	2.045±0.005	-26.786	2×1500	B600+G5323	1.37
SDSSJ031033.45-060957.8	2.050±0.002	-27.424	2×900	B600+G5323	1.26
SDSSJ031331.22-070422.8	2.777±0.002	-27.844	2×1200	B600+G5323	1.51
SDSSJ032832.77-070750.3[a]	2.917±0.005	-27.223	2×1500	B600+G5323	1.36
SDSSJ033223.51-065450.5	3.708±0.008	-27.646	1×1500	B600+G5323	1.10
SDSSJ033224.95-062116.1	2.761±0.002	-27.487	2×900	B600+G5323	1.50
SDSSJ034946.61-065730.3[b]	3.973±0.011	-27.313	2×1800	B600+G5323	1.27
SDSSJ035335.67-061802.5	2.165±0.002	-27.218	2×1200	B600+G5323	1.67
SDSSJ035749.11-061121.9	2.006±0.002	-26.976	2×1400	B600+G5323	1.53
SDSSJ073535.44+374450.4	2.751±0.002	-28.259	1×1500	B600+G5307	1.10
SDSSJ081823.46+484910.8	2.015±0.002	-26.584	4×900	B600+G5307	1.28
SDSSJ081925.00+032455.7	2.239±0.002	-27.022	2×600	B600+G5323	1.36
SDSSJ082813.47+065326.4	2.968±0.004	-27.779	2×900	B600+G5323	1.35
SDSSJ083718.63+482806.1	3.646±0.003	-28.484	1×1200	B600+G5307	1.25
SDSSJ084023.51+063739.1[c]	3.801±0.010	-27.170	1×1362	B600+G5323	1.25
SDSSJ084408.29+423226.9	2.964±0.002	-28.215	1×1500	B600+G5307	1.40
SDSSJ085006.08+072959.0	2.690±0.002	-28.622	2×300	B600+G5323	1.41

[a] Excluded due to lack of observable continuum bands $<$1549Å

[b] Excluded due to 80 percent cloud cover

[c] Excluded due to shortened integration time.

[d] Observed in 2008.

Redshifts taken from Hewett & Wild (2010)

Table 3.2: WHT/ISIS (upper panel) and Gemini/GMOS (lower panel) long-slit spectroscopic observations of SDSS quasars (continued).

Object	z	Absolute i-band Magnitude	Exp. time	Grating	Mean Airmass
		Mmag	(s)		
SDSSJ085104.05+051539.8[d]	3.222±0.003	-28.480	6×600	B600+G5303	1.04
SDSSJ092557.52+044035.9	2.271±0.002	-27.174	2×600	B600+G5323	1.53
SDSSJ092639.34+383656.7	2.155±0.002	-27.292	2×1200	B600+G5307	1.32
SDSSJ093251.98+023727.0	2.169±0.002	-28.106	2×400	B600+G5323	1.37
SDSSJ095224.84+064732.0	2.174±0.002	-27.877	2×400	B600+G5323	1.42
SDSSJ100021.72+035116.5	2.017±0.002	-27.314	1×600	B600+G5323	1.32
SDSSJ100312.63+402505.6	3.247±0.003	-27.342	3×900	B600+G5307	1.38
SDSSJ101056.68+355833.3	2.301±0.002	-27.334	1×1200	B600+G5307	1.04
SDSSJ104059.79+055524.4	2.450±0.002	-27.023	2×1500	B600+G5323	1.40
SDSSJ105334.57+425724.9	2.719±0.003	-27.221	4×900	B600+G5307	1.17
SDSSJ110041.19+003631.9	2.020±0.002	-27.497	2×600	B600+G5323	1.22
SDSSJ110339.90+011928.5	2.056±0.002	-27.203	2×600	B600+G5323	1.28
SDSSJ111516.08+460234.6[c]	4.175±0.010	-27.376	1×721 & 1×900	R400+G5305	1.16
SDSSJ112733.69+343008.8	4.060±0.009	-28.594	4×900	R400+G5305	1.06
SDSSJ114722.09+373720.7	2.199±0.002	-26.380	4×900	B600+G5307	1.05
SDSSJ115007.66+542737.1[d]	3.534±0.004	-28.016	6×600	R400+G5305	1.22
SDSSJ125628.67+393548.0	2.138±0.002	-27.309	1×1200	B600+G5307	1.07
SDSSJ142244.45+382330.6[d]	3.741±0.010	-28.566	6×600	R400+G5305	1.06
SDSSJ143604.64+350428.5	3.035±0.006	-26.625	3×900	B600+G5307	1.04
SDSSJ143632.25+501403.6	2.784±0.002	-27.502	2×1500	B600+G5307	1.67
SDSSJ151601.51+430931.4	2.610±0.002	-28.373	2×1200	B600+G5307	1.11
SDSSJ153226.22+313138.1[c]	2.889±0.003	-28.194	1×336 & 1×1200	B600+G5307	1.21
SDSSJ165248.29+325032.3	2.832±0.008	-26.558	1×1500	B600+G5307	1.03
SDSSJ205659.48-071123.1	2.083±0.002	-27.547	2×900	B600+G5323	1.10
SDSSJ210436.62-070738.3	2.360±0.004	-27.268	2×1500	B600+G5323	1.17
SDSSJ211718.17+010248.9	2.928±0.003	-27.550	2×1500	B600+G5323	1.17
SDSSJ213138.93-070013.3	2.045±0.002	-27.425	2×900	B600+G5323	1.37
SDSSJ222505.28-084542.7	2.085±0.003	-27.121	2×900	B600+G5323	1.17

[a] Excluded due to lack of observable continuum bands <1549Å

[b] Excluded due to 80 percent cloud cover

[c] Excluded due to shortened integration time.

[d] Observed in 2008.

Redshifts taken from Hewett & Wild (2010)

modelled continuum. These regions were then tested using a BAL identification algorithm to determine their status (BAL or non-BAL) based on the modified BI. From the total quasar sample, 38 Si IV and 59 C IV BALs were identified, these were then subjected to the variability testing stage (see Section 3.2.2). A total of 38 objects showed lines from both transitions while 12 contained C IV BALs only (there were no quasars in the sample in which a Si IV BAL was unaccompanied by a C IV BAL). Some BALs were identified exclusively in the epoch 2 (Gemini or WHT) spectra, these were investigated in Section 3.3.5 as examples of appearing BALs. Three examples of BALQSO spectra and their modelled continua are shown in Figure 3.1.

3.2.2 Variability Testing

Prior to testing for BAL variability, each object had the higher resolution spectrum of the two epochs undergo smoothing by convolving with a Gaussian of appropriate full-width half maximum (FWHM) in order to approximately degrade to the resolution of the object's other spectrum. The two spectra for each object were then resampled onto a common 2.2 Å grid for those observed with Gemini/GMOS, closely matching the maximum linear wavelength bin width of the lower resolution SDSS spectra, and 3.7 Å for those taken with WHT/ISIS, which is approximately the width of the two-pixel binning in the WHT/ISIS spectra. These wavelength intervals correspond to velocity space intervals, for the redshift range covered in our sample, of between $\approx$85 and $\approx$140 km s^{-1} for the Gemini spectra and $\approx$140 to $\approx$240 km s^{-1} in the WHT/ISIS spectra (measured at a typical BAL absorber location of $\approx -10\,000$ km s^{-1} from the C IV emission line). Small differences (a few Å) in wavelength calibration between the SDSS and Gemini or WHT spectra were removed by aligning narrow emission or absorption features within each object in the Gemini or WHT spectra to those in the SDSS spectra where a consistent difference between several of these features was obvious.

The EW of each BAL was then calculated at both epochs based on the fitted continuum used for BAL identification, propagating errors during the procedure using the SDSS and Gemini or WHT error spectra and assuming a conservative 10 percent continuum error to ensure a high threshold for those BALs deemed 'variable'. A BAL was classed as variable if the significance of the EW difference between the two epochs exceeded 2.5σ. It should be noted that, given the high threshold for variability, those BALs not classed as 'variable' are not definitively claimed to not vary. The variability classification adopted here instead ensures that those BALs deemed variable do in fact definitely vary. If the contin-

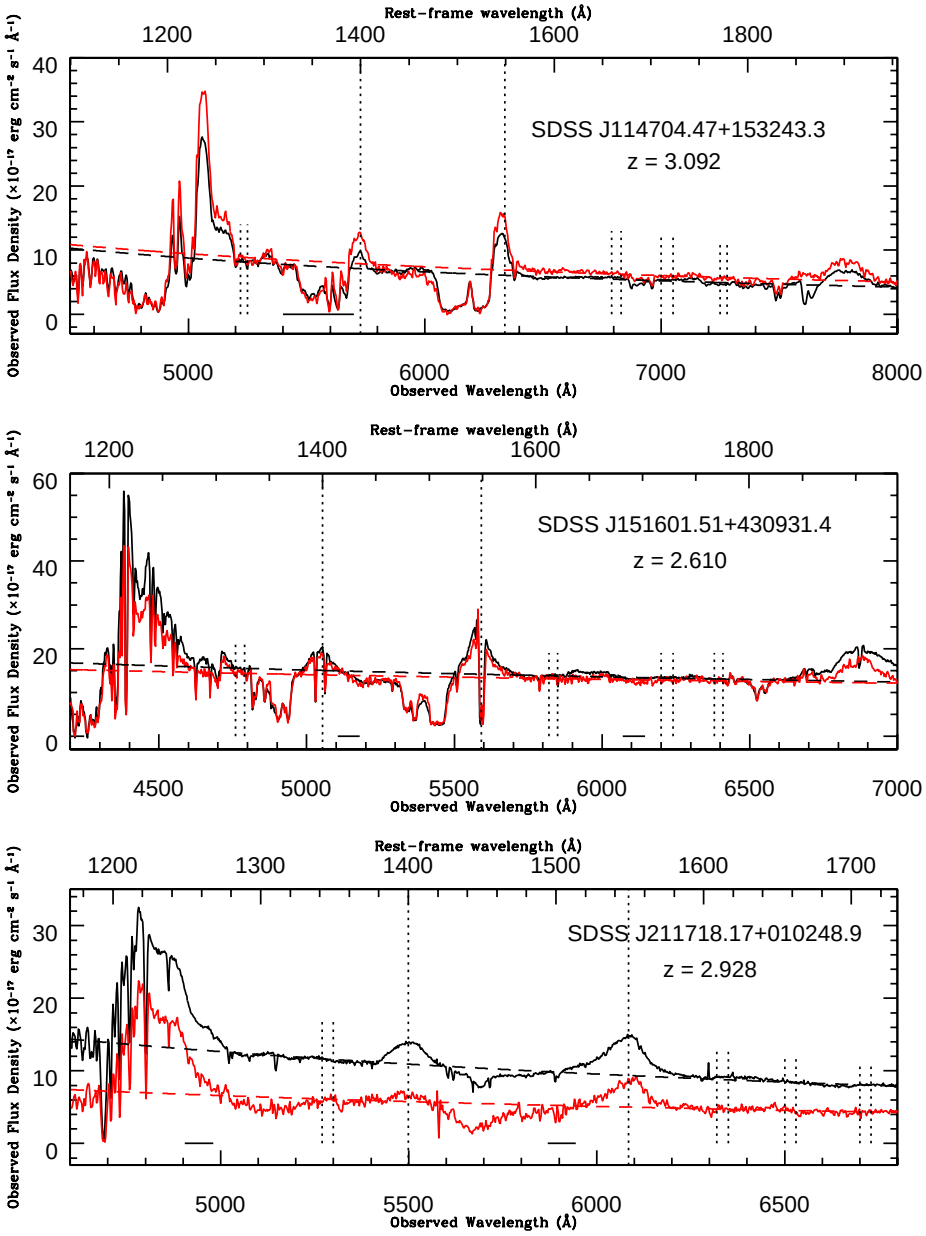

Figure 3.1: Power-law continuum fits to three example BALQSOs from our sample. Shown are SDSS-observed epoch 1 (red) and epoch 2 (black) spectra. Continuum models (dashed lines) are fitted to spectral bands (bracketed by short vertical dotted lines). The Si IV λ1400 and C IV λ1549 broad emission lines are indicated by long vertical dotted lines. The top panel object's epoch 2 observations were undertaken with WHT/ISIS, the middle and lower panel objects were observed in epoch 2 with Gemini/GMOS. Black horizontal lines indicate the spectral region of the combined ISIS dichroic overlap region (top panel) or the GMOS chip gaps (middle and lower panels).

uum error criteria is loosened such that it is 5 percent of the continuum level, the number of variable BALs increases by 60 percent. Adopting this approach, a total of 22 Si IV and 27 C IV BALs from 35 quasars were identified as variable, giving the percentage of varying BALs as 58 percent for Si IV and 46 percent for C IV. This subsample includes 14 objects which contain one variable BAL of each ion, allowing for comparisons of behaviour between both types of BAL within these particular objects.

3.2.3 Non-negative Matrix Factorisation reconstruction method

Generation of all the reconstructions of unabsorbed spectra for the BALQSOs examined in this chapter were carried out by Dr James Allen (The University of Sydney) using the method described in this section. The unabsorbed continuum plus emission line spectra of the BALQSOs – the pseudo continuum spectra – were reconstructed using the non-negative matrix factorisation (NMF) method described in Allen et al. (2011). For the epoch 1 (SDSS) spectra the reconstructions were the same as those used in Allen et al. (2011); new fits were produced for the epoch 2 (Gemini and WHT) spectra, with some minor modifications to the method. All processing steps were performed in the quasar rest frame, using the redshifts derived by Hewett & Wild (2010). The following description of the NMF process used to generate reconstructions is based on that provided in Allen et al. (2011).

Non-negative Matrix Factorisation is a technique which involves factorising a matrix V with non-negative elements into two matrices W and H, also with non-negative elements, such that V=WH. In the case of the work performed in this chapter, V is an $n\times m$ matrix whose elements are flux values, with n (rows) representing quasars and m (columns) representing wavelengths. The matrix H is an $r\times m$ array whose elements are the fluxes of r components at m wavelengths, while W is an $n\times r$ array representing the weights applied to the components to generate V. The technique employed to generate the unabsorbed BALQSO spectra required two steps. First, component spectra were generated from SDSS-selected unabsorbed quasar spectra *without* broad absorption in a particular $\Delta z = 0.1$ redshift bin. Second, these components were applied to the sample of BALQSOs to be investigated in order to generate reconstructions.

For the initial step, V represents the fluxes of the unabsorbed quasar spectra, of which there were up to 500 drawn from SDSS Data Release 6, in the redshift bin under consideration. By initially using random values for the elements of the W and H matrices, two multiplicative update rules are applied

in order to minimise the Euclidean distance between WH and the data in V, which is defined by:

$$||V - WH|| = \sqrt{\sum_{ij} \left(V_{ij} - \sum_{k} W_{ik} H_{kj} \right)^2}, \tag{3.1}$$

Each iteration of the process to minimise $||V - WH||$ is performed using the aforementioned update rules, which are defined as

$$W_{ik} \leftarrow \frac{W_{ik} \left[VH^T \right]_{ik}}{\left[WHH^T \right]_{ik}}, \tag{3.2}$$

and

$$H_{kj} \leftarrow H_{kj} \frac{\left[W^T V \right]_{kj}}{\left[W^T WH \right]_{kj}}, \tag{3.3}$$

where the elements in W and H are substituted by those on the right hand side of Equations 3.2 and 3.3. These iterations were repeated until a stable solution was reached. The number of components used varied from 8–14 depending on the quality of the fitting. This was judged independently for each redshift bin, and was set to be the greatest number (between 8 and 14) that could be generated before overfitting of any of the input spectra occurred. Overfitted spectra are identified as those having much lower χ^2_ν values than others in the input sample.

In the second step, components generated from the first step could be linearly combined to reconstruct the spectrum of each of the BAL quasars to be studied. This was done using a similar procedure to the first step, this time with V containing the fluxes of the BAL quasars to be reconstructed and H containing the component fluxes generated in the first step. Random values were assigned to the weights in W and the iteration procedure was performed using Equation 3.2 only in order to find the correct weights. Because the component spectra were based on non-BAL quasar spectra, the resulting reconstructions were of the unabsorbed pseudo continuum. To execute this step for the Gemini and WHT spectra, they were first placed on the SDSS logarithmic wavelength scale, using a linear interpolation between pixels. An iterative procedure was used to mask out the absorption regions from the fit, the initial masking regions being (in the object rest-frame) λ(Å)$\leq$1240, 1295$\leq\lambda$(Å)$\leq$1400, 1430$\leq\lambda$(Å)$\leq$1546,

and $1295 \leq \lambda(\text{Å}) \leq 1880$. At each step in this procedure, the component spectra were fit to the observed spectrum using the current mask, and a new mask was generated by searching for regions where the observed flux fell significantly below the reconstruction. The iteration continued until the change in the mask from one step to the next was small.

The most highly reddened quasar spectra from the SDSS sample were given an empirical dust correction, assuming a power-law reddening curve (Pei, 1992), to match their overall shape to that of a typical quasar at the same redshift. After the component spectra were fitted to the de-reddened spectrum, both the BALQSO spectrum and the reconstruction had the dust correction removed, matching the reconstruction to the shape of the original observed spectrum. For the Gemini and WHT spectra, the spectral coverage was insufficient to give reliable measurements of the continuum slope. However, the three objects in the original sample whose SDSS continua required a reddening correction (J032832.77−070750.3, J034946.61−065730.3 and J111516.08+460234.6) were all excluded for other reasons; we hence assumed that no such corrections were required for the Gemini and WHT spectra of the remaining objects.

For the SDSS spectra, unphysical reconstructed emission line profiles in C IV were detected automatically and corrected by reducing the number of components used in the fit. Additionally, spectra that failed certain automated quality control measurements were visually inspected for failures in the automatic masking procedure, and in such cases a manually-defined mask was applied and the components re-fitted. For the Gemini and WHT data, the small number of spectra meant that they could all be visually inspected for both of these potential problems. The same corrections as for SDSS spectra were applied in the cases where unphysical emission line profiles or poorly-defined masks were seen. Of the 35 quasars with variable BALs, three required corrections because of their emission line profiles and nine because of poor automatically-constructed masks. The higher rate of manual intervention relative to SDSS spectra is primarily due to the smaller wavelength range of the Gemini spectra, and does not affect the quality of the final reconstructions.

The uncertainty on the reconstructed flux level was determined using the synthetic BALQSO spectra described in Section 7.1 of Allen et al. (2011). A sample of 50 non-BAL quasars was selected in each redshift bin, and a series of BAL troughs with known depth and shape were inserted into each spectrum. Extra noise was also added. The modified spectra were run through the same pseudo continuum fitting procedure as the observed spectra. The fits derived in this way were then compared to the fits

Table 3.3: Table of median RMS errors derived for quasars in each redshift bin.

Minimum z	Maximum z	Median RMS error
1.6	1.7	0.1031
1.7	1.8	0.0813
1.8	1.9	0.0908
1.9	2.0	0.0833
2.0	2.1	0.0759
2.1	2.2	0.0720
2.2	2.3	0.0342
2.3	2.4	0.0299
2.4	2.5	0.0293
2.5	2.6	0.0278
2.6	2.7	0.0358
2.7	3.0	0.0375
2.0	2.5	0.0353
3.5	4.0	0.0496
4.0	4.5	0.0549

produced for the original unabsorbed spectra in the wavelength range of the inserted BAL trough, defined as all pixels with a (known) flux ratio < 0.9 when normalised to the reconstruction. The error in each spectrum was characterised using the root mean square (RMS) of the fractional difference between reconstructions followed by taking the median value of this RMS over all spectra in each bin of redshift and per-pixel S/N in the r-band. The resulting uncertainty was assumed to be dominated by the uncertainty in the normalisation of the pseudo continuum, rather than its shape, resulting in the errors in all pixels being perfectly correlated with each other. Table 3.3 indicates the median RMS errors used for each wavelength bin, while Table 3.4 shows the median RMS errors at various S/N (signal/noise) bins in the $2.0 \leq z \leq 2.1$ redshift bin. The median RMS errors as a function of S/N show the same shape across all redshift bins.

The above steps produced a reconstruction of the unabsorbed pseudo continuum for each observed spectrum. For a given BALQSO, the reconstructions of the two epochs were derived in a consistent

Table 3.4: Table of median RMS errors derived for quasars in each S/N bin.

Minimum S/N ratio	Maximum S/N ratio	Median RMS error
1	2	0.1711
2	3	0.1195
3	4	0.1132
4	5	0.0922
5	6	0.0909
6	7	0.0777
7	8	0.0775
8	9	0.0643
9	10	0.0530
10	11	0.0496
11	12	0.0404
12	13	0.0402
13	14	0.0391
14	15	0.0301
15	16	0.0366
16	17	0.0272
17	18	0.0271
18	19	0.0308
19	20	0.0166
20	21	0.0249
21	22	0.0172
22	23	0.0167

fashion, having used the same NMF components and the same fitting algorithms, but are independent of each other.

3.2.4 Pseudo Equivalent Width

In order to investigate the variability properties of the variable BALs, a modified equivalent width was defined using the following equation, which is referred to hereafter in this chapter as a 'pseudo equivalent width':

$$EW_p = \int \frac{f_{cp} - f_l}{f_{cp}} dv \,, \tag{3.4}$$

This quantity was normalised to the NMF reconstructions (the pseudo continuum) as opposed to the modelled continuum EW used for BAL identification in Section 3.2.1. In this case, EW_p is the pseudo equivalent width, f_l is the line flux density and f_{cp} is the pseudo continuum flux density (in each velocity bin). The depth $f_{cp} - f_l$ at each point in velocity space is therefore the difference between the absorption line flux and the sum of emission and continuum flux thought to be entering the absorber. Both transitions have a doublet structure, with Si IV having a larger separation (1900 km s^{-1}) than C IV (500 km s^{-1}). This may cause Si IV BALs to be identified as slightly wider than C IV BALs of the same intrinsic width but should not affect the validity of the BAL variability measurements which were taken over the entire absorption line. The conventions adopted for measuring the velocities of absorption features were that blueshifted absorption was defined as negative, with pseudo equivalent widths being positive for regions of absorbed pseudo continuum. However when referring to the velocities of absorbers, terms such as greater or larger refer to the magnitude of the velocity, i.e. $|v|$.

The observed wavelengths were first translated to quasar rest-frame velocities, with the laboratory wavelength of the red line of the doublet belonging to the appropriate transition defined as zero velocity. This ensured that the velocities of outflowing absorbing features were always measured as negative at any velocity greater than zero. These zero velocities correspond to positions in wavelength space of 1402.77 Å for Si IV and 1550.77 Å for C IV. At each bin, wavelengths were converted to velocities using the relativistic Doppler shift formula given as follows:

$$\frac{v}{c} = \frac{1 - \left(\frac{\lambda_{line}}{\lambda_{abs}}\right)^2 (1+z)^2}{1 + \left(\frac{\lambda_{line}}{\lambda_{abs}}\right)^2 (1+z)^2}\,, \tag{3.5}$$

where λ_{line} is the rest-frame wavelength and λ_{abs} is the observed wavelength of the absorption feature. Pseudo EW values were calculated by summing the products of pseudo continuum-normalised depths and velocity bin widths Δv_i over the BAL velocity range v_{min} to v_{max} using:

$$EW_p = \sum_{i=v_{min}}^{v_{max}} \left[\left(1 - \frac{f(i)}{f_{cp}(i)} \right) \Delta v_i \right] , \tag{3.6}$$

By using the median RMS error estimates in the position of the pseudo continuum as listed in Tables 3.3 and 3.4, a fractional error on the pseudo-continuum (P_{frac} of each spectrum can be derived using the fact that the median RMS error as a function of per-pixel r-band S/N follows the same shape as that in Table 3.4 across all redshift bins. By additionally utilising the SDSS, Gemini/GMOS and WHT/ISIS error spectra, a total pseudo EW error was obtained. This consists of two functions A and B as follows

$$A = \sum_{i=v_{min}}^{v_{max}} \left[\left(\frac{\sigma_f(i)}{f_{cp}(i)} \right)^2 \Delta v_i^2 \right] , \tag{3.7}$$

$$B = \sum_{i=v_{min}}^{v_{max}} \left[\left(\frac{f(i)}{f_{cp}(i)} \right) P_{frac} \Delta v_i \right] , \tag{3.8}$$

The total error in the pseudo EW calculation is then given by:

$$\sigma_{EW_p} = \sqrt{A + B^2}\,, \tag{3.9}$$

3.2.5 BAL pseudo EW Variability

Following the method of Lundgren et al. (2007) (for pseudo EW rather than continuum-based EW), the fractional change in BAL pseudo EW given by $\Delta EW_p / \langle EW_p \rangle$ was measured, where ΔEW_p is the difference in pseudo EW and $\langle EW_p \rangle$ is the average pseudo EW across the two epochs. Fractional

pseudo EW changes are a robust method of measuring variability since they represent, for a mean value across the two epochs, a change in the BAL gas covering fraction or the fractional change, driven by ionising continuum fluctuations, in the absorbing ion population for a non-saturated absorber. Comparisons of fractional pseudo EW variations for an object which contains BALs from both ions and which overlap in velocity space can provide insight into outflow structure and possible contributions of ionisation changes or covering fraction variations. A summary of all variable BALs, including velocity boundaries (v_{max} and v_{min}), the pseudo EWs at each epoch, the time interval between epochs in the quasar rest frame (t_{qrest}) and the fractional pseudo EW change $\Delta EW_p/\langle EW \rangle$ is presented in Table 3.5 and continued in Table 3.6.

Of the 50 quasars studied in this chapter, 15 had no variable BALs. The spectra of these objects in velocity space relative to the rest-frame wavelength of the red doublet component of the Si IV and C IV lines are shown in Figure 3.2. The spectra of the variable quasars are shown later in this chapter in appropriate sections.

The epoch spearation timescales which were studied in this chapter represent an intermediate epoch rest frame separation time between the C IV short term data in Lundgren et al. (2007) of a few weeks to months and the mostly longer timescales investigated in Gibson et al. (2008) and the timescales between the Large Bright Quasar Survey (LBQS) and Hobby-Eberly Telescope (HET) observations in Gibson et al. (2010). The Gibson et al. (2008) study produced results based on a 3 to 6 year quasar rest frame epoch separation time for C IV only. The Gibson et al. (2010) study, on the other hand, was a multi-epoch study with the longest rest frame time period being ≈5 to 7 years additionally including the Si IV absorption region. Notably, Gibson et al. (2010) only had full spectral coverage (defined as 0 to 30 000 km s^{-1}) for Si IV in the LBQS and HET spectra and so could only provide results for the Si IV absorption region on corresponding time scales. Figure 3.3 illustrates the fractional change in EW of BALs in the sample investigated in this chapter plotted against the rest frame time interval, which indicates no obvious relationship between the two variables. A detailed investigation of the trends in variability with respect to time and other variables is reported at the end of this chapter in Section 3.3.

Table 3.5: Two-epoch pseudo equivalent widths and fractional variability of variable BALs.

Object (BAL No.)	Δt_{qrest} (days)	Ion	v_{max} (km s^{-1})	v_{min} (km s^{-1})	EW_{p1} (km s^{-1})	EW_{p2} (km s^{-1})	$\Delta EW_p/\langle EW_p \rangle$
SDSSJ001025.90+005447.6	1052	C IV	-13200	-8200	2941±240	3361±77	0.133±0.080
SDSSJ004613.54+010425.7	1282	Si IV	-20400	-3000	2986±380	2245±243	-0.284±0.174
		C IV	-28100	-6300	5449±575	4514±276	-0.188±0.129
SDSSJ025720.43-080322.5	1332	Si IV	-25500	-21800	1222±502	1121±135	-0.086±0.444
SDSSJ031033.45-060957.8	1296	Si IV	-20200	-14800	673±319	1253±76	0.602±0.355
SDSSJ031331.22-070422.8	1064	Si IV	-17100	-5600	5213±178	5638±53	0.078±0.034
		C IV	-17400	-5800	7634±199	8292±47	0.083±0.026
SDSSJ033223.51-065450.5	830	Si IV	-19500	-10100	3595±384	3343±75	-0.073±0.113
SDSSJ035749.11-061121.9	1328	C IV	-13600	-7000	2394±178	656±102	-1.139±0.155
SDSSJ073535.44+374450.4	994	Si IV	-19800	-5000	3729±238	5074±87	0.305±0.058
		C IV	-28000	-7500	7716±355	8978±99	0.151±0.044
SDSSJ081823.46+484910.8	1252	C IV	-14100	-5300	3703±488	2512±411	-0.383±0.209
SDSSJ081925.00+032455.7	1032	Si IV	-9000	-4000	1686±148	1109±44	-0.412±0.113
SDSSJ083718.63+482806.1	804	Si IV	-16100	-4500	5210±177	6132±92	0.163±0.035
SDSSJ084408.29+423226.9	775	Si IV	-17800	-5200	2825±145	3364±80	0.174±0.054
		C IV	-21300	-4700	5712±436	6475±86	0.125±0.073
SDSSJ085006.08+072959.0	819	C IV	-27300	-13900	1313±188	0±113	-2.000±0.472
SDSSJ085104.05+051539.8	446	Si IV	-12600	-5300	2112±176	3662±32	0.537±0.064
		C IV	-11300	-4000	5578±87	5814±21	0.041±0.016
SDSSJ092639.34+383656.7	912	C IV	-22800	-8600	3772±645	2841±185	-0.282±0.205
SDSSJ093251.98+023727.0	1272	Si IV	-30700	-6300	1086±901	2536±648	0.801±0.660
		C IV	-29400	-11000	6211±475	7443±179	0.180±0.075
SDSSJ100312.63+402505.6	606	Si IV	-13400	-7200	2503±277	2857±72	0.132±0.107
SDSSJ101056.68+355833.3	687	C IV	-13100	-3400	6407±149	6333±127	-0.012±0.031
SDSSJ104059.79+055524.4	963	Si IV	-15600	-4500	2295±396	4202±55	0.587±0.128

† These objects were observed using WHT/ISIS, unmarked objects were observed using Gemini/GMOS.

* May include contamination from C II LoBAL.

Outflow velocities are rounded to the nearest 100 km s^{-1} as the error in velocity width is ≈200 km s^{-1}. EW_{p1} and EW_{p2} denote pseudo EW for earlier and later epochs respectively.

Table 3.6: Two-epoch pseudo equivalent widths and fractional variability of variable BALs (continued).

Object (BAL No.)	Δt_{qrest} (days)	Ion	v_{max} (km s^{-1})	v_{min} (km s^{-1})	EW_{p1} (km s^{-1})	EW_{p2} (km s^{-1})	$\Delta EW_p/\langle EW_p \rangle$
SDSSJ110041.19+003631.9	1346	Si IV	-17000	-5500	2909±435	633±185	-1.285±0.317
		C IV	-22100	-5000	7029±505	3246±233	-0.736±0.115
SDSSJ110339.90+011928.5	1173	Si IV	-10800	-4800	1909±400	2871±128	0.403±0.179
SDSSJ112733.69+343008.8	436	C IV	-19500	-11100	2377±418	2857±129	0.184±0.168
SDSSJ113831.42+351725.3†	360	Si IV	-14100	-1600	4381±621	1501±180	-0.979±0.245
		C IV	-20900	-1700	8905±782	4764±236	-0.606±0.125
SDSSJ114704.47+153243.3†	303	Si IV	-20600	-3200	7354±403	7157±145	-0.027±0.059
		C IV	-27300	-3200	10323±620	7918±200	-0.264±0.072
SDSSJ134458.82+483457.5†	615	C IV	-21100	-7100	2688±1058	5493±319	0.686±0.288
SDSSJ142244.45+382330.6	311	C IV	-16500	-7400	2542±239	3808±60	0.399±0.079
SDSSJ143604.64+350428.5	616	Si IV	-20600	-10800	4342±663	3837±238	-0.124±0.172
		C IV	-16800	-7000	7828±557	5146±183	-0.413±0.092
SDSSJ151601.51+430931.4	691	Si IV	-15300	-5700	3633±196	4169±85	0.138±0.055
		C IV	-25800	-4600	5712±380	6755±122	0.167±0.064
SDSSJ162657.47+405848.0†	551	C IV	-13100	-2500	5884±238	4886±107	-0.185±0.049
SDSSJ164152.30+305851.7†	611	Si IV	-30400	-1800	26259±1468*	26519±212*	0.010±0.056*
		C IV	-27600	-1800	13166±1166	13886±212	0.053±0.088
SDSSJ210436.62-070738.3	1080	C IV	-23500	-9800	2674±462	5922±58	0.756±0.116
SDSSJ211718.17+010248.9	860	Si IV	-27700	-13100	1931±512	292±121	-1.475±0.588
		C IV	-25800	-15100	3348±372	664±85	-1.338±0.229
SDSSJ212412.60+095923.3†	737	Si IV	-13300	-3300	1054±966	227±450	-1.291±1.981
		C IV	-14000	-2900	6299±515	3872±434	-0.477±0.136
SDSSJ213138.93-070013.3	1188	C IV	-27400	-3800	5368±1185	5697±557	0.059±0.237
SDSSJ222505.28-084542.7	1176	C IV	-26900	-7500	4464±1165	2380±467	-0.609±0.384

† These objects were observed using WHT/ISIS, unmarked objects were observed using Gemini/GMOS.

* May include contamination from C II LoBAL.

Outflow velocities are rounded to the nearest 100 km s^{-1} as the error in velocity width is ≈200 km s^{-1}. EW_{p1} and EW_{p2} denote pseudo EW for earlier and later epochs respectively.

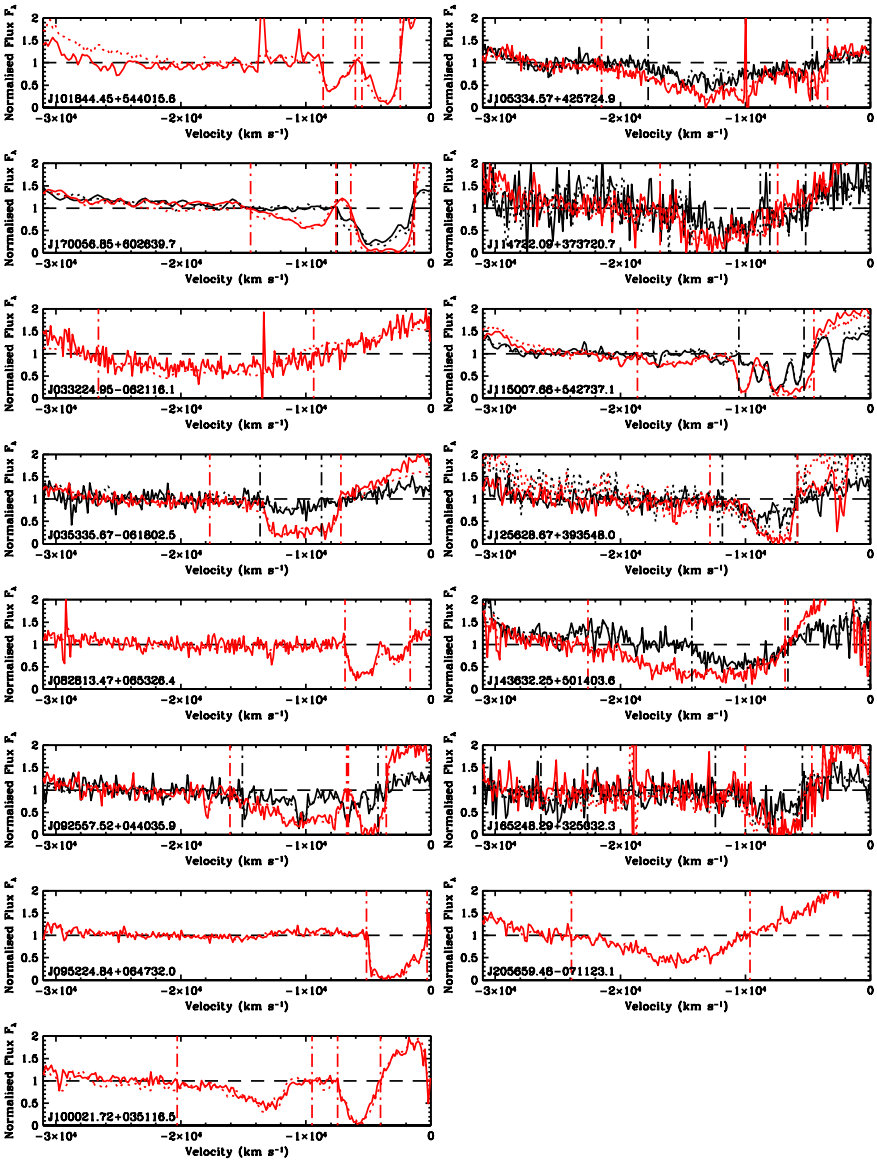

Figure 3.2: Behaviour of Si IV (black) and C IV (red) BAL regions plotted in velocity space for quasars having no variable BALs. Solid lines represent the SDSS spectra while dotted lines represent the Gemini/WHT spectra. Vertical dash-dot lines represent the BAL boundaries. Six of these quasars contain C IV BALs only.

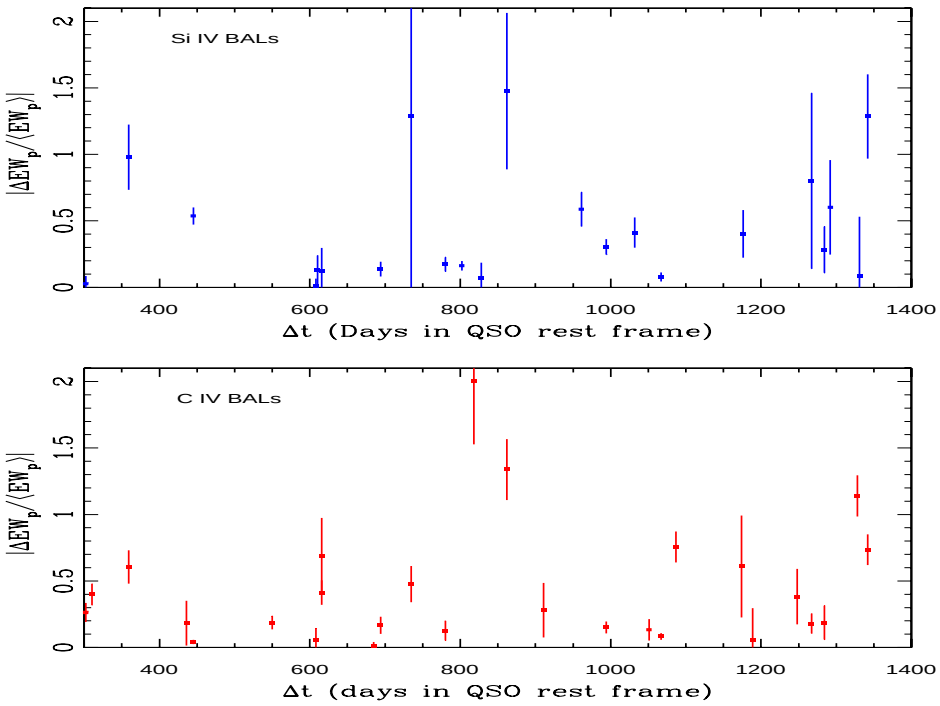

Figure 3.3: Magnitude of fractional change in pseudo EW against quasar rest frame time interval between epochs for Si IV (upper panel) and C IV (lower panel).

3.3 Discussion

3.3.1 Trends, comparisons of C IV and Si IV properties and variability

Attempts to understand the physical mechanisms giving rise to BAL variability require an investigation into the correlations, if any, of the amplitude of variation with other properties. Such properties investigated as part of the work in this chapter included the luminosity of the host quasar, elapsed rest frame time between observations, the velocity of the bulk of the outflowing gas and BAL pseudo EW (comprising depth, width and velocity). To achieve this, a series of Spearman rank correlation tests were carried out to determine the likelihood of dependence of $|\Delta EW_p/\langle EW_p\rangle|$ and $|\Delta EW_p|$ on such parameters, the results of which are presented in Table 3.7. This was achieved by calculating the p-value for the likelihood of a null hypothesis (no underlying correlation) and subtracting it from 100 percent probability. A correlation probability was considered highly significant if it was greater than 99 percent. Significance values of between 95 percent and 99 percent were considered plausible but no

Table 3.7: Results of Spearman rank Correlation Tests

Comparison	Si IV Confidence (Sign of ρ)	C IV Confidence (Sign of ρ)
$\lvert\Delta EW_p\rvert$ vs. $\langle EW_p\rangle$	72%[b] (-)	41% (-)
$\lvert\Delta EW_p/\langle EW_p\rangle\rvert$ vs. B_{vel}	78% (-)	93% (+)
$\lvert\Delta EW_p\rvert$ vs. B_{vel}	92% (-)	71% (+)
$\lvert\Delta EW_p/\langle EW_p\rangle\rvert$ vs. $\langle B_{depth}\rangle$	>99.99%[b] (-)	99.95% (-)
$\lvert\Delta EW_p\rvert$ vs. $\langle B_{depth}\rangle$	98%[b] (-)	93% (-)
$\lvert\Delta EW_p/\langle EW_p\rangle\rvert$ vs. M_i	61% (+)	93% (+)
$\lvert\Delta EW_p\rvert$ vs. M_i	6% (-)	97% (+)
$\lvert\Delta EW_p/\langle EW_p\rangle\rvert$ vs. t_{qrest}	78% (+)	63% (+)
$\lvert\Delta EW_p\rvert$ vs. t_{qrest}	51% (+)	15% (+)
$\lvert\Delta EW_p/\langle EW_p\rangle\rvert$ vs. V_{width}	40%[b] (+)	40% (-)
$\lvert\Delta EW_p\rvert$ vs. V_{width}	83%[b] (+)	58% (+)

[b]The unusual Si IV $\langle EW_p\rangle$ measurement for J164152.30+305851.7 was not included in this test.

definitive conclusions were drawn from such values.

The variability dependence tests were split into correlation testing of particular parameters with fractional change and absolute change in EW_p. This was considered useful as the former could indicate that a parameter's increase or decline correlated with the fraction of outflowing gas along the line of sight affected by the variability inducing effect (possibly ionisation fraction changes or changes in covering fraction). The latter, if detected, was considered to indicate that the parameter change was correlated with absolute changes in line of sight column density.

The fractional change in pseudo EW with respect to quasar rest frame time scale did not show a significant correlation, with only 63 percent confidence for C IV and 78 percent for Si IV. This indicated that time dependence of variability amplitude was not visible in the sample over the timescales investigated. The absolute change ΔEW_p was also not correlated with rest frame time interval in either ion. It was considered to be worthwhile investigating whether or not the rest frame timescales had an impact on the variability categorisation of the BALs. The 35 quasars containing BALs classed as variable had a mean t_{qrest} of 757 days, compared with 833 days between observations for the 15 quasars contain-

ing no variable BALs. This difference was not considered to be significant as the standard deviation on the range of rest frame timescales of variable quasars was $\sigma(\Delta t)$=316 days. These findings contrasted with studies on shorter and longer rest-frame timescales (Lundgren et al., 2007; Gibson et al., 2010) in which the most variable absorption features were concentrated at the longest rest-frame time intervals. Quasars in the sample containing variable BALs had a mean absolute i-band maginitude of M_i=−27.583 mag compared to a mean of M_i=−27.307 mag for quasars containing no variable BALs. As in the case of time separation, this was not considered to be a significant difference since, for the distribution of absolute i-band maginitudes in variable quasars, $\sigma(M_i)$=0.626 mag.

The BALQSO SDSS J164152.30+305851.7 was the only object in our sample which showed evidence for LoBAL absorption features. Obvious examples of these features were visible in both the WHT and SDSS observations of this object and correspond to the transitions of Al III at 1860 Å and Mg II at 2798 Å. In addition to these, in Hall et al. (2002) a rarer LoBAL resulting from the C II transition at 1334 Å was found in several LoBAL QSOs. A measurement of the average pseudo EW between −1800 and −30 400 km s^{-1} from the Si IV emission line centre in SDSS J164152.30+305851.7 gave an exceptionally large value of $\langle EW_p \rangle$=26 389±742 km s^{-1}, several times that of the next strongest BAL in the Si IV sample. It was therefore considered very plausible that this measurement was contaminated by additional C II LoBAL absorption in the Si IV BAL absorption range, given that the centre of the C II emission line is located approximately −15 000 km s^{-1} from the centre of the Si IV emission line. Further evidence for the possible existence of such absorption was provided by the fact that the Al III LoBAL spans a velocity range of approximately 0 to −14 000 km s^{-1}, providing the likely position of any C II absorption (indicated in Figure 3.4). For these reasons, the Si IV BAL from J164152.30+305851.7 was not included in the tests for dependence on average pseudo EW, or its component quantities of depth and width.

A significant correlation was not observed in the $|\Delta EW_p|$ vs. $\langle EW_p \rangle$ relationship, which the Spearman rank test gave as 72 percent confidence for Si IV and 41 percent for C IV. The value of $\langle EW_p \rangle$ can be split into two more fundamental properties, one being the velocity width (V_{width}) of the BAL, corresponding to the difference in velocity between the upper and lower boundaries of the BAL trough, the other being the depth $\langle B_{depth} \rangle$, defined as the mean pseudo continuum normalised depth across the BAL trough averaged between the two epochs. A test of $|\Delta EW_p / \langle EW_p \rangle|$ vs. V_{width} did not give a significant correlation for either Si IV or C IV (significance of 40 percent for both ions). This was in stark contrast with the strong inverse correlation found for the $|\Delta EW_p / \langle EW_p \rangle|$ vs. $\langle B_{depth} \rangle$

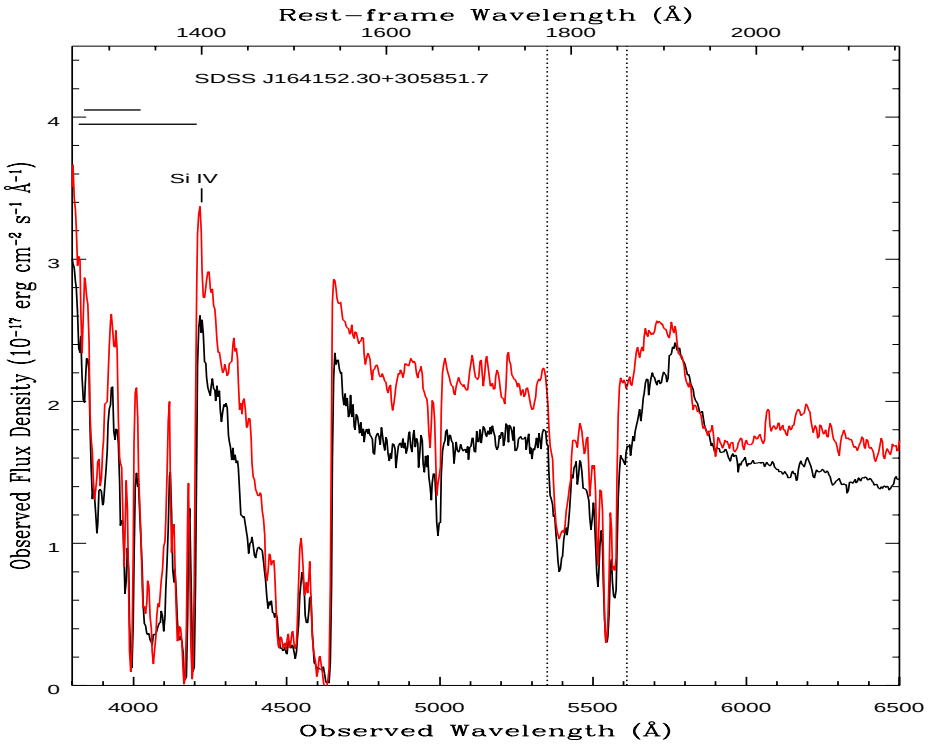

Figure 3.4: WHT/ISIS spectrum (black) and Gemini/GMOS spectrum (red) of the LoBAL quasar SDSS J164152.30+305851.7. Dotted vertical lines indicate the extent of Al III LoBAL absorption (from zero to approximately -14000 km s^{-1}). The Si IV emission line is also labelled. The lower thick horizontal black line indicates the range of BAL absorption measured blueward of the Si IV emission line, while the upper thick horizontal black line indicates the possible location of C II LoBAL absorption based on the extent of the Al III absorption.

dependence, which the Spearman rank test revealed to be >99.99 percent for the Si IV sample and 99.95 percent for the C IV sample, with the negative sign of ρ indicating an inverse scaling (see Figure 3.5). However this result was likely to be due to the fact that $\langle EW_p \rangle$ showed a strong positive correlation with $\langle \mathrm{B}_{depth} \rangle$ in both Si IV (99.97 percent significance) and C IV (99.93 percent significance). Since the fractional pseudo EW measure incorporates $\langle EW_p \rangle$ as the denominator, such a correlation was not inferred to represent anything physical. Correlation probability was possibly significant (98 percent) in the $|\Delta EW_p|$ vs. B_{depth} relationship for Si IV BALs but not so in the C IV sample (93 percent), with negative ρ in both cases. This was similar to the findings of Gibson et al. (2008) for C IV BALs, which found no correlation between the absolute change in absorption strength in velocity ranges which varied and the depth of those regions. There was no discernible correlation between $|\Delta EW_p|$ and V_{width} (83 percent correlation confidence for Si IV and 58 percent for C IV). Work undertaken prior to the writing of this thesis which compared BAL variability to velocity width is minimal, although Filiz Ak

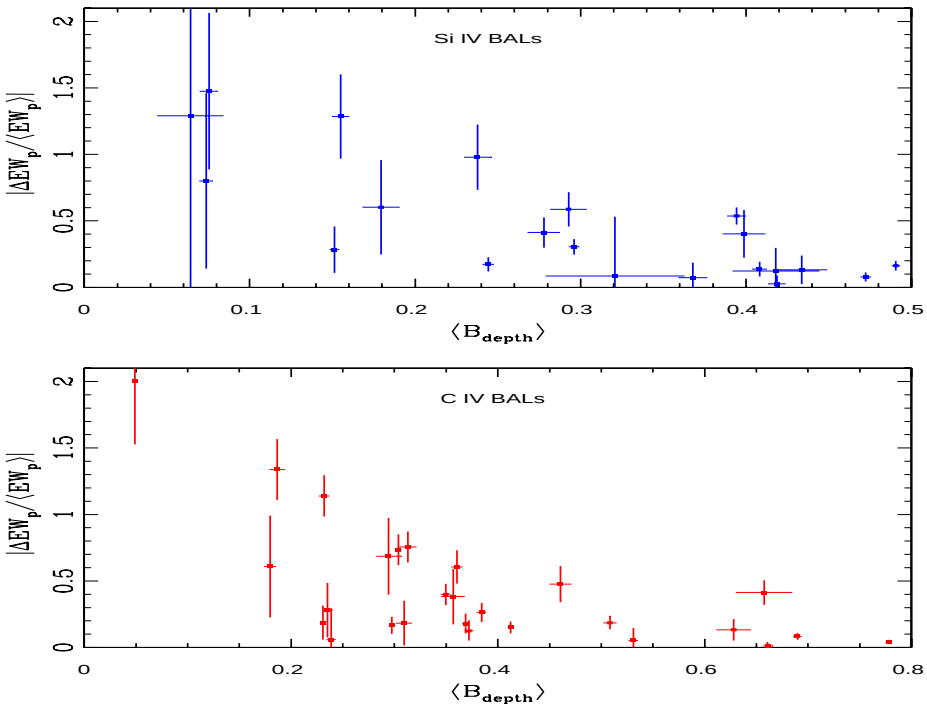

Figure 3.5: Fractional pseudo EW variability for Si IV BALs (top panel) and C IV BALs (bottom panel) vs. average mean normalised BAL depth across the two epochs. Outlying Si IV BAL measurement from J164152.30+305851.7 was not included.

et al. (2012) found tentative evidence that relatively narrow C IV BALs are more likely to undergo disappearance than wider BALs.

For this study, the BAL velocity (B_{vel}) was defined as the velocity of the depth centroid of the BAL feature, giving the best estimate of the value for the column density weighted mean of the velocity of the outflowing gas. A study of the dependence of variability amplitude on velocity across a range of velocity bins in a sample of C IV BALs in Capellupo et al. (2011) showed a relationship of strengthening variability with increased velocity. The test for the correlation of $|\Delta EW_p/\langle EW_p\rangle|$ on B_{vel} in the dataset used for this chapter returned a probability of 78 percent for Si IV and 93 percent for C IV, implying that there is no discernible correlation. Although this was not exactly the same type of study as in Capellupo et al. (2011), since the work described in this chapter reports on statistics for the whole BAL features rather than portions thereof, this may suggest a contradiction with those previously reported results. For the $|\Delta EW_p|$ vs. B_{vel} relationship, correlation significances of 92 percent for Si IV BALs and 71 percent for C IV BALs were found.

The dependence or otherwise of the host quasar luminosity on BAL variability can shed light on the contribution of ionisation fraction changes to the variability, as it is a general property of quasars that emission line variability, which is known to be driven by ionisation continuum variations, has an inverse dependence on host luminosity (Vanden Berk et al., 2004). Luminosity was defined in terms of the SDSS i-band absolute magnitude (M_i) as listed in Shen et al. (2011). There was no strong evidence found in this sample, in either C IV or Si IV BALs, of a correlation in the $|\Delta EW_p/\langle EW_p\rangle|$ vs. M_i relationship, given the correlation probabilities of 93 percent and 61 percent respectively. The Spearman rank test also gave a confidence of 6 percent for SiIV and 97 percent for C IV correlation with respect to $|\Delta EW_p|$ vs. M_i, which, given a positive value of ρ, may indicate an inverse scaling between the absolute variability and luminosity for C IV BALs. BAL variability dependence on host quasar luminosity has not been extensively studied, however Filiz Ak et al. (2012) reported no correlation between quasar luminosity and the rate of C IV BAL disappearance.

3.3.2 Quasars containing both Si IV and C IV variable BALs

An interesting subsample of quasars containing variable BALs were those which contained examples in both Si IV and C IV, allowing direct comparison of the behaviour of these absorption features within the same objects. There were 14 such quasars in our sample, each consisting of one BAL from each ion. Two notable facts were apparent in this subsample, namely (1) for any given quasar, both BALs changed in the same direction (as has been noted previously in Capellupo et al. (2012)) and (2) when the velocity range over which the BALs spanned was considered, there was found to be a considerable overlap between the C IV and Si IV outflows. This suggested that the same outflowing structure is responsible for such BALs and that the dominant variability mechanism is the same in each case.

Comparisons of the average values of several BAL parameters between each ion can provide an insight into the likely physical mechanisms leading to variability. For example, if the outflows of one ion were found to be at a significantly different mean velocity from that of the other ion then, following the model of Elvis (2000), this would provide evidence for the ions forming in different physical locations. Mean values calculated of several BAL or quasar properties in the dual ion variable BAL subsample are provided in Table 3.8, while Figure 3.6 displays the spectra of these objects.

This sample included the LoBAL quasar SDSS J164152.30+305851.7 which contained a Si IV BAL

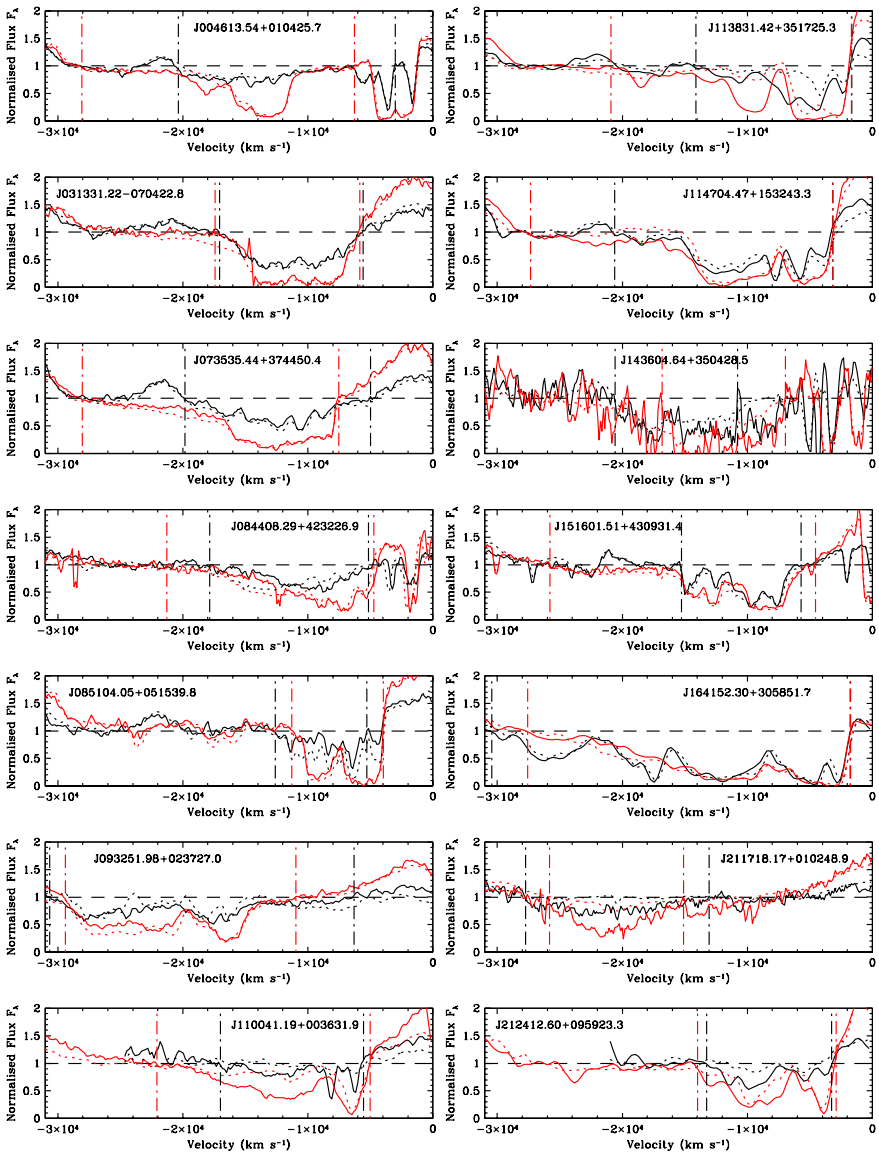

Figure 3.6: Behaviour of Si IV (black) and C IV (red) BAL regions plotted in overlapping velocity space for each of the dual ion variable BAL quasar sample. Spectra are smoothed using a 3-pixel boxcar smoothing for clarity. Solid lines represent the SDSS spectra while dotted lines represent the Gemini/WHT spectra. Vertical dash-dot lines represent the BAL boundaries. A can be seen, the overlap region forms the majority of the width of both BALs in every case.

Table 3.8: Mean BAL Properties for quasars containing variable BALs from both ions.

Property	Si IV mean	C IV mean
B_{vel}	-13181±55 km s^{-1}	-11762±53 km s^{-1}
B_{vel}*	-12271±56 km s^{-1}	-11880±54 km s^{-1}
$\langle EW_p \rangle$	4881±92 km s^{-1}	6738±80 km s^{-1}
$\langle EW_p \rangle$*	3226±80 km s^{-1}	6216±72 km s^{-1}
$\lvert \Delta EW_p / \langle EW_p \rangle \rvert$	0.536±0.159	0.345±0.028
$\lvert \Delta EW_p / \langle EW_p \rangle \rvert$*	0.577±0.171	0.367±0.030
V_{width}	14439±111 km s^{-1}	16812±107 km s^{-1}
V_{width}*	13345±113 km s^{-1}	16120±109 km s^{-1}
$\langle B_{depth} \rangle$	0.308±0.003	0.431±0.002
$\langle B_{depth} \rangle$*	0.262±0.003	0.423±0.003*

*SDSS J164152.30+305851.7 excluded

region of exceptionally large average pseudo EW of $\langle EW_p \rangle$=26 389±742 km s^{-1}, which was not matched by a similarly large C IV BAL and may have been due to C II absorption contaminating the measurement. Table 3.8 therefore includes a duplicate set of comparisons from which the quasar SDSS J164152.30+305851.7 was excluded. If all 14 quasars had been taken into account, the mean BAL velocity of Si IV would have been larger than that of C IV by ≈1419 km s^{-1}, however this reduces to a difference of <400 km s^{-1}, about twice the typical BAL velocity error, in the 13 quasar sample. This difference was therefore considered to be consistent with zero. The mean epoch averaged pseudo EW was larger in C IV than in Si IV by 38 percent, which increased dramatically to 93 percent in the 13 quasar sample from which the apparent large Si IV BAL from SDSS J164152.30+305851.7 was excluded. This difference was mainly explained by the fact that the C IV BALs were on average 40 percent deeper (61 percent in the 13 quasar sample) than Si IV in the BALQSO sample investigated in this chapter. However, there was also found to be a difference in velocity width, with the mean value for C IV being ≈2400 km s^{-1} larger, or ≈2800 km s^{-1} larger without the LoBAL quasar, than that for Si IV. Also, the Si IV BALs showed a 55 percent (57 percent for the 13 quasar sample) stronger mean fractional pseudo EW variability than C IV.

To determine what relationship, if any, exists between the variability of all the Si IV and C IV BALs in this quasar subsample, a Spearman Rank test was carried out to determine the significance of a

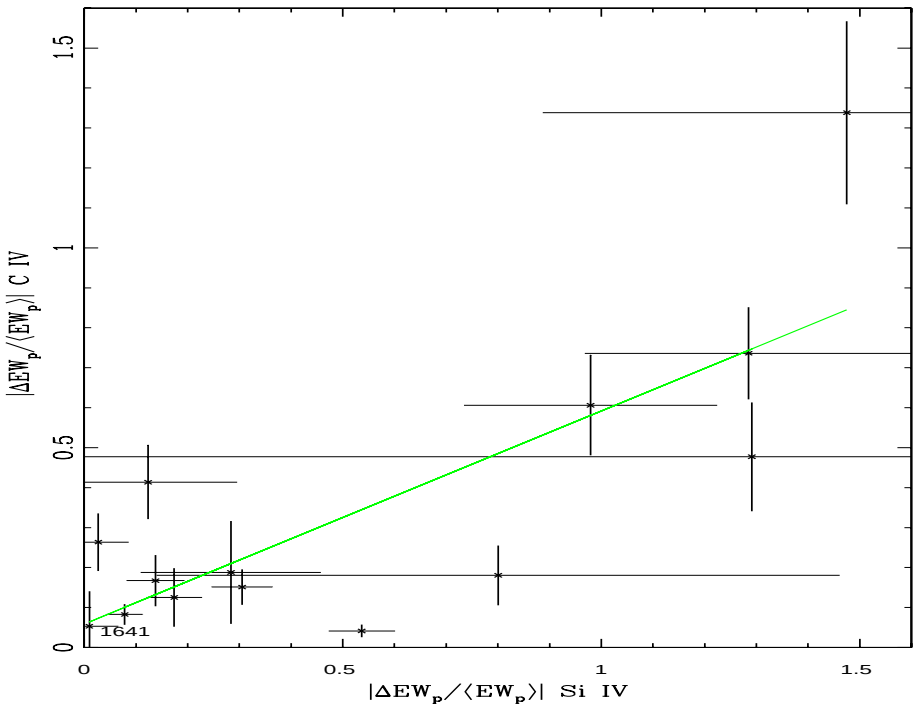

Figure 3.7: Fractional change in pseudo EW for C IV (vertical axis) and Si IV (horizontal axis). The green line represents a least squares fit to the data.

correlation between the Si IV and C IV values of $|\Delta EW_p/\langle EW_p\rangle|$. This revealed a probability of 98 percent of correlation, just below the threshold of 99 percent for strong significance. The test was also performed on the dependence of $|\Delta EW_p|$ of Si IV to that of C IV, which revealed a probability of correlation of 91 percent, too low to be considered significant. This relationship between the fractional changes in BAL pseudo EW of the two ions is illustrated in Figure 3.7 and shows that a least squares fit line closely matched 8 of the data points, including that of the LoBAL SDSS J164152.30+305851.7 (marked "1641" in the plot). No properties of the BALs nor their host quasars were found that distinguished those which fell relatively close to the best fit line from those which did not.

In the study by Gibson et al. (2010), a significant correlation was found (>99 percent) between the absolute fractional change in the total pseudo equivalent width in the absorption regions of C IV and Si IV (defined in that study as all spectral bins spanning 0 to -30 000 km s^{-1} from the rest wavelength of the red doublet component, as opposed to only the identified BAL regions which were used in this study) of 9 quasars over rest frame time intervals of ≈5-7 years. This high correlation depended on the exclusion of one outlying quasar, 1235+1453, which displayed a strong variability in the C IV BAL,

but virtually no change in the Si IV BAL and showed a very blue continuum component which declined over subsequent observations and was not absorbed by the BAL region. A fitted line to this data (see Figure 12 in Gibson et al. (2010)) gave a gradient of 1.44±0.45 and intercept -0.05±0.019 for the Si IV vs. C IV pseudo EW. Equivalent values from the data in this chapter gave a gradient of 1.88 and intercept of -0.11, well within the margin of error for both quantities.

3.3.3 Quasars containing both variable and non-variable BALs

Of the 35 quasars containing at least one variable BAL, 15 also contained at least one non-variable BAL. Included in these were 8 containing a varying Si IV BAL and a non-varying C IV BAL, 5 containing a varying C IV BAL and a non-varying Si IV BAL and 5 containing a varying C IV BAL while a second C IV BAL did not vary. These instances are recorded in Table 3.9.

Object Name	Varying Si IV+non-varying C IV	Varying C IV+non-varying Si IV	Varying C IV+non-varying CIV
SDSSJ001025.90+005447.6	no	yes	yes
SDSSJ004613.54+010425.7	no	no	yes
SDSSJ025720.43-080322.5	yes	no	no
SDSSJ031033.45-060957.8	yes	no	no
SDSSJ033223.51-065450.5	yes	no	no
SDSSJ081925.00+032455.7	yes	no	no
SDSSJ083718.63+482806.1	yes	no	no
SDSSJ100312.63+402505.6	yes	no	no
SDSSJ101056.68+355833.3	no	yes	no
SDSSJ104059.79+055524.4	yes	no	no
SDSSJ110339.90+011928.5	yes	no	no
SDSSJ134458.82+483457.5	no	yes	yes
SDSSJ142244.45+382330.6	no	yes	yes
SDSSJ162657.47+405848.0	no	yes	no
SDSSJ210436.62-070738.3	no	no	yes

Table 3.9: Quasars containing both variable and non-variable BALs.

The 13 quasars showing variability in one ion and no variability in the other are particularly interesting as it was possible to investigate the extent, if any, of the velocity overlap. The spectral extent in velocity space of the BALs is illustrated in Figure 3.8.

There was no velocity overlap at all between the two BALs in J142244.45+382330.6 (bottom right panel), while J134458.82+483457.5 (top left panel) and J025720.43-080322.5 (middle left panel) only

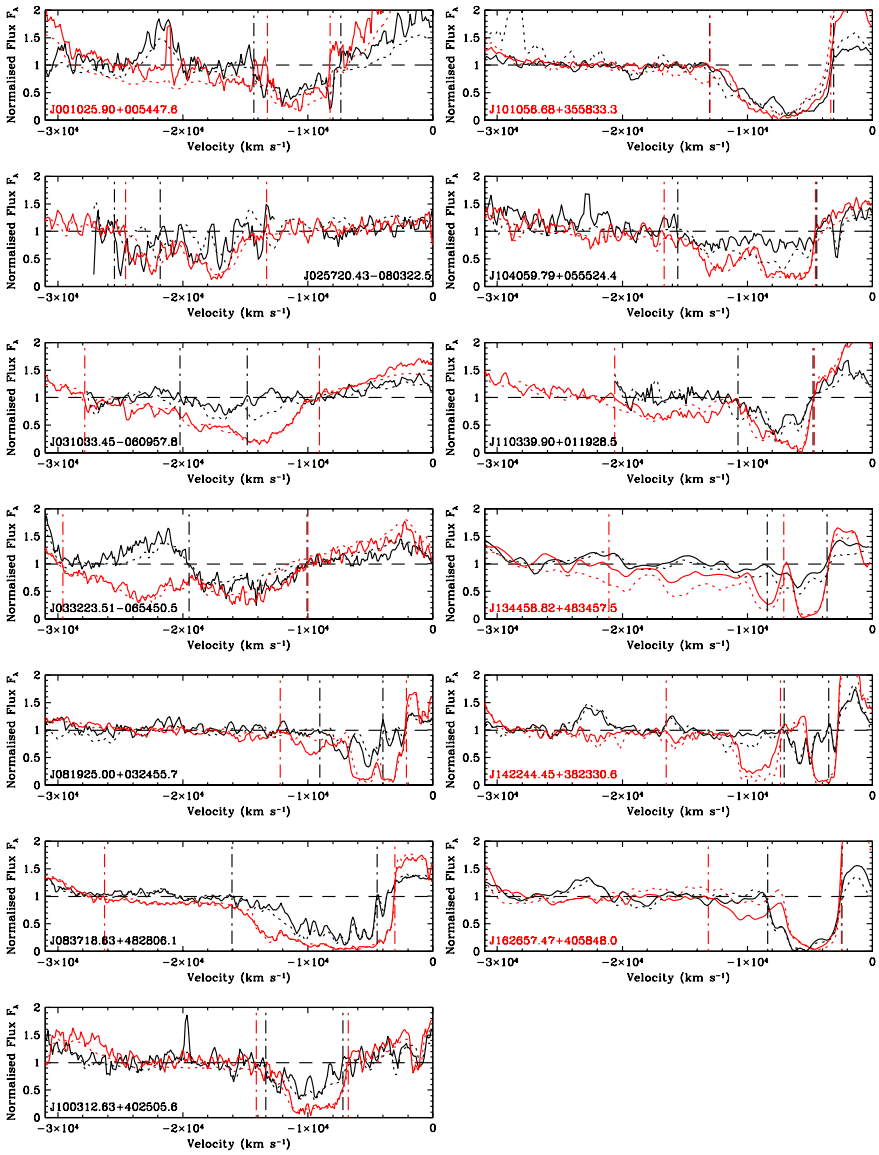

Figure 3.8: Behaviour of Si IV (black) and C IV (red) BAL regions plotted in overlapping velocity space for each of the one ion variable, one ion non-variable quasar sample (from Table 3.9). Spectra were smoothed using a 3-pixel boxcar smoothing procedure for clarity. Solid lines represent the SDSS spectra while dotted lines represent the Gemini/WHT spectra. Vertical dash-dot lines represent the BAL boundaries. The object name is printed in black if the variable BAL is of Si IV and red if the variable BAL is of C IV. A gap occurs between -12 500 km s^{-1} and -9200 km s^{-1} in the SDSS spectrum of Si IV in J025720.43-080322.5 due to an unknown instrumental issue.

showed minimal overlap. The BALs in quasar J162657.47+405848.0 overlapped but the region where the C IV BAL varied was largely non-overlapped. Of the 9 remaining quasars which showed substantial velocity overlap in variable regions, 2 showed C IV variation without Si IV variation while the remaining 7 showed the reverse situation. A lack of velocity space overlap in these objects suggested that their BALs did not form in the same region, see Section 3.4.2 for a further discussion.

3.3.4 Quasars containing a variable C IV BAL and no Si IV BALs

In the BALQSO sample studied in this chapter, all objects which contained Si IV BALs also contained at least one C IV BAL. However several contained at least one C IV BAL without showing the presence of Si IV BALs. Of these quasars, 8 exhibited one variable C IV BAL. The spectra of these 8 objects in the C IV BAL region is indicated in Figure 3.9. The quasar SDSS J210436.62-070738.3 was the only one of the 8 quasars to contain two C IV BALs, one of which met the variability criteria and one which did not.

3.3.5 BAL appearance and disappearance

There is now a substantial body of evidence showing spectral regions containing BALs transforming into regions where absorption features no longer meet the BAL definition. This can occur for both HiBALs and LoBALs (Hamann et al., 2008; Vivek et al., 2012) and are referred to as cases of disappearing BALs. Disappearing BALs can transform into either spectral regions of no absorption or weaker absorption features. Such weaker features include mini-BALs (Rodriguez Hidalgo et al., 2012; Capellupo et al., 2012) and NALs. Other BALs have been observed to emerge from apparently absorption free regions or from the types of aforementioned weaker absorption features and are referred to as appearing BALs. For this study, such events are confirmed only if the following two criteria are met, that disappearance or appearance takes place based on the BAL definition outlined in chapter 1 and the significance meets the 2.5σ variability criteria. Unlike in previous sections of this chapter, we allow identification of BALs from second epoch data alone in order to record instances of BAL appearance. Table 3.10 provides a list of disappearing and appearing BALs along with their strengths as measured by the pseudo EW at epochs 1 and 2.

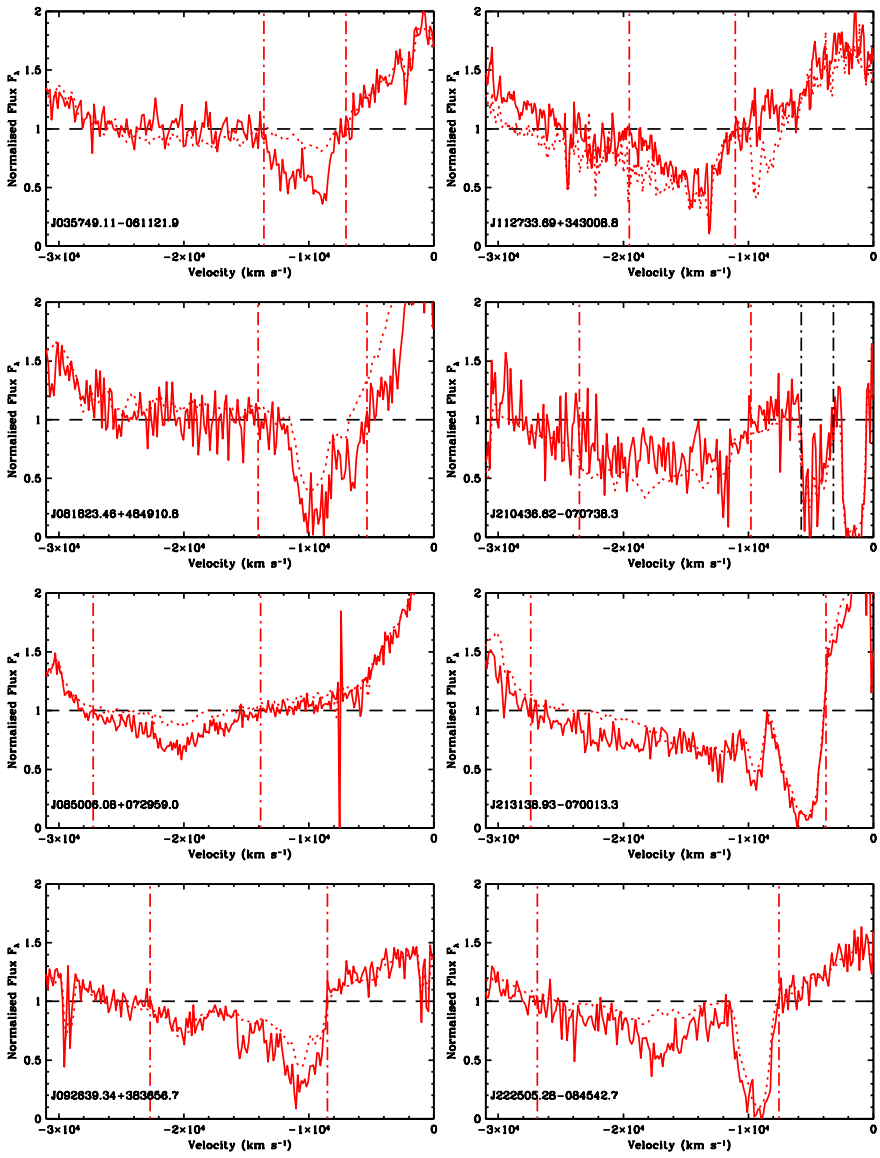

Figure 3.9: Behaviour of C IV BAL regions (red) plotted in velocity space for quasars having a variable C IV BAL and no Si IV BALs. Solid lines represent the SDSS spectra while dotted lines represent the Gemini/WHT spectra. Vertical dash-dot lines represent the BAL boundaries. The additional non-variable BAL in J210436.62-070738.3 is indicated by black boundaries lines.

Object	Ion	EW_{p1} (km s^{-1})	EW_{p2} (km s^{-1})	ΔEW_p (km s^{-1})	T$_{no.}$ (Si IV/C IV)
SDSSJ100021.72+035116.5	Si IV	589±159	1509±99	920±187	2/2
SDSSJ100021.72+035116.5	Si IV	99±209	1229±123	1130±243	2/2
SDSSJ112733.69+343008.8	Si IV	1004±717	1549±295	545±775	1/2
SDSSJ112733.69+343008.8	C IV	0±177	787±52	787±184	1/2
SDSSJ085006.08+072959.0	C IV	1313±188	0±113	-1313±219	0/1
SDSSJ211718.17+010248.9	Si IV	1931±512	292±121	-1639±526	1/1
SDSSJ212412.60+095923.3	Si IV	1054±966	227±450	-827±1065	1/1

Table 3.10: Appearing (upper panel) and disappearing (lower panel) BALs. Total number of BALs in each quasar for each ion is given by T$_{no.}$. Pseudo equivalent widths are calculated over the velocity ranges which the single epoch BALs occupy.

There was a noteworthy appearance of a C IV BAL in the spectrum of J112733.69+343008.8 from a spectral region that was formerly almost entirely above continuum level (see Figure 3.10). This appearance was significant as it was accompanied by the emergence of a Si IV BAL where previously there had been a few non-contiguous NALs. This was more of a merging than a strengthening as the change in pseudo EW was formally consistent with zero given the calculated uncertainties. Although the width of the Si IV BAL was 16 100 km s^{-1}, much wider than the 2600 km s^{-1} C IV BAL, the deepest feature of the Si IV BAL largely occupied the same velocity range, while most of the Si IV BAL outside this range was so shallow as to be consistent with zero absorption. It is therefore likely that these two BALs represented absorption from the same outflow. In addition, this object hosted a second faster C IV BAL with a minimum velocity ≈1200 km s^{-1} greater than that of the maximum velocity of the appearing C IV BAL. Although this velocity separation suggested that it did not form in the same region as the emerging C IV BAL, it also underwent a strengthening of ΔEW_p=480±437 km s^{-1}.

In the case of J100021.72+035116.5 two Si IV BALs of similar strength appeared to emerge in an almost contiguous absorption region save for a small break of ≈200 km s^{-1} which protrudes above the continuum and separates them (see Figure 3.11). The lower velocity BAL of the two contained a mini-BAL at epoch 1 which strengthened significantly to become a BAL of width 3300 km s^{-1}. The higher velocity BAL emerged from a spectral region having pseudo EW consistent with zero (99±209 km s^{-1}). At the second epoch the same spectral region contained a BAL of width 4000 km s^{-1}.

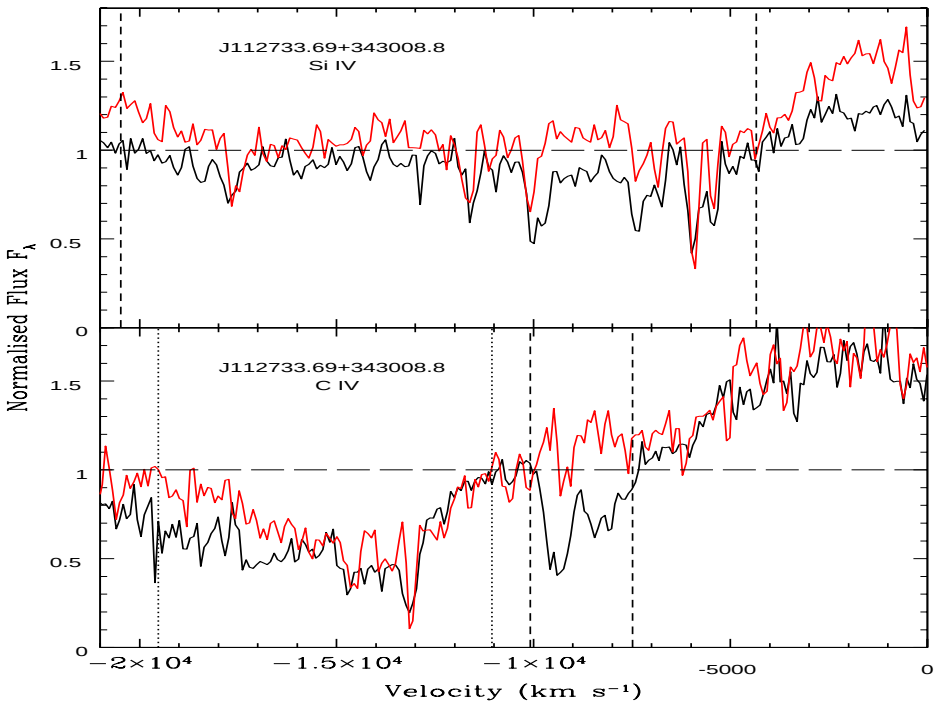

Figure 3.10: Appearance of a Si IV BAL (top panel) and a C IV BAL (bottom panel) in the quasar SDSS J112733.69+343008.8 with SDSS observation in red and Gemini/GMOS observation in black. Vertical dashed lines indicate boundaries of appearing BALs. Vertical dotted lines indicate the position of the second C IV BAL which undergoes strengthening.

The lower velocity Si IV BAL coexisted with a C IV BAL at a mostly overlapping velocity range. Interestingly this C IV BAL did not show significant variability. There was also a second C IV BAL at higher velocity with width 9800 km s^{-1} which overlapped most of the velocity range ($\approx$3000 km s^{-1}) of the higher velocity Si IV BAL. This C IV BAL also does not show significant variability. However only shallow parts of this BAL were in the overlapping region.

As the disappearing BALs all met the variability criteria and were present in the first epoch, they are also listed in Table 3.5 and Table 3.6. Figure 3.12 illustrates the spectra of these features across the two epochs for all instances of BAL disappearance.

In Filiz Ak et al. (2012), 21 examples of C IV BAL disappearance were reported from a sample of 582 BALQSOs on similar rest frame timescales to the investigation in this chapter (1.1 to 3.9 years). One case of such behaviour was observed in a C IV BAL from the sample described in this chapter, namely

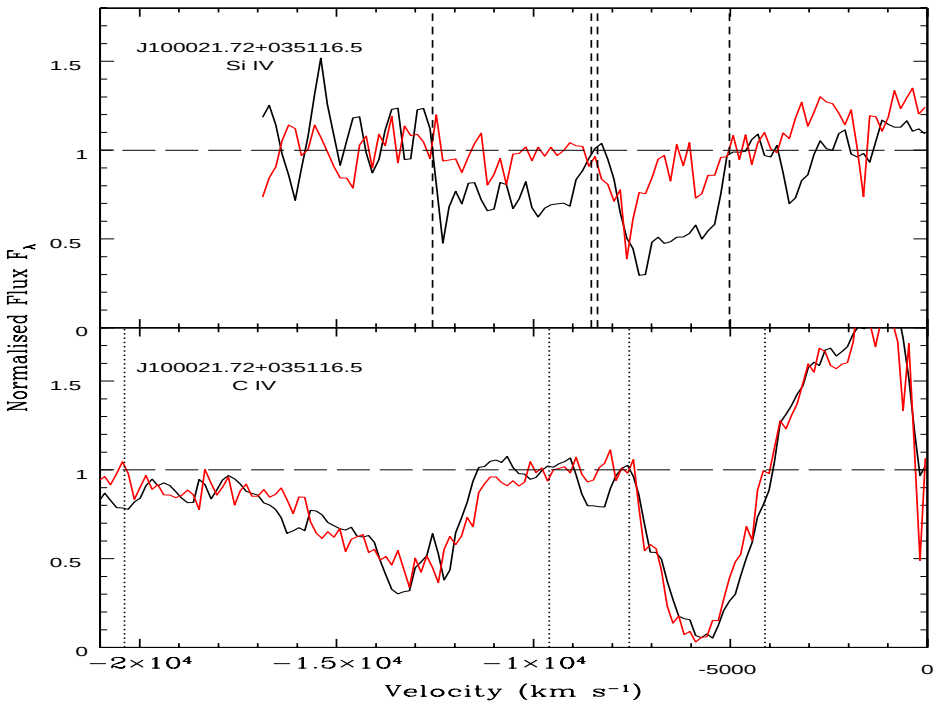

Figure 3.11: Appearance of a Si IV BAL (top panel) and a C IV BAL (bottom panel) in the quasar SDSS J100021.72+035116.5 with SDSS observation in red and Gemini/GMOS observation in black. Vertical dashed lines indicate boundaries of appearing BALs. Vertical dotted lines indicate the position of the C IV BALs which do not meet the variability criteria.

that of the disappearance from J085006.08+072959.0, where the BAL appeared to have transformed into a narrower and significantly weaker feature (≈4000 km s^{-1} width without being sub-90 percent of continuum over a contiguous 2000 km s^{-1}) which met the criteria for a mini-BAL. This changed the quasar's categorisation from BALQSO to non-BALQSO as there were no other BALs present of either ion in the second epoch. Over the entire velocity range formerly occupied by the BAL, the pseudo EW had declined to a level consistent with zero. The solitary C IV BAL disappearance in one quasar out of the whole 50-object sample containing 59 C IV BALs gives an overall C IV BAL disappearance rate of 1.7 percent. It also provides a fraction of quasars hosting C IV BALs undergoing an episode of disappearance of 2 percent. This is consistent with the statistics reported in Filiz Ak et al. (2012) of ≈2.3 percent of C IV BALs disappearing and ≈3.3 percent of BALQSOs hosting one of these disappearances over similar rest-frame timescales.

Disappearance of a Si IV BAL occurred in J211718.17+010248.9, with the remaining absorption

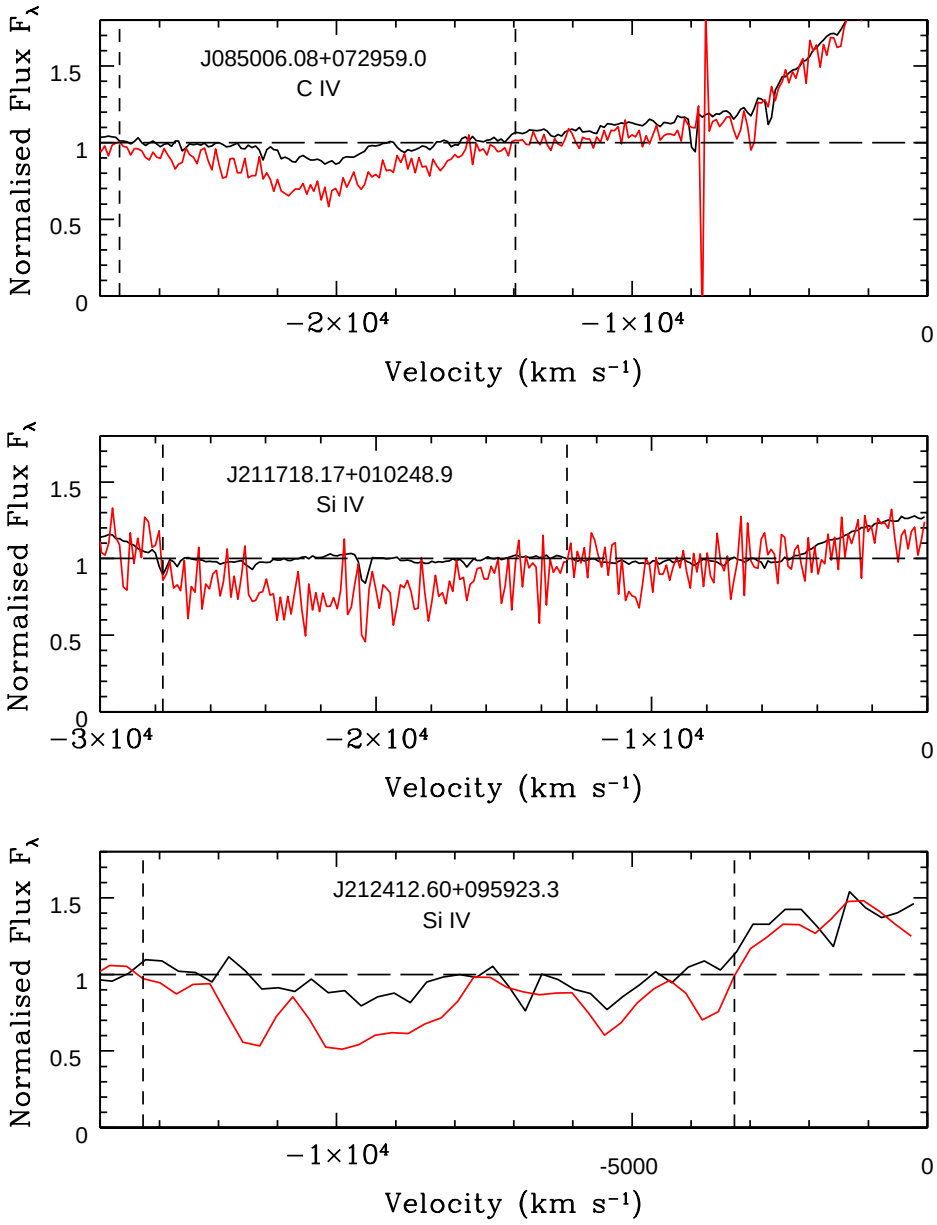

Figure 3.12: Disappearing BAL continuum normalised spectra in velocity space zeroed at emission line red doublet component. Epoch 1 spectra are in red, epoch 2 in black.

in the wavelength range spanned by the BAL reduced to a few narrow and weak absorption features. This was accompanied by the strong reduction in strength of the C IV line in this object by ΔEW_p=$-$2684$\pm$382 km s^{-1}, with which it overlapped almost entirely in velocity range (this can be seen by comparing the spectra of J211718.17+010248.9 in Figure 3.12 to Figure 3.6. There was also a significant case of disappearance of a weak Si IV BAL in J212412.60+095923.3, which reduced the total absorption in the region to a pseudo EW within 1σ of zero. The weakness of this feature was highlighted by the fact that, as in the case of the appearing Si IV BAL in J112733.69+343008.8, the error on the change in pseudo EW makes it consistent with zero. Again this was accompanied by a strong reduction in the strength of the C IV feature of ΔEW_p=$-$2427$\pm$673 km s^{-1} over a very similar velocity range (again compare Figure 3.12 with Figure 3.6). The fraction of Si IV BALs that disappeared is 2 out of 38, giving a disappearance rate of 5.26 percent. This is also the disappearance rate per Si IV hosting quasar since no object hosts more than one Si IV BAL.

3.3.6 Evidence of a covered continuum and uncovered BLR

It was reported in Arav et al. (1999) that a section $\approx$1700 km s^{-1} wide in the profile of the C IV BAL in FIRST J160354.2+300209 showed evidence of being due to an outflow which almost entirely absorbed the continuum while leaving the overlapping C IV broad emission line unabsorbed. This was thought to be due to an optically thick absorber which completely covers the continuum emitting region while leaving the much larger broad line region unobscured. This same effect was looked for in the BALQSO sample investigated in this chapter by seeking out those C IV troughs where the base overlaps with the emission line velocity range and shows a gradient consistent with the emission line profile. To create a model profile of the uncovered emission, an appropriate fraction of the continuum (up to 100 percent) was selected to be subtracted from the original reconstructed emission. The continuum fraction to be subtracted was determined by finding the value which minimised chi-square between the observed spectrum and this model over a velocity range where the trough profile appeared to be similar to the reconstructed emission profile. A good match was found in 5 C IV BALs, one in each of 5 quasars. Details for these C IV BALs are provided in Table 3.11, while their spectra are illustrated in Figure 3.13. None of these objects showed evidence for the same effect in Si IV BALs.

When considering the variation between the two epochs, no strong evidence was found for a change in the covering fraction over these velocity ranges. It was also notable that 4 of the 5 C IV BALs were not

Object	V_{max} (km s^{-1})	V_{min} (km s^{-1})	epoch 1 covering fraction ($\pm$10%)	epoch 2 covering fraction ($\pm$10%)
SDSSJ035335.67-061802.5	-12 600	-11 800	0.71	0.86
SDSSJ073535.44+374450.4	-12 900	-8100	0.78	0.82
SDSSJ100312.63+402505.6	-10 500	-8000	0.84	0.88
SDSSJ114722.09+373720.7	-14 300	-8400	0.64	0.71
SDSSJ143632.25+501403.6	-12 000	-8700	0.79	0.88

Table 3.11: C IV BALs showing evidence of both an absorbed continuum and unabsorbed broad line region.

variable. Only the BAL in SDSS J073535.44+374450.4 met the variability criteria, however within the velocity range over which the BAL profile followed the emission line profile, this feature also showed no variability.

3.3.7 Other notable objects

SDSS J113831.42+351725.3

This object contained one C IV and one Si IV BAL which showed the largest absolute change in pseudo equivalent width out of any BAL of their respective ions in the entire variable BAL sample. The C IV BAL underwent a change of ΔEW$_p$=-4142$\pm$817 km s^{-1}, larger than the corresponding absolute change in Si IV of ΔEW$_p$=$-$2880$\pm$647 km s^{-1}. However the situation was reversed when the fractional change in pseudo EW was considered, where for the Si IV BAL it was $\Delta EW_p/\langle EW_p\rangle$=$-0.979\pm$0.245, while for the C IV BAL it was $\Delta EW_p/\langle EW_p\rangle$=$-0.606\pm$0.125. Apart from variability, the properties of this quasar were not found to be exceptional. An in-depth investigation of this quasar's BAL behaviour is described in Chapter 4 of this thesis.

SDSS J164152.30+305851.7

As discussed earlier in Section 3.3.1 (see Figure 3.4), this is the only quasar in the sample which showed evidence of LoBAL absorption, with both Mg II and Al III BALs being visible in both the WHT and Gemini Spectra. It is likely that a C II BAL overlapped the Si IV broad absorption in this quasar as otherwise the Si IV BAL would have had extreme properties, with a pseudo EW of $\langle$EW$_p\rangle$=26 389$\pm$742 km s^{-1}, a width of 28 661$\pm$512 km s^{-1} and a depth of $\langle B_{depth}\rangle$=0.909$\pm$0.029.

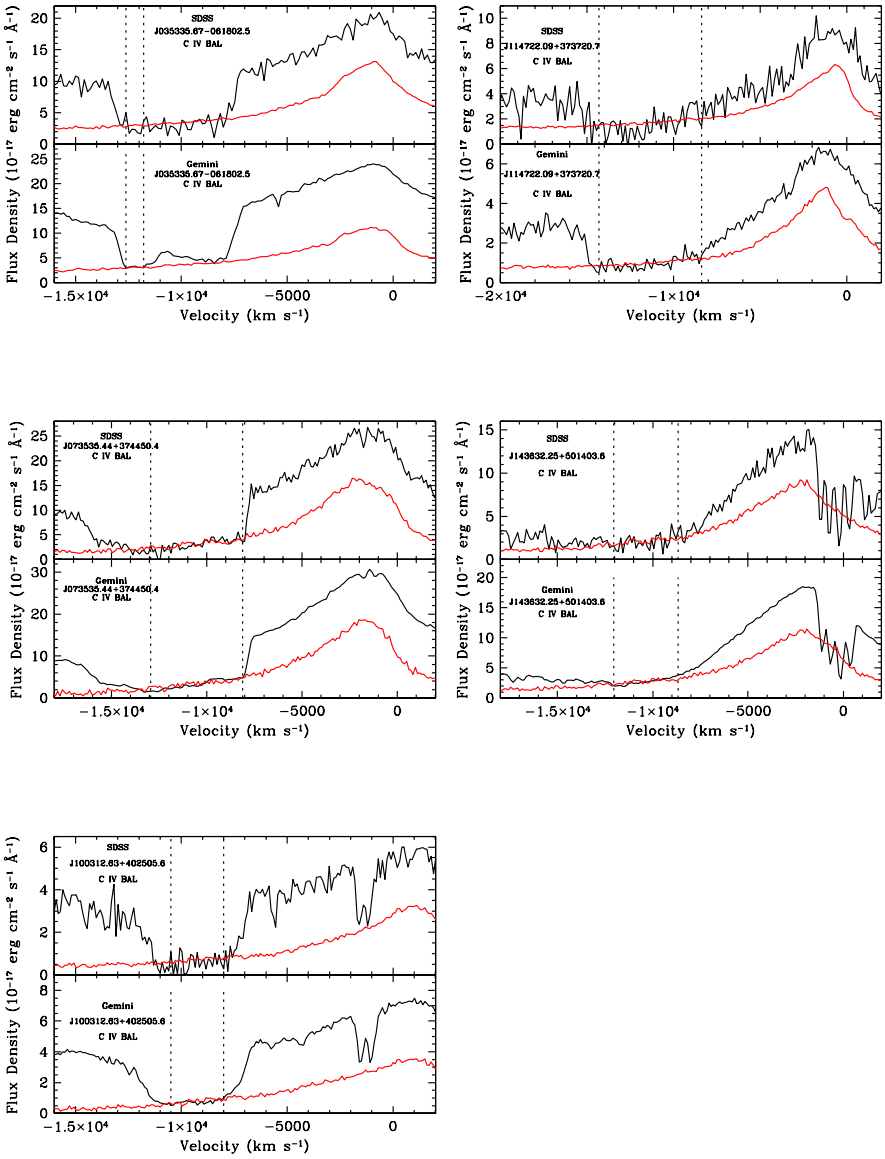

Figure 3.13: SDSS observations (upper panels) and Gemini/GMOS observations (lower panels) for 5 C IV BALs showing evidence for a gas geometry where the broad emission line is unobscured while most of the continuum region is covered by an optically thick absorber. Reconstruction minus covered continuum is in red, while observed spectrum is in black. The velocity range over which the continuum-subtracted reconstruction was determined by fitting to the trough profile is bracketed by vertical dotted lines.

These quantities would have been by far the largest for any Si IV BAL in the variable sample (the second strongest Si IV BAL sample had $\langle \mathrm{EW}_p \rangle$=7255±214 km s^{-1}) and would also have been stronger than any C IV BAL in the variable sample, including the C IV BAL in the same object. This would have been unusual as Si IV BALs were weaker than C IV BALs in every other object containing variable BALs of both kinds. Aside from the presence of LoBAL absorption, this quasar was also interesting as it exhibited a C IV BAL with the highest pseudo EW of any C IV BAL in the variable sample ($\langle \mathrm{EW}_p \rangle$=13 526±593 km s^{-1}).

3.4 Conclusions

3.4.1 Epoch separation time and velocity dependence

By performing a comparative study using data sets from Barlow (1993), Lundgren et al. (2007) and their own sample, Gibson et al. (2008) found an increase in C IV absorption variability with increased epoch separation time. The results of this chapter suggest a mean value of $|\Delta EW_p/\langle EW_p \rangle|$=0.43±0.03 for all C IV BALs identified as variable. This compares with a mean value of $|\Delta EW_p/\langle EW_p \rangle|$=0.55±0.03 for the sample of 16 BALs which showed significant variability in Lundgren et al. (2007). However the mean in the Lundgren et al. (2007) sample is skewed by three outlying features, the lowest of which had an EW more than double that of the next most variable BAL. If these BALs are excluded, a mean value of $|\Delta EW_p/\langle EW_p \rangle|$=0.31±0.03 is recovered, lower than the value for the sample in this chapter and consistent with a positive correlation between BAL variability amplitude and epoch separation time when considering timescales ranging from months to several years. However, the range of timescales studied within the quasar sample in this chapter are not sufficient to provide evidence of variability dependence on the epoch separation time studied.

No evidence was found of the proposed spike in variability in the velocity range $-12\,000$ km s^{-1} to $-15\,000$ km s^{-1} as proposed in Lundgren et al. (2007). In fact, no trends were found relating the velocity width or BAL centroid velocity with variability. If variability was mainly driven by differences in covering fraction, then the absence of any correlation between BAL centroid velocity and variability amplitude could indicate that the outflow velocity along the line of sight was not well correlated with velocity across the line of sight. This would be the case if the crossing velocity of the absorbing gas

was not predominantly due to the influence of the outflow acceleration mechanism. For example, it could instead be due to orbital motion.

3.4.2 What gives rise to BAL variability?

Fractional pseudo equivalent width variability was strongly inversely correlated with the mean BAL depth averaged over the two epochs. This is what would be expected if ionising continuum changes altering the fractions of the ions making up the outflowing gas were responsible for variability in the strength of the BALs, as deeper troughs may indicate an optically deeper outflow. However this is questionable for two reasons: (1) the depth measure and the epoch averaged EW showed a strong positive correlation, suggesting that this relationship was an artifact of the denominator in the fractional change, and (2) the study found no strongly significant correlation between rest frame absolute i-band magnitude (M_i) and BAL variability. There was a moderately significant probability of an inverse correlation between absolute change in pseudo EW and absolute i-Band magnitude in the variable C IV BAL sample. However, under the assumption of lower luminosity sources driving stronger variability in the case where ionisation changes are responsible, it would be expected that a corresponding signal would be detected indicating absolute change in pseudo EW was inversely correlated with $\langle \mathrm{B}_{depth} \rangle$ for C IV BALs, which was not found. In fact, Si IV BALs showed a moderate probability of the same correlation, leading to the conclusion that there was no real correlation in these cases and that there was no strong evidence for ionisation changes driving the BAL variability.

An alternative explanation is that the observed variability was driven by covering fraction changes. One such possibility is an inhomogeneous absorber model in which the column density along the line of sight is due to clumpy absorbers which can move laterally into and out of the line of sight at any radial distance from the continuum source. The clumpy inhomogeneous model has received support from Capellupo et al. (2012) who found the strongest variability within small velocity regions of BAL troughs, which may correspond to movements of individual clouds with narrow velocity ranges. An alternative to the inhomogeneous absorber model is a so-called pure partial coverage scenario in which the gas is relatively homogeneous along the radial axis but moves laterally with respect to the line between the Earth and the quasar emission region.

Given the lack of correlation between i-band luminosity and variability as discussed previously, it can

be assumed that some variant of covering fraction changes are driving the variability. The Si IV BALs were observed to vary more often than the C IV BALs and within those quasars that showed both types of BAL varying, the Si IV BALs underwent the greatest fractional variability. This evidence would therefore seem to favour the clumpy absorber model over the homogeneous absorber scenario as it could be due to an outflow in which the greater column density of C IV ions over Si IV means that C IV is more likely to be saturated. In such an outflow, a cloud moving into the line of sight may not affect the absorption line profile since a particular cloud would be entering into a portion of the outflowing column which is already opaque at the narrow range of wavelengths that the cloud could absorb. This could result in a scenario where a column of clumpy absorbers only partially covers the emission from the quasar, but due to the spatial extent along the line of sight of the entire outflow, a cloud moving into the line of sight does not affect the absorption profile. Higher frequency of saturation of C IV as compared to Si IV (due to the greater abundance of carbon compared to silicon, or possibly ionisation effects favouring C IV over Si IV) was also supported by the fact that of the five quasars showing BALs with an uncovered BLR and covered continuum, the uncovered BLR emission spectra did not fit the Si IV BAL profiles. In such a saturated C IV BAL case, moving clouds into and out of the line of sight would not significantly change the depth of C IV troughs when compared with Si IV variability.

The fact that the 14 quasars which showed variability in both ions had BALs with largely overlapping outflow velocities, in which the direction of change with respect to time was the same, was strong evidence for the two types of BAL being part of the same outflow and influenced by the same variability mechanism in these cases. The sample of 9 quasars which showed one type of BAL varying while the other did not, with substantial velocity overlap between the two, seemed to contradict such a conclusion. However, the variable BAL in 7 of these cases was Si IV, while the C IV BAL did not vary. If C IV was saturated in these cases, this would allow Si IV to vary without affecting the C IV BAL variability amplitude in the overlapping velocity range, allowing consistency with the clumpy absorber model.

Despite this, ionisation changes are not entirely ruled out as a driver of BAL variability. The luminosity dependence that was used as a proxy for EUV variability is two steps removed from a direct observation of the ionising continuum flux and it is possible that the complexity of the response of the outflowing gas to ionising continuum changes may not be analogous to that of the emission lines. The hint of a positive correlation between the fractional variability of Si IV and C IV where an approximately linear relationship exists between the two quantities with a gradient not equal to 1 (see Section 3.3.3) would seem to fit more naturally with ionising continuum variability as the explanation rather than gas

line of sight changes. However this is far from certain given the value of only 98 percent correlation probability derived from a Spearman rank test and the fact that the least squares fit line only appeared to fit 8 out of the 14 quasars showing variability in both types of BAL (to 1σ). Other possible indicators of ionising continuum changes included 2 cases of C IV variability which are *unaccompanied* by Si IV variability at the same velocities. This is hard to explain in terms of gas covering fraction changes as it would have required some sort of spatial separation between Si IV and C IV outflows. Calculations of theoretical ionisation fractions across ionisation parameter space suggest this is unlikely as there is substantial overlap in the Log ion fraction vs. Log ionisation parameter curves of each ion (see Figure 4 in Hamann et al. (2001)).

Future investigations may be able to find more definitive evidence for continuum variations by accurately measuring continua in a high S/N quasar sample across several epochs with photometric quality spectra and looking for correlations with BAL variability. An underlying assumption in investigations into continuum variability correlations with BAL variability is that the outflowing gas is dense enough to undergo recombinations on relatively short timescales. Although the column densities of absorbers can be estimated using optical depth calculations (these are lower limits in the case of non-black saturation), the extent of the BAL flow is still a subject of debate, with estimates placing the flow as far as the kiloparsec scale from the central engine (Dunn et al., 2010). If this was the case, given the estimated outflow column densities of log$N_H \approx$21 to 22 cm^{-2} (Hamann et al., 2008) the gas density could be as low as $\approx$10 cm^{-3}. Given a recombination coefficient value of $\approx 10^{-11}$ cm^3 s^{-1} for C IV and Si IV and assuming the gas is almost completely ionised, recombination timescales could be as long as a few hundred years. In this case ionisation changes could not cause any of the observed absorption line variability.

In order to gain a greater insight in to the physical influences driving BAL variability, larger BALQSO sample sizes are needed. The ongoing Baryon Oscillation Spectroscopic Survey (BOSS), part of the Sloan Digital Sky Survey-III (SDSS-III) (Eisenstein et al., 2011) should prove helpful in this regard. One of the ancillary projects conducted as part of this survey will provide much greater numbers of BALQSO repeat observations on multi-year timescales than previous studies by comparing BOSS BALQSO spectra with earlier SDSS-I and II data, as for example in Filiz Ak et al. (2013).

3.4.3 BAL disappearance and BAL lifetimes

The fraction of C IV BALs in the sample which disappeared is 1.7 percent, lower than the 5.3 percent value found for Si IV BALs. However this resulted from only three examples of BAL disappearance, so definitive conclusions are not drawn, except to say that the disappearance rate for C IV was broadly consistent with that found in Filiz Ak et al. (2012). If Si IV BALs do show a greater tendency to disappear, this would fit in with the general picture of Si IV BALs exhibiting greater occurrences of variability and greater amplitudes of variability in a variable BAL sample. The disappearing BALs were weaker than average, as were the BALs which appeared. In fact the disappearing C IV BAL was the weakest of all the C IV BALs in the variable sample. This conforms with the tendency of shallower BALs to exhibit stronger fractional variability.

The average lifetime of a BAL can be estimated by dividing the fraction of BALs that disappear by the average rest-frame lifetime of the observations, as described in Chapter 1, Section 1.2.5. This gave an average BAL rest frame lifetime of ≈142 years for C IV and ≈43 years for Si IV based on the timescales and disappearing fractions from the sample studied in this chapter. The estimated C IV lifetime from the sample is similar to the value of 109^{+31}_{-22} years estimated in (Filiz Ak et al., 2012).

3.4.4 Outflow geometry insight provided by covered-continuum-uncovered-BLR subsample

Reverberation studies of the variable continuum and broad emission-line region in AGN indicate that the "size" of the BLR scales with UV ionising continuum luminosity such that $R \propto L_{UV}^{1/2}$ (Bentz et al., 2006), as predicted by photoionisation models. The luminosities of the subsample of five objects which showed evidence of C IV BALs shaped by a covered continuum+uncovered BLR were not biased towards more or less luminous objects. This indicated that the difference between this subsample and other BAL quasars is not due to a smaller BLR and is instead determined by the geometry of the outflow along the line of sight. Given that the shape of the troughs in this subsample were well modelled by a mostly absorbed continuum and an entirely unobscured BLR, the characteristic radius of any clumpy absorber clouds would have to be similar to the UV continuum emitting region size. Assuming that the central supermassive black hole is accreting at close to the Eddington rate and a peak ionising UV continuum temperature corresponding to a photon energy of ≈50 eV, the ratio of the UV luminosity

to the bolometric luminosity would be of the order $\approx 10^{-1}$ (Kelly et al., 2008). Given the bolometric luminosity span of the 5 objects (obtained from Shen et al. (2011)) the size of the UV continuum emitting region and hence the size of an obscuring cloud would be in the range $\approx 10^{13}$ to 10^{14} cm. Two possibilities therefore exist, either the characteristic size of the clouds or the radius (across the line of sight) of a homogeneous outflow column must be able to vary greatly between objects, from continuum region size up to $\approx R_{BLR}$, or the radius of the absorbing column emerging from the disc can vary between quasars by having considerably different numbers of approximately UV continuum emitting region sized clouds across the sight line. These possibilities are illustrated in Figure 3.14.

3.5 Summary

A brief summary of the main results from this chapter are provided here.

1. Si IV BALs are more likely to be variable than C IV BALs (58% vs. 46% respectively). Within the sample of variable BALs, the average fractional change in pseudo EW was higher for Si IV BALs (0.577 vs. 0.367 for C IV BALs when excluding the LoBAL quasar SDSS J164152.30+305851.7).

2. Both Si IV and C IV BALs have fractional changes in pseudo EW which are strongly correlated (greater than 99.9 percent significance) with their epoch averaged depths. A strong possibility is that this is a result of the strong positive correlation between BAL depth and pseudo EW rather than a real physical effect. No strong evidence was found of absolute change in pseudo EW dependence on epoch averaged pseudo EW, nor any correlation of absolute change in pseudo EW with BAL depth or width.

3. No correlation was found between BAL variability and the absolute i-band magnitude of their host quasars. Since ionising continuum changes drive broad emission line variability, this result suggested that variability of the ionising continuum does not play a significant role in BAL variability, assuming the outflowing gas is in ionisation equilibrium with the photoionising continuum.

4. Within each of the 14 quasars which exhibited both a varying Si IV and a varying C IV BAL, the change in pseudo EW was in the same direction (strengthening or weakening) across the two BALs. Furthermore, each of these objects showed significant overlap in velocity space of the spectral regions spanning the two, suggesting that the BALs of both ions originated in the same outflow. There is

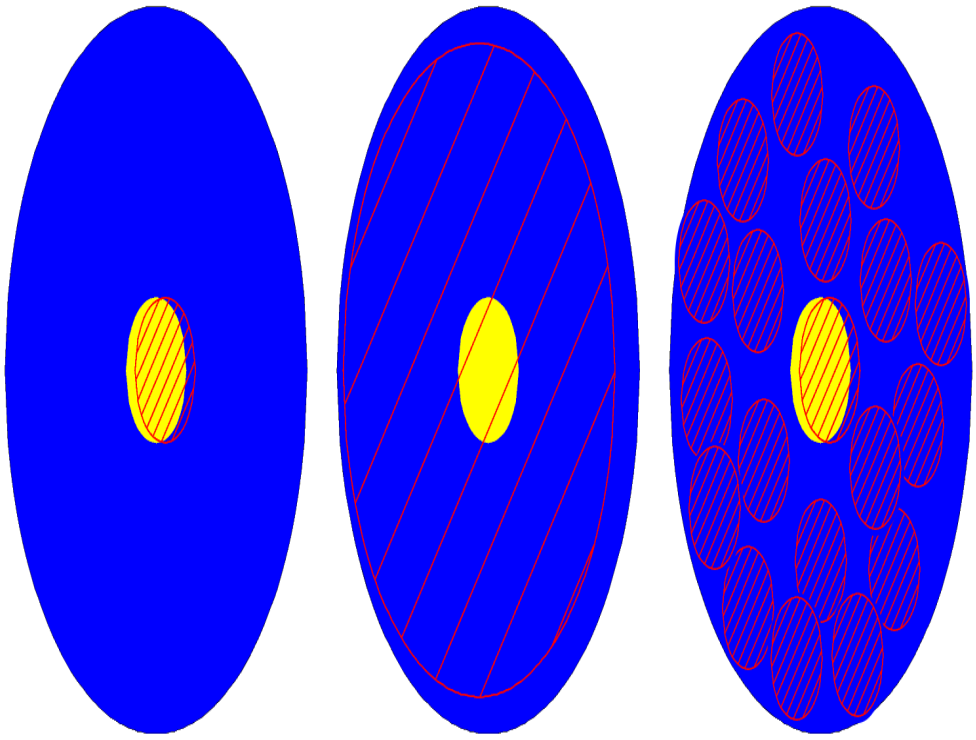

Figure 3.14: Schematic illustration of three different possibilities (left to right) for continuum-emission and/or broad emission line region coverage by an absorber along an observer's line-of-sight. The continuum emission region is in yellow, the broad line region is in blue while the absorbers are red circles with diagonal line shading. The leftmost image describes a mostly covered continuum-emission region (by either a cloud or homogeneous outflow stream) with an almost completely uncovered BLR, producing an absorber trough spectral profile similar to the continuum-subtracted BEL profile as seen in Figure 3.13. The middle image shows a homogeneous outflow stream with a radius large enough to cover almost all of the BLR as well as the continuum region, producing absorption troughs which do not follow the profile of the overlapping broad emission line. The rightmost image is similar to the middle image, covering most of both the continuum region and the BLR, except that the coverage is provided by multiple clouds of similar size to the continuum region, again producing no noticeable BEL profile in the absorber trough.

marginal evidence (98 percent significance) that the fractional change in pseudo EW of Si IV and C IV BALs are correlated.

5. Examples of both BAL appearance and disappearance were found, with instances in both Si IV (3 appearance, 2 disappearance) and C IV (1 appearance, 1 disappearance). Their relative recurrence rates suggest Si IV and C IV BAL lifetimes of 43 years and 142 years respectively. Appearing and disappearing BALs are weaker than average, complying with the general trend noted in point 2.

6. There was evidence in 5 objects of a mostly covered continuum region combined with an uncovered BLR. This was seen as a trough profile in deep C IV BALs which followed the emission line profile once a substantial fraction of the continuum has been subtracted. This suggests a range in maximum cloud radius for the clumpy inhomogeneous absorber model of $\approx 10^{13}$ to 10^{14} cm for the outflows from these quasars, assuming accretion is close to the Eddington rate.

Chapter 4

SDSS J1138+3517: A quasar showing remarkably variable BALs

This chapter takes an extensive look at the highly variable absorption lines in the most variable quasar from the sample used in Chapter 3, SDSS J113831.4+351725.2, which was originally studied in Chapter 5 of Cottis (2010). This more detailed analysis included two additional epochs of data and an improved treatment of the underlying unabsorbed emission-line profile. In particular, a novel method of reconstructing the un-absorbed (broad line+continuum) emission was performed using the NMF profiles of Allen et al. (2011) (as used in Chapter 3), which allowed accurate normalised absorber profiles to be constructed even at low line-of-sight velocities ($\leq$3000 km s^{-1}) where there is substantial overlap with the corresponding broad emission line. Furthermore, a more accurate treatment of absorbing columns was included by using an input SED for the photoionisation models in this Chapter with a more realistic big blue bump temperature of 240 000 K when compared with the value of 10^6 K used previously.

This chapter assumes a flat ΛCDM cosmology with H_0=67 km s^{-1} Mpc^{-1}, Ω_M=0.315 and Ω_Λ=0.685, as reported from the latest results of the Planck satellite (Planck Collaboration XVI, 2014).

4.1 The Unusual BAL behaviour of SDSS J1138+3517

The quasar examined in this chapter, SDSS J113831.4+351725.2 (hereafter SDSS J1138+3517), has a redshift of z=2.122 (Hewett & Wild, 2010) and was investigated as part of the multi-BALQSO variability study undertaken in the rest-frame UV by Wildy et al. (2014) and in Chapter 3 of this thesis, in which Si IV λ1400 and C IV λ1549 BALs were identified from a sample of 50 quasars and statistics were gathered on their EW changes over 2 epochs separated by quasar rest-frame timescales ranging from approximately 1 to 4 years. Of the 50 BALQSOs studied in Chapter 3, SDSS J1138+3517 showed the largest absolute change in EW in both Si IV and C IV absorption as well as a large fractional EW change ($|\Delta EW/\langle EW\rangle|$), occurring over a rest-frame time interval of $\sim$1 year. A third epoch indicated another dramatic variation in the BALs, while a fourth epoch showed relatively little change from the third except for significant variability in one C IV absorber, with these subsequent observations also having been made in successive 1-year rest-frame time intervals.

In Filiz Ak et al. (2013), the variability of 428 C IV BALs in 291 quasars was found to produce a ΔEW dependence on rest-frame time interval which was well modelled by a *random-walk* model. Random-walk behaviour is found in many physical phenomena such as Brownian motion and diffusion. In Filiz Ak et al. (2013) an attempt was made to find the best fitting parameters which allowed a one-dimensional random-walk to generate behaviour similar to that observed in the variability of the C IV BALs. The two parameters needed were the number of 'steps' taken (n) and the equivalent width change at each step (δEW). Such a model produces a binomial distribution of ΔEW values, and after calculating best-fitting parameters of n=6 and δEW=1.65 Å, the resulting distribution was found to be a good match to the C IV EW variability over epoch separation timescales spanning 2.0–2.5 years (over which a large number of the C IV BALs were sampled) and much better than the best-fitting Gaussian distribution, as indicated in figure 27 of Filiz Ak et al. (2013). Taking the mid-point of these timescales as T=2.25 years, the time interval of each step could be calculated using δt=T/n, providing a value of δt=137 days. Using the same BAL identification scheme as the Filiz Ak et al. (2013) study, the variation across the two observational epochs examined in Chapter 3 of the most variable C IV BAL region in SDSS J1138+3517 (spanning $-23\,400$ km s^{-1} to -7500 km s^{-1}) was ΔEW=-13.8 ± 2.9 Å. This value lies well outside the random-walk model prediction at the epoch separation time-interval of 360 days in the quasar rest-frame (see figure 29 of Filiz Ak et al. (2013), also shown here as Figure 4.1). Consequently, SDSS J1138+3517 may exhibit a variability mechanism which is rare in the BALQSO

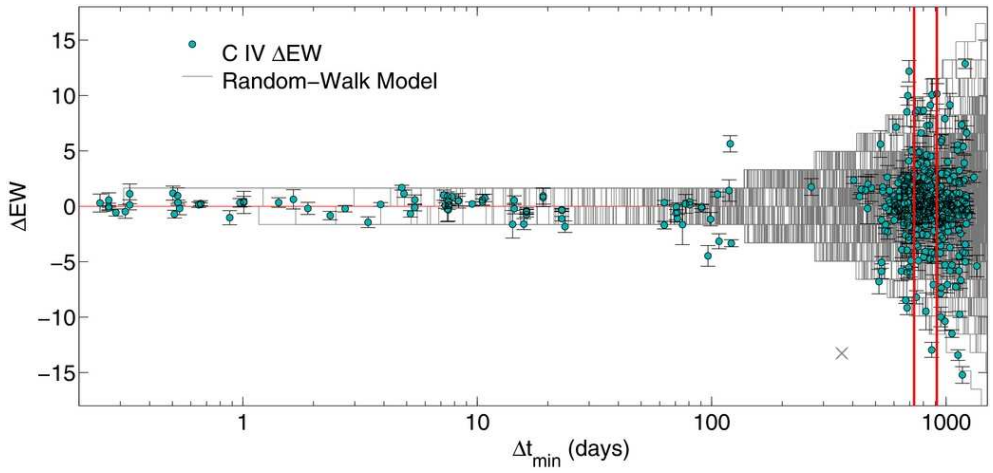

Figure 4.1: Figure adapted from "Broad absorption line variability on multi-year timescales in a large quasar sample" by Filiz Ak et al. (2013), indicating variability and time interval between observations of C IV BALs in their sample. The location of the most variable C IV BAL in SDSS J1138+3517 is marked with an X. The random-walk model is indicated in gray. The vertical red lines indicate timescales in the range 2.0–2.5 years.

population given the success with which the random-walk model predicts the variability of the BALs studied in Filiz Ak et al. (2013). The quasar SDSS J1138+3517 was not part of the Filiz Ak et al. (2013) investigation simply because the sample of objects chosen in that paper was small compared to the total number of known BALQSOs (the catalogue of Scaringi et al. (2009) found 3552) meaning any particular BALQSO was unlikely to be selected at random for the study.

In Filiz Ak et al. (2014), which uses the same BAL identification scheme as above, the variability of C IV BALs was investigated over rest-frame timescales ranging from $\sim$1 to a few years, including those in quasars additionally containing Si IV BALs of overlapping velocity. Again examining the most variable C IV BAL in SDSS J1138+3517 identified using their definition, the value of ΔEW, along with a value of $\Delta EW/\langle EW\rangle$=$-1.3\pm0.3$ would place it among the top few most variable C IV BALs in their sample of 454 (includes C IV BALs both unaccompanied by Si IV absorption and overlapping in velocity with a Si IV BAL), highlighting the extreme variability of this source. In addition, an investigation by Gibson et al. (2010) included observations of two quasars over a similar rest-frame time interval of between 0.5 and 2 years, neither of which showed variability as dramatic as in SDSS J1138+3517.

Answering the question of what drives the strong BAL variability observed in SDSS J1138+3517 is the principal objective of the investigation described in this chapter. Observations of the source are detailed in Section 4.2. In Section 4.3 details of the calculations performed to obtain the Si IV and

C IV ionic column densities are provided through the use of different assumptions regarding the line-of-sight geometry, including models where there is incomplete coverage of the emission region by a homogeneous absorber. These calculations were aided by the use of Gaussian profiles to fit the Si IV absorption components, which allowed calculations to be performed based on the changes in these components even where they were not fully un-blended. In Section 4.4 details of the computation of grids of photoionisation models are provided, allowing examination of the theoretical variation of ionic column density over a range of ionisation parameter at given hydrogen number densities and column densities. These grid models were compared to the best results for the ionic column densities from Section 4.3, allowing the testing of the hypothesis of changes in ionising flux being the driver of BAL variability. In Section 4.5 the results from Sections 4.3 and 4.4 and their implications for the variability mechanism are discussed. An attempt at constraining the mass outflow rate and hence kinetic luminosity is also described.

4.2 Observations

Initial observations were undertaken using spectra from the SDSS, with three follow-up observations taken using the WHT ISIS spectrograph. These are detailed in Table 4.1

Table 4.1: Details of observations obtained of SDSS J1138+3517.

Epoch	Observation Date	Δt_{qrest} (days)	Type	Exp. time (s)	Grating	Pixel Resolution (5000 Å) (km s^{-1})	Mean Airmass
1	03 May 2005	0	SDSS	6×2400	Red & Blue	150	1.01
2	27 May 2008	359	WHT	3×1200	R158B & R158R	108	1.14
3	29 May 2011	710	WHT	2×1800	R300B & R316R	56	1.80
4	09 May 2014	1053	WHT	2×1800	R300B & R316R	56	1.06

Δt_{qrest} is quasar rest-frame time interval since epoch 1

4.3 Spectral Analysis

4.3.1 Spectral Properties

The observed spectra at each epoch correspond to rest-frame UV wavelengths which include the region containing Si IV and C IV emission and the corresponding blueshifted absorption lines resulting from those same atomic transitions in outflowing gas. Since the spectral resolution differs between spectra, in order to accurately identify changes in absorption between each epoch the SDSS and WHT epoch 3 and epoch 4 spectra were convolved with Gaussians of appropriate full-width half maxima to approximate the resolution of the WHT epoch 2 observation (using skyline widths as a guideline), followed by resampling of all 4 spectra onto a wavelength grid of 3.7 Å. This closely matches the bin width of the epoch 2 observation. Small differences in wavelength calibration were removed by aligning narrow emission and absorption features in the WHT spectra with the same lines in the SDSS spectrum. The work in this chapter used the same SDSS observation of SDSS J1138+3517 as was used in Chapter 3, with the resolution matching and wavelength shift for that observation as used in this chapter identical to that described in that chapter.

By using the reconstruction of the unabsorbed SDSS spectrum from Chapter 3 originally developed in Allen et al. (2011), appropriate reconstructions were also generated for the three WHT observations. This was achieved as follows: (i) A power-law continuum was fitted to each spectrum using line-free continuum bands as outlined in Chapter 3, (ii) The SDSS continuum was subtracted from the SDSS reconstruction, (iii) The WHT spectra had their respective continua subtracted, (iv) In the continuum subtracted SDSS reconstruction, the Si IV λ1400, C IV λ1549, O I λ1304 and C II λ1334 emission line boundaries were identified, (v) The emission lines from part (iv) were scaled to match the red (unabsorbed) side of the emission lines in each of the WHT observations, and (vi) The continuum was added to the scaled emission lines for each of the WHT observations, creating appropriate reconstructions for epochs 2,3 and 4.

For the SDSS reconstruction used in the subsequent analysis, the procedure was carried out to scale the Si IV emission line, as the original reconstruction underestimated the Si IV emission (the reconstructions were optimised for C IV as described in Allen et al. (2011)). The region used for calculating the appropriate C IV line scaling was restricted to the interval between line centre and an observed wave-

length of 4866 Å to avoid the He II+OIII absorption and emission complex immediately longward of C IV. The Si IV emission line was shifted by two wavelength bins blueward in the epoch 2 reconstruction relative to the SDSS reconstruction to match the shifted peak of the emission line in the epoch 2 spectrum. Based on the synthetic BAL based error estimation method described in Section 3.2.3, the fractional error on the reconstruction for a quasar of this r-band S/N and redshift was estimated to be 5 percent of the flux value at each resolution element for all calculations described in this chapter. The observed spectra for all 4 epochs (solid black lines), as well as their final reconstructions (solid red lines), are illustrated in Figure 4.2. Since the reconstructed broad emission lines of the WHT observations are simply scaled versions of the same lines in the SDSS reconstructions, the method assumes that the shape of these lines does not change between observational epochs. This appears to be a safe approach since the red (unabsorbed) side of the reconstructed WHT broad emission lines closely follows the observed profiles.

The dramatic variability of both ions' absorbers across the first three epochs was clear when the spectra were normalised to the reconstructions. The transitions of interest are both doublets, with rest-frame laboratory wavelengths of 1393.76 and 1402.77 Å contributing to Si IV λ1400 and correspondingly 1548.20 and 1550.77 Å for C IV λ1549. Relative to the laboratory rest-frame wavelength of the red component of each doublet, absorption was significant between 0 and $\sim$−13 000 km s^{-1} for Si IV and between 0 and $\sim$−20 000 km s^{-1} for C IV, where a negative value indicates outflowing material (blueshifted). As can be seen in Figure 4.3, the C IV troughs were deeper than the Si IV troughs at similar velocities. The deepest troughs showed the least variability and were located at the lowest (least negative) velocities, as has been reported in previous BAL studies (Lundgren et al., 2007; Capellupo et al., 2011).

Due to its relative lack of variation from the previous observation, especially in the Si IV absorption lines where identifiable doublets were present, epoch 4 was left out of the analysis in subsequent parts of Section 4.3 and Section 4.4. Epoch 4 is instead discussed further in Section 4.5.3.

4.3.2 Lower Limits for Outflow Column Densities using Direct Integration

Minimum values for both the Si IV and C IV column densities were estimated by assuming that the absorbers were unsaturated and completely covered the emitting line+continuum region along the line-

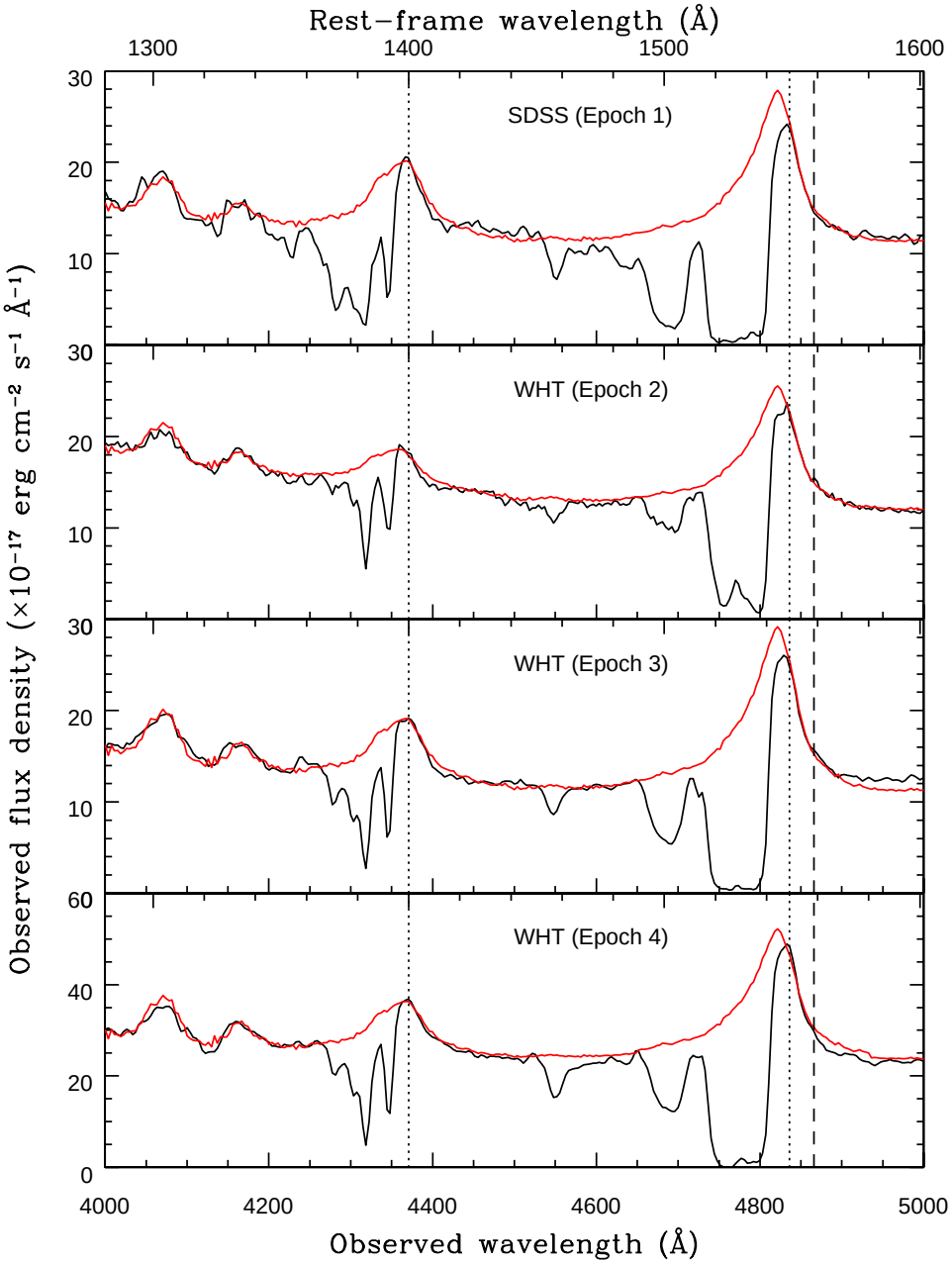

Figure 4.2: Spectra for epochs 1 to 4 of SDSS J1138+3517, with top panel to bottom panel in order of observation date starting with the earliest. The observed spectrum is in black while the reconstruction of the unabsorbed spectrum is in red. Vertical dotted lines indicate the laboratory wavelengths of the Si IV and C IV emission lines. The vertical dashed line indicates the maximum wavelength used in calculating the C IV emission scaling, emission longward of this point is not accurately reconstructed.

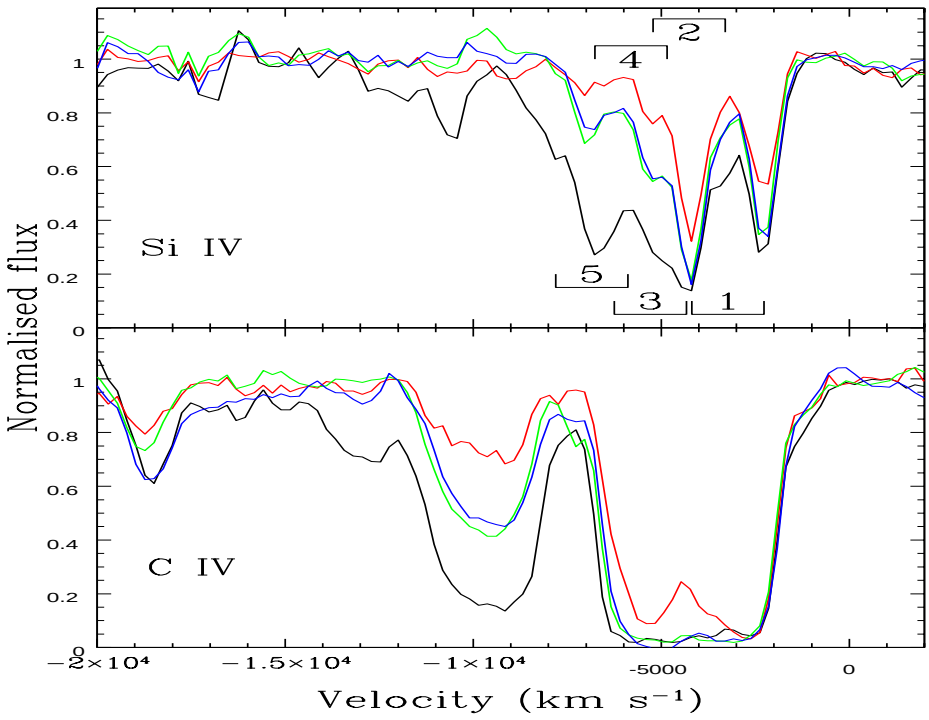

Figure 4.3: Si IV (upper panel) and C IV (lower panel) absorption regions in red component velocity space. Epoch 1 (SDSS) spectra are in black, epoch 2 (1st WHT) spectra are in red, epoch 3 (2nd WHT) spectra are in green and epoch 4 (3rd WHT) spectra are in blue. Spectra are normalised to the un-absorbed reconstruction. The Si IV Gaussian components (described in Section 4.3.3) are numerically labelled in order of increasing outflow velocity.

of-sight to Earth, with a constant optical depth across the tangential plane (Savage & Sembach, 1991). The C IV and Si IV transitions have a doublet structure with known oscillator strengths. The total column density of the ion contributing to a given doublet component was therefore calculated according to

$$N_{ion} = \frac{m_e c}{\pi e^2 f \lambda} \int \tau\left(v\right) dv\,, \tag{4.1}$$

where N_{ion} is the ionic column density, v is the velocity relative to the laboratory rest-frame wavelength, m_e is the electron mass, c is the speed of light, e is the elementary charge, f is the oscillator strength, λ is the laboratory rest-frame wavelength and $\tau(v)$ is the optical depth at a given velocity. At a redshift of $z = 2.122$, the doublet separation at zero velocity is approximately 28.1 Å for Si IV and 8.0 Å for C IV. As the C IV separation is only slightly greater than two wavelength bins, it was prac-

Table 4.2: C IV and Si IV velocity limits and ionic column densities for each epoch using direct integration of the absorption profile.

Transition	Velocity Limit† (km s^{-1})	epoch 1 Ionic Column Density ($\times 10^{14}$cm^{-2})	epoch 2 Ionic Column Density ($\times 10^{14}$cm^{-2})	epoch 3 Ionic Column Density ($\times 10^{14}$cm^{-2})
Si IV λ1400	-13 100	24.7±2.66	7.21±2.37	11.7±2.41
C IV λ1549	-19 700	190±15.2	95.8±8.64	151±11.3

†Integration spans zero velocity to velocity limit

tically impossible, given their large intrinsic widths, to identify individual C IV components. Though some Si IV components were well-separated, many of the doublets were blended to various extents with neighbouring absorption features. However, the optical depth of overlapping components is the sum of the individual components and the optical depth of the red component is known to be half that of the blue component for both ions, given the ratio of their oscillator strengths. Therefore, by integrating over all of the absorption for a given transition using the value of f corresponding to the red component, a minimum value of N_{ion} was found by taking 1/3 of the calculated value. The velocity ranges which were integrated over and the resulting estimated ionic column densities are shown in Table 4.2.

Since the C IV doublet was unresolved, this method was the only means of estimating a lower limit for the column density of that ion. For Si IV, methods involving modelling the components needed to be checked for consistency with the lower limit derived here.

4.3.3 Gaussian Components of the Si IV Outflow

The Si IV doublet velocity separation is $\sim$1920 km s^{-1}, which allowed the identification of some individual components. Assuming narrow components of quasar absorption lines follow an approximately Gaussian profile, e.g. Hamann et al. (2011), model profiles were able to be constructed for the doublet lines. Spectral fitting was performed using the *specfit* routine, part of the *contrib* package within IRAF. Figure 4.4 shows an IRAF screenshot of the component fitting of the SDSS observation within *specfit*.

The *specfit* routine requires three free parameters for each Gaussian component, namely the wavelength at line centre, line FWHM and line EW. Appropriate restrictions were applied to these parameters, i.e.

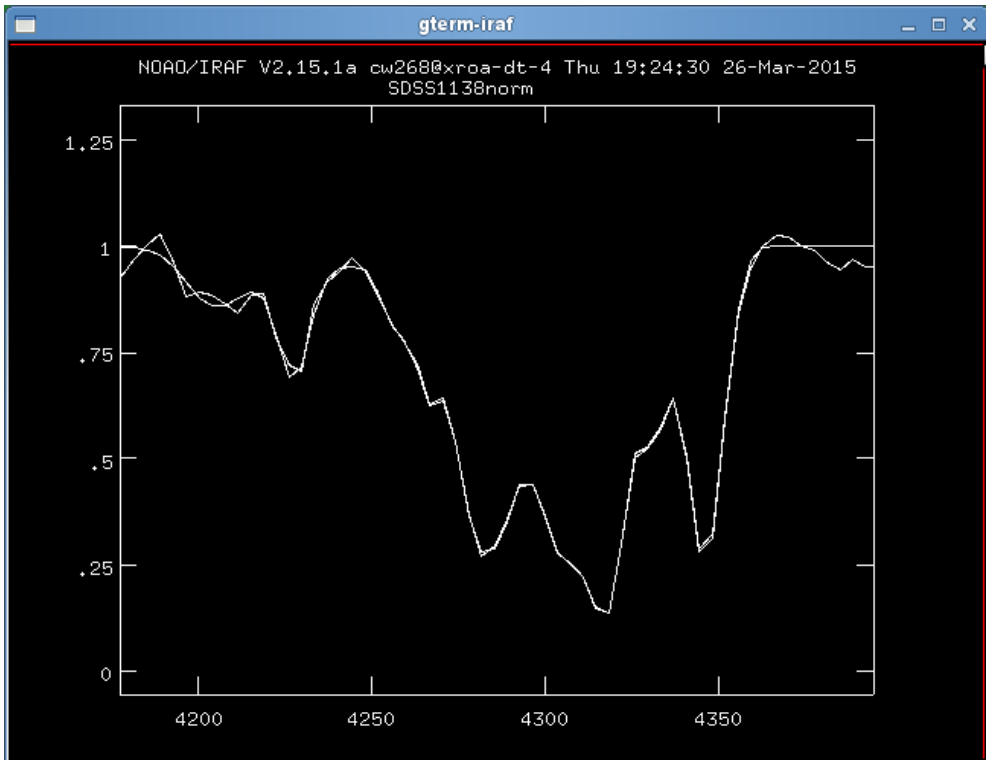

Figure 4.4: Example of *specfit* being used to fit the Si IV absorption components of the SDSS observation.

the EW ratio between the blue and red components of the doublet was restricted to between 2:1 and 1:1, the difference in velocities at line centre was not allowed to differ from the expected doublet separation by more than one velocity bin, and the widths needed to be the same. By using an initial 'guess' for these parameters' values, spectral fitting was performed using chi-square minimisation. In total, five Si IV doublets were identified across the 3 epochs, spanning the range $-10\,000 \leq v \leq 0$ km s^{-1}. These are shown in Figure 4.5.

By comparing the Gaussian fit to the almost un-blended red component of the lowest velocity doublet in epoch 2 (shown in red in Figure 4.5) to the data points at these velocities, a fractional error in the fit of 0.033 was calculated. To be conservative a larger error of 5 percent on each point of all Gaussian profiles was assumed for calculations involving these model profiles. While the EW and occasionally the FWHM changed from one epoch to the next, there was no significant change in the line centre velocity and hence no evidence for acceleration of the outflowing material. This lack of acceleration has been noted in previous studies, e.g. Hamann et al. (2008); Rodríguez Hidalgo et al. (2011). The best-fit parameters obtained by *specfit* for each doublet component are provided in Table 4.3.

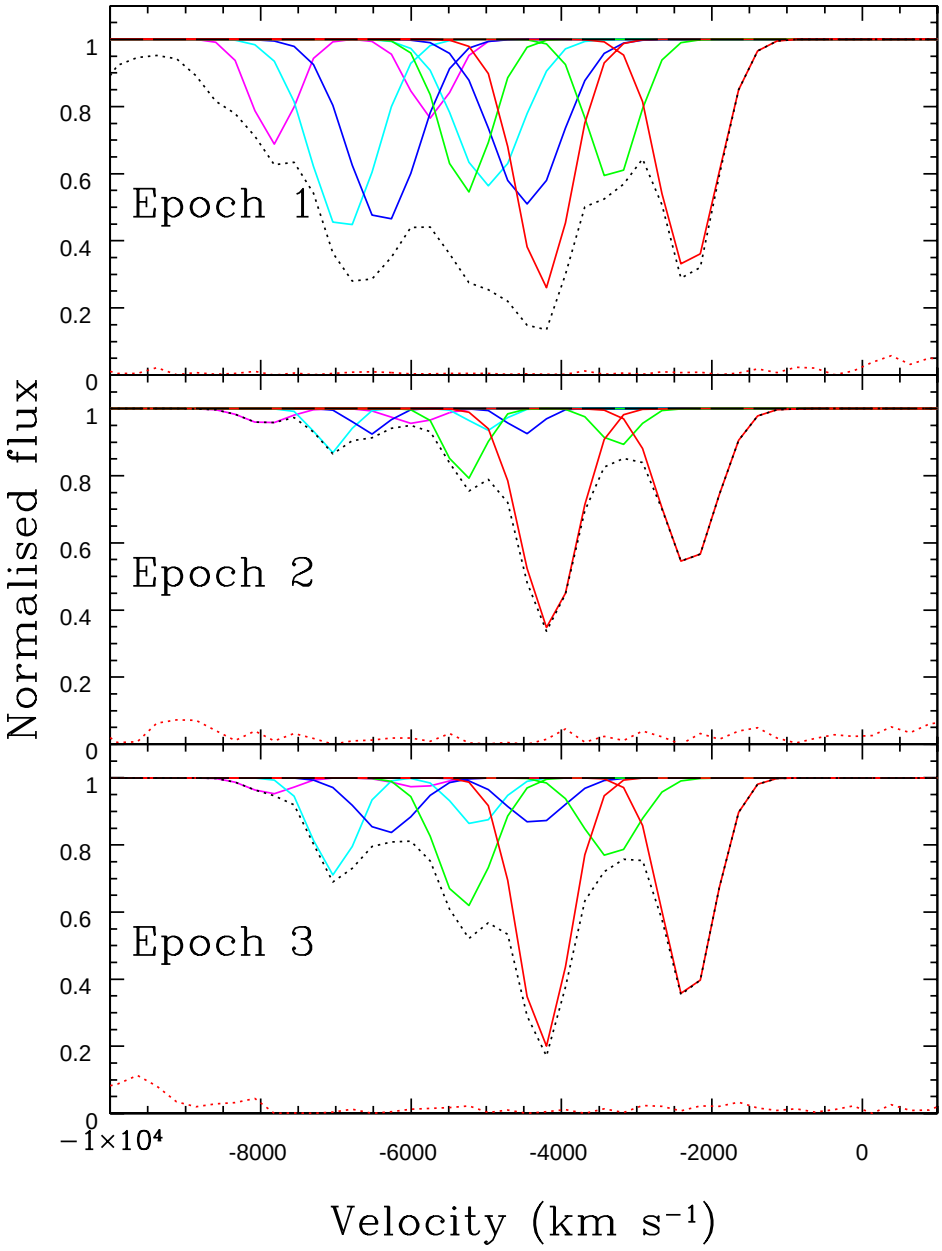

Figure 4.5: Epoch 1 (top panel), epoch 2 (middle panel) and epoch 3 (lower panel) models of Si IV doublet absorption lines in red component velocity space (related doublet components are shown in the same colour). The black dotted line describes the total model absorption profile, while the red dotted line near the bottom of each panel indicates the absolute difference between the model profile and the observed profile.

Table 4.3: List of components with parameters for Gaussian model profiles. Doublets are listed in order of increasingly negative velocity (1 is lowest, 5 is highest). Doublet velocity is measured from the red component rest wavelength.

Absorber	Velocity‡ (km s^{-1})	epoch 1		epoch 2		epoch 3	
		FWHM‡ (km s^{-1})	EW† (Å)	FWHM‡ (km s^{-1})	EW† (Å)	FWHM‡ (km s^{-1})	EW† (Å)
1 (Red)	−2300	900	3.18±0.09	900	2.03±0.07	800	2.69±0.04
1 (Blue)			3.18±0.16		2.80±0.07		3.21±0.05
2 (Red)	−3300	800	1.65±0.12	600	0.32±0.07	900	1.01±0.06
2 (Blue)			1.76±0.08		0.60±0.08		1.62±0.07
3 (Red)	−4300	1100	2.62±0.24	500	0.19±0.08	900	0.60±0.11
3 (Blue)			2.92±0.18		0.19±0.07		0.72±0.07
4 (Red)	−4800	1000	2.21±0.22	500	0.16±0.08	700	0.48±0.07
4 (Blue)			2.88±0.18		0.21±0.08		0.97±0.06
5 (Red)	−5900	700	0.77±0.15	700	0.15±0.08	700	0.09±0.06
5 (Blue)			1.02±0.13		0.15±0.11		0.16±0.06

†EW in quasar rest-frame

‡Error ∼200 km s^{-1}

Upon examination of an individual component, the following equation was used to estimate the column density giving rise to the doublet to which it belonged (Peterson, 1997):

$$N = \frac{m_e c b}{\sqrt{\pi} e^2 f \lambda} \tau_0 \,, \tag{4.2}$$

where τ_0 is the peak optical depth and b is the Doppler parameter (related to line width by $b = \sqrt{2} \times \mathrm{FWHM}/2.355$). This equation assumes a Voigt profile for the absorbers, which tends towards the Gaussian case in the limit of low optical depth. Red components are less likely to be affected by saturation since they are weaker than their corresponding blue components. As a result, column

density measurements were taken from red doublet lines. As in Section 4.3.2, estimates of the absorbing column density were lower limits as the absorber may not have covered 100 percent of the emission region. The values obtained for the five doublets listed in Table 4.3 were summed to give estimates of the total column densities, resulting in values of $N_{\mathrm{Si\ IV},1}$=33.5$\pm$1.49, $\mathrm{N_{Si\ IV},2}$=7.79$\pm$0.50 and $\mathrm{N_{Si\ IV},3}$=14.7$\pm$0.47 in units of 10^{14} cm^{-2} for the first, second and third epochs respectively. As expected, these were larger than the limits in Table 4.2 since blue:red doublet component ratios are less than 2:1.

4.3.4 A Pure Partial Coverage Model

Many absorption line systems have been found to be best described by a situation in which material of a certain optical depth covers a fraction of the emission source, leaving the rest of the source uncovered (Arav et al., 1999; de Kool et al., 2001) otherwise known as a pure partial coverage (PPC) model. Under these conditions the apparent optical depth $\tau = ln(1/I_{res})$, where I_{res} is the residual intensity (normalised to the unabsorbed continuum+line emission flux), will underestimate the true optical depth of the absorbing gas and consequently will underestimate the column density. The observed flux I_{app} is related to the covering fraction C by $I_{app} = CI_{out} + (1-C)I_0$, where I_0 is the unabsorbed emission flux and I_{out} is the true output flux from the absorber. Thus the covering fraction C as a function of velocity is given by

$$C\left(v\right) = \frac{I_r^2\left(v\right) - 2I_r\left(v\right) + 1}{I_b\left(v\right) - 2I_r\left(v\right) + 1}, \tag{4.3}$$

where $\mathrm{I}_r\left(v\right)$ and $\mathrm{I}_b\left(v\right)$ are the apparent residual fluxes of the red and blue components respectively at a given velocity v. Since the true optical depth $\tau = ln(I_0/I_{out})$, the following is also true

$$\tau = -ln\left(\frac{I_r - I_b}{1 - I_r}\right), \tag{4.4}$$

where τ is the optical depth of the red component at a specific velocity. Since $C \leq 1$, the values of I_r and I_b can be shown to be constrained to the range $I_r \geq I_b \geq I_r^2$. Assuming this condition is met, it is then straightforward to calculate the column density using Equation 4.1.

Evidence for pure partial covering can be obtained by comparing the residual flux velocity dependence of a (almost) saturated absorption line to the profile of $1 - C$. Similar profiles would suggest the shape of the absorption profile is determined by the velocity-dependent covering fraction of an opaque absorber rather than intrinsic differences in optical depth. An additional test is to compare the profile of $e^{-\tau}$ to the red component of an absorption doublet. If the profiles do not match, the absorption line profile cannot be due to an absorber which is homogeneous and completely covers the emission region. In order to carry out these tests, a doublet with unblended components is desirable. The closest example available in the dataset was absorber 1 in the epoch 2 spectrum. From the values of the EWs of the red and blue components (see Table 4.3), the blue:red ratio was less than 2:1, indicating that the blue component was probably saturated. After placing the blue component onto the red component velocity grid by interpolation, six velocity bins were found which followed the general shape of the corresponding Gaussian models for both the red and blue components. Five of these points satisfied $I_r \geq I_b \geq I_r^2$ and are illustrated in Figure 4.6.

From the profile traced by $1 - C$ (Figure 4.6, dashed green line), it was clear that the saturated blue component could have its profile determined by the uncovered fraction. It was also obvious that the residual intensity of the red component was a poor match to $e^{-\tau}$. Together these provided *strong evidence that partial coverage was a significant effect in this absorber* and possibly others in this quasar.

Given that this was the only doublet where meaningful results could be obtained on an individual velocity bin basis, and even in this case it could only be done close to the peak of the absorption components, it was necessary to use the Gaussian models to achieve estimates of column density across a greater proportion of the Si IV absorption for the 3 epochs. Individual velocity bins in the Gaussian models have no physical realisation, so unlike for the previous example it was impossible to construct $1-C$ profiles using Equation 4.3. However if for each doublet component, model fluxes were averaged over all velocities spanned by the absorption, individual components could be treated as individual velocity bins. This method could subsequently be used to estimate average values of covering fraction and true optical depth for each doublet. Using this true optical depth in Equation 4.1 gave the doublet's column density along the line of sight when N_{ion} was multiplied by the covering fraction. These values are listed in Table 4.4. Due to the weakness of absorbers 3 to 5 in epochs 2 and 3 this could only be performed across all absorbers in epoch 1, since at small absorber depths optical depth and covering fraction measurements are unreliable due to their sensitive dependence on doublet component ratio.

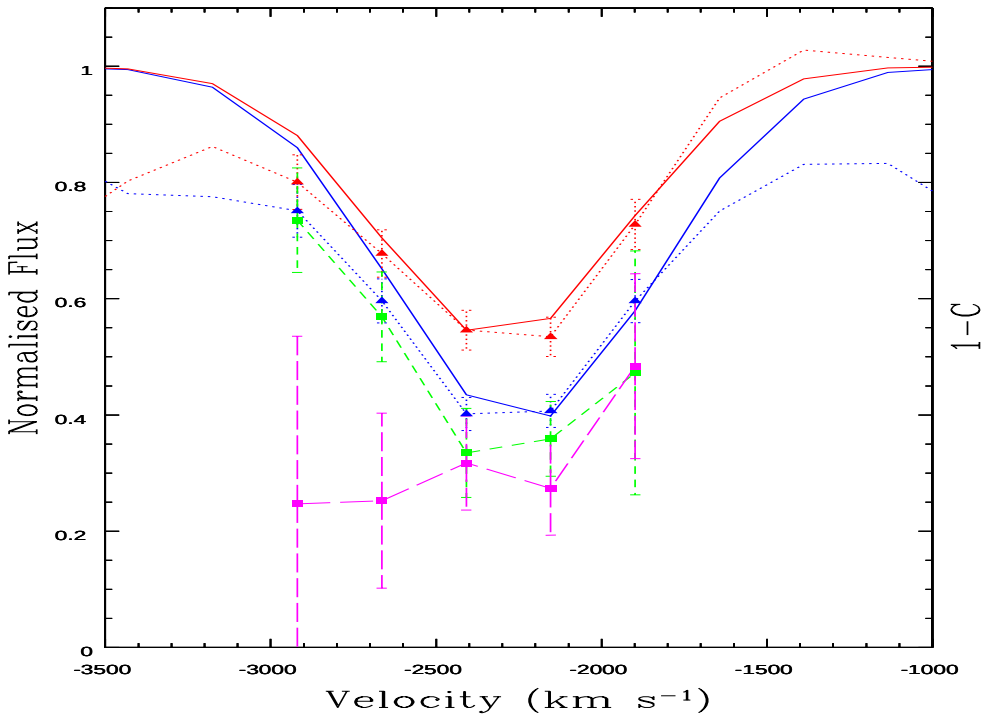

Figure 4.6: The absorber 1 profiles of the red and blue components interpolated onto the red component's velocity grid. The solid red and blue lines represent the Gaussian models, the dotted lines represent the observed fluxes, the green short-dashed line indicates the $1 - C$ values at these points and the magenta long-dashed line represents the $e^{-\tau}$ values of the red component. Appropriately coloured triangles and squares represent the observed points in velocity space. While the $1 - C$ profile is a good match for the blue absorber, the $e^{-\tau}$ profile does not match the red profile.

The PPC method cannot be used if the red component becomes highly saturated such that the apparent blue:red optical depth ratio moves close to 1:1, as in this case the calculated column density tends to infinity.

4.4 Photoionisation Simulations

4.4.1 Cloudy Setup

Modelling the column densities and ionising fractions of ions in quasar outflows by specifying the shape of the ionising continuum and various gas (column) densities can provide insight into the physical

Absorber	epoch 1		epoch 2		epoch 3	
	C	N_{ion} $\times 10^{14}$cm^{-2}	C	N_{ion} $\times 10^{14}$cm^{-2}	C	N_{ion} $\times 10^{14}$cm^{-2}
1	0.225±0.013	$23.3^{+15.6}_{-14.0}$	0.234±0.042	$7.17^{+3.56}_{-2.87}$	0.236±0.020	$12.3^{+4.40}_{-3.881}$
2	0.187±0.017	$11.0^{+8.68}_{-7.40}$	$0.318^{+0.682}_{-0.318}$	$0.773^{+13.7}_{-0.773}$	0.275±0.165	$2.898^{+4.010}_{-0.165}$
3	0.339±0.017	$14.1^{+4.20}_{-3.88}$				
4	0.366±0.032	$8.45^{+2.34}_{-2.09}$				
5	0.122±0.043	$2.94^{+3.61}_{-2.27}$				

Table 4.4: Table of covering fractions and column densities calculated for absorbers 1 to 5. Absorbers 3 to 5 are not listed for epochs 2 and 3 due to their low strength.

location of the outflowing plasma and the changing nature of the relationship between the ionising photon flux and ionising state, especially if ionisation changes are the principal driver of absorption line variability. Photoionisation simulations used for the investigation in this chapter were performed using CLOUDY version c13.02 (Ferland et al., 1998, 2013).

The CLOUDY code combines these input parameters with a model of the input spectral energy distribution (SED) to calculate the total ionising photon flux. It models the input SED using input parameters for the big blue bump temperature (T_{BB}) and power-law indices determining continuum behaviour of the form $F_\nu \propto \nu^\alpha$, including optical to near-UV spectral index (α_{uv}) for optical wavelengths above 2500 Å, UV to soft x-ray spectral index (α_{ox}) between 2500 Å and 2 keV, and x-ray spectral index (α_x) from 2 keV to 100 keV. The α_{uv} value used in this investigation was α_{uv}=0, which is within the range found by other studies, for example Natali et al. (1998) found an average value of α_{uv}=-0.33 ± 0.59. A value of $\alpha_{ox} = -1.98$ was adopted, which was calculated using the method of Wilkes et al. (1994) in Equation 4.5

$$\alpha_{ox} = -1.53 - 0.11 \times log\left(\frac{L_o}{10^{30.5}}\right) , \tag{4.5}$$

where L_o is the specific intensity at 2500 Å in the quasar rest-frame in units of erg s^{-1} Hz^{-1}. This is towards the more negative end of the range found in Grupe et al. (2010), however tests with values of α_{ox} between a more typical value of -1.6 and the adopted value showed no significant difference in Si IV and C IV column densities, so any discrepancies between the adopted value and the true value

should not have dramatically altered the results presented in this chapter. According to Zdziarski et al. (1996) the value of α_x is typically between -0.8 and -1.0, so a value of -1.0 was adopted in this investigation for simplicity. It is possible to estimate T_{BB} from the ratio of the bolometric to Eddington luminosity and the mass of the black hole using the method of Bonning et al. (2007):

$$T_{max} = 10^{5.56} M_8^{-\frac{1}{4}} \frac{L_{bol}}{L_{Edd}}\,, \tag{4.6}$$

where T_{max} is the maximum accretion disc temperature, M_8 is the black hole mass in units of $10^8 M_\odot$, L_{bol} is the bolometric luminosity and L_{Edd} is the Eddington luminosity. The value of L_{Edd} can be found from the black hole mass using $L_{Edd} = 10^{46.1} M_8$. Using estimates of M_8 and L_{bol} from Shen et al. (2011) gave a value of T_{max}∼240 000 K, with the peak flux of the big blue bump occurring at $2.1{\times}10^{16}$ Hz (∼140 Å or 87 eV). The value of T_{max} can be used as the approximate value of T_{BB} in the cloudy input. Using the aforementioned parameters, the CLOUDY code generates the AGN SED as detailed in section 6.1 of *Hazy1* using the following equation

$$F_\nu = \nu^{\alpha_{uv}} exp\left(\frac{-h\nu}{kT_{BB}}\right) exp\left(\frac{-kT_{IR}}{h\nu}\right) + a\nu^{\alpha_x} \tag{4.7}$$

where the term kT_{IR} represents an infrared exponential cutoff of the big bump occurring at an energy of kT_{IR}=0.01 Ryd. The coefficient a is selected so that the last term additionally produces the correct contribution in the spectral range to which α_{ox} is applicable. The contribution from ν^{α_x} is only nonzero at energies above 0.1 Ryd since if it were extended to the infrared, strong free-free heating would result. The last term is set to zero below 1.36 eV, and above 100 keV it is assumed to fall off as ν^{-2}. The SED produced by these parameters was illustrated earlier in this thesis in Chapter 2 (Figure 2.11).

A grid of simulations containing column density data for Si IV and C IV was generated using the input continuum, with grid-points at hydrogen column densities log (N_H / cm^{-2})=21, 22 and 23, hydrogen number densities log (n_H / cm^{-3})=5, 7 and 9 and log U values spanning -5.0 to 3.0 in intervals of 0.2 dex. The default CLOUDY inner radius of 10^{30} cm was used to calculate the SEDs used for the grid, therefore they were effectively not normalised to any particular luminosity. Normalisation of the SEDs to the correct total ionising flux is described in Section 4.4.2. The hydrogen number densities spanned typical narrow line region to broad line region densities, the maximum density being close

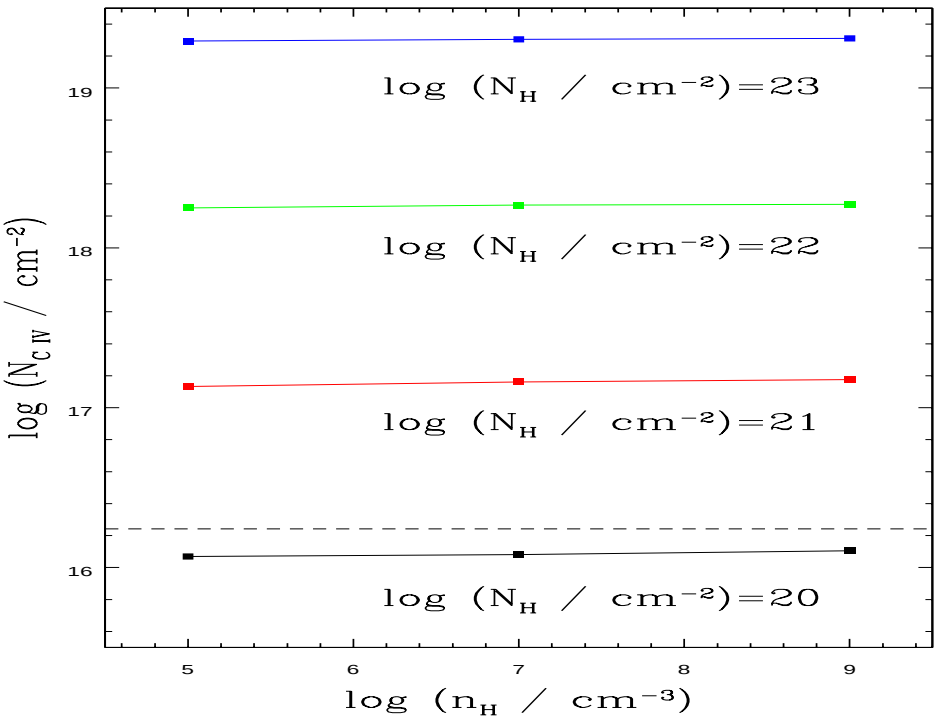

Figure 4.7: Predicted C IV column densities as a function of hydrogen number density for given hydrogen column densities. Solid squares indicate the CLOUDY input hydrogen densities, which are linked by solid lines of constant hydrogen column density. The horizontal dashed line gives the minimum C IV column density predicted by the SDSS observation, which shows the strongest absorption of all epochs. It is clear that log (N_H / cm^{-2})$\leq$20 is ruled out by this limit.

to the critical density of C III]. The density was unlikely to be higher than this as this would have suggested that the absorber originated from within the BLR, conflicting with the fact that individual absorption components are relatively narrow in comparison to the broad emission lines. This was also apparent from the need for the deepest troughs to be absorbing both the broad emission line and the continuum. The ionising parameter range encompassed all reasonable values given the existence of the absorbers, while the hydrogen column density range was chosen to span a range above the minimum ionic column density for C IV, $N_{\rm C\,IV}$, and below a density at which Thomson scattering becomes significant. This ruled out column densities of log (N_H / cm^{-2})$\leq$20 as these generated $N_{\rm C\,IV}$ values below the minimum value calculated from direct integration (see Figure 4.7).

4.4.2 Application of Cloudy Models to Estimated Column Densities

The CLOUDY models were applied to results reported in previous sections of this chapter to provide parameters governing the properties of the quasar continuum source which affected the outflowing gas. A simplifying assumption was made that all absorption components were formed in the same location and under the same ionisation parameter. Initially it was necessary to find the correct normalisation of the continuum SED described in Section 4.4.1, which could be used to find the total ionising luminosity L_{ion} and ionising photon emission rate $Q(H)$ and hence the distance from the continuum source to the inner edge of the outflowing gas (facing the source) and the mass outflow rate. The correct ionising SED was found by scaling the output to the rest-frame corrected flux of the observed SDSS spectrum. Output parameters from the simulation included the total ionising photon flux $\phi(H)$ which could be used to find the true values of the ionising luminosity, L_{ion}, the rate of emission of Lyman continuum photons, $Q(H)$ and the ionising source distance to the absorbing gas, R. The calculated value of the inner radius R varies depending on the grid parameters (U,N_H and n_H); however since the same SED was used in each case, values of ionising luminosity and ionising photon production rate were found which were applied universally; they are L_{ion}=4.17$\times10^{46}$ erg s^{-1} and $Q(H)$=9.80$\times10^{56}$ s^{-1}.

In order to apply the grid of models calculated in Section 4.4.1, limits for the ionic column densities of Si IV and C IV needed to be found. Since there were no resolvable doublets available for C IV, only the lower limits found from direct integration in Section 4.3.2 could be used for this ion. For Si IV, the strength of the doublets at epoch 1 meant that total column densities could be estimated using the PPC model for all 5 absorbers as listed in Table 4.4. For epochs 2 and 3, PPC could be used for absorbers 1 and 2, which were the predominant contributors to the total line of sight column density at these epochs, plus a contribution from absorbers 3 to 5 using the peak optical depth (POD) method outlined in Section 4.3.3 modified to take account of partial coverage. Here it was assumed that the covering fractions of absorbers 3 to 5 at epochs 2 and 3 were the same as those at epoch 1. The true optical depth could be found once the covering fraction was known. Multiplying the original POD-derived $N_{\rm Si\ IV}$ by the covering fraction and the ratio of the integrated real optical depth over the integrated apparent optical depth spanning the velocity range of the red component of the doublet, gave an estimate of the true column density. The $N_{\rm Si\ IV}$ and their upper and lower limits are shown in Table 4.5. The total column density lower limits were assumed to be the totals derived from the POD method (listed in Section 4.3.3), while the upper limits were calculatd from the column density and

Epoch	$N_{\mathrm{Si\ IV}}$ ($\times 10^{14}$ cm^{-2})	$N_{\mathrm{Si\ IV}}$ lower limit ($\times 10^{14}$ cm^{-2})	$N_{\mathrm{Si\ IV}}$ upper limit ($\times 10^{14}$ cm^{-2})
1	59.8	33.5	94.2
2	9.18	7.79	27.5
3	18.3	14.7	27.9

Table 4.5: Total column densities and their limits for Si IV at each epoch.

covering fraction errors for each component as listed in Table 4.4. Upper limits on the value of $N_{\mathrm{Si\ IV}}$ at epoch 2 were comparatively large due to the large uncertainty in the covering fraction of absorber 2, however the best value lay towards the lower end of this interval.

Using the CLOUDY output at each combination of log N_H and log n_H, plots could be made of predicted ionic column densities across the entire range of ionising parameter U. The span of log U covered the peak of both N_{ion} for all combinations, resulting in cases where there were two possible regions in which the ionic column density values could be located. Given that only lower limits of the C IV column density could be found, the column densities for this ion were estimated by locating the positions in log U space of allowed $N_{\mathrm{Si\ IV}}$ and using the equivalent values for C IV. By assuming that ionising continuum changes were the main factor driving variability, it was possible to identify the range of log U which satisfied the ionic column density limits at each epoch. Although there were nine possible combinations of log N_H and log n_H, only 2 are shown (Figures 4.8 and 4.9). It was apparent from these Figures that the lower region of allowed log U values (where the gradient of log N_{ion} vs. log U is positive) was invalid as the allowed range of $N_{\mathrm{Si\ IV}}$ for epoch 3 did not permit any $N_{\mathrm{C\ IV}}$ values above the lower limit. This was found to be true for all 9 density/column density combinations, giving one continuous span of allowed log U values in each case.

4.4.3 Outflow properties derived from models

The estimation of mass outflow rates ($\dot{M}_{out}$) was based on the method used in Crenshaw et al. (2009) which related $\dot{M}_{out}$ to other parameters by considering a spherical surface at distance R from the central engine which is partially covered by an outflow moving at velocity v. The following equation then relates these quantities

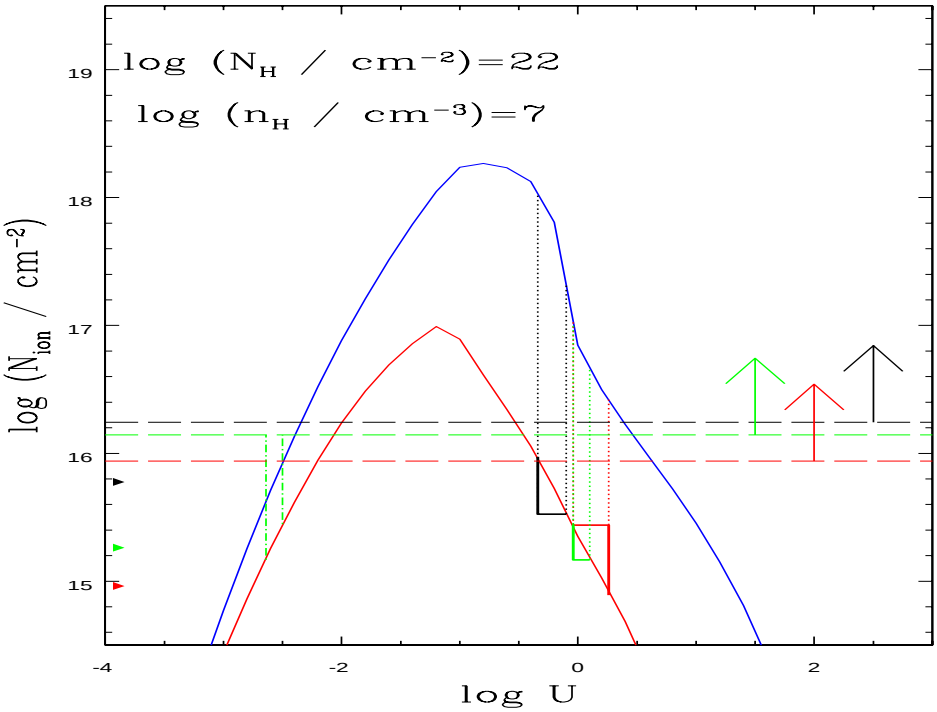

Figure 4.8: Predicted Si IV (solid red lines) and C IV (solid blue lines) column densities as a function of ionising parameter at log (N_H / cm^{-2})=22 and log (n_H / cm^{-3})=7. Black, red and green dashed lines with arrows indicate the lower limits of the C IV column density for epochs 1, 2 and 3 respectively. Using the same colour scheme, the solid triangles represent the best values of the Si IV column densities, while the thick solid 'L-shapes' denote the regions of the curves which span the confidence limits on these values and are allowed after taking the C IV lower limits into account. Vertical dotted lines link the upper and lower limit log$U$ values of the allowed region on the SiIV curve to the corresponding positions on the C IV curve. The vertical green dot-dashed lines link the upper and lower log$U$ values of the region allowed by the Si IV column density limits on the positive-gradient part of the epoch 3 curve to the corresponding points on the lower limit line on the C IV column density, indicating that this lower limit is not satisfied in this region for any points on the C IV curve.

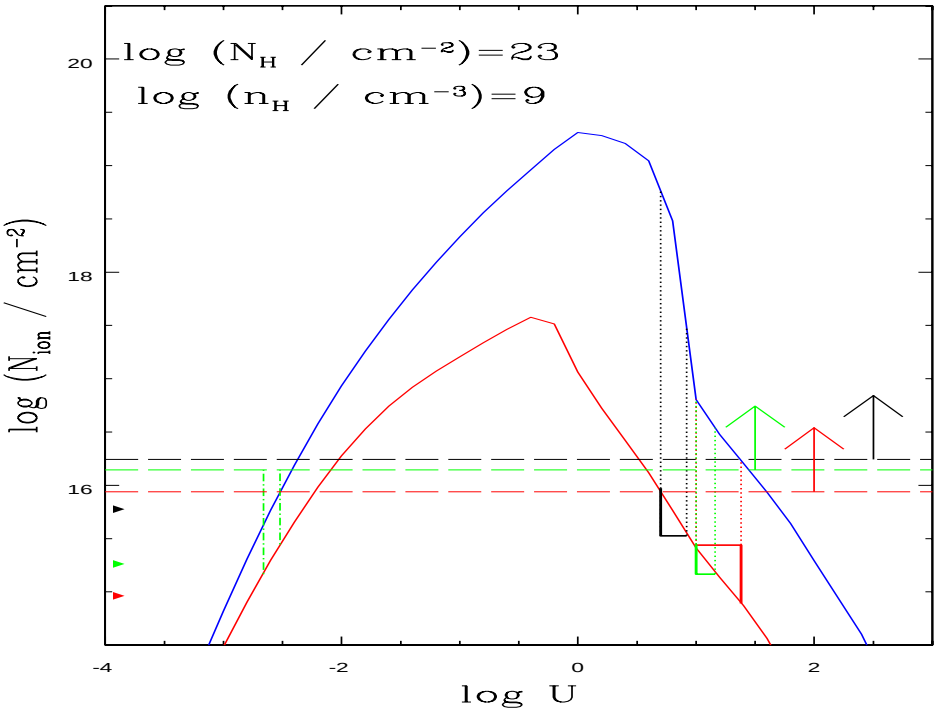

Figure 4.9: Predicted Si IV (solid red lines) and C IV (solid blue lines) column densities as a function of ionising parameter at log (N_H / cm^{-2})=23 and log (n_H / cm^{-3})=9. Black, red and green dashed lines with arrows indicate the lower limits of the C IV column density for epochs 1, 2 and 3 respectively. Using the same colour scheme, the solid triangles represent the best values of the Si IV column densities, while the thick solid 'L-shapes' denote the regions of the curves which span the confidence limits on these values and are allowed after taking the C IV lower limits into account. Vertical dotted lines link the upper and lower limit log$U$ values of the allowed region on the SiIV curve to the corresponding positions on the C IV curve. The vertical green dot-dashed lines link the upper and lower log$U$ values of the region allowed by the Si IV column density limits on the positive-gradient part of the epoch 3 curve to the corresponding points on the lower limit line on the C IV column density, indicating that this lower limit is not satisfied in this region for any points on the C IV curve.

$$\dot{M}_{out} = 8\pi R N_H \mu m_p C_q |v| \, (M_\odot yr^{-1}) \,, \tag{4.8}$$

where μ is the mean atomic mass per proton ($\mu \sim 1$), m_p is the proton mass, C_q is the covering fraction of the outflow as seen from the quasar and v is the mean velocity of the outflow. The value of C_q is assumed to be $\sim$0.1 given the fraction of quasars showing broad absorption lines. It was not obvious what the mean outflow velocity of the predominantely hydrogen outflow was, so the centroid velocity of the C IV outflow was adopted, being v~ -7600 km s^{-1}.

In Table 4.6 information on mass outflow rate, distance to the inner face of the outflowing gas from the ionising continuum source and C IV column density is provided at the values of U allowed by the limits on $N_{\rm Si\ IV}$ and lower limits on $N_{\rm C\ IV}$ at each grid point. Mass outflow rates much greater than the accretion rate are ruled out since, assuming winds are launched close to the central engine, e.g. Proga et al. (2000), such outflow rates would quickly exhaust the quasar's accreting fuel. The numbers calculated for this table provided an overview of the allowed range in physical states of the outflow, as well as possible effects a changing ionising parameter could exert. Linear interpolation between the 0.2 dex interval-separated log U values was used to estimate values at intervals of 0.02 dex.

As expected, the range of log U allowed was strongly dependent on N_H rather than n_H, leaving the value of the hydrogen number density uncertain, with the caveat that it probably did not exceed the BLR density. By assuming ionising continuum flux variations were driving the variability, then given the values of log U and their possible ranges indicated by the third and fourth columns of Table 4.6, it was possible to estimate how the ionising parameter was changing across the time scales sampled. Between epochs 1 and 2, log U would have changed by increments of between 0.06 dex and 0.76 dex, with best estimates of $\sim$0.5 to $\sim$0.6 dex. For the epoch 2 to epoch 3 interval, log U would have changed by increments of between 0 and 0.38 dex, with ~ -0.2 dex being the best estimate. Since, at fixed values of R and n_H, the change in U represents the change in $Q(H)$, this factor represents the change in ionising flux reaching the outflowing gas. Changes of similar scale to these best estimates for the change in log U have been observed in the extreme ultraviolet (EUV) of at least one other quasar of similar redshift over a comparable rest-frame timescale e.g. in Reimers et al. (2005), where the flux at a rest-frame wavelength of 335 Å changed by a factor of $\sim$3 in a rest-frame timescale of $\sim$0.65 years. Since the EUV is the main contributor to the ionisation of the outflow, this indicates the results reported here are plausible.

Table 4.6: Table of parameters derived from CLOUDY simulations for various hydrogen densities and column densities.

log N_H log(cm^{-2})	log n_H log(cm^{-3})	log U	log U range	log $N_{\rm C\ IV}$ log(cm^{-2})	log $N_{\rm C\ IV}$ range log(cm^{-2})	log R log(cm)	Outflow Rate M$_\odot$/year
epoch 1							
21	5	-1.20	-1.36≤log U≤-1.06	17.09	16.91≤log $N_{\rm C\ IV}$≤17.12	20.8±0.1	$36.1^{+9.4}_{-7.4}$
21	7	-1.24	-1.38≤log U≤-1.06	17.10	16.88≤log $N_{\rm C\ IV}$≤17.15	19.8±0.1	$3.61^{+0.94}_{-0.74}$
21	9	-1.18	-1.34≤log U≤-1.02	17.07	16.85≤log $N_{\rm C\ IV}$≤17.15	18.8±0.1	$0.361^{+0.093}_{-0.074}$
†22	5	-0.20	-0.30≤log U≤-0.08	17.90	17.32≤log $N_{\rm C\ IV}$≤18.03	20.3±0.1	114^{+30*}_{-23}
22	7	-0.24	-0.34≤log U≤-0.10	17.87	17.33≤log $N_{\rm C\ IV}$≤18.03	19.3±0.1	$11.4^{+3.0}_{-2.3}$
22	9	-0.20	-0.30≤log U≤-0.08	17.76	17.22≤log $N_{\rm C\ IV}$≤17.94	18.3±0.1	$1.14^{+0.30}_{-0.23}$
†23	5	0.80	0.68≤log U≤0.92	18.79	17.66≤log $N_{\rm C\ IV}$≤18.98	19.8±0.1	361^{+94*}_{-74}
23	7	0.76	0.66≤log U≤0.90	18.72	17.73≤log $N_{\rm C\ IV}$≤18.94	18.8±0.1	$36.1^{+9.4}_{-7.4}$
23	9	0.80	0.70≤log U≤0.92	18.48	17.48≤log $N_{\rm C\ IV}$≤18.76	17.8±0.1	$3.61^{+0.94}_{-0.74}$
epoch 2							
21	5	-0.64	-0.98≤log U≤-0.62	16.37	16.31≤log $N_{\rm C\ IV}$≤16.81	$20.5^{+0.2}_{-0.1}$	$18.1^{+10.6}_{-3.7}$
21	7	-0.66	-1.00≤log U≤-0.62	16.34	16.29≤log $N_{\rm C\ IV}$≤16.80	$19.5^{+0.2}_{-0.1}$	$1.81^{+1.05}_{-0.37}$
21	9	-0.62	-0.94≤log U≤-0.58	16.33	16.28≤log $N_{\rm C\ IV}$≤16.74	$18.5^{+0.2}_{-0.1}$	$0.181^{+0.106}_{-0.037}$
†22	5	0.26	-0.02≤log U≤0.30	16.46	16.40≤log $N_{\rm C\ IV}$≤17.03	$20.0^{+0.2}_{-0.1}$	$57.4^{+33.3}_{-11.9}$
22	7	0.24	-0.04≤log U≤0.26	16.44	16.42≤log $N_{\rm C\ IV}$≤17.04	$19.1^{+0.2}_{-0.1}$	$7.20^{+4.20}_{-1.48}$
22	9	0.28	-0.02≤log U≤0.30	16.42	16.39≤log $N_{\rm C\ IV}$≤16.95	$18.0^{+0.2}_{-0.1}$	$0.574^{+0.333}_{-0.119}$
†23	5	1.32	1.00≤log U≤1.36	16.33	16.27≤log $N_{\rm C\ IV}$≤16.90	$19.5^{+0.2}_{-0.1}$	181^{+106*}_{-37}
23	7	1.30	0.98≤log U≤1.34	16.32	16.27≤log $N_{\rm C\ IV}$≤17.00	$18.5^{+0.3}_{-0.1}$	$18.1^{+18.0}_{-3.7}$
23	9	1.34	1.00≤log U≤1.38	16.29	16.23≤log $N_{\rm C\ IV}$≤16.81	$17.5^{+0.2}_{-0.1}$	$1.81^{+1.06}_{-0.37}$
epoch 3							
21	5	-0.86	-0.98≤log U≤-0.82	16.63	16.57≤log $N_{\rm C\ IV}$≤16.81	20.6±0.1	$22.8^{+5.9}_{-4.7}$
21	7	-0.88	-1.00≤log U≤-0.82	16.63	16.54≤log $N_{\rm C\ IV}$≤16.80	19.6±0.1	$2.28^{+0.59}_{-0.47}$
21	9	-0.84	-0.96≤log U≤-0.78	16.60	16.52≤log $N_{\rm C\ IV}$≤16.77	18.6±0.1	$0.228^{+0.059}_{-0.047}$
†22	5	0.08	-0.02≤log U≤0.12	16.77	16.70≤log $N_{\rm C\ IV}$≤17.03	20.1±0.1	$72.0^{+18.7}_{-14.8}$
22	7	0.06	-0.04≤log U≤0.10	16.74	16.67≤log $N_{\rm C\ IV}$≤17.04	19.2±0.1	$9.05^{+2.35}_{-1.85}$
22	9	0.08	-0.02≤log U≤0.14	16.72	16.62≤log $N_{\rm C\ IV}$≤16.95	18.1±0.1	$0.720^{+0.187}_{-0.148}$
†23	5	1.12	1.00≤log U≤1.16	16.66	16.59≤log $N_{\rm C\ IV}$≤16.90	19.6±0.1	228^{+59*}_{-47}
23	7	1.08	0.98≤log U≤1.14	16.68	16.57≤log $N_{\rm C\ IV}$≤17.00	18.6±0.1	$22.8^{+5.9}_{-4.7}$
23	9	1.12	1.00≤log U≤1.16	16.61	16.54≤log $N_{\rm C\ IV}$≤16.81	17.6±0.1	$2.28^{+0.58}_{-0.47}$

* These outflow rates are much greater than the accretion rate and are therefore ruled out.

† These N_H,n_H grid-points are ruled out due to the large outflow rates indicated by *.

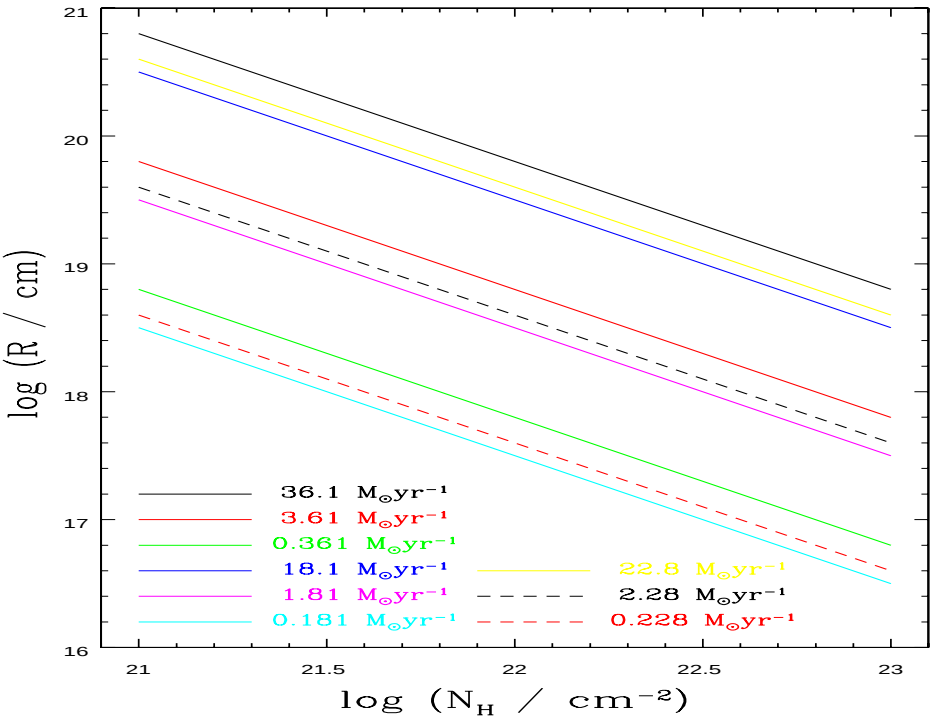

Figure 4.10: Dependence of log R on log N_H for constant mass outflow rates. Values are from Table 4.6.

As indicated in Column 7 of Table 4.6, the log R values did not change significantly between epochs for given combinations of log N_H and log n_H. The dependence of log R on log N_H is indicated in Figure 4.10. It was appropriate to consider how the predicted absorber distances compared to the size of the BLR. Using the method of Kaspi et al. (2005), the BLR radius R_{BLR} could be estimated using R_{BLR}=AL$^B\times$10 lt-days, where L is λL_λ(1450 Å)/10^{44}(erg s^{-1}) and A and B are constants, with a set of values found using the FITEXY method and the mean Balmer line's time lag in Kaspi et al. (2005) to be A=2.12 and B=0.496. This set of values was used as the index B is consistent with subsequent studies, e.g. Bentz et al. (2006), which found it to be $\sim$0.5 This is consistent with the fact that $U\propto Q_H/R^2$, leading to $R\propto L^{0.5}$. The procedure provided a value of $R_{BLR}\sim7.6\times10^{17}$ cm (a few hundred light-days). Comparing this with the values found for R in Table 4.6 suggested that the outflowing gas was outside the BLR in 8 out of 9 cases, the exception being the grid-point log (N_H / cm^{-2})=23, log (n_H / cm^{-3})=9.

The mass outflow rates calculated ranged from tenths of a solar mass to hundreds of solar masses per year. The estimated mass outflow rates, which depended upon the product RN_H, were in the range indicated in Table 4.6. Given the uncertainties in the mass outflow rate, they did not change significantly

between epochs. It was possible to calculate the accretion rate at Eddington luminosity in this object and hence compare it to the actual accretion rate and the mass outflow rate. This required an estimation of the black hole mass, which could be calculated using the following

$$M = \frac{fv^2 R_{BLR}}{G}, \tag{4.9}$$

where v is the orbital velocity of the BLR gas, G is the gravitational constant and f is the virial coefficient which has been estimated to be $\sim$5.25 (Woo et al., 2010). The value of v was estimated as $v\sim$4100 km s^{-1} using the width of the C IV broad emission line. This gave a value of $M_{BH}\sim5.1\times10^9$ $M_\odot$. This was checked for consistency by comparing with the value obtained using Equation 3 in Vestergaard (2004), which provided a very similar value of $\sim5.3\times10^9$ $M_\odot$. The Eddington luminosity could then be found using the relation L_{Edd}=$10^{46.1} M_8$ erg s^{-1}, where M_8 is black hole mass in units of $10^8 M_\odot$, giving L_{Edd}=6.4×10^{47} erg s^{-1}. The Eddington accretion rate $\dot{M}_{Edd}$=$L_{Edd}/\eta c^2$ implied $\dot{M}_{Edd}\sim113$ $M_\odot$ yr^{-1}.

The actual accretion rate could be calculated from the bolometric luminosity, which could be found using the luminosity at 1450 Å by applying $L_{bol}\sim4.36\lambda L_\lambda$ (at 1450 Å) (Warner et al., 2004). For a bolometric luminosity of $L_{bol}\sim9.5\times10^{46}$ erg s^{-1}, the resultant value of the accretion rate in terms of that at Eddington was $\sim$0.15 $\dot{M}_{Edd}$ ($\sim$17.0 $M_\odot$ yr^{-1}), meaning that this object's accretion rate was a substantial portion of the value at the Eddington limit. This allowed the ruling out of two combinations of hydrogen column density and hydrogen number density (log (N_H / cm^{-2})=22, log (n_H / cm^{-3})=5 and log (N_H / cm^{-2})=23, log (n_H / cm^{-3})=5) due to their excessively high outflow rates compared to the accretion rate, as indicated in Table 4.6. By comparing the remaining allowed values, the mass outflow rate could be calculated to be approximately between 1 percent and 200 percent of the mass accretion rate, corresponding to a kinetic luminosity range of $\sim3.3\times10^{42}$ to 6.6×10^{44} erg s^{-1}. The upper limit of this range gave a kinetic energy to luminosity ratio of $\sim$0.7 percent, high enough to have a significant impact on the evolution of the surrounding galaxy (Hopkins & Elvis, 2010), however definite conclusions regarding the outflow's importance in this regard were impossible given the weakness of the constraint.

4.5 Discussion

4.5.1 Were changes in the outflow geometry responsible for variability?

Changes in covering fraction within the context of the PPC model were one possibility considered as being behind the dramatic variability seen in this quasar's absorption lines. From Section 4.3.4 (Figure 4.6) it was clear that the deepest parts of the blue absorber 1 trough in epoch 2 were accurately described by a saturated absorber whose depth is determined by the fraction covering the emission source. By assuming that absorption takes place within the context of PPC, it was possible to determine how the covering fraction had changed between epochs using the Gaussian profile models. From the vslues listed in Table 4.4 it was clear that there was no significant change in C for absorber 1 between epochs (changes being within 1σ for $\sigma \leq 0.042$). There was also no discernible change in the covering fraction of absorber 2. Conclusions regarding covering fraction variations in absorber 2 are weak for two reasons. First, the epoch 2 doublet was entirely unsaturated and therefore the covering fraction estimation was completely unconstrained. Secondly, when comparing the epoch 1 value (C=0.187$\pm$0.017) with the epoch 3 value (C=0.275$\pm$0.165), the large uncertainty in the latter allowed a significant range which prevented any strong conclusion regarding the presence of covering fraction variations. Given the lack of significant variability in either the strongly constrained absorber 1 or the weakly constrained absorber 2, the conclusion could be drawn that there was no evidence for covering fraction variation being the dominant mechanism behind the variability.

4.5.2 Evidence for ionising changes driving variability

Ionisation fraction changes within the outflowing gas could be generated either by intrinsic changes in the ionising radiation emitted from the central ionising continuum source or shielding of this radiation by gas in the region between the accretion disc and the BAL gas. There were several indicators that suggested ionising fraction changes were implicated in the absorption line variability in this object, the strongest being coordinated changes seen across large velocity separations. A similar result was noted in Trevese et al. (2013) regarding the quasar APM 08279+5255, where they observed coordinated variability in two Gaussian-modelled components of a C IV BAL separated by $\sim$5000 km s^{-1}. The large velocity separations between absorption troughs implied that the absorption arises in physically

distinct regions, hence making covering fraction changes an unlikely explanation due to the level of coordination required across such large separations, e.g. Filiz Ak et al. (2013). This phenomenon was especially evident in the C IV absorption troughs (see Figure 4.3). The visibly saturated absorption trough centred at $\sim$−4000 km s^{-1} underwent weakening between epochs 1 and 2 before strengthening again in epoch 3, which is a pattern also seen in the features at $\sim$−9500 km s^{-1} and $\sim$−18 500 km s^{-1}. Since there is a lot of blending of the Si IV components, the same effect was not as obvious in this ion. However, it was instructive to look at the behaviour of the modelled Gaussian Si IV doublets in Figure 4.5, where the same effect was apparent.

No part of the power-law continuum contributing to this spectrum was observable short-ward of Ly-α, however it was reasonable to expect that it extends in to the EUV portion of the spectrum (Kriss et al., 1999), which is largely responsible for the flux which controls the ionising fractions of the plasma in the accretion disc's environment. Therefore variability in the observed continuum could indicate variability in the ionising radiation from the accretion disc. There was evidence for an excess in the blue part of the spectrum during epoch 2 (first WHT observation) when compared to the prior and subsequent observations, as indicated in Figures 4.11 and 4.12, which could indicate that there was an increase in the ionising continuum flux at this epoch. At the 3rd epoch the blue excess seemed to have disappeared, with the flux in this range appearing to follow the continuum from epoch 1 once again.

Evidence from the CLOUDY simulations also supported an ionising continuum change driving the variability. Given the decrease in the Si IV column density between epochs 1 and 2, an increase in ionisation parameter must have occurred between these observations (See Figures 4.8 and 4.9), with an estimated log U change of $\sim$0.5 to $\sim$0.6 dex. An increase in log U agrees with the observed steepening of the continuum at the blue end of the spectrum between epochs 1 and 2, assuming the continuum extends to ionising energies. There was a large overlap in predicted Si IV column densities between epochs 2 and 3, however the epoch 3 range lay at the higher end of the epoch 2 range, with the best epoch 3 value having been 0.3 dex above the best epoch 2 value. A log U change of -0.2 dex was needed to drive this increase in Si IV column density between epochs 2 and 3. A decrease in ionisation parameter between these two epochs was supported by the apparent disappearance of the aforementioned blue excess in the continuum.

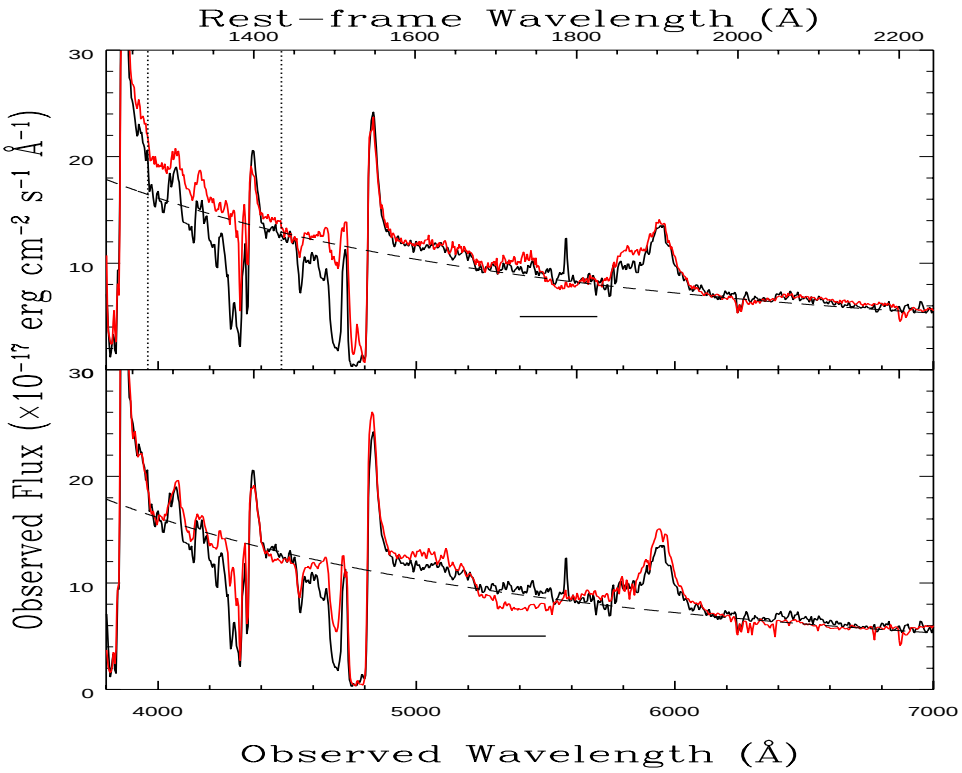

Figure 4.11: Upper panel: Epoch 1 observation (black line) and epoch 2 observation (red line) with power-law continuum (dashed black line) fitted to the epoch 1 spectrum. Vertical dotted lines indicate the boundaries of where the blue excess is apparent. The thick black horizontal line indicates the dichroic overlap region in the WHT observation. Lower panel: Same as upper panel but with red line indicating the epoch 3 observation.

4.5.3 Fourth Observation

The quasar SDSS J1138+3517 was observed again by the WHT in May 2014 and is included in Figure 4.3. In contrast to the earlier WHT observations, the Si IV components were largely unchanged from the previous epoch's spectrum. The deep C IV features centred at ~ -4500 and ~ -9500 km s^{-1} did not show changes comparable to previous variability when going from epoch 3 to epoch 4. However the weaker feature at $\sim -18\,500$ km s^{-1} showed a significant strengthening, with its profile becoming comparable to that of the epoch 1 observation. The absorption line centred at $\sim -13\,000$ km s^{-1}, which was very conspicuous at epoch 1 but almost unidentifiable at epochs 2 and 3, showed a slight increase in strength, however the significance of this change was only 1.08σ. Although these changes from epoch 3 to epoch 4 were in the weakest C IV components and therefore did not significantly change the minimum column density estimate made in epoch 3, the localisation in velocity space of this strength-

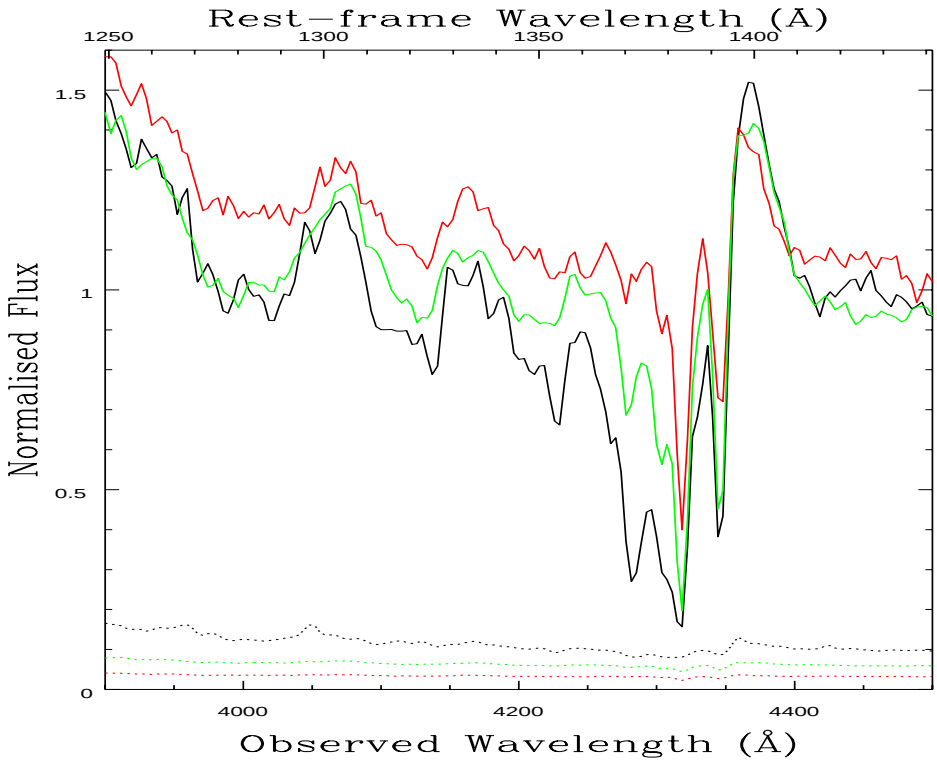

Figure 4.12: Epoch 1 observation (black), epoch 2 observation (red) and epoch 3 observation (green), normalised to the epoch 1 continuum shown in Figure 4.11 over the blue excess range, with dotted lines representing the errors. The epoch 2 spectrum appears to lie almost everywhere above the epoch 1 continuum.

ening to a range of $\sim$6000 km s^{-1} was interesting. If the increase in absorption was only considered to be significant in the stronger of the two features, then the region over which the change occurred was reduced to $\sim$4600 km s^{-1}. A single varying trough allowed for the possibility of a change in the covering fraction of the absorber to explain the phenomenon. This trough was also interesting in that it did not show as great a change between epoch 2 and 3 as the feature centred at $-$9500 km s^{-1}. This could have been due to either (a) the line being the result of a moderately saturated outflow whose peak trough depth describes the peak covering fraction, or (b) the outflow was located in a region where it was relatively shielded from the ionising continuum flux variations (the large velocity separation from the other troughs suggests it was in a physically distinct location).

4.6 Summary

The following summarises the conclusions that could be drawn from the investigation described in this chapter.

(i) When compared to large-sample statistical studies of BALQSOs (Filiz Ak et al., 2013, 2014; Wildy et al., 2014), BALs in SDSS J1138+3517 were exceptionally variable, especially in the 360 day rest-frame time interval between epoch 1 and epoch 2. When measuring BAL variability using the method of Filiz Ak et al. (2013, 2014), the most variable C IV BAL in this object underwent a change of ΔEW=−13.8 Å. When compared to Figure 29 of Filiz Ak et al. (2013), this change in ΔEW is far outside the range predicted by their random-walk model at an equivalent time interval. This could indicate that SDSS J1138+3517 belongs to a rare class of highly variable BALQSOs whose variability mechanism is not the same as that driving the random-walk behaviour observed in Filiz Ak et al. (2013).

(ii). When applying Gaussian fitting to model the Si IV outflows in Section 3.3, it was found that the components of individual doublets rarely exhibited the expected 2:1 blue to red optical depth ratio and also do not reach zero intensity at line centre. This suggested saturation of the blue component combined with spatially dependent line-of-sight optical depth.

(iii). The use of Gaussians to model absorption components allowed an estimate of the PPC-modelled Si IV column density in epoch 1, which was unavailable in Cottis (2010) due to the lack of unblended doublets at that epoch and that study's reliance on unblended pixel-by-pixel calculations to determine the PPC model column densities. The use of both blended and unblended absorption components facilitated a more accurate determination of the total Si IV column density when compared with Cottis (2010), yielding a best value approximately 40 percent higher.

(iv). There was no evidence for a change of covering fraction across the epochs when calculating C from the (Gaussian modelled) doublets representing the two deepest absorbers, suggesting line-of-sight covering fraction changes were not the dominant mechanism driving the absorption line variability. However the weak C IV feature centred at $\sim$−18 500 km s^{-1} may have undergone a covering fraction change between epochs 3 and 4.

(v). There was evidence that ionisation changes played a significant role in the variability, most notably from the coordinated changes in both Si IV and C IV absorption troughs separated widely in velocity space. There was also a hint that the ionising flux may have increased in epoch 2, given the apparent steepening of the continuum in the blue part of the spectrum. This conclusion would be supported if AGN have steeper α_{ox} at higher luminosities as indicated in Vignali et al. (2003). The photoionisation simulations were consistent with this scenario, since the column densities of both ions decreased with increasing ionising parameter in the log U range spanned by the outflow. The best values for the changes in ionising parameter were within the scope of quasar EUV variability.

(vi). The location of the inner face of the outflowing gas was not well constrained, being located between approximately 0.1 and 200 parsecs from the continuum source. This range placed it somewhere in a region spanning the BLR radius to narrow line region distances. However, the lowest velocity (and deepest) C IV trough must have been absorbing both BLR and continuum emission, meaning that this outflow was located outside the BLR. Given the width of the absorption components, which were substantially less than BLR widths, and the value of R_{BLR}, it seems likely that the inner face was at least $\sim$1 parsec from the continuum source.

(vii). The magnitude of the mass outflow rate could have been a substantial fraction of or even exceeded the mass accretion rate. However due to the uncertainties on R, strong constraints on the true value of the mass outflow rate were not achieved. The derived kinetic luminosity range of $\sim 3.3 \times 10^{42}$ to 6.6×10^{44} erg s^{-1} indicated that feedback effects such as quenching of star formation may have been possible if the true value was near the upper limit of this range.

Chapter 5

Physical properties and the variability mechanism of the He I outflow in NGC 4151

This chapter investigates the absorption lines resulting from the absorption of photons at 3889 and 10 830 Å by helium atoms in the 2^3S state, as well as that due to the transition from the singlet state (2^1S) at 20 587 Å. A diagram showing helium energy levels and the aforementioned transitions is illustrated in Figure 5.1.

The results of this investigation are used to attempt to identify the variability mechanism and constrain the absorber properties. To our knowledge this is the first attempt to examine an AGN outflow using absorption from all three of the aforementioned transitions. As mentioned in Chapter 1, previous studies have observed absorbers in this object in the optical and UV portions of the spectrum. This Chapter therefore compares the helium absorber to these previously studied features.

5.1 NGC 4151 observations

Five spectra of NGC 4151 in both the NIR and optical wavebands were observed quasi-simultaneously in the years 2004–2010. The wavelengths in each waveband were chosen to span the He I* emission

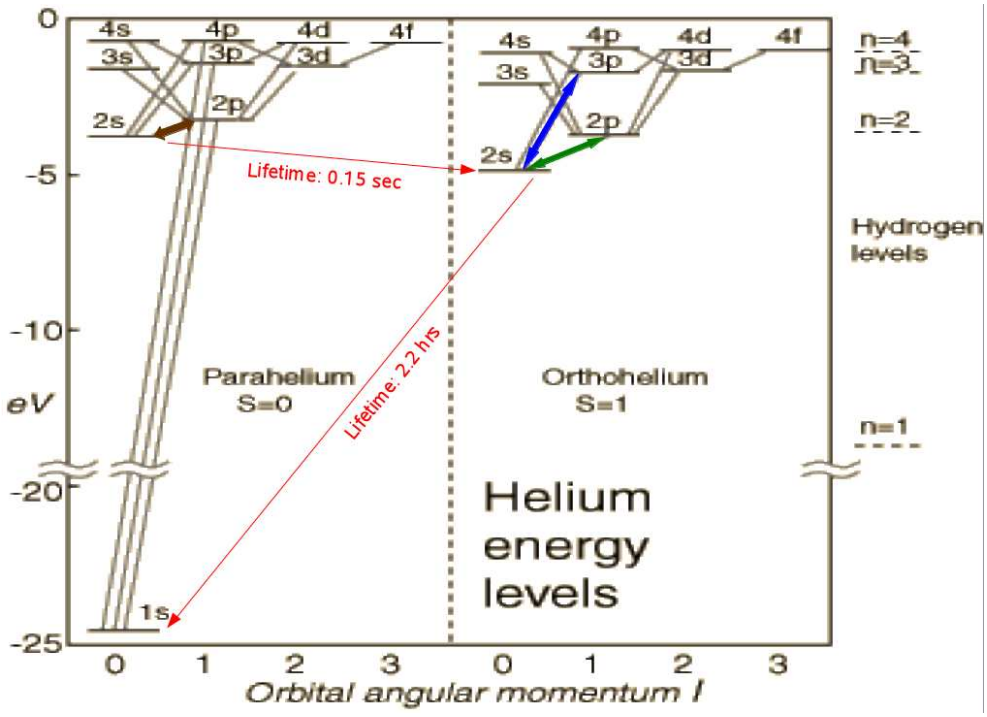

Figure 5.1: A diagram of the energy levels in the helium atom. Levels in both parahelium ($S = 0$) and orthohelium ($S = 1$) are shown. The double headed arrows indicate the transitions of interest (both absorption and emission). Each arrow is colour coded, with the 3889 Å transition in blue, the 10 830 Å transition in green and the 20 587 Å transition in brown. Red arrows indicate the transitions leading to the depopulation of the two metastable states, with their lifetimes described in red text. *Image adapted from:* HyperPhysics by Rod Nave, Georgia State University.

and absorption features resulting from the components at 3889 Å and 10 830 Å. The observation dates and rest-frame time intervals for these observations are provided in Table 5.1. The near-IR spectroscopy was obtained with the SpeX spectrograph at the NASA IRTF in the short cross-dispersed mode (SXD, $0.8 - 2.4$ μm). All data except those from 2010 were obtained through a slit of $0.8 \times 15''$ giving an average spectral resolution of full width at half maximum (FWHM) $\sim$ 400 km s^{-1}. A narrower slit of $0.3 \times 15''$ was used for the 2010 epoch. The three epochs spanning the years $2004 - 2007$ were presented in Landt et al. (2011), with the 2004 observation also discussed in Landt et al. (2008). The NIR spectra from 2002 and 2010 were originally presented in Riffel et al. (2006) and Schnülle et al. (2013), respectively. The optical spectra were obtained with the FAST spectrograph at the Tillinghast 1.5 m telescope using the 300 l/mm grating and a $3''$ long-slit. This set-up resulted in a wavelength coverage of $\sim 3720 - 7515$ Å and an average spectral resolution of FWHM $\sim$ 330 km s^{-1}. Except for the 2004 data, all spectra were observed at a very low airmass ($\sec\ z \sim 1.05$). At such a low airmass

Table 5.1: Dates and rest-frame time intervals for observations obtained of NGC 4151. *Top panel*: optical observations. *Bottom panel*: near-infrared observations.

Epoch	Observation Date	Δt_{qrest} (days)
1	11 Apr 2002	0
2	28 May 2004	775
3	29 May 2006	1504
4	09 Feb 2007	1759
5	18 Feb 2010	2860
1	23 Apr 2002	0
2	23 May 2004	758
3	12 Jun 2006	1505
4	24 Jan 2007	1730
5	27 Feb 2010	2856

Δt_{qrest} is AGN rest-frame time interval since epoch 1

the effects of atmospheric differential refraction, where the atmosphere disperses different wavelengths to different extents resulting in an apparent difference in position of the object at different wavelengths, is not significant. In cases of high airmass, differential refraction effects can be mitigated by rotating the slit so that its long axis is aligned with the parallactic angle. The May 2004 spectrum was observed at an airmass of $\sec\ z \sim 1.3$ and so the flux loss due to atmospheric differential refraction at the slit rotation (position angle of 70°) was expected to be $\sim 20\%$ at the observed wavelength of He I* λ3889 relative to that at wavelengths ≥ 5000 Å (Filippenko, 1982).

5.2 The spectrum of NGC 4151

5.2.1 Spectral adjustments and continuum fitting

After both the NIR and optical images were reduced and the spectra extracted, small additive wavelength shifts were made in both wavebands to account for differences in wavelength calibration across the epochs. These adjustments were made to align the spectra with narrow absorption features present in the epoch 2 spectrum. A straight line was fitted to relatively line-free regions on either side of the optical He I* emission+absorption region (3770 Å–3790 Å and 4030 Å–4050 Å) to approximate the continuum emission. After subtraction of this continuum, in order to account for small differences in resolution and slit position, the optical spectra were convolved with Gaussians of appropriate FWHM and scaled to match both the resolution and line flux of the narrow forbidden line [Ne III] λ3968 in the epoch 2 observation, the output spectra having an average wavelength bin width of 1.47 Å. Upon examination of the spectral region bracketed by the wavelength bands used for continuum fitting and comparing to the I Zw 1 Fe II template obtained from Véron-Cetty et al. (2004), it was determined that emission from Fe II was negligible in this region.

A similar procedure was followed for the NIR spectral region near metastable He I* λ10 830. A combination of power-law and blackbody models was fitted to each epoch in relatively line-free wavelength bands to generate a continuum model. These bands spanned 8670–8730 Å, 9400–9450 Å, 9720–9770 Å, 10 350–10 400 Å, 11 500–11 600 Å and 12 100–12 200 Å. The model continuum was subtracted and the spectra were matched to the resolution and flux of the narrow forbidden [S III] λ9533 line from the epoch 2 observation using the same Gaussian convolution method described for the optical observations, with an average output sampling of 2.77 Å per wavelength bin between 8000 Å and 13 000 Å. Blue-shifted absorption was also seen arising from the metastable He I λ20 587 transition, therefore a linear continuum was fitted to relatively line-free spectral regions either side of the line in the bands 19 800 Å–19 880 Å and 20 840 Å–20 915 Å, avoiding the H_2 emission features located at 19 570 Å, 20 332 Å and 21 213 Å (Rodríguez-Ardila et al., 2004). The spectral region spanned by the continuum fit near the He I λ20 587 line had a wavelength bin size of $\sim$5 Å ($\sim$78 km s^{-1}).

Scaling to narrow lines was considered to be a suitable method for ensuring the measured flux was consistent across the observational epochs since the narrow line region of AGN occupies a very large

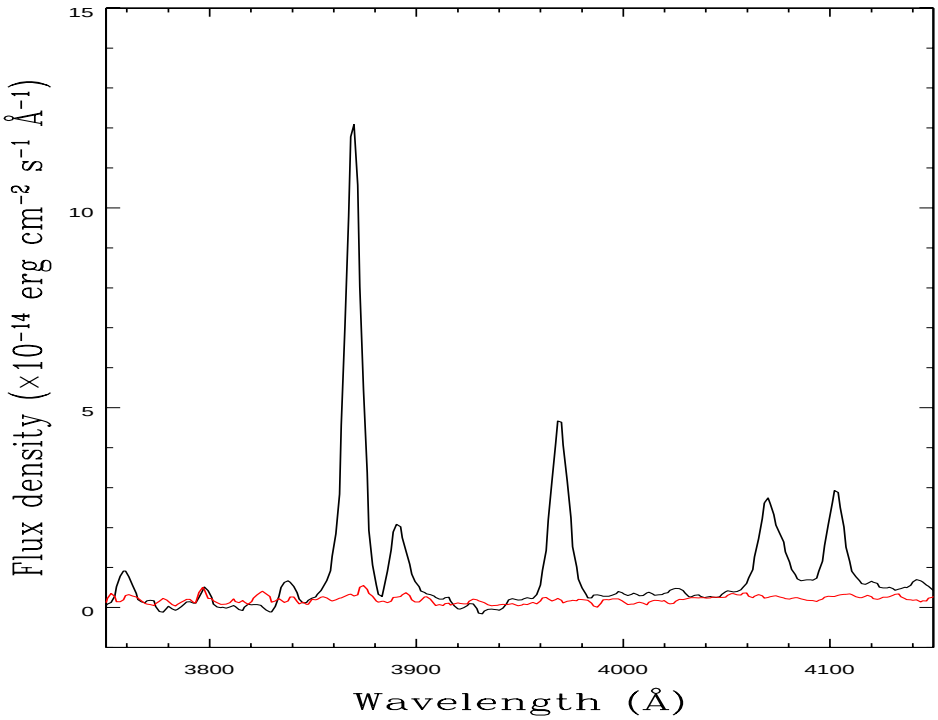

Figure 5.2: An RMS continuum-subtracted optical spectrum (red line) and mean spectrum (black line) of NGC 4151 in the region of the He I* λ3889 line.

spatial region (see Chapter 1). This implies that an individual narrow emission line would not be able to respond to ionisation or large scale geometry changes of the NLR on the epoch separation timescales examined in this chapter. This hypothesis was supported by the generation of continuum-subtracted RMS spectra of both the optical and NIR observations, which indicated minimal changes (the total RMS-spectrum flux in the S III λ9069 line is $\sim$10 percent of the multi-epoch mean spectrum) in narrow emission line strength across the observational epochs. An RMS spectrum (F_{rms}) can be calculated, at each wavelength bin, using:

$$F_{rms} = \sqrt{\sum_{i=1}^{n} \frac{(F_i - F_{mean})^2}{n-1}}\,, \tag{5.1}$$

where i is the epoch of observation, F_i is the flux at epoch i, n is the total number of epochs and F_{mean} is the multi-epoch mean flux. The resulting RMS spectra are shown in Figures 5.2 and 5.3 for the optical and NIR observations respectively.

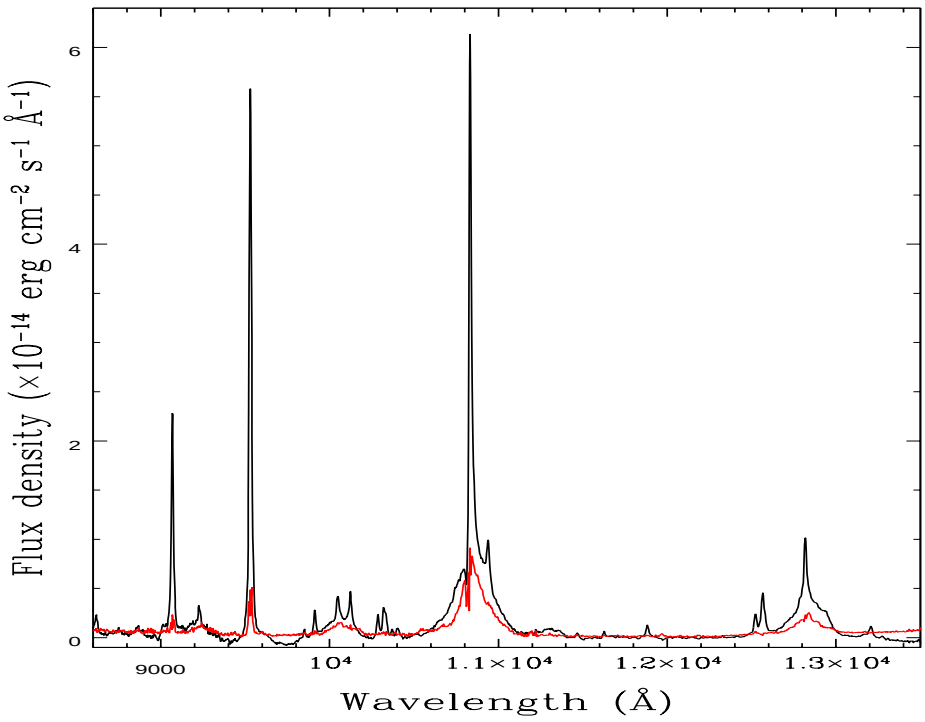

Figure 5.3: An RMS continuum-subtracted NIR spectrum (red line) and mean spectrum (black line) of NGC 4151 in the region of the He I* λ10 830 line.

A contribution to the spectral flux, especially in the optical part of the spectrum, was from the host galaxy. Since host galaxy contribution to an AGN spectrum is constant while the AGN continuum varies (especially in a highly variable object such as NGC 4151) the relative contribution of the AGN continuum compared to the galactic continuum to the total flux in the spectrum will vary. In cases where the AGN continuum flux exceeds that of the galactic continuum, it can be said that the spectrum is 'AGN dominated'. In cases where it is not AGN dominated, a power-law component plus black-body emission from dust in the NIR, representing the emission from the central engine and the torus, will not be a good fit to the continuum level across the optical to NIR parts of the spectrum. From Figure 5.4 it appears that NGC 4151 is AGN dominated in the epoch 5 and possibly the epoch 1 spectrum. Epoch 5 was also the observation with the strongest continuum flux, with other epochs having too weak an AGN continuum contribution to be AGN dominated.

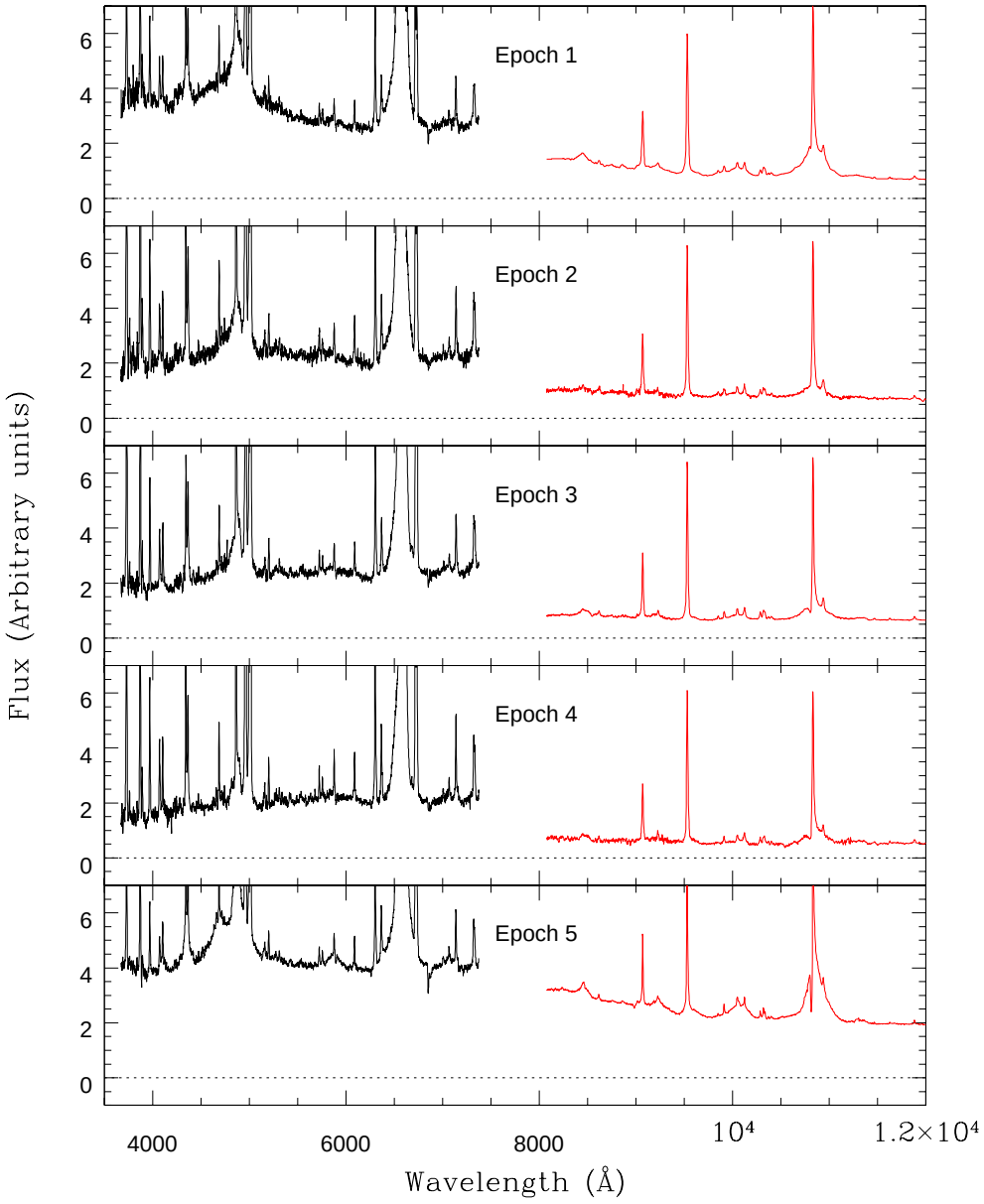

Figure 5.4: The spectra at each of the five observational epochs of NGC 4151 spanning the optical (black line) to NIR (red line) portions of the spectrum. The gap in coverage between 7370 Å and 8070 Å was not covered by either the Tillinghast (optical) or IRTF (NIR) observations.

5.2.2 The unabsorbed spectrum

Reconstruction of the unabsorbed spectrum was necessary in order to measure the depth of the absorption features. This process was complicated by the overlap of emission from several different sources, namely the continuum, the broad line region (BLR) and the NLR. In order to reconstruct the BLR emission, templates were taken at each epoch from the broad component of the relatively unblended Paβ line. This line was blended with narrow forbidden lines and a He I narrow+broad feature at 12 531 Å. The broad component of Paβ in the epoch 2 spectrum appeared weaker than at all other epochs and in this weak state the broad component could be readily modelled as a single Gaussian of FWHM 6200 km s^{-1}. Therefore to isolate the broad component across all epochs the continuum was first subtracted from the epoch 2 spectrum. The narrow forbidden lines were modelled with Gaussians of FWHM 450 km s^{-1}, while the Paβ narrow component was modelled with 2 Gaussians. The He I λ12 531 line, which was found to not vary significantly across the epochs, was modelled with two Gaussians. A blend of Fe II lines was modelled as a single broad Gaussian at 13 197 Å. The Paβ spectral region along with the model fit is shown in Figure 5.5.

By subtracting off the narrow forbidden lines (which do not vary), the He I λ12 531 line and the narrow component of Paβ, the broad component of Paβ remained. Using the fact that the narrow lines do not vary across the epochs, the epoch 2 forbidden line and Paβ narrow component Gaussian models and the epoch 2 He I λ12 531 Gaussian model were all subtracted from all other Paβ blends, leaving only the broad components at each epoch. These broad components were then interpolated and scaled to provide templates for the broad components of the metastable helium lines both in the NIR and optical spectra.

As with the Paβ line, the broad component of the He I* λ10 830 line was found to be in a weak state during epoch 2 and could therefore be modelled by a single Gaussian. This line was blended with the Paγ line which consists of a narrow component and a weak broad component which was undetectable in the epoch 2 spectrum. For this epoch, the spectrum was fitted with a broad Gaussian together with a narrow Gaussian for the Paγ line. These lines were then subtracted off to reveal the narrow component of the He I* λ10 830 line. The epoch 2 Paβ and Paγ narrow components were then subtracted from the He I* λ10 830 blend at every epoch, leaving only the broad components. After interpolation into the wavelengths spanned by the λ10 830 line, the Paβ broad component was scaled to the broad component at each epoch in the region 1000 to 1200 km s^{-1} red-ward of the He I* line centre. A small contribution

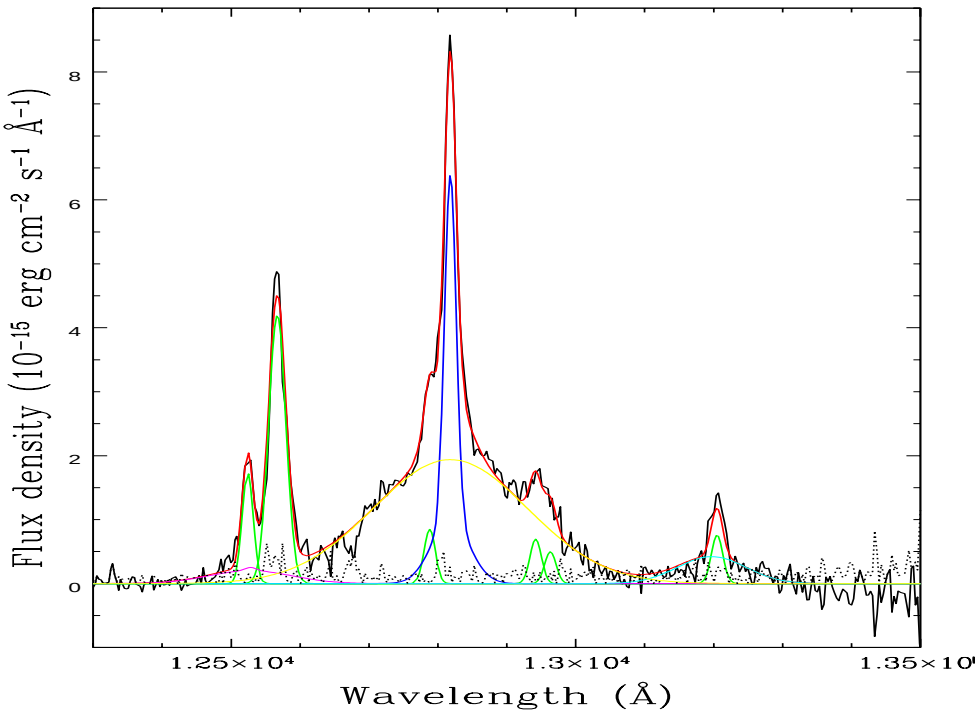

Figure 5.5: Continuum-subtracted epoch 2 spectrum (black) and total emission model (red) in the Paβ spectral region. The Paβ broad and narrow components are shown in yellow and blue respectively. Narrow emission lines are in green, while the broad He I component is in magenta and the Fe II blend is in cyan. The dotted black line indicates the residuals between the total model and the spectrum.

from the broad component of the Paγ line was modelled by interpolating and scaling the Paβ broad component to the remaining difference between the model Paβ broad component and the narrow-line subtracted spectrum in the region 1000 to 2400 km s^{-1} red-ward of the He I* line centre. By adding together the continuum, the narrow and the broad component, a reconstruction of the unabsorbed profile in the He I* λ10 830 spectral region was generated at each epoch (see Figure 5.6).

A similar procedure was adopted in order to generate the unabsorbed reconstruction in the spectral region near He I* λ3889. First, the continuum was subtracted at each epoch. The reconstructed broad component of the He I* λ10 830 line was then interpolated into the wavelength space of the optical line and scaled to the region 3905 to 3920 Å and then subtracted from the spectrum. The narrow component of the He I* λ10 830 line line was interpolated, scaled and Gaussian blurred to match the resolution of the [Ne III] λ3869 line and then scaled and interpolated onto the remaining narrow component of He I* λ3889 in the range 3890 to 3900 Å. Reconstructing the emission near the optical

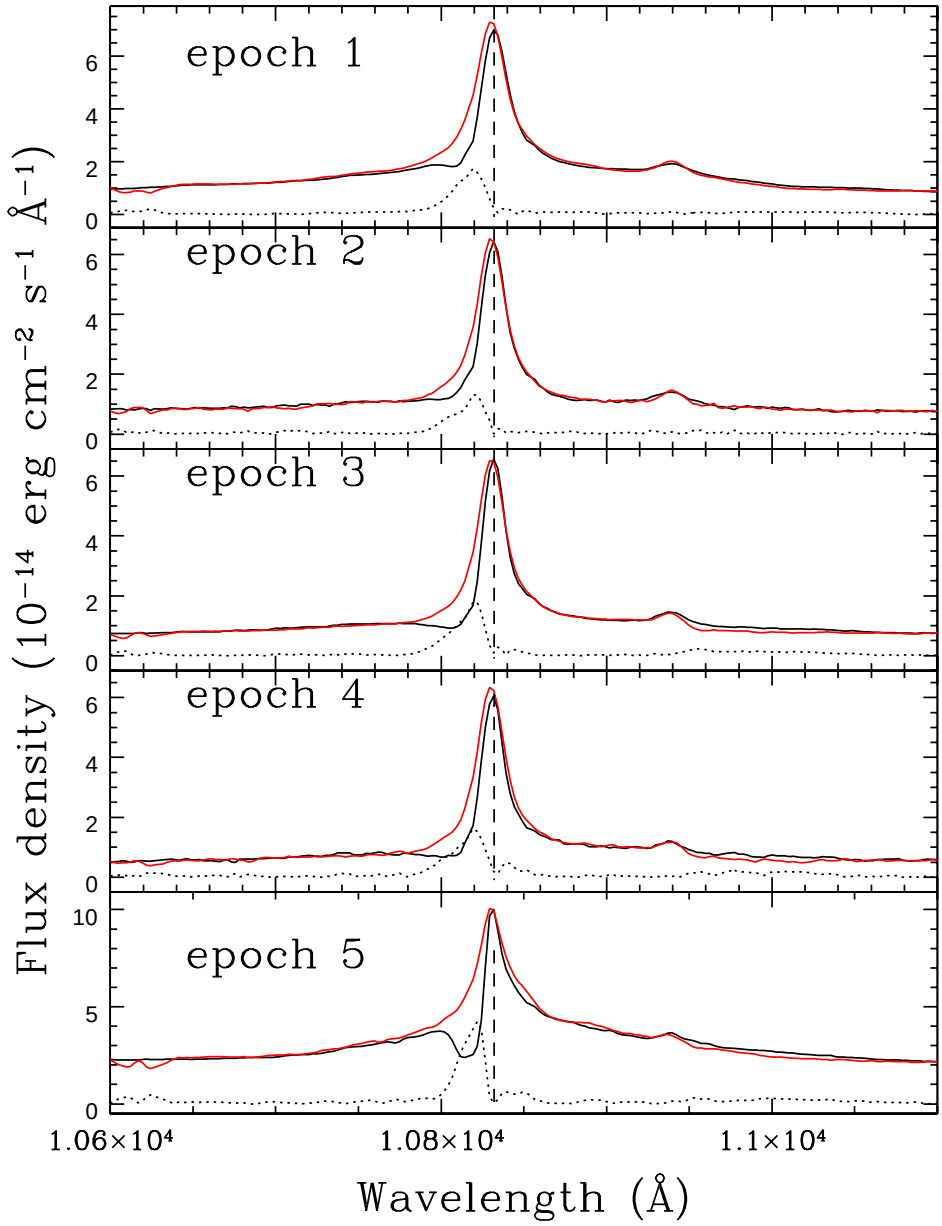

Figure 5.6: Observed spectrum (solid black line) and unabsorbed reconstruction (solid red line) in the spectral region near He I* λ10 830 (line centre indicated by the black vertical dashed line). Residuals are indicated by the dotted black line.

He I* line was complicated by the presence of the [Ne III] λ3968 line, whose line centre is located at ≈ -1550 km s^{-1} relative to the helium line centre and therefore may be affected by the blueshifted absorption. The epoch 5 line was used as a template for all epochs due to the narrowness of the absorption (see Figure 5.10) and hence minimal overlap with the [Ne III] emission line in that spectrum. To generate the reconstructions, the continuum was added to the scaled narrow and broad components of the He I* line and the epoch 5 [Ne III] template at each epoch. These reconstruction are shown in Figure 5.7. It should be noted that all previous unabsorbed-profile reconstruction methods assume that the Paβ, Paγ and the two He I* lines have broad emission components which vary little in their spectral profile. This is probably a safe assumption as all of these lines can form in regions covering a large range in ionisation parameter.

Reconstructing the unabsorbed flux in the spectral region of He I λ20 587 was performed by subtracting the continuum from the epoch 2 spectrum and interpolating the narrow H_2 λ21 213 emission line into its wavelength space, which was then scaled to the He I emission line peak. This scaled narrow component was then added to the continuum at each epoch to create the unabsorbed spectra. The broad component of this weak line was not apparent at any epoch and therefore was not considered in the reconstruction. The continuum normalised reconstruction and observed spectrum are illustrated in Figure 5.8.

For the purposes of subsequent calculations involving normalised absorption line profiles, the errors on the He I* $\lambda\lambda$3889,10 830 reconstructed profiles were assumed to be equal to the standard deviation of the difference between the reconstruction and the fitted spectrum in the emission line scaling regions, except in the optical [Ne III] λ3869 overlap region extending from ≈ -1800 to -700 km s^{-1} relative to the He I λ3889 line centre, where the standard deviation between the spectrun and the model in that region is found and added in quadrature to that obtained from the He I* scaling region. For the errors on the He I λ20 587 reconstructions, the values were assumed to be the standard deviation of the difference between the unabsorbed profile and the observed spectrum in the region $0 \leq v \leq 500$ km s^{-1} red-ward of the emission line centre.

5.2.3 Triplet state metastable helium column densities

The column density of helium in the 2^3S metastable state was found by normalising the observed spectra to the unabsorbed reconstructions. A method similar to that adopted by Leighly et al. (2011) was

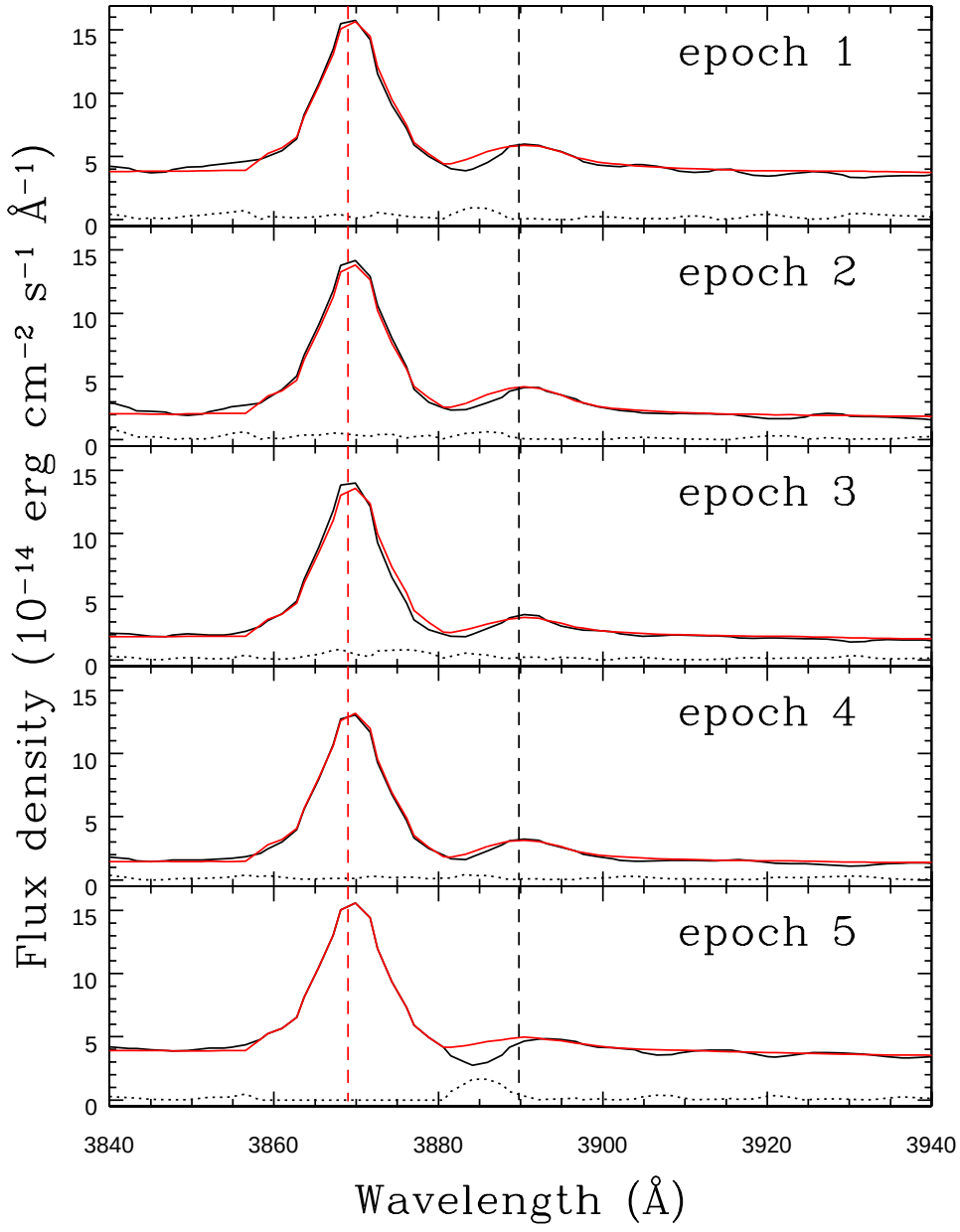

Figure 5.7: Observed spectrum (solid black line) and unabsorbed reconstruction (solid red line) in the spectral region near metastable He I* λ3889 (black vertical dashed line indicates line centre). The nearby [Ne III] λ3869 line centre is indicated by the vertical dashed red line. Residuals are indicated by the dotted black line.

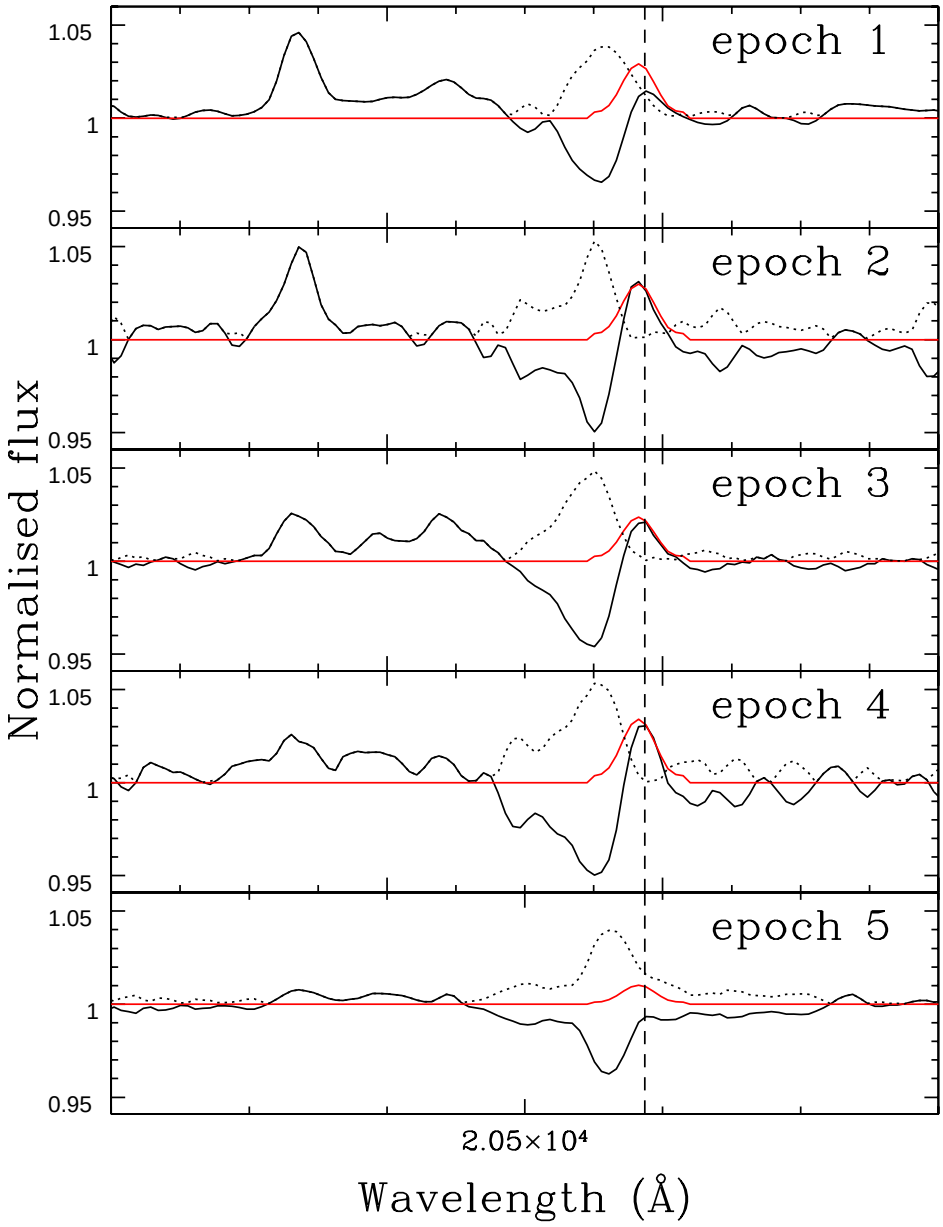

Figure 5.8: Continuum-normalised observed spectrum (solid black line) and unabsorbed reconstruction (solid red line) in the spectral region near He I λ20 587 (line centre indicated by the vertical black dashed line). The dotted black line indicates the normalised continuum+residuals.

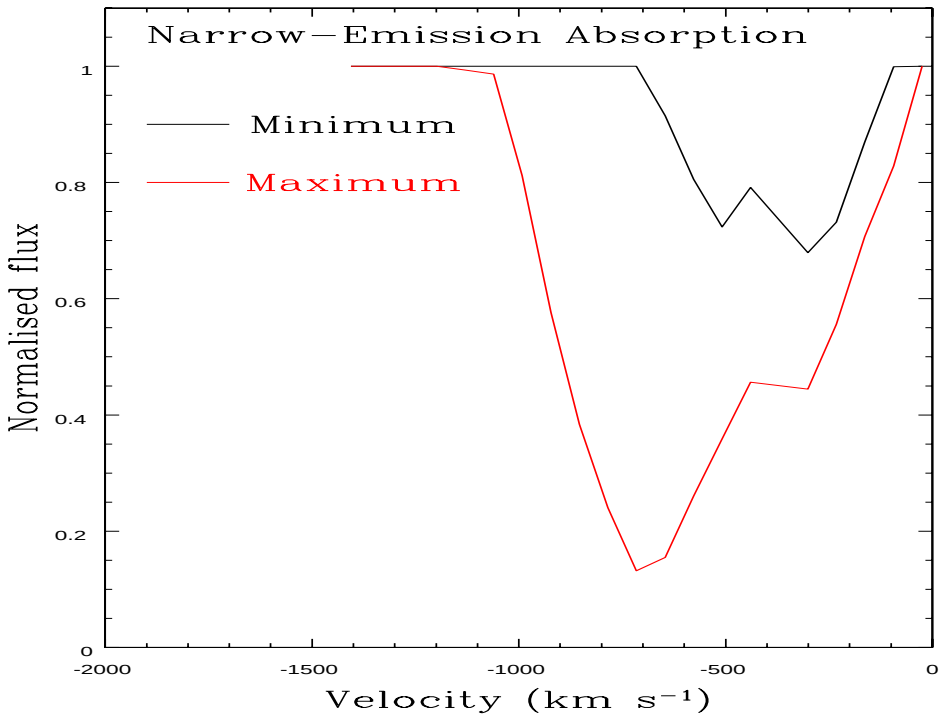

Figure 5.9: Maximum and minimum curves of possible NLR absorption derived from the spectral region near He I* λ10 830.

used, applying a pure partial coverage model (PPC) to the optical and NIR metastable He I* absorption doublet components. This had the advantage of allowing column densities to be calculated without deconvolving the absorption of individual emission components (such as NLR, BLR and continuum) and their covering fractions, since both doublet components arise from the same gas. This solution was reinforced by evidence from the NIR spectra that at least some of the NLR was absorbed, which was found to be the case after comparing the absorption depth to the combined BLR and continuum strengths. It was also possible to derive a maximum NLR absorption curve, although in reality it is likely that the true amount of NLR absorption was closer to the minimum value than the maximum given its spatially-extended nature. These curves are applicable across the entire range of observational epochs as it was assumed that a NLR absorber would not undergo significant changes on the timescale sampled. The maximum and minimum NLR absorption curves are indicated in Figure 5.9.

Although the investigation of Leighly et al. (2011) also included a power-law inhomogeneous model in addition to PPC, this yielded column densities not significantly different from the PPC model in that study and hence it was not used in this investigation. The PPC model was originally applied to quasar

absorption lines (Hamann et al., 1997; Arav et al., 1999) and relates the observed flux density within an individual wavelength bin to the total flux from the emission source and the covering fraction as follows:

$$\frac{I_{\rm app}}{I_0} = Ce^{-\tau} + (1 - C) \ , \tag{5.2}$$

where $I_{\rm app}$ is the apparent flux, I_0 is the flux from the emission region, C is the fraction of the total emission covered by the absorber and τ is the optical depth. In order to compare the normalised depth of each doublet component, the normalised NIR absorption line spectrum was interpolated into the velocity space of the normalised optical spectrum with velocity bin width of $\sim$110 km s^{-1} and both spectra smoothed using a 3-pixel moving average. By taking into account the 23.3 times greater optical depth of the NIR component as compared to the optical component, the doublet strengths could be compared using the equation

$$\left(\frac{I_{\rm op} - 1}{C} + 1\right)^{23.3} - \frac{(I_{\rm IR} - 1)}{C} - 1 = 0 \, , \tag{5.3}$$

where $I_{\rm op}$ and $I_{\rm IR}$ are the normalised fluxes of the optical and NIR components respectively. It was clear from the normalised absorption profiles at each epoch (see Figure 5.10) that the NIR component was saturated, since the predicted profiles of the optical absorption using the NIR profiles and the theoretical 23.3:1 optical depth ratio (indicated by the magenta line) significantly underestimated the absorption strength of the observed optical profiles.

The calculation of column density depended on finding a solution for C in Equation 5.3. Since this equation has no analytic solution, a numerical test was performed by varying C in steps of 0.001 between 0 and 1 at each velocity bin, with the value closest to the true solution adopted as the value of C. Errors on C at each velocity bin were found by calculating the standard deviation of test values of C resulting from values of $I_{\rm op}$ and $I_{\rm IR}$ in equally spaced intervals of 1 percent of the total range between the lower limit and upper limit of the calculated $I_{\rm op}$ and $I_{\rm IR}$ values. Once found, the value of C at each velocity bin could be used to find the total column density as follows:

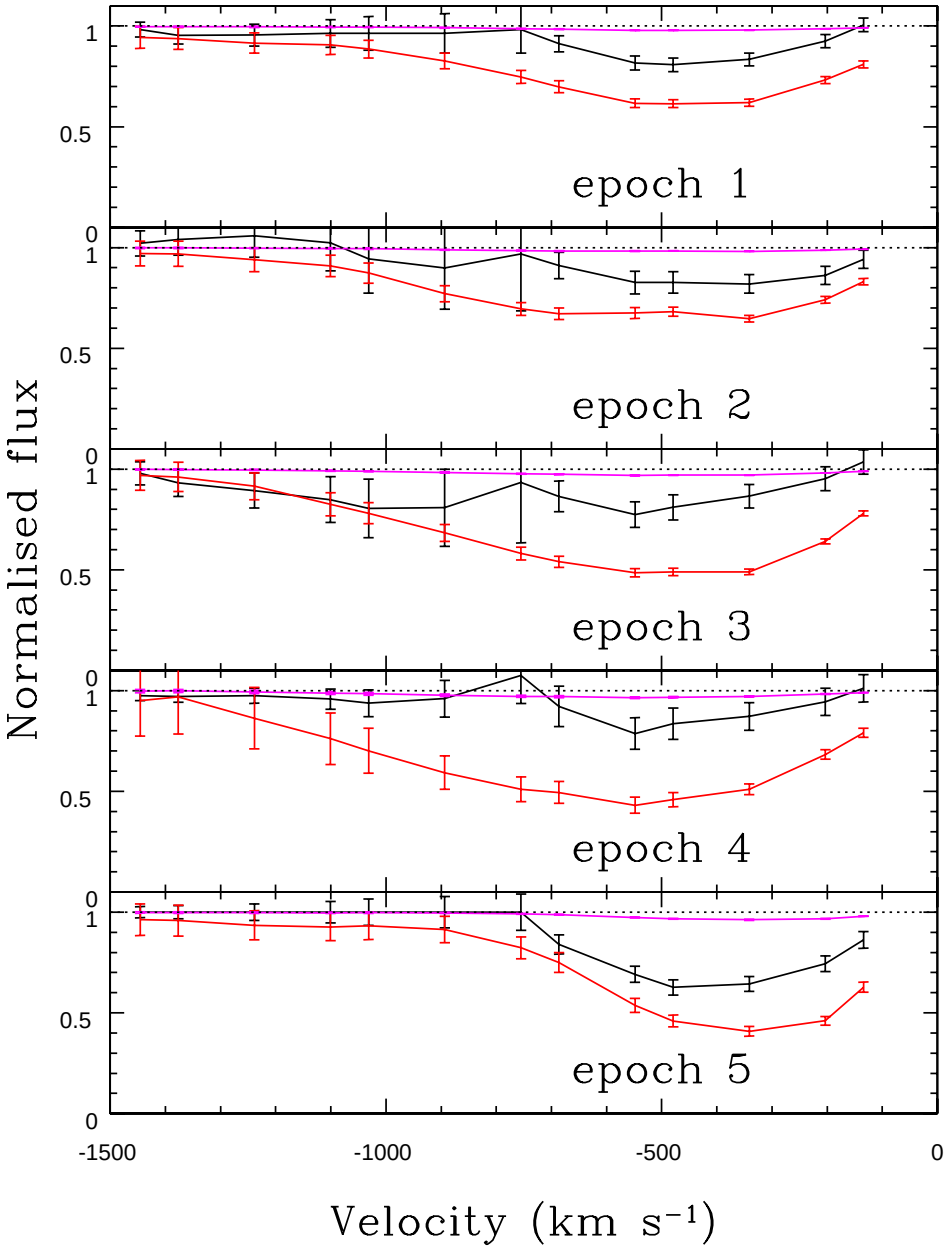

Figure 5.10: Normalised absorption profiles of the optical (black) and NIR (red) components of metastable He I*. The NIR component-predicted optical absorption profiles (magenta) are much weaker than the observed profiles at certain velocities, indicating that the NIR component is saturated at those velocities. Errors are calculated from the line fitting regions.

$$N_{\rm ion} = \frac{m_{\rm e} c}{\pi e^2 f \lambda} \int \tau\left(v\right) C\left(v\right) dv\,, \tag{5.4}$$

where $N_{\rm ion}$ is the column density, $m_{\rm e}$ is the electron mass, c is the vacuum speed of light, e is the elementary charge, f is the oscillator strength of the transition and v is the absorber velocity (negative values indicate outflows). To be physically realistic, two conditions regarding the optical and NIR components' residual intensity must be satisfied. First, the residual flux of the optical component at each velocity bin must be greater than or equal to the residual flux of the NIR component due to that component's greater theoretical optical depth. Second, the NIR component residual intensity must be greater than or equal to that of the optical component raised to the power 23.3, since the optical component (being 23.3 times lower in theoretical optical depth) is equal to the NIR component when raised to the power 23.3 in the case where the NIR component is unsaturated, with any degree of saturation resulting in $I_{op}^{23.3}<I_{IR}$. These two conditions can be summarised in the inequality $I_{\rm op}\geq I_{\rm IR}\geq {I_{\rm op}}^{23.3}$. Due to the relatively large error bars on the optical normalised fluxes in the overlap region of the [Ne III] λ3869 emission line (blue-ward of ≈-700 km s^{-1}), this condition was not always satisfied in that region.

To estimate the column density and its limits, a combination PPC and direct integration of the He I* λ10 830 profile were employed as follows: (a) at each epoch an upper limit to the column density was found by propagating the error through the PPC calculation over the entire absorption region (≈-1500 to 0 km s^{-1}), (b) a best fit value of the column density was found using the PPC model over the part of the trough which was deepest and that did not overlap with the [Ne III] emission line (≈-700 to 0 km s^{-1}) and adding this value to the column density predicted using a simple (not PPC) integration of the NIR profile in the region (≈-1500 to 700 km s^{-1}), and (c) the lower limit was found by adding in quadrature the errors in the two regions described in (b). Instances of ${I_{\rm op}}^{23.3}>I_{\rm IR}$ were calculated by assuming ${I_{\rm op}}^{23.3}$=$I_{\rm IR}$. The results are shown in Table 5.2.

5.2.4 Singlet state helium column densities

Using the unabsorbed reconstructions in the spectral region of the He I λ20 587 line (Figure 5.8), a minimum value of the column density in this state could be estimated from the normalised spectral profile of the absorbed region. Before calculations were performed, these normalised spectra were

Epoch	He I* column density ($\times 10^{14}$ cm^{-2})	He I* column density upper limit ($\times 10^{14}$ cm^{-2})	He I* column density lower limit ($\times 10^{14}$ cm^{-2})
1	2.17	3.22	1.65
2	2.40	3.73	1.93
3	4.47	11.5	1.63
4	1.83	4.09	1.38
5	4.27	4.81	4.26

Table 5.2: Column densities for helium in the metastable 2^3S state. Upper and lower limits are 1-sigma from the reported value.

smoothed using a 3-pixel moving average. The profiles are shown in Figure 5.11.

Since this transition is a singlet, only a lower limit for the column density could be obtained using direct integration of the profile, which would be found to be an underestimate of the column density if partial coverage and saturation are present (Savage & Sembach, 1991). The lower limits of the 2^1S column density for each epoch were obtained from

$$N_{\rm ion} = \frac{m_{\rm e}c}{\pi e^2 f \lambda} \int \tau\left(v\right) \, , \tag{5.5}$$

providing the values listed in Table 5.3.

5.2.5 Balmer Absorption

Balmer absorption was detected in NGC 4151 by Hutchings et al. (2002) arising from the Hβ transition. In Leighly et al. (2011), the lack of Balmer absorption in the quasar FBQS J1151+3822 was used to place an upper limit on the n=2 hydrogen state column density. The spectral region of Hβ in each of the five epochs studied in this chapter was examined to determine whether or not Hβ absorption was present. To allow for the construction of the unabsorbed profile, a linear continuum fit to relatively line-free regions either side of this line (4150–4200 Å and 5450–5500 Å) at each epoch was removed. A small contribution from the Fe II emission to the flux in the subtracted spectra was removed by scaling the Véron-Cetty et al. (2004) iron template to the Fe II blend at $\sim$5533 Å and subtracting the scaled

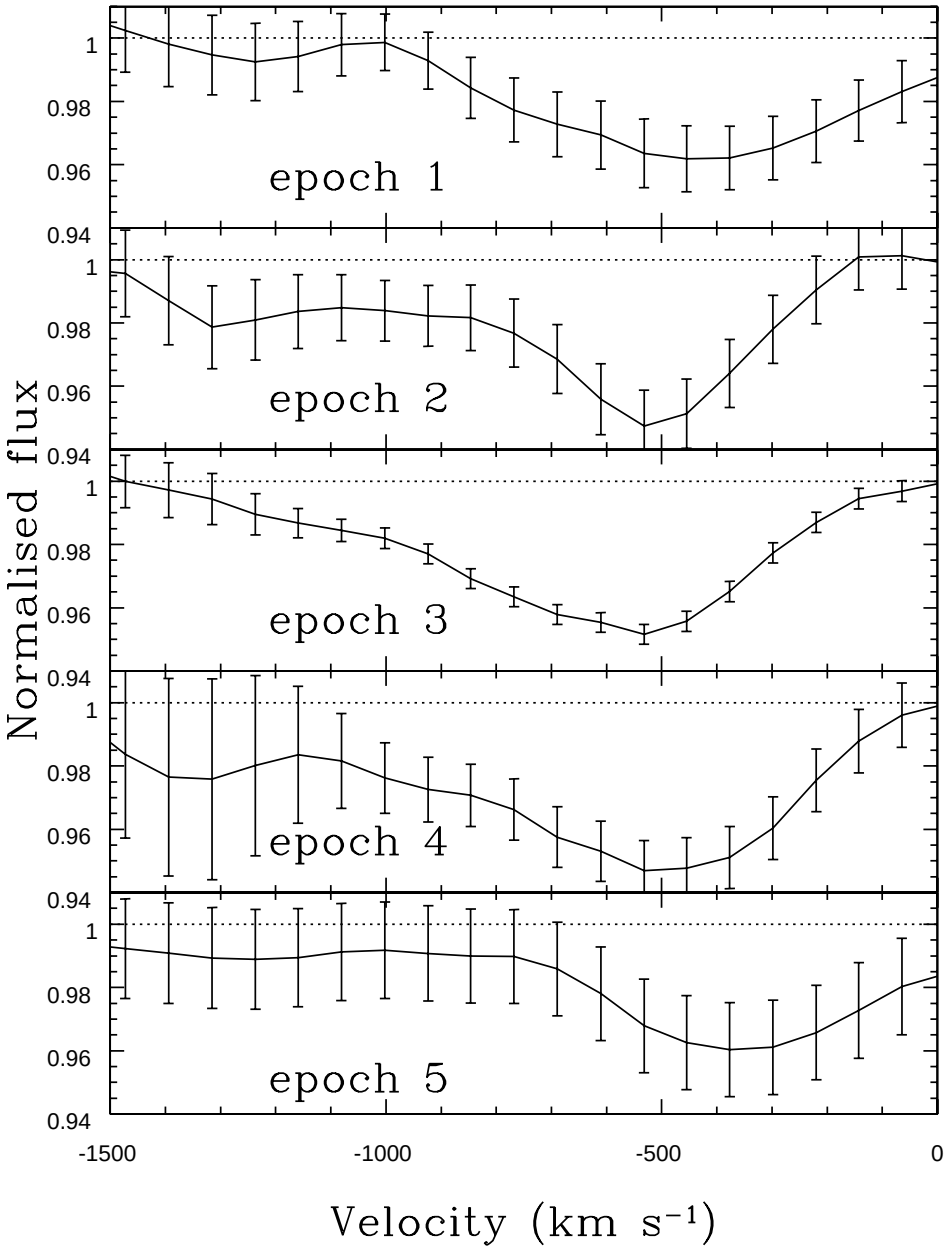

Figure 5.11: Normalised absorption profiles for the He I λ20 587 transition. Errors are calculated by propagating the error on the unabsorbed reconstructions as described in Section 5.2.2

Epoch	He I 2^1S column density ($\times 10^{12}$ cm^{-2})
1	1.32±0.18
2	1.58±0.16
3	1.60±0.08
4	2.16±0.29
5	1.39±0.26

Table 5.3: Minimum column densities for helium in the 2^1S state.

template from the spectrum.

To reconstruct the emission lines in the Hβ blend, the broad emission lines needed to be removed first to leave a template for the narrow components of the Balmer, He II and [O III] (at 4959 and 5007 Å) emission lines. As before, epoch 2 was ideal for this purpose, due to its weak and symmetrical broad emission line profile in Hβ and very weak He II λ4686 broad emission. The epoch 2 Paβ broad emission line (isolated in Section 5.2.2) was interpolated into the wavelength space of the Hβ line and scaled to the emission in the region 4880 to 4900 Å. No absorption was apparent. Furthermore, when the broad component was subtracted off and the narrow component inverted about the line centre, the inverted profile followed the original narrow line profile very closely, showing no evidence for absorption (see Figure 5.12 top panel).

To generate the unabsorbed templates for epochs 1,3 and 4; the Paβ broad emission line was scaled to the broad component of Hβ and the narrow emission line contribution isolated in epoch 2 was added back on. A contribution from the broad component of the He II λ4686 emission line was added by interpolating and scaling the Paβ broad component to this line at each epoch. The spectra and their reconstructions are shown in Figure 5.12 (middle panel). Due to the complexity of the emission no attempt was made to reconstruct the narrow blends in epoch 5. However, isolation of the broad component strongly suggested no presence of absorption (Figure 5.12 lower panel).

In addition to the Balmer lines, absorption arising from the He I transitions at 4473 Å, 5878 Å and 7067 Å was also searched for. The emission lines at 4473 and 7067 Å were extremely weak, implying observation of any associated absorption would be extremely difficult. The spectral regions of these

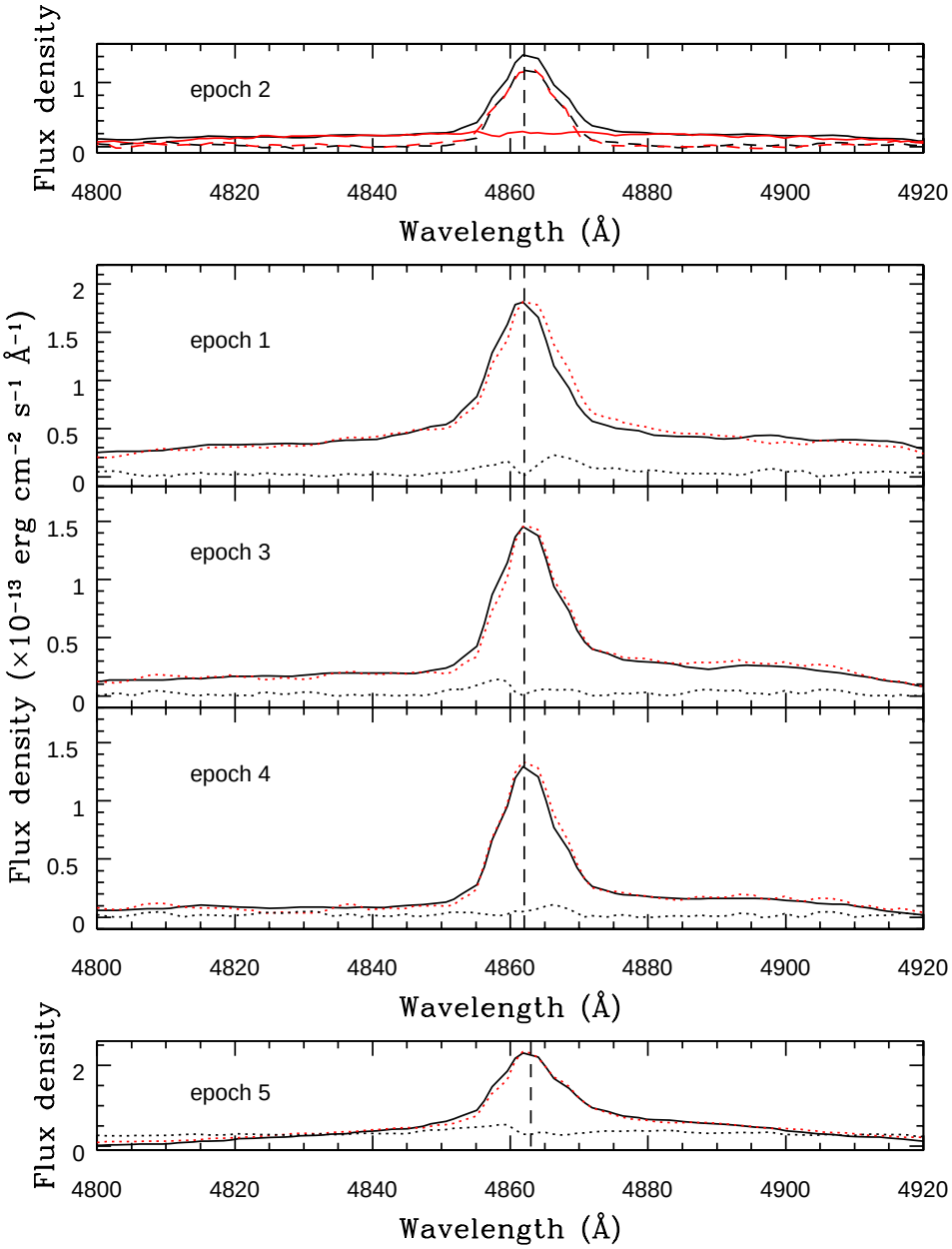

Figure 5.12: *Top panel*: Epoch 2 total Hβ emission (solid black line), broad emission profile (solid red line), Hβ narrow component (dashed black line) and Hβ inverted narrow component (dashed red line). No absorption is evident from the line inversion. *Middle Panel*: Epoch 1,3 and 4 emission profile (solid black line) and reconstruction (dotted red line). Residuals are indicated by the dotted black line. No Hβ absorption is evident. *Bottom Panel*: Epoch 5 close-up view of Hβ emission region (solid black line) and reconstruction (dotted red line). Residuals are indicated by the dotted black line. No absorption is evident. Note: The centre of the Hβ line at each epoch is denoted by the vertical dashed black lines.

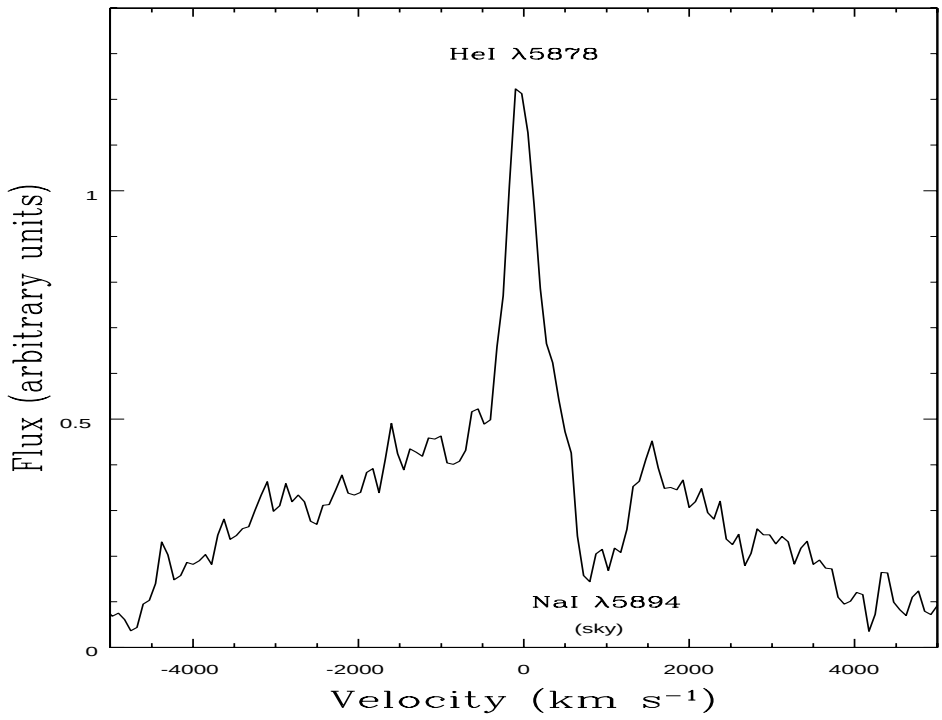

Figure 5.13: Spectral region of the He I λ5878 emission line for the epoch 5 observation. No obvious absorption features associated with this transition are apparent. The overlapping Na I λ5894 sky absorption feature is also marked.

two emission lines were checked for absorption and unsurprisingly no obvious signature was found. The He I λ5878 emission line was stronger, with distinct broad and narrow components visible in the spectrum. However, no absorption associated with this transition was visible either, even in the epoch 5 spectrum which shows the strongest metastable helium absorption (see Figure 5.13).

5.3 Photoionisation simulations: setup and coarse grid

5.3.1 CLOUDY simulations

In order to locate the absorber in ionisation parameter, number density and column density space, grids of photoionisation models were calculated. The photoionisation models carried out for this paper were performed using CLOUDY version c13.02 (Ferland et al., 2013) for which the setup was similar to that described in paragraph 1 of Section 3.1 in Leighly et al. (2011). The input SED was assumed to follow

the shape of the AGN continuum as described in Korista et al. (1997). The calculations required two runs of the code over each grid. The first run was used to find the thickness of the absorbing cloud to be integrated through to reach the spectroscopically-determined column density of helium in the 2^3S metastable state. This allowed the total hydrogen ($N_{\rm H}$) and 2^1S state helium column densities to be calculated. The second run performed an integration through to the N_H values determined from the first run to find the hydrogen level populations, which could then be used to determine if a particular grid-point exceeded the allowed Balmer absorption. The spectral observations in Section 5.2.3 (Table 5.2) indicated that the intervals between the upper and lower limits for the metastable helium column density values for epochs 1 to 4 had significant overlap, hence these epochs were treated together for the purposes of simulation comparisons. The average triplet metastable state He I* column density in these epochs, excluding epoch 3 as it was an outlier, was calculated to be $N_{\rm He}(2^3S)$=$2.13^{+0.94}_{-0.28}\times10^{14}$ cm^{-2}. Spectroscopic constraints on the column density of helium in the 2^1S state were lower limits, meaning that CLOUDY-derived values needed to exceed a particular representative value for epochs 1 to 4 to be considered valid. This value was assumed to be the lower limit of the maximum value of the first four epochs (epoch 4), which was $N_{\rm limHe}(2^1S)$=1.87×10^{12} cm^{-2} (See Section 5.2.4 Table 5.3).

The CLOUDY output provided the fraction of helium in the sum of all singlet states at each principal quantum state rather than the individual singlet states at different total azimuthal quantum numbers. Helium in the n=2 singlet state exists in both ^1S and ^1P configurations, meaning the latter of these needed to be taken into account to derive the fraction in the 2^1S state. This state is formed by the combined effect of He^+ + e^- recombinations and collisional excitation from the 2^3S metastable state. Approximately one third of helium recombinations to a singlet state of n=2 or higher ultimately results in population of the 2^1S state, while the rest lead to the ground state (Osterbrock & Ferland, 2006). Therefore, using the recombination and collisional rate coefficient values derived from Smits (1996); Benjamin et al. (1999) and Bray et al. (2000) respectively as listed in Osterbrock & Ferland (2006), the fraction of helium in the 2^1S state at each CLOUDY output zone could be found as follows:

$$F\left(2^1S\right) = F\left(2^1\right) \times \frac{\alpha_{c1} n_{He}\left(2^3S\right) + 0.33\alpha_{rec} n_{He+}}{\alpha_{c1} n_{He}\left(2^3S\right) + \alpha_{c2} n_{He}\left(2^3S\right) + \alpha_{rec} n_{He+}}\,, \tag{5.6}$$

where, for a specific zone, $F(2^1S)$ is the fraction of helium in the 2^1S state, $F(2^1)$ is the CLOUDY-calculated value of the helium fraction in the n=2 singlet states, α_{c1} is the 2^3S–2^1S collisional rate coefficient, α_{c2} is the 2^3S–2^1P collisional rate coefficient, $n_{He}(2^3S)$ is the number density of helium

in the 2^3S state, $n_{He}(2^1S)$ is the number density of helium in the 2^1S state and α_{rec} is the sum of the recombination rate coefficients to all singlet states at n=2 or above. The bulk of the zone temperatures were within the ranges listed in tables 2.4 and 2.5 of Osterbrock & Ferland (2006), therefore linear interpolation was used to find the appropriate rate coefficients at individual zones. For those zone temperatures outside the ranges listed, linear extrapolation was used.

5.3.2 First coarse run

It was considered convenient to initially generate a "coarse" grid measuring 8×7 using a range in ionisation parameter U of $-2.5 \leq \log U \leq 1.0$ in steps of 0.5 dex and a range in hydrogen number density $n_{\rm H}$ of $3.0 \leq \log(n_{\rm H}$ / cm$^{-3}) \leq 9.0$ in steps of 1.0 dex. Having found the gridpoints which satisfied the conditions dervied from the spectra, a "fine" grid could then be calculated to narrow down the allowed values in the parameter space neighbouring the allowed coarse gridpoints. The gas hydrogen column density at each gridpoint was set equal to $\log n_{\rm H}$=24.5+$\log U$ to allow the code to integrate through the relatively high-ionisation region occupied by He I*. The grid was generated by performing the following steps: (i) The He I* column density output from CLOUDY was compared to the epoch 1 to 4 spectroscopically-derived average ($N_{\rm He}(2^3S)$). Grid points which produced values lower than this were ruled out, (ii) for those grid points that satisfied condition (i), the He I* 2^3S number density in each output zone generated by the code was calculated by multiplying the fraction of helium in the He I* state by the helium abundance and $n_{\rm H}$, (iii) the He I 2^1S number density in each output zone was found by calculating $F(2^1S)$ in each zone using Equation 5.6 and multiplying the result by the helium abundance and n_H, (iv) the absorber thickness was found by performing the integral $\int n_{\rm He}(2^3S)$dr through each zone from the irradiated face of the cloud inward until the epoch 1 to 4 average value was reached, with the radius at which this value was reached giving the total thickness, (v) this integration was performed over the same zones as in (iv) to find the 2^1S column density using $\int n_{\rm He}(2^1S)$dr, and (vi) the total thickness by $n_{\rm H}$ for the grid in question to find the hydrogen column density $N_{\rm H}$.

5.3.3 Second coarse run

The absence of Hβ absorption, as described in Section 5.2.5, could be used to obtain an upper limit on the column density of hydrogen in the n=2 state and therefore rule out gridpoints where the CLOUDY

models suggest this upper limit was exceeded. To do this, a second set of CLOUDY models was generated for the coarse grid, using a method very similar to that described in paragraph 3 of Section 3.1 in Leighly et al. (2011). The normalised profile shape for the He I* λ3889 absorber was assumed to be the shape that any hydrogen absorption would follow and therefore the epoch 1 absorption profile for this transition was used as a template. Balmer absorption can arise from hydrogen atoms in either of the two n=2 states (^2S or ^2P), so to calculate the correct column density the relative populations of atoms in each state needed to be known. Using the $N_{\rm H}$ values obtained from the first run, CLOUDY was set to integrate through to these values and then run for a second time to determine the hydrogen n=2 population values.

The minimum H I n=2 column density at which a measurement would become significant is estimated by replacing the fλ value in Equation 5.4 by a weighted mean value which depended upon the proportion of atoms in each of the two hydrogen n=2 states and using the same $C(v)$ profile as was calculated for He I*. The depth at every velocity bin of this profile was then scaled by factors of between 0.001 and 1 in steps of 0.001, with the column density calculated at each step using Equation 5.4. The first value of the column density at which the uncertainty in the calculation was exceeded was assumed to be the maximum column density of hydrogen in the n=2 state.

The constraints on the allowed coarse gridpoints obtained from the metastable Helium, n=2 singlet-state helium and maximum Balmer absorption are illustrated in Figure 5.14

5.4 Discussion

5.4.1 Variability mechanism

In Section 5.3, the calculations were performed exclusively for epochs 1 to 4 due to the lack of significant change in the metastable helium column density across those epochs, while epoch 5 appeared different for two reasons. First, the profile of the absorption appeared to have narrowed during this epoch, an effect which was visible in both the metastable helium doublet components (Figure 5.10) and the singlet state helium absorber (Figure 5.11). Second, the column density of metastable helium underwent a significant strengthening between epochs 4 and 5 due to a strengthening in the velocity range -500 km s$^{-1}\leq v \leq$ 0 km s^{-1}. The origin of the observed variability in the strength of the

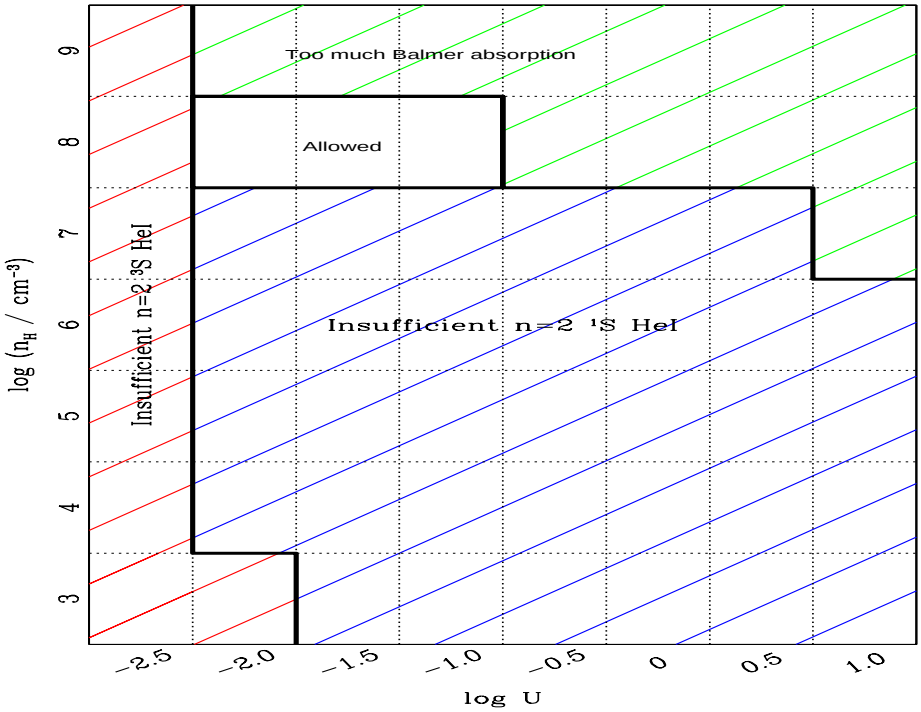

Figure 5.14: Allowed and ruled out coarse gridpoints. Gridpoints showing insufficient metastable 2^3S helium absorption were ruled out first (red shaded area). Gridpoints showing too much Balmer absorption were ruled out second (green shaded area). Gridpoints showing insufficient helium in the 2^1S state were ruled out third (blue shaded area). The remaining allowed region is unshaded.

absorption is examined in this section.

Between epochs 4 and 5, the continuum flux in the region of He I* λ3889 increased to become approximately double the average of the other four epochs and also appeared to undergo a steepening of the slope towards the blue end of the spectrum. If the optical continuum in AGN represents a continuation of the spectral shape into the ionising extreme ultra-violet (EUV) region (Kriss et al., 1999), then these changes could have indicated an increase in the ionising photon flux incident on the absorbing gas. However, the observed changes in the absorption feature were not consistent with an ionisation state change in response to increased incident ionising photon flux. This was for two reasons. First, evidence from the optical doublet component suggested that the NIR component should be saturated near -500 km s^{-1}, meaning ionisation changes should not have had a significant effect in this spectral location. Second, the expected result of an ionisation change would be a change in the absorber strength co-ordinated across the absorber profile, which was contradicted by the observed decrease in

absorber depth at outflow velocities greater (more negative) than ≈ -500 km s^{-1} despite an increase at lower (less negative) velocities (see Figure 5.10). This evidence suggested movement of the absorber across the line-of-sight could provide a better explanation for the dominant mechanism which drove the variablity.

5.4.2 A crossing-clouds model

The plausibility of changes in gas covering fraction as an explanation for the variability was tested using a method very similar to the "crossing disc" model applied in Capellupo et al. (2013, 2014). In this model, a disc-shaped absorber moves across a disc-shaped emission source. Changes in the observed absorption line strength are then due to changes in the fraction of the emission region covered by the absorber. For the purposes of this study, the model related the velocity of gas across the line-of-sight (the transverse velocity) to the crossing time as follows:

$$v_t = \frac{(\Delta A_{\rm BLR})^{\frac{1}{2}}\, D_{\rm BLR}}{\Delta t}\,, \tag{5.7}$$

where v_t is the transverse velocity of a disc-shaped cloud, $\Delta A_{\rm BLR}$ is the change in the covering fraction of the BLR only, $D_{\rm BLR}$ is the diameter of the BLR and Δt is the cloud crossing time. The BLR diameter was chosen as the best representation of the size of the emission region crossed by the absorber for two reasons. First, the large spatial extent of the NLR rendered it unrealistic for moving gas to significantly change the fraction of this region obscured along the line-of-sight. Second, given the depth of the NIR absorption, some of the BLR must have been obscured at epochs 2 to 5, indicating that the absorber did not just cover the small continuum emitting region. For the BLR diameter, we used a value twice that of the Hβ-derived BLR radius of approximately 3.1 light-days found in Bentz et al. (2006), obtained from the reverberation mapping campaign described therein, therefore the diameter of the BLR was calculated to be $D_{\rm BLR}\approx 1.6\times10^{16}$ cm.

The calculation of $\Delta A_{\rm BLR}$ was performed by measuring the change in flux of the stronger (NIR) doublet absorption component in the spectral range which underwent a reduction in strength between epochs 4 and 5 (-1500 to -500 km s^{-1}). As it was assumed that changes in the flux were due to changes in the obscuration of the BLR, the change in the sum of the flux in all velocity bins in this

range was measured as a fraction of the total flux calculated from the interpolated and scaled broad component of Paβ described in Section 5.2.2, in which the reconstructed broad component of He I* λ10 830 is described. The resulting value of this normalised flux change was $\Delta A_{\rm BLR}$=0.39.

Using the values $\Delta A_{\rm BLR}$, $D_{\rm BLR}$ and the value of Δt set equal to the AGN rest-frame epoch separation interval (1126 days), the velocity across the line-of-sight could be calculated using Equation 5.7. This provided a value of v_t=1050$\pm$440 km s^{-1}. One candidate explanation for movement of absorbing gas across the line-of-sight to an AGN is simply that it is in orbital motion moving at Keplerian velocity. This interpretation seemed likely in this case, as the absorber centroid velocity (v_c=$-$615 km s^{-1}) is too low to explain the transverse velocity. Therefore, the transverse velocity calculated using the crossing-disc model was a lower limit to the true orbital velocity, since the transverse velocity cannot exceed the Keplerian velocity (Moe et al., 2009). This is because the Keplerian velocity vector will only be parallel to the transverse velocity at the point where the observer, absorber and SMBH all lie along the same line.

As a second check on the accuracy of the Keplerian model, the variability between epochs 2 and 3 was also tested over the same velocity range. Although no significant change was detected in the metastable helium column density betweeen these observations, a visual inspection of Figure 5.10 suggested there was an increase in the depth of NIR absorption. A similar flux change to that observed between epochs 4 and 5 had occured ($\Delta A_{\rm BLR}$=0.37) indicating a crossing velocity of v_t=1540$\pm$650 km s^{-1}. The consistency of this value with the epoch 4 to 5 case suggested the proposed scenario, absorbing gas crossing the line-of-sight while undergoing a Keplerian orbit, was broadly consistent with the data.

5.4.3 Fine grid simulation

The lower limit constraint on the orbital velocity calculated in Section 5.4.2 could be used to calculate an upper limit on the distance of the material from the central black hole. Using the estimated supermassive black hole mass of $M_{\rm BH}$=4.57$\times$10^7 $M_\odot$ from Bentz et al. (2006) the upper limit based on the epoch 4 to epoch 5 crossing-disc model gave $r_{\rm kep}$=GM/$v_t{}^2$=5.47$\times$10^{17} cm, or approximately 68 times the BLR radius found in Bentz et al. (2006). The SED used in the CLOUDY calculations could be appropriately scaled using the value of the bolometric luminosity given by $L_{\rm bol}$=7.3$\times$10^{43} erg s^{-1} (Kaspi et al., 2005). Using this scaled SED, we could estimate the distance from the ionising continuum source

log$U$	log$N_{\rm H}$	radial distance
	log(cm^{-2})	cm
-2.0	21.05	1.34$\times10^{18}$
-1.5	21.39	7.53$\times10^{17}$
-1.0	21.84	4.24$\times10^{17}$

Table 5.4: Table of Hydrogen column densities and SMBH radial distance at ionisation parameter values allowed by the coarse grid.

to the incident surface of the absorber. From the coarse grid calculations carried out in Section 5.3, it was found that the radial distance of the absorber increased with decreasing ionisation parameter (See Table 5.4).

Equipped with this knowledge, a second investigation using the same two-run method described in Section 5.3 was undertaken to further constrain the absorber properties at a finer resolution. A new grid measuring 19×19 spanning the ranges $-2.4 \leq \log U \leq -0.6$ and $7.1 \leq \log(n_{\rm H}/cm^{-3}) \leq 8.9$, both in step sizes of 0.1 dex, was generated. The 2^1S–state helium column density at any particular log$n_{\rm H}$ gridpoint was not a strong function of log U over this range. Given the minimum value of $N_{\rm limHe}(2^1S)$=1.87$\times10^{12}$ cm^{-2}, log($n_{\rm H}$/cm^{-3}) values lower than 7.5 were not allowed, as indicated in Figure 5.15. All gridpoints with values of log($n_{\rm H}$/cm^{-3}) greater than 8.4 were ruled out due to excess Balmer absorption, while all log$U$ gridpoints less than -2.2 were ruled out due to insufficient helium in the 2^3S state.

By applying the upper distance limit of the radial location of the absorber (r_{kep}=5.47$\times10^{17}$ cm), log$U$ values at each value of log$n_{\rm H}$ in the constrained range ($7.5 \leq \log(n_{\rm H}/{\rm cm}^{-3} \leq 8.4$) could be ruled out, as indicated in Figure 5.16. Across all number densities in this range, log$U < -1.6$ is ruled out.

The density and location of the absorber may imply it originates near the inner edge of the dusty torus. Such a torus is thought to surround the central regions of AGN including NGC 4151. The study of Minezaki et al. (2004) suggests a hot inner edge of the torus in NGC 4151 located at ≈0.04 pc from the central ionising source, with a maximum possible extent of the torus being ≈4 pc as indicated by Riffel et al. (2009). A number density of between $10^{7.5}$ and $10^{8.4}$ cm^{-3} is intermediate to the BLR and NLR densities, as would be expected from such a location. Assuming similarities in the density of

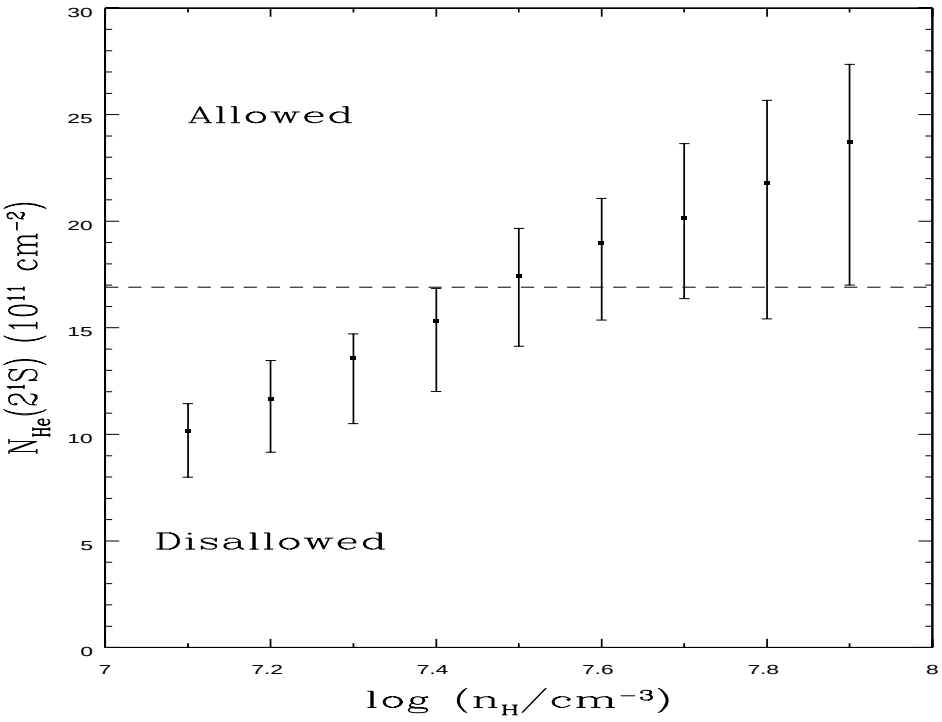

Figure 5.15: Mean He I 2^1S column density at log$n_{\rm H}$ gridpoints across the fine-grid log$U$ range. The range of allowed values across log$U$ space are indicated by errorbars. The spectroscopically-derived minimum column density is indicated by the dashed line. Only values of 7.5 and greater overlap with the allowed region.

this region across AGN, this range is also in accordance with the study of Rose et al. (2011) into the forbidden high-ionisation-line region in SDSS J11311.05+162739, which was reported to be cospatial with the inner face of the torus.

5.4.4 Total hydrogen column densities and mass outflow rates

Values of the total hydrogen column densities were required to calculate the mass outflow rates. At a given log$U$ gridpoint, these values were a very weak function of log$n_{\rm H}$. Therefore only set of points corresponding to log($n_{\rm H}$/cm^{-3})=8.4, representing logN_H as a function of log$U$, are indicated in Figure 5.17.

Mass outflow rates $\dot{M}_{\rm out}$ could be estimated using the method of Crenshaw et al. (2009) as follows:

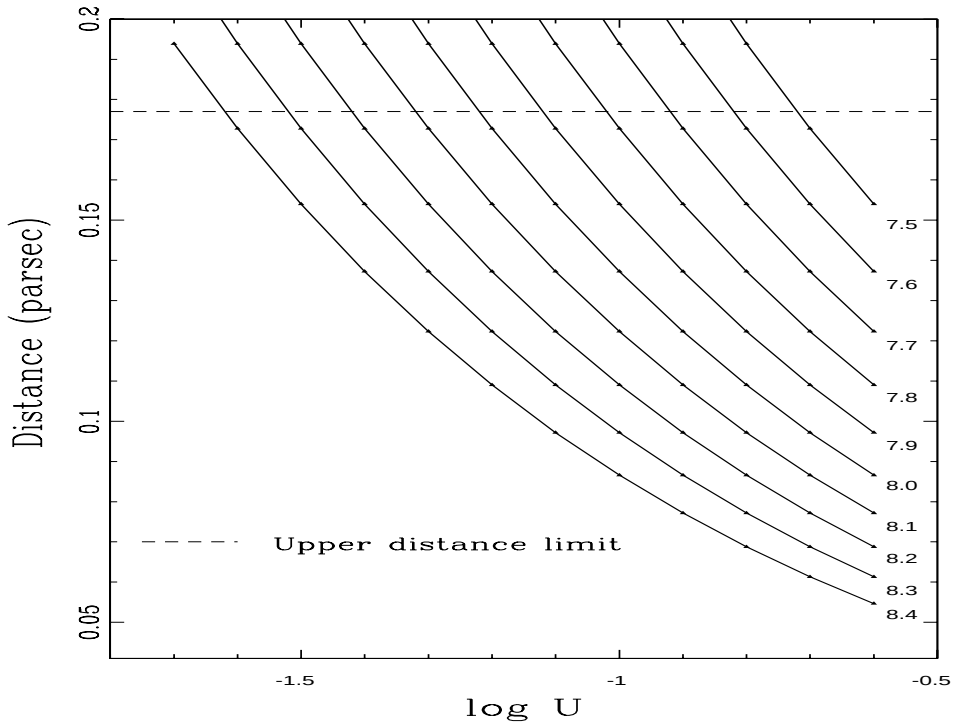

Figure 5.16: Radial distance as a function of log$U$, indicated by curves of constant logn_H.The logn_H values are indicated to the right of the solid black curves in units of log(cm^{-3}). The dashed line indicates the upper distance limit derived from the crossing-cloud model.

$$\dot{M}_{\rm out} = 8\pi R N_{\rm H} \mu m_{\rm p} C_{\rm AGN} |v| \,, \tag{5.8}$$

where μ is the mean atomic mass per proton ($\mu\sim$1.4), $m_{\rm p}$ is the proton mass, $C_{\rm AGN}$ is the covering fraction of the outflow as seen from the active nucleus and v is the mean velocity of the outflow. Using an 80° opening angle (Hutchings et al., 1998), the covering fraction could be estimated as $C_{\rm AGN}$=0.23. The velocity of the (predominantely hydrogen) outflow was assumed to be approximately the same as the velocity centroid of the helium absorption. The calculation of the average centroid across epochs 1 to 4 provided a value of $|v_c|$=615 km s^{-1}. The dependence of mass outflow rates and corresponding kinetic luminosities on radial distance obtained for the fine-grid points used in Figs. 5.16 and 5.17 are indicated in Figure 5.18.

Examination of the outflow's hydrogen column density, radial distance and outflow rate across the permitted gridpoints allowed constraints to be placed on these quantities. The hydrogen column density

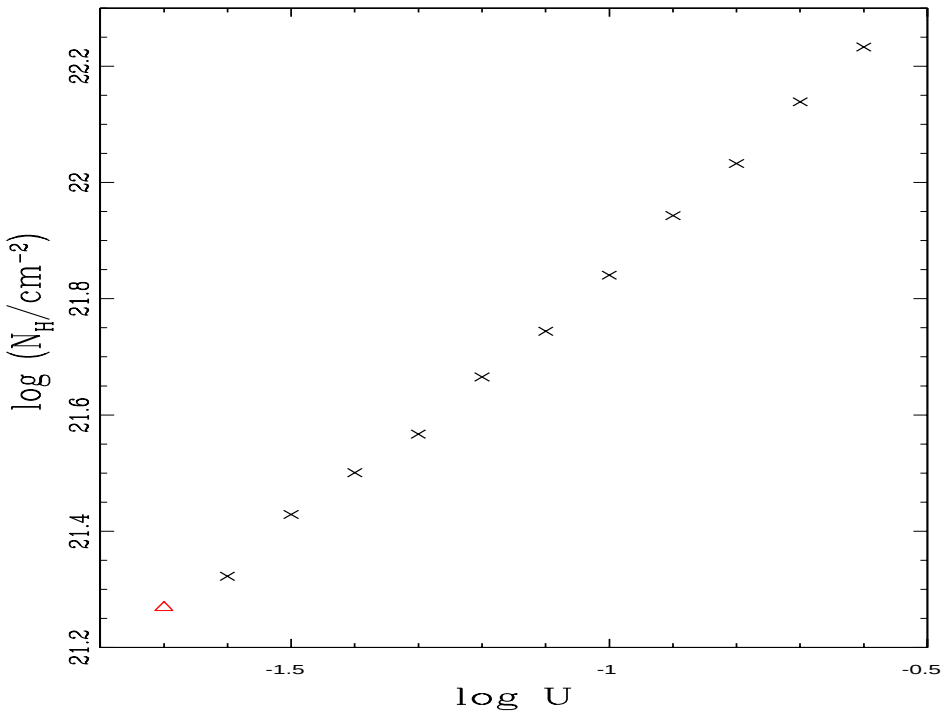

Figure 5.17: Plot of logN_H against log$U$ at log($n_{\rm H}$/cm^{-3})=8.4 over the same ionisation parameter range as used in Figure 5.16. One grid-point, ruled out by the distance criterion, is indicated by a red triangle, while allowed values are indicated by black crosses.

constraints were 21.25 $\leq$ log($N_{\rm H}$/cm^{-2}) $\leq$ 22.23. The radial distance constraints were calculated to be 1.69$\times$10^{17} $\leq$ $R(cm)$ $\leq$ 5.33$\times$10^{17} (0.055 to 0.173 pc) while those for the mass outflow rate the limits were 0.015 $\leq$ $M_{\rm out}$ ($M_{\odot}$ yr^{-1}) $\leq$ 0.109, which corresponded to a kinetic luminosity range of 1.78$\times$10^{39} to 1.30$\times$10^{40} erg s^{-1}. The weakness of this outflow, with a kinetic luminosity of at most 0.018 percent of the bolometric luminosity, indicated that it was probably not a significant contributor to galaxy feedback (Di Matteo et al., 2005; Hopkins & Elvis, 2010).

5.4.5 Comparison with previous observations

Since incidents of absorption from He I* are effectively high ionisation transitions, the observed absorption should also have been visible in high ionisation UV transitions resulting from species such as C IV and P V. Although no simultaneous UV spectra were available for comparison with the observations describedin this chapter, the width and centroid of the absorber was similar to the 'D+E' feature

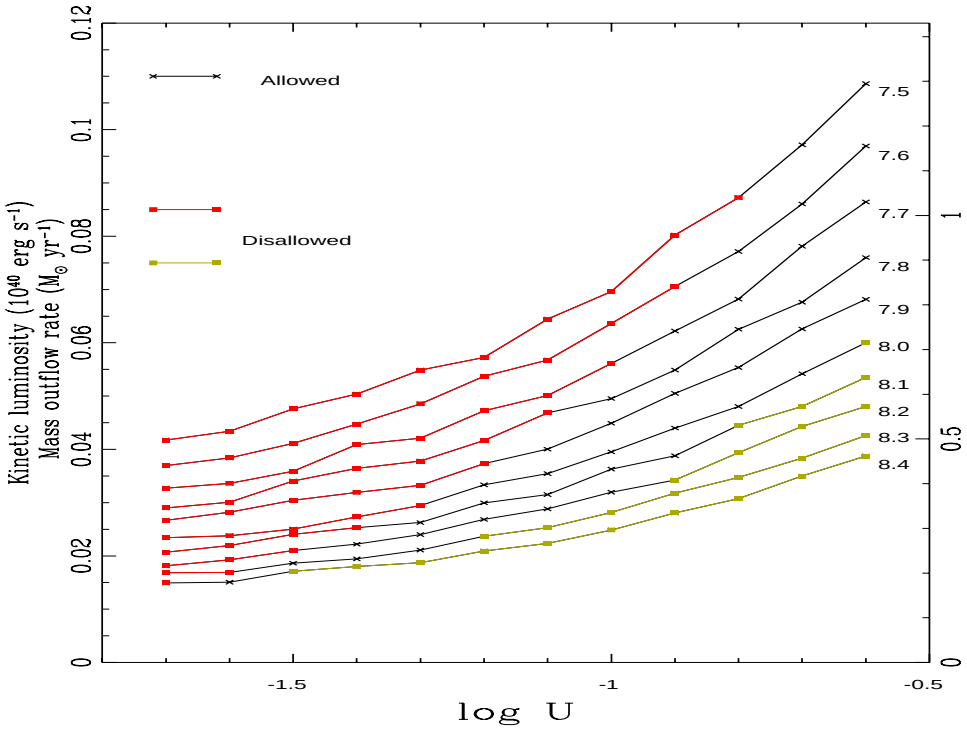

Figure 5.18: Curves of constant logn_H indicating the dependence of mass outflow rate (values on left vertical axis) and kinetic luminosity (values on right vertical axis) on log$U$. The logn_H values are indicated to the right of the solid black curves in units of log(cm^{-3}). Grid-points ruled out by the distance criterion are indicated by solid red squares, those ruled out by predicting too much Balmer absorption are indicated by solid gold squares, while allowed values are indicated by black crosses.

described in Kraemer et al. (2005, 2006) and Crenshaw & Kraemer (2007) which had a FWHM of 1170 km s^{-1}. The absorber studied in this chapter seemed to coincide with the values listed in Crenshaw & Kraemer (2012) for the ionisation parameter, radial distance and mass outflow rate found for the UV sub-components labelled 'D+Eb' and 'D+Ec', with the strong 'D+Ea' component and the X-ray component labelled 'Xhigh' not contributing. The lack of the 'D+Ea' component may not be totally surprising given the lack of detection of Hβ absorption, in contrast to that found in the June 2000 HST observation reported in Crenshaw & Kraemer (2007). Consequently, the reported mass outflow rates in this chapter are lower than those reported in that paper. Given the variety of location and ionisation parameter reported for the absorbers in Crenshaw & Kraemer (2012), it is likely that the observations investigated in this chapter only detected an outflow between the inner narrow line region and the BLR, possibly the location of an *intermediate line region* from where self-absorption occurs (Crenshaw & Kraemer, 2007).

5.5 Summary

The results of the investigation described in ths chapter can be summarised as follows:

(i) The absorption due to He I λ20 587 had a similar profile to that at 10 830 Å, indicating they originated in the same outflowing gas. Use of this line, which is not commonly examined in AGN studies, in combination with the triplet state transitions provided useful constraints on the parameter space occupied by the outflow.

(ii) The NIR component of the triplet state helium absorber was likely to be saturated close to the line centroid, since the depth of the optical component was significantly stronger over at least one velocity bin across all epochs than that predicted by an absorption profile obtained by scaling down the optical depth of the NIR component by a factor 23.3, as predicted by the fλ ratio.

(iii) The line profile and centroid velocity showed similarities to that arising from the absorber complex labelled 'D+E' in the studies of x-ray and UV absorption in NGC 4151 reported in (Kraemer et al., 2005, 2006; Crenshaw & Kraemer, 2007, 2012). The properties of the He I absorber seemed to coincide with those of the 'D+Eb' and 'D+Ec' features (see point (vi)).

(iv) The increase in optical luminosity between epochs 4 and 5 suggested the ionising flux reaching the absorber should have increased between these epochs, providing a potential explanation for the observed variability. However, the absorption line profile did not show a consistent change in the same sense (increasing or decreasing) across velocity space as would have been expected if ionisation changes were driving the variability. The increase in measured column density between epochs 4 and 5 was due to a strengthening in the spectral region $-500 \leq v \leq 0$ km s^{-1}, which was likely to be saturated and therefore unresponsive to ionisation-state changes.

(v) Testing the absorption line variability by means of a crossing-disc model provided two possible values of the crossing velocity, namely 1050$\pm$440 and 1540$\pm$650 km s^{-1} from the epoch 2 to 3 and epoch 4 to 5 changes respectively. The similarity of these velocities suggested this explanation is self-consistent. This also effectively provided an upper limit to the true distance (5.47×10^{17} cm) due to the comparatively low outflow centroid velocity in comparison to the crossing velocity, implying that the

velocity transverse to the line-of-sight was due to orbital motion.

(vi) Photoionisation simulations were used to constrain the physical properties using results from the three measured He I lines together with the lack of observable Balmer absorption. These suggested that the absorber was located between 0.055 and 0.173 pc from the central ionising continuum source (equivalent to between 21 and 68 times the BLR radius). The absorber location, together with the estimated number density, suggest the absorber could be coincident with the inner edge of the dusty torus. The column density lay in the range $21.25 \leq \log(N_{\rm H}/cm^{-2}) \leq 22.23$ and the mass outflow rate ranges between 0.015 and 0.109 $M_{\odot}$ yr^{-1}. This outflow rate implied a contribution to the kinetic luminosity which is low in comparison to the bolometric luminosity (at most 0.018 percent) and therefore the outflow was probably not a significant contributor to feedback effects.

Chapter 6

Conclusions and future work

In this work absorption lines were investigated both from a large sample of objects (Chapter 3) and from individual objects (Chapters 4 and 5). The large sample study of 50 quasars allowed deductions to be made about the variability properties of the BALQSO population. The individual BALQSO investigation allowed the variability mechanism to be determined and limits to be put on the mass outflow rate. From the observations of NGC 4151 the apparent variability was used to weigh-up the arguments in favour and against different variability driving mechanisms, as well as constraints being put on the physical properties of the outflow.

6.1 Large-sample properties of BALQSOs

The 50 BALQSOs studied in Chapter 3 were selected to be representative of the BI, redshift and luminosity distribution functions of the BALQSO population as a whole, as verified by K-S tests. This allowed the use of the sample to test for possible correlations between BAL variability behaviour and the properties of the BALs or their host quasars. One of the most significant outcomes was that no correlation was found between BAL variability and host BALQSO luminosity. Since the vast majority of a quasar's power output is in the form of the continuum, a quasar's luminosity should track the size of the continuum emission region. A simple light-travel time argument means that quasars with more variable continuum output are likely to have smaller continuum emitting regions. Therefore, less luminous quasars should have greater continuum variability. This continuum is capable of ionising metals

to highly-ionised states such as C IV and Si IV, therefore changes in the continuum state could change the equilibrium fractions of the ionisation states of elements in the outflowing material. This process is responsible for the BLR response to the continuum, utilised in reverberation mapping. A Spearman rank test indicated that the variability of the BALs in the sample is not correlated with quasar rest-frame i-band luminosity, suggesting ionisation changes are not the major BAL variability mechanism in the BALQSO population.

There was no significant sign of a link between epoch-separation timescale and BAL variability in the 50 quasar sample. The results in Filiz Ak et al. (2013) suggested that variability is best modelled by a random walk on multi-year timescales, which should prove significant over the timescales sampled in our study. One possible reason for this discrepancy is the small sample size of our study in comparison with that of Filiz Ak et al. (2013), masking the true increase in variability in the wider BAL population as a function of epoch separation time. A C IV BAL lifetime of 142 years was calculated based on the disappearance rate which matches that predicted in Filiz Ak et al. (2012). A shorter lifetime of 43 years was found for the Si IV BALs which probably reflects their greater susceptibility to variability.

6.2 The extreme variability in SDSS J1138+3517

SDSS J1138+3517 was a member of the sample studied in Chapter 3, from which a visual inspection of the first three epochs' spectra indicated an unusual level of BAL variability. The quasar underwent its largest change between the first and second epochs, during which a general weakening of the BALs was observed, being coordinated both within the BAL troughs and across separated troughs. This coordinated weakening was obvious in both Si IV and C IV BALs. Between epochs 2 and 3 there was a similarly coordinated strengthening of the BALs. Such coordinated changes have been witnessed in quasars in several studies and are generally taken to indicate that changes in the ionisation state of the gas are responsible for the variability.

The extreme nature of the variability was confirmed by comparison of the C IV variability of the most variable BAL in SDSS J1138+3517 with of the large sample of BALs in Filiz Ak et al. (2013). This indicated that it would make the top 1 percent of most variable C IV BALs in their 428-strong sample. The finding is rendered even more surprising when the time interval over which the variability is measured is taken into account. The variability of the most variable C IV BAL in SDSS J1138+3517

between the first and second epochs is strongly under-predicted by the random-walk model of Filiz Ak et al. (2013), as described in Chapter 4. This could indicate that the variability mechanism is likewise unusual, as the random-walk model is a good predictor of the variability in the quasars sampled by their study. Given the evidence in favour of ionisation change driven variability in SDSS J1138+3517 presented in Chapter 4, such a conclusion would suggest that variability caused by ionisation changes are (i) very unusual, and (ii) produce the largest EW changes.

6.3 The variable He I outflow in NGC 4151

The study of NGC 4151 described in Chapter 5 provided five epochs of observational data, which is the largest number of repeat observations out of the three investigations in this thesis. As well as utilising observations of absorption due to the He I doublet at 3889 Å and 10 830 Å, this study also provided the first example of a He I λ20 587 line being used to constrain a Seyfert galaxy's outflow properties. Unlike the case of SDSS J1138+3517, the bulk of evidence suggests that clouds crossing the line-of-sight are the best explanation for the He I absorption line variability detected in NGC 4151.

Under the assumption that changes in the absorber covering fraction are responsible for the variability of He I absorption in NGC 4151, the velocity of the crossing-clouds is found to be consistent across epochs 2 to 3 and epochs 4 to 5. Using the fact that it is unlikely that such a cloud could be moving at speeds faster than the local Keplerian velocity, an upper limit to the distance of the absorber from the continuum emission region could be found. This restriction, along with limits on the He I column density obtained from the spectra, allowed the mass outflow rate to be constrained as well as the physical properties in the outflow such as the total hydrogen number density, column density and the ionisation parameter. These physical properties are in good agreement with the absorbers previously labelled 'D+Eb' and 'D+Ec' by Crenshaw & Kraemer (2007) and references therein.

6.4 Discussion and future prospects

After investigating variability of absorption lines in both quasars and a Seyfert galaxy, a question to be asked is: can any conclusions be drawn on the dominant variability mechanism across all types of

AGN? It seems that in the case of quasars, there is probably a contribution both from ionisation changes and covering fraction changes to the variability across the BALQSO population. However, how the unusual behaviour of SDSS J1138+3517 fits in with the general variability behaviour of BALQSOs seems puzzling. It may be that ionisation changes driving variability are rare in the BALQSO population, possibly resulting in the most variable BALQSOs such as SDSS J1138+3517. However, this seems to be contradicted by papers such as Filiz Ak et al. (2013) and Gibson et al. (2010) which indicate coordinated BAL variations among separated troughs. These two possibilities could be reconciled if the ionisation changes are being produced by more than one process. An obvious possibility is a change in the ionising flux generated by the continuum source. However, an alternative is that the intrinsic continuum is constant, while a gas closer to the accretion disc than the observed BAL absorber could shield the absorber from the ionising continuum. Evidence for such a shielding gas has been reported in previous studies, e.g. Misawa et al. (2007). Changes in the 'shielding strength' could, in this scenario, induce changes in the ionisation fractions of the observed absorbing gas.

A curious discovery in the 50 BALQSO population was the fact that 10 percent seem to show evidence for the BAL gas obscuring a large fraction of the continuum while leaving the BLR uncovered. Such a discovery puts a lower limit on the size of individual clouds in such objects, since the absorber must be large enough to cover the continuum emission region. A possible future research project could involve studying the population of such objects in the SDSS survey. In Chapter 3 the absorbers in these objects were inferred to have a maximum radius of between 10^{13} and 10^{14} cm. Large sample statistics from the hundreds of BALQSOs observed in the SDSS could improve this estimate. Since the SDSS contains many repeat observations, variability in the covering fraction of such absorbers could also be recorded, giving an estimate of the line-of-sight cloud crossing velocity. A discovery of a negative correlation between the incidence of the phenomenon and quasar luminosity could indicate that objects with smaller continuum emission regions are more likely to obscured by an absorbing cloud, as would be expected if such clouds have a characteristic size across objects, while the emission region size can vary.

The work described in Chapter 4 regarding SDSS 1138+317 assumes that the partial coverage of the emission region can be modelled as *pure partial coverage* (PPC). In a PPC model, the optical depth profile across the face of the absorber along the line-of-sight resembles a step-function, where it abruptly increases from zero to a constant value. However this is not the only possibility for a non-constant optical depth profile across the line-of-sight. So-called *Inhomogeneous absorber models*, where the

optical depth follows a mathematical function such as a power-law or Gaussian along the plane perpendicular to the line-of-sight, have been studied in several papers, e.g. de Kool et al. (2002); Arav et al. (2005). The paper used as the basis for much of the work in Chapter 5, Leighly et al. (2011), calculated absorber column densities using both a power-law inhomogeneous model and a PPC model, with no significant difference in the values obtained from each model. If this equivalence is in fact due to the inhomogeneous absorber approximating a step-function, then it could be concluded that in such an instance the outflowing clouds are sharply defined by not having densities which 'tail-off' at the edges. If this behaviour is common in the quasar population, then only using a PPC model to calculate column densities in cases of partial coverage is appropriate. To give a more intuitive sense of what examples of possible inhomogeneous absorber models could look like and to give a sense of how they could approximate a step function, the models used in de Kool et al. (2002) are illustrated in Figure 6.1).

Observations of absorption arising from He I λ20 587 seem to be rare in the literature. However, the use of the He I 20 587 Å absorption line seems to have excellent use as an indicator of high density outflows, as indicated in Chapter 5, where total hydrogen number densities lower than 10^7 cm^{-3} were ruled out. Measuring this absorption feature should therefore be considered in future attempts to constrain the physical properties of AGN outflows. Observations of the NIR part of the spectrum allow for simultaneous measurement of He I λ20 587 and He I* λ10 830 as described in Chapter 5 of this thesis. Together with optical observations of the second metastable component at 3889 Å, observations of these lines provide an excellent framework for measuring the properties of high-density absorbers.

Since the paper by Leighly et al. (2011) it is known that He I* λ10 830 can appear as a BAL in some quasars. Study of absorption due to this transition could provide an alternative to Si IV and C IV in attempts to observe the 'ghost of Lyα' in BALQSOs (described in Arav (1996)). This feature shows up as a decrease in the strength of absorption at an outflow velocity of approximately 5 900 km s^{-1}, equal to the separation between Lyα and N V. It is due to Lyα photons being redshifted from the perspective of outflowing N V ions, allowing for their resonance absorption by these ions, thereby providing radiation-driven acceleration. This causes a dip in the number of ions present at this velocity, hence the decrease in absorption strength. It is complicated in the aforementioned high-ionisation UV lines due to the effects of overlapping doublet components and strong saturation, leading to difficulties in obtaining reliable detections (Cottis et al., 2010). The fact that He I* λ10 830 absorption is unblended and less prone to saturation could make it a more suitable choice for detecting Lyα ghosts.

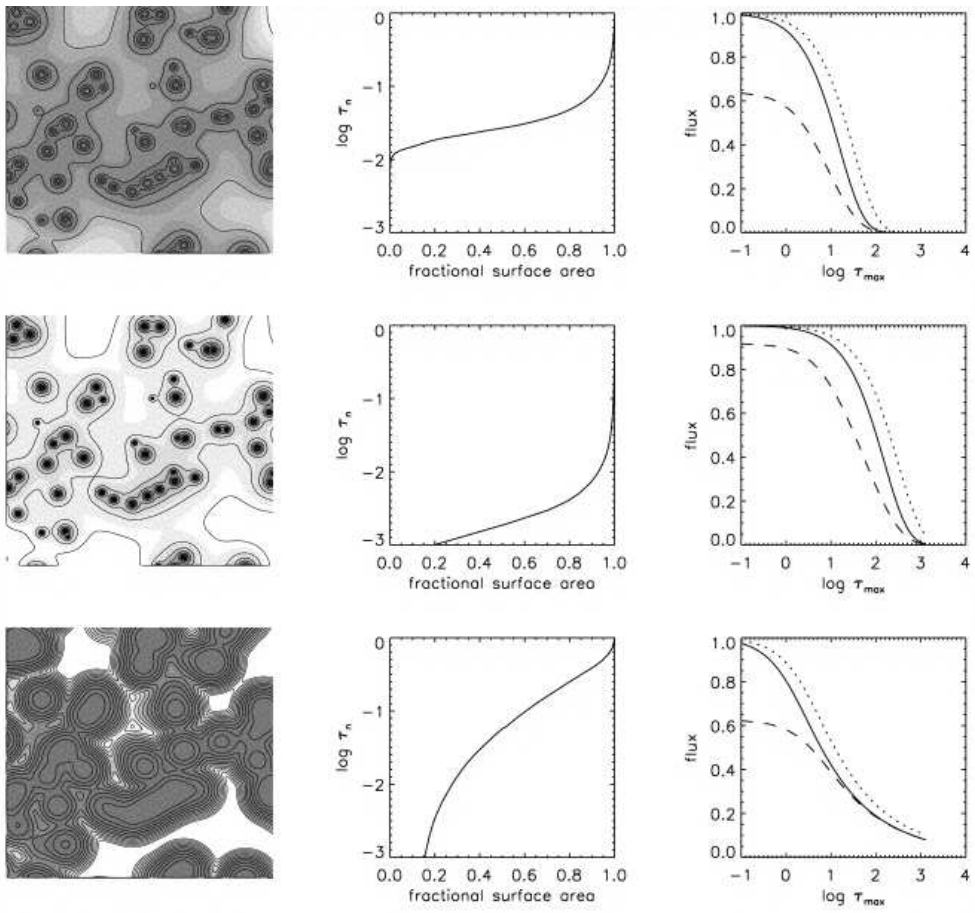

Figure 6.1: Three inhomogeneous absorber models as described in "The effects of inhomogeneous absorbers on the formation of intrinsic quasar absorption lines" by de Kool et al. (2002) (image is Figure 5 in that paper). Each model is represented by a row of 3 images. The leftmost image is a graphical representation of the two-dimensional distribution of absorber strengths along the line-of-sight, with logarithmic optical depth contours. The darker colours represent more absorption (less transmission). The middle image indicates the distribution of optical depth across the line-of-sight surface area. The right image represents the normalised flux of two doublet components (solid and dotted lines) of oscillator strength ratio 2:1, while the dashed line indicates the uncovered fraction which would be derived from a homogeneous (PPC) analysis of the inhomogeneous absorber.

Bibliography

Adelman-McCarthy J. K., Agüeros M. A., Allam S. S., et al. 2007, *ApJS* , 172, 634

Ahn C. P., Alexandroff R., Allende Prieto C., et al. 2014, *ApJS* , 211, 17

Alexandroff R., Strauss M. A., Greene et al. 2013, *MNRAS* , 435, 3306

Allen J. T., Hewett P. C., Maddox N., Richards G. T., et al. 2011, *MNRAS* , 410, 860

Allende Prieto C., Lambert D. L., Asplund M., 2001, *ApJL* , 556, L63

Allende Prieto C., Lambert D. L., Asplund M., 2002, *ApJL* , 573, L137

Antonucci R. R. J., Miller J. S., 1985, *ApJ* , 297, 621

Arav N., 1996, *ApJ* , 465, 617

Arav N., 1998, in Kaper L., Fullerton A. W., eds, Cyclical Variability in Stellar Winds Outflows in Quasars: Radiative Acceleration and Variability. p. 402

Arav N., Becker R. H., Laurent-Muehleisen S. A., et al. 1999, *ApJ* , 524, 566

Arav N., Kaastra J., Kriss G. A., et al. 2005, *ApJ* , 620, 665

Banerji M., Alaghband-Zadeh S., Hewett P. C., et al. 2015, *MNRAS* , 447, 3368

Barlow T. A., 1993, PhD thesis, California University

Barlow T. A., 1994, *PASP* , 106, 548

Barvainis R., 1987, *ApJ* , 320, 537

Beall J. H., Guillory J., Rose D. R., et al. 2003, Chinese Journal of Astronomy and Astrophysics Supplement, 3, 137

Benjamin R. A., Skillman E. D., Smits D. P., 1999, *ApJ* , 514, 307

Bentz M. C., Denney K. D., Cackett E. M., et al. 2006, *ApJ* , 651, 775

Bentz M. C., Peterson B. M., Pogge R. W., et al. 2006, *ApJ* , 644, 133

Blandford R. D., McKee C. F., 1982, *ApJ* , 255, 419

Boksenberg A., 1985, Vistas in Astronomy, 28, 531

Bonning E. W., Cheng L., Shields G. A., et al. 2007, *ApJ* , 659, 211

Bottorff M., Korista K. T., Shlosman I., et al. 1997, *ApJ* , 479, 200

Bowyer S., Byram E. T., Chubb T. A., et al. 1964, *Nature* , 201, 1307

Bray I., Burgess A., Fursa D. V., et al. 2000, *A&AS* , 146, 481

Capellupo D. M., Hamann F., Barlow T. A., 2014, *MNRAS* , 444, 1893

Capellupo D. M., Hamann F., Shields J. C., et al. 2011, *MNRAS* , 413, 908

Capellupo D. M., Hamann F., Shields J. C., et al. 2012, *MNRAS* , 422, 3249

Capellupo D. M., Hamann F., Shields J. C., et al. 2013, *MNRAS* , 429, 1872

Cardelli J. A., Clayton G. C., Mathis J. S., 1989, *ApJ* , 345, 245

Carroll B. W., Ostlie D. A., 2006, An introduction to modern astrophysics and cosmology

Chelouche D., Netzer H., 2001, *MNRAS* , 326, 916

Cottis C., 2010, PhD thesis, University of Leicester

Cottis C. E., Goad M. R., Knigge C., et al. 2010, *MNRAS* , 406, 2094

Crenshaw D. M., Kraemer S. B., 2007, *ApJ* , 659, 250

Crenshaw D. M., Kraemer S. B., 2012, *ApJ* , 753, 75

Crenshaw D. M., Kraemer S. B., Hutchings J. B., et al. 2000, *ApJL* , 545, L27

Crenshaw D. M., Kraemer S. B., Schmitt H. R., et al. 2009, *ApJ* , 698, 281

Crenshaw D. M., Rodriguez-Pascual P. M., Penton S. V., et al. 1996, *ApJ* , 470, 322

Cushing M. C., Vacca W. D., Rayner J. T., 2004, *PASP* , 116, 362

Dai X., Shankar F., Sivakoff G. R., 2012, *ApJ* , 757, 180

Dawson K. S., Schlegel D. J., Ahn C. P., et al. 2013, *AJ* , 145, 10

de Kool M., Arav N., Becker R. H., et al. 2001, *ApJ* , 548, 609

de Kool M., Korista K. T., Arav N., 2002, *ApJ* , 580, 54

de Vaucouleurs G., de Vaucouleurs A., Corwin Jr. H. G., et al. 1991, Third Reference Catalogue of Bright Galaxies. Volume I: Explanations and references. Volume II: Data for galaxies between 0^h and 12^h. Volume III: Data for galaxies between 12^h and 24^h.

Deutsch L. K., Hora J. L., Adams J. D., et al. 2003, in Iye M., Moorwood A. F. M., eds, Instrument Design and Performance for Optical/Infrared Ground-based Telescopes Vol. 4841 of Society of Photo-Optical Instrumentation Engineers (SPIE) Conference Series, MIRSI: a Mid-InfraRed Spectrometer and Imager. pp 106–116

Di Matteo T., Springel V., Hernquist L., 2005, *Nature* , 433, 604

Drake G. W., 1971, *Phys. Rev. A* , 3, 908

Dubbeldam M., Content R., Allington-Smith J. R., et al. 2000, in Iye M., Moorwood A. F., eds, Optical and IR Telescope Instrumentation and Detectors Vol. 4008 of Society of Photo-Optical Instrumentation Engineers (SPIE) Conference Series, Integral field unit for the Gemini near-infrared spectrograph. pp 1181–1192

Dunn J. P., Bautista M., Arav N., et al. 2010, *ApJ* , 709, 611

Edelson R. A., Alexander T., Crenshaw D. M., 1996, *ApJ* , 470, 364

Edge D. O., Shakeshaft J. R., McAdam W. B., et al. 1959, *MemRAS* , 68, 37

Eisenstein D. J., Weinberg D. H., Agol E., et al. 2011, *AJ* , 142, 72

Elvis M., 2000, *ApJ* , 545, 63

Everett J. E., 2005, *ApJ* , 631, 689

Fabricant D., Cheimets P., Caldwell N., et al. 1998, *PASP* , 110, 79

Fath E. A., 1909, Lick Observatory Bulletin, 5, 71

Ferland G. J., Korista K. T., Verner D. A., et al. 1998, *PASP* , 110, 761

Ferland G. J., Peterson B. M., Horne K., et al. 1992, *ApJ* , 387, 95

Ferland G. J., Porter R. L., van Hoof P. A. M., et al. 2013, *Rev. Mex. Astron. Astr.*, 49, 137

Ferrarese L., Merritt D., 2000, *ApJL* , 539, L9

Filippenko A. V., 1982, *PASP* , 94, 715

Filippenko A. V., Ho L. C., Sargent W. L. W., 1993, *ApJL* , 410, L75

Filiz Ak N., Brandt W. N., Hall P. B., et al. 2012, *ApJ* , 757, 114

Filiz Ak N., Brandt W. N., Hall P. B., et al. 2013, *ApJ* , 777, 168

Filiz Ak N., Brandt W. N., Hall P. B., et al. 2014, *ApJ* , 791, 88

Friedman H., Byram E. T., 1967, Science, 158, 257

Fukugita M., Ichikawa T., Gunn J. E., et al. 1996, *AJ* , 111, 1748

Gaibler V., 2014, Astronomische Nachrichten, 335, 531

Gandhi P., Horst H., Smette A., et al. 2009, *A&A* , 502, 457

Gaskell C. M., Benker A. J., 2007, ArXiv:0711.1013

Giacconi R., Gursky H., Paolini F. R., et al. 1962, Physical Review Letters, 9, 439

Gibson R. R., Brandt W. N., Gallagher S. C., et al. 2010, *ApJ* , 713, 220

Gibson R. R., Brandt W. N., Schneider D. P., et al. 2008, *ApJ* , 675, 985

Giustini M., Proga D., 2012, *ApJ* , 758, 70

Godfrey L. E. H., Lovell J. E. J., Burke-Spolaor S., et al. 2012, *ApJL* , 758, L27

Green P. J., Aldcroft T. L., Mathur S., et al. 2001, *ApJ* , 558, 109

Grevesse N., Sauval A. J., 1998, *Space Sci. Rev.*, 85, 161

Grier C. J., Peterson B. M., Pogge R. W., 2012, *ApJL* , 744, L4

Grupe D., Komossa S., Leighly K. M., et al. 2010, *ApJS* , 187, 64

Gunn J. E., Carr M., Rockosi C., et al. 1998, *AJ* , 116, 3040

Gunn J. E., Siegmund W. A., Mannery E. J., et al. 2006, *AJ* , 131, 2332

Haardt F., Maraschi L., 1991, *ApJL* , 380, L51

Hall P. B., Anderson S. F., Strauss M. A., et al. 2002, *ApJS* , 141, 267

Hamann F., Barlow T. A., Junkkarinen V., et al. 1997, *ApJ* , 478, 80

Hamann F., Capellupo D., Chartas G., et al. 2013, ArXiv e-prints

Hamann F., Kanekar N., Prochaska J. X., et al. 2011, *MNRAS* , 410, 1957

Hamann F., Kaplan K. F., Rodríguez Hidalgo P., et al. 2008, *MNRAS* , 391, L39

Hamann F., Sabra B., 2004, in Richards G. T., Hall P. B., eds, AGN Physics with the Sloan Digital Sky Survey Vol. 311 of Astronomical Society of the Pacific Conference Series, The Diverse Nature of Intrinsic Absorbers in AGNs. p. 203

Hamann F. W., Barlow T. A., Chaffee F. C., et al. 2001, *ApJ* , 550, 142

Hewett P. C., Wild V., 2010, *MNRAS* , 405, 2302

Hodapp K. W., Jensen J. B., Irwin E. M., et al. 2003, *PASP* , 115, 1388

Holweger H., 2001, in Wimmer-Schweingruber R. F., ed., Joint SOHO/ACE workshop "Solar and Galactic Composition" Vol. 598 of American Institute of Physics Conference Series, Photospheric abundances: Problems, updates, implications. pp 23–30

Hönig S. F., Watson D., Kishimoto M., et al. 2014, *Nature* , 515, 528

Hook I. M., Jørgensen I., Allington-Smith J. R., et al. 2004, *PASP* , 116, 425

Hopkins P. F., Elvis M., 2010, *MNRAS* , 401, 7

Horne K., 1986, *PASP* , 98, 609

Hutchings J. B., Crenshaw D. M., Kaiser M. E., et al. 1998, *ApJL* , 492, L115

Hutchings J. B., Crenshaw D. M., Kraemer S. B., et al. 2002, *AJ* , 124, 2543

Ji T., Zhou H., Jiang P., et al. 2015, *ApJ* , 800, 56

Jiang L., Fan X., Ivezić Ž., et al. 2007, *ApJ* , 656, 680

Kaiser M. E., Bradley II L. D., Hutchings J. B., et al. 2000, *ApJ* , 528, 260

Kaspi S., Maoz D., Netzer H., et al. 2005, *ApJ* , 629, 61

Kelly B. C., Bechtold J., Trump J. R., et al. 2008, *ApJS* , 176, 355

Khachikian E. E., Weedman D. W., 1971, Astrofizika, 7, 389

King A. R., 2010, *MNRAS* , 402, 1516

Knigge C., Scaringi S., Goad M. R., et al. 2008, *MNRAS* , 386, 1426

Korista K., Baldwin J., Ferland G., et al. 1997, *ApJS* , 108, 401

Korista K. T., Voit G. M., Morris S. L., et al. 1993, *ApJS* , 88, 357

Koski A. T., 1978, *ApJ* , 223, 56

Kraemer S. B., Crenshaw D. M., Gabel J. R., et al. 2006, *ApJS* , 167, 161

Kraemer S. B., Crenshaw D. M., Hutchings J. B., et al. 2001, *ApJ* , 551, 671

Kraemer S. B., George I. M., Crenshaw D. M., et al. 2005, *ApJ* , 633, 693

Kriss G. A., Davidsen A. F., Zheng W., et al. 1999, *ApJ* , 527, 683

Landt H., Bentz M. C., Ward M. J., et al. 2008, *ApJS* , 174, 282

Landt H., Elvis M., Ward M. J., et al. 2011, *MNRAS* , 414, 218

Leighly K. M., Dietrich M., Barber S., 2011, *ApJ* , 728, 94

Liu F. K., Zhang Y. H., 2002, *A&A* , 381, 757

Liu W.-J., Zhou H., Ji T., et al. 2015, ArXiv e-prints

Lundgren B. F., Wilhite B. C., Brunner R. J., et al. 2007, *ApJ* , 656, 73

Lupton R., Gunn J. E., Ivezić Z., et al. 2001, in Harnden Jr. F. R., Primini F. A., Payne H. E., eds, Astronomical Data Analysis Software and Systems X Vol. 238 of Astronomical Society of the Pacific Conference Series, The SDSS Imaging Pipelines. p. 269

Magorrian J., Tremaine S., Richstone D., et al. 1998, *AJ* , 115, 2285

McGregor P., Hart J., Stevanovic D., et al. 2004, in Moorwood A. F. M., Iye M., eds, Ground-based Instrumentation for Astronomy Vol. 5492 of Society of Photo-Optical Instrumentation Engineers (SPIE) Conference Series, Gemini South Adaptive Optics Imager (GSAOI). pp 1033–1044

McGregor P. J., Hart J., Conroy P. G., et al. 2003, in Iye M., Moorwood A. F. M., eds, Instrument Design and Performance for Optical/Infrared Ground-based Telescopes Vol. 4841 of Society of Photo-Optical Instrumentation Engineers (SPIE) Conference Series, Gemini near-infrared integral field spectrograph (NIFS). pp 1581–1591

Minezaki T., Yoshii Y., Kobayashi Y., et al. 2004, *ApJL* , 600, L35

Misawa T., Eracleous M., Charlton J. C., et al. 2007, *ApJ* , 660, 152

Moe M., Arav N., Bautista M. A., et al. 2009, *ApJ* , 706, 525

Mortlock D. J., Warren S. J., Venemans B. P., et al. 2011, *Nature* , 474, 616

Murray N., Chiang J., Grossman S. A., et al. 1995, *ApJ* , 451, 498

Narayanan D., Hamann F., Barlow T., et al. 2004, *ApJ* , 601, 715

Natali F., Giallongo E., Cristiani S., et al. 1998, *AJ* , 115, 397

Ogle P. M., Cohen M. H., Miller J. S., et al. 1997, *ApJL* , 482, L37

Osterbrock D. E., Ferland G. J., 2006, Astrophysics of gaseous nebulae and active galactic nuclei

Pei Y. C., 1992, *ApJ* , 395, 130

Penston M. V., Robinson A., Alloin D., et al. 1990, *A&A* , 236, 53

Peterson B. M., 1997, An Introduction to Active Galactic Nuclei

Peterson B. M., 2014, *Space Sci. Rev.*, 183, 253

Peterson B. M., Wanders I., Bertram R., et al. 1998, *ApJ* , 501, 82

Planck Collaboration XVI 2014, *A&A* , 571, A16

Pogge R. W., 1989a, in Meurs E. J. A., Fosbury R. A. E., eds, European Southern Observatory Conference and Workshop Proceedings Vol. 32 of European Southern Observatory Conference and Workshop Proceedings, Extended Ionized Gas in Seyferts and Unified Seyfert Models. p. 411

Pogge R. W., 1989b, *ApJ* , 345, 730

Popović L. Č., 2003, *ApJ* , 599, 140

Pounds K. A., King A. R., Page K. L., et al. 2003, *MNRAS* , 346, 1025

Prieto M. A., Reunanen J., Tristram K. R. W., et al. 2010, *MNRAS* , 402, 724

Proga D., Stone J. M., Kallman T. R., 2000, *ApJ* , 543, 686

Rayner J., Bond T., Bonnet M., et al. 2012, in Society of Photo-Optical Instrumentation Engineers (SPIE) Conference Series Vol. 8446 of Society of Photo-Optical Instrumentation Engineers (SPIE) Conference Series, iSHELL: a 1-5 micron cross-dispersed R=70,000 immersion grating spectrograph for IRTF. p. 2

Rayner J. T., Toomey D. W., Onaka P. M., et al. 2003, *PASP* , 115, 362

Reichard T. A., Richards G. T., Hall P. B., et al. 2003, *AJ* , 126, 2594

Reichard T. A., Richards G. T., Schneider D. P., et al. 2003, *AJ* , 125, 1711

Reimers D., Hagen H.-J., Schramm J., et al. 2005, *A&A* , 436, 465

Riffel R., Rodríguez-Ardila A., Pastoriza M. G., 2006, *A&A* , 457, 61

Riffel R. A., Storchi-Bergmann T., McGregor P. J., 2009, *ApJ* , 698, 1767

Rodríguez-Ardila A., Mazzalay X., 2006, *MNRAS* , 367, L57

Rodríguez-Ardila A., Pastoriza M. G., Viegas S., et al. 2004, *A&A* , 425, 457

Rodríguez Hidalgo P., Hamann F., Hall P., 2011, *MNRAS* , 411, 247

Rodriguez Hidalgo P. R., Hamann F., Eracleous M., et al. 2012, in Chartas G., Hamann F., Leighly K. M., eds, AGN Winds in Charleston Vol. 460 of Astronomical Society of the Pacific Conference Series, Variability of Mini-BAL and BAL Outflows in Quasars. p. 93

Rose M., Tadhunter C. N., Holt J., et al. 2011, *MNRAS* , 414, 3360

Savage B. D., Sembach K. R., 1991, *ApJ* , 379, 245

Scaringi S., Cottis C. E., Knigge C., et al. 2009, *MNRAS* , 399, 2231

Schippers S., Müller A., Gwinner G., et al. 2001, *ApJ* , 555, 1027

Schlegel D. J., Finkbeiner D. P., Davis M., 1998, *ApJ* , 500, 525

Schmidt G. D., Hines D. C., 1999, *ApJ* , 512, 125

Schmidt M., 1963, *Nature* , 197, 1040

Schnülle K., Pott J.-U., Rix H.-W., et al. 2013, *A&A* , 557, L13

Schultz G. V., Wiemer W., 1975, *A&A* , 43, 133

Seyfert C. K., 1943, *ApJ* , 97, 28

Shakura N. I., Sunyaev R. A., 1973, *A&A* , 24, 337

Shen Y., Richards G. T., Strauss M. A., et al. 2011, *ApJS* , 194, 45

Shure M. A., Toomey D. W., Rayner J. T., et al. 1994, in Crawford D. L., Craine E. R., eds, Instrumentation in Astronomy VIII Vol. 2198 of Society of Photo-Optical Instrumentation Engineers (SPIE) Conference Series, NSFCAM: a new infrared array camera for the NASA Infrared Telescope Facility. pp 614–622

Silk J., Rees M. J., 1998, *A&A* , 331, L1

Smits D. P., 1996, *MNRAS* , 278, 683

Sprayberry D., Foltz C. B., 1992, *ApJ* , 390, 39

Springel V., Di Matteo T., Hernquist L., 2005, *MNRAS* , 361, 776

Stoughton C., Lupton R. H., Bernardi M., et al. 2002, *AJ* , 123, 485

Tinker J., SDSS-IV Collaboration 2015, in American Astronomical Society Meeting Abstracts Vol. 225 of American Astronomical Society Meeting Abstracts, The Start of SDSS-IV and eBOSS. p. 125.06

Tody D., 1986, in Crawford D. L., ed., Instrumentation in astronomy VI Vol. 627 of Society of Photo-Optical Instrumentation Engineers (SPIE) Conference Series, The IRAF Data Reduction and Analysis System. p. 733

Trevese D., Saturni F. G., Vagnetti F., et al. 2013, *A&A* , 557, A91

Trump J. R., Hall P. B., Reichard T. A., et al. 2006, *ApJS* , 165, 1

Turnshek D. A., 1988, in Blades J. C., Turnshek D. A., Norman C. A., eds, QSO Absorption Lines: Probing the Universe BAL QSOs: Observations, Models and Implications for Narrow Absorption Line Systems. p. 17

Unger S. W., Pedlar A., Axon D. J., et al. 1987, *MNRAS* , 228, 671

Urry C. M., Padovani P., 1995, *PASP* , 107, 803

Vanden Berk D. E., Richards G. T., Bauer A., et al. 2001, *AJ* , 122, 549

Vanden Berk D. E., Wilhite B. C., Kron R. G., 2004, *ApJ* , 601, 692

Véron-Cetty M.-P., Joly M., Véron P., 2004, *A&A* , 417, 515

Véron-Cetty M.-P., Véron P., 2006, *A&A* , 455, 773

Vestergaard M., 2004, *ApJ* , 601, 676

Vignali C., Brandt W. N., Schneider D. P., 2003, *AJ* , 125, 433

Vivek M., Srianand R., Mahabal A., et al. 2012, *MNRAS* , 421, L107

Warner C., Hamann F., Dietrich M., 2004, *ApJ* , 608, 136

Weymann R. J., Morris S. L., Foltz C. B., et al. 1991, *ApJ* , 373, 23

Wildy C., Goad M. R., Allen J. T., 2014, *MNRAS* , 437, 1976

Wildy C., Goad M. R., Allen J. T., 2015, *MNRAS* , 448, 2397

Wilhite B. C., Vanden Berk D. E., Brunner R. J., et al. 2006, *ApJ* , 641, 78

Wilkes B. J., Tananbaum H., Worrall D. M., et al. 1994, *ApJS* , 92, 53

Woo J.-H., Treu T., Barth A. J., et al. 2010, *ApJ* , 716, 269

York D. G., 2000, *AJ* , 120, 1579

Zakamska N. L., Greene J. E., 2014, *MNRAS* , 442, 784

Zdziarski A. A., Gierlinski M., Gondek D., et al. 1996, *A&AS* , 120, C553

Zier C., Biermann P. L., 2002, *A&A* , 396, 91